Solid State NMR Studies of Structure and Dynamics in Systems of Biological Interest

by

Joanna R. Long

B.S. Chemistry

University of Arkansas, 1990

Submitted to the Department of Chemistry
in Partial Fulfillment of the Requirements for the Degree of
Doctor of Philosophy in Physical Chemistry

at the

Massachusetts Institute of Technology

February 1997

Signature of Author: _____
Department of Chemistry
September 26, 1996

Certified by: _____
Robert G. Griffin
Professor of Chemistry
Thesis Supervisor

Accepted by: _____
Dietmar Seyferth
Professor of Chemistry
Chairman, Departmental Committee on Graduate Students

This Doctoral thesis has been examined by a Committee of the Department of Chemistry as follows:

Professor Bruce Tidor _____
Chairman

Professor James R. Williamson _____

Professor Robert G. Griffin _____
Thesis Supervisor

Solid State NMR Studies of Structure and Dynamics
in Systems of Biological Interest

by
Joanna R. Long

Submitted to the Department of Chemistry
September 26, 1996 in partial fulfillment of the requirements for the Degree of Doctor of Philosophy in Physical Chemistry

ABSTRACT

Deuterium NMR provides insight into dynamics over a wide range of kinetic rates. Experimental data can be rigorously fit and rates as well as motional mechanisms extracted. Temperatures dependent studies yield activation energies for key dynamic processes. Two model systems with well-characterized motions were studied to demonstrate this. The ammonium group in L-alanine has an activation energy of 40.5 kJ/mol for three-site hopping. The hopping rate at room temperature is on the order of 10^6/sec and is comparable to the radio frequency fields and cycle times of many solid state NMR experiments. This explains the anomalous broadening observed in nitrogen magic angle spinning spectra and proton multiple pulse spectra. Barium chlorate monohydrate provides an excellent model system for examining the accuracy and specificity of simulations. Twofold flips of the water molecule about its bisector fit the observed data and simulations yield an activation energy of 30 kJ/mol. Inclusion of vibrational averaging of the quadrupole coupling and nonzero eta lead to a 10% difference in simulated rates.

The dynamics of cerebroside bilayers in the L_α phase were observed using standard inversion recovery and broadbanded Jeener-Broekaert techniques. The deuterium lineshapes of labelled positions in the polymethylene chain are axially symmetric with splittings dependent on temperature and the position. The first seven segments have similar splittings with slight oscillations or an even-odd effect. These oscillations differ from those seen in phosphatidylcholine bilayers. This discrepancy may be explained by incorporating distortions of the polymethylene chain relative to the molecular director. Various models of motion and their corresponding correlation functions are discussed. The calculations of correlation functions in systems with multiple motions is simplified if the motions are uncorrelated. Models incorporating gauche-trans isomerization with axial diffusion via either three-site hopping or continuous rotation are inadequate in modeling the observed relaxation behavior. Reorientation of the molecular director must be taken into account.

The recent discovery of short helices which form appreciable amounts of helix provides an ideal system in which helix formation may be observed via deuterium NMR. The helical structure of one such peptide was determined via solid state NMR dipolar recoupling techniques. This peptide was then synthesized with deuterium labels using solid-phase peptide synthesis on two different resins. The dynamic behavior of the peptide on these two resins is markedly different. On one of the resins evidence of significant long-term interactions is observed. This has implications for combinatorial peptide libraries on which assays are done while the peptides are still attached to the resin. The second resin-peptide system displays intermediate range dynamics which are being investigated further.

Thesis Supervisor: Dr. Robert G. Griffin
Title: Professor of Chemistry

For my parents who encouraged me,

my siblings who helped me keep things in perspective,

and the boys, James, Jonathan, and Tahsis, who play with me

Table of Contents

Acknowledgments

As anyone who does solid state NMR of biological compounds knows, doing experiments requires the cooperation of many people in addition to the instrumentation and chemistry. When I first joined the lab, Ling Zheng showed me how to do deuterium NMR as well as simulations; Ken Fishbein was always happy to open a box up and explain what was inside. Sunil Das Gupta synthesized the lipid samples. The nitrogen simulations of the L-alanine date were done by Boqin Sun. Peter Lansbury's group was kind enough to teach me how to do peptide synthesis and purification. Several other members of the Griffin group have also contributed to my graduate experience. I had many helpful discussions with Doug Maus and John Gross on deuterium dynamics. The probe used for the dipolar recoupling experiments was built by Chad Rienstra; Andrew Bennett, Phil Costa, and Chad provided insights on dipolar recoupling experiments. Ajay Thakkar and Peter Allen patiently put up with all my requests for machining and taught me how to solder. Just about everyone in the group, as well as many past members, has encouraged or inspired me at some point. Finally, Bob has put up with my outspoken style a lot more than some advisors would and admirably supported me when I did the unthinkable and had "twins!" while in graduate school.

Outside of the lab I have had the opportunity to know many other members of the MIT community. Our years at Bexley Hall will be fondly remembered and I look forward to telling my sons stories of when they lived at Bexley and all the friends and adventures they had. My life would not be complete without the desk discussions, dry ice bombs, encouragement of James' crazy schemes, and general mayhem that is life at Bexley.

1. Structure and Dynamics in Biology

1.1 Lipid Bilayers

One of the most fundamental aspects of our existence is the ability to compartmentalize and control chemical reactions. This is made possible by numerous membranes and infrastructure. The basis of these membranes is the lipid bilayer, which is comprised of ampipathic lipid molecules which each have a hydrophilic head group linked to hydrophobic hydrocarbon chains. When placed in water, the lipid molecules spontaneously self associate so that the hydrophobic regions interact with each other and not the surrounding water. The result is the polar headgroups lie on the surfaces of the bilayer and is known as the hydrophobic effect (Figure 1.1a). Compartmentalization is not enough by itself; there must be some permeability of the membrane and the ability to regulate it. Additionally the headgroups may associate with proteins and other molecules with some actually implanting into the lipid bilayer. These characteristics mean that the lipid bilayer itself has some control over intercellular communication, cellular association, and enzymatic reactions.

In order to be biologically relevant, a lipid bilayer must be in the fluid phase. This means that the interactions between lipid molecules are short lived. The fluid mosaic model (Figure 1.1b) for how lipids form the cell wall and interact with their surroundings was first proposed by Singer and Nicholson (Singer & Nicholson, 1972). In this model, proteins are dissolved in the membrane. Since the membrane is fluid, the proteins and lipid molecules may move freely in two dimensions, but their motion in the third direction, perpendicular to the plane of the bilayer, is restricted. More recently, it has also been shown that some degree of control may be exhibited in the two dimensions parallel to the plane of the bilayer. Phase separation within the bilayer as well as the restriction of a protein in the bilayer have been demonstrated (Darnell et al., 1990). These constraints may be imposed by interactions of lipids and membrane proteins with other proteins, the cytoskeleton, or even cations.

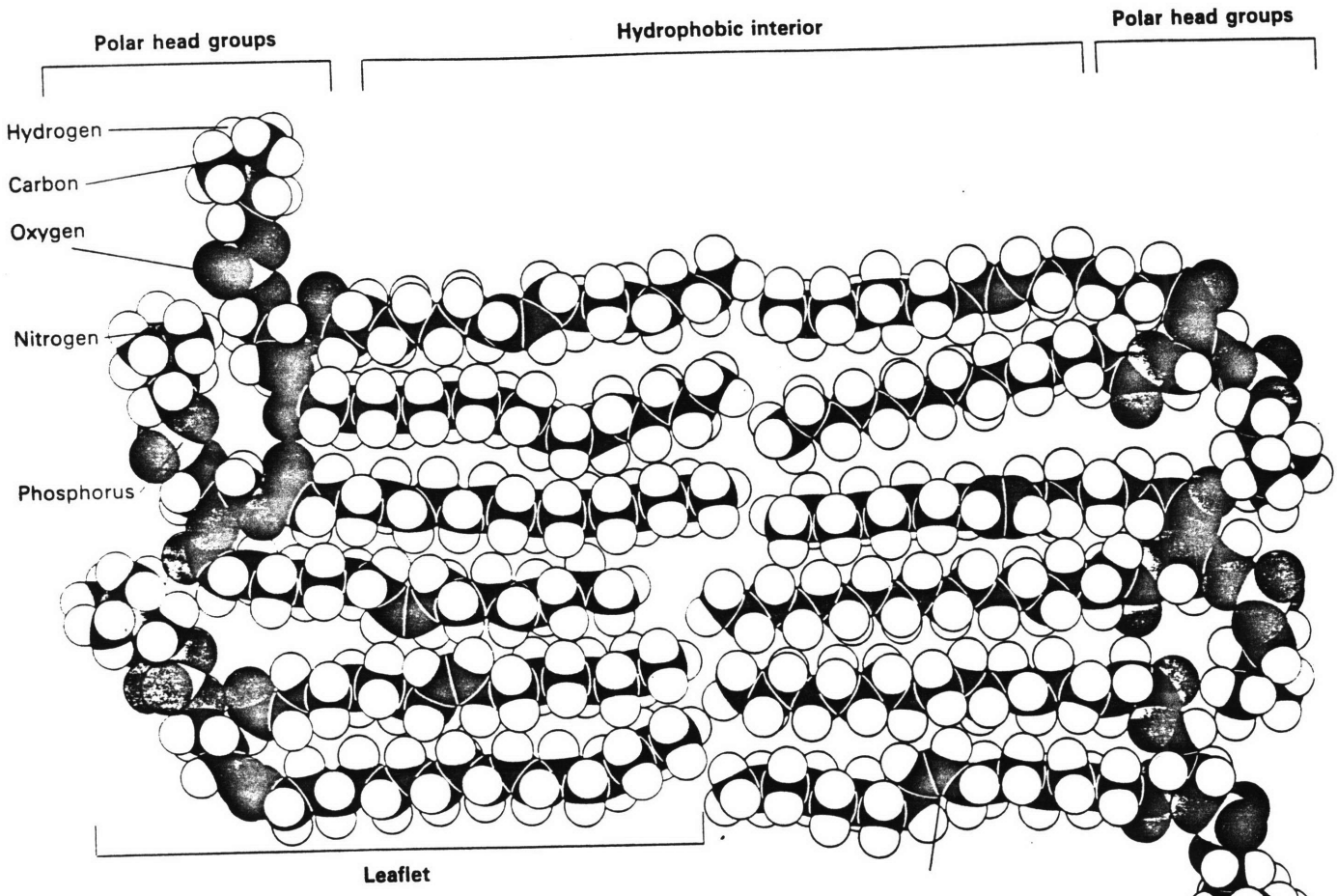

Figure 1.1a Space-filling model of a phospholipid bilayer (from Stryer, 1988).

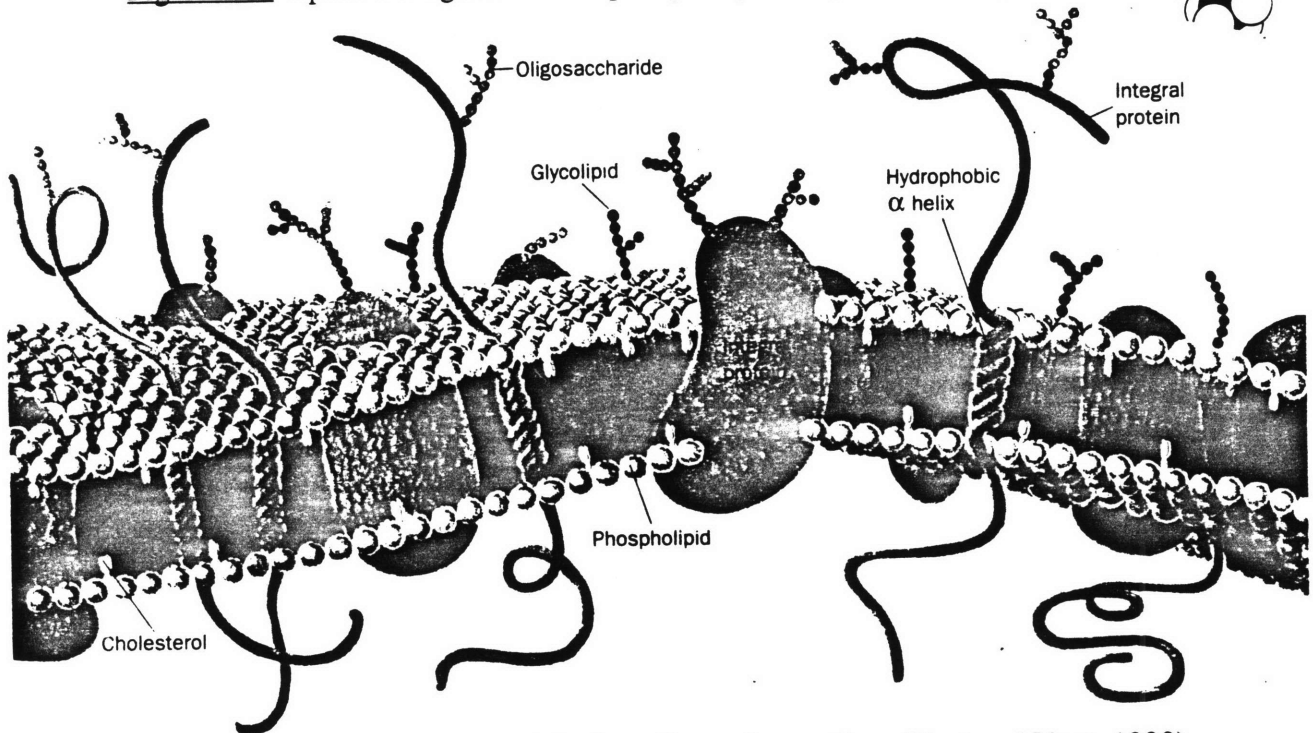

Figure 1.1b The fluid mosaic model of a cell membrane (from Voet and Voet, 1990).

Studies of plasma membranes have revealed that the lipid composition of the two sides or leaflets in the bilayer are distinct. Phospholipids and cholesterol and are found in equal amounts, but glycolipids are primarily found on the extracellular side of the membrane. In contrast, lipids with headgroups that are negatively charged are found on the cytoplasmic side (Rothman & Lenard, 1977). In order to understand how the components of a complex cell membrane contribute to the physical and biochemical properties, many lipids have been purified or synthesized and studied in depth. These simplified systems, consisting of a single type of lipid or a biologically relevant stoichiometric combination of two or three lipids, form bilayers which display many of the characteristics of cell membranes.

A pure lipid bilayer made up of a specific type of lipid molecule will undergo a distinct phase transition at a characteristic temperature. The length and degree of saturation of the hydrocarbon chains as well as the type of headgroup have profound effects on what this temperature is. The temperature as well as the sharpness of the transition is altered by the addition of other components to the bilayer such as other types of lipids or cholesterol . Other physical characteristics, such as bilayer thickness and viscosity, can also be altered either by a temperature change or by association of the lipids with either cations in the water environment or anesthetics in the hydrophobic region (Voet & Voet, 1990). A change in bilayer thickness can alter the association of membrane spanning proteins and peptides with the bilayer and cause changes in their internal conformations. Thus cell wall permeability is very sensitive to its component lipids, intercalcating molecules, intracellular and extracellular interactions, and temperature.

Over the years numerous studies have been conducted in order to understand the structure and dynamics of lipid bilayers and the effects of interactions with various intra- and extracellular constituents. However, since a fluid bilayer is not strictly a liquid or solid but instead somewhat intermediate between them, most of these experiments have focused on determining overall physical properties such as viscosity, melting tempera-

ture, or bilayer thickness. Understanding the molecular basis of even simple interactions such as cholesterol intercalcation into different types of lipid bilayers has only recently been attempted. Much of our present understanding of lipids at a molecular level has been accomplished through the use of solid state NMR.

Although many lipids have been studied and several models of molecular motion have been investigated (Davis, 1993; Meier et al., 1986; Seelig, 1977; Seelig & Seelig, 1980; Speyer et al., 1989), there is yet to be published in the literature a comprehensive study of the conformation and dynamics of hydrocarbon chains in a pure lipid bilayer. The research here accomplishes this task. These models of lipid conformation and dynamics are critically assessed and the determination of kinetic rates and activation energies using various models is assessed. In addition, the interaction of cholesterol with the bilayer has been studied.

The lipid molecule chosen for these studies is N,N-palmitoylgalactosylsphingosine (NPGS) (Figure 1.2a). This lipid is most prevalent in the membranes of neurons in the brain. It has been of particular interest in the Griffin lab over the years because of its high melting temperature as well its interaction with cholesterol. In contrast to phospholipids with the same hydrocarbon chains, NPGS has a melting temperature approximately 40° C higher.

When studying pure lipid bilayers in water, the bilayers actually form liposomes which are large, multilamellar bilayer vesicles. Liposomes are generally of the size on the order of hundreds of angstroms and therefore tumble more slowly than the msec timescale on which the NMR experiments are performed. In the absence of other molecules, hydrated NPGS exists in one of two phases. At lower temperatures, the gel phase is observed. This phase is relatively ordered and in deuterium NMR it is characterized by any axial diffusion being slower than the frequency of the quadrupolar interaction. Above the transition temperature, the bilayer becomes "liquid crystalline" referring to its more disordered fluid phase. Fast rotational diffusion significantly narrows the

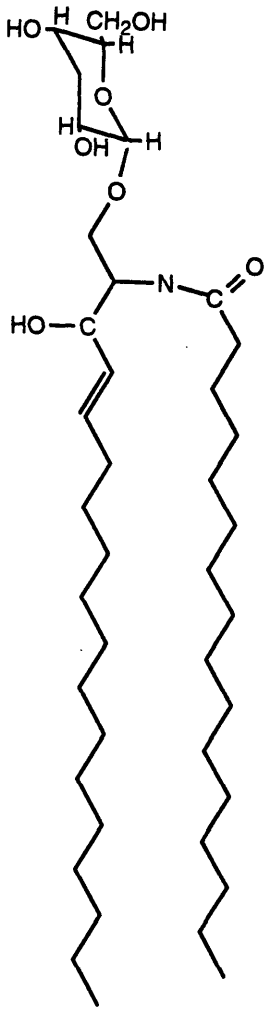

Figure 1.2a N-palmitoylgalactosylsphingosine (NPGS)

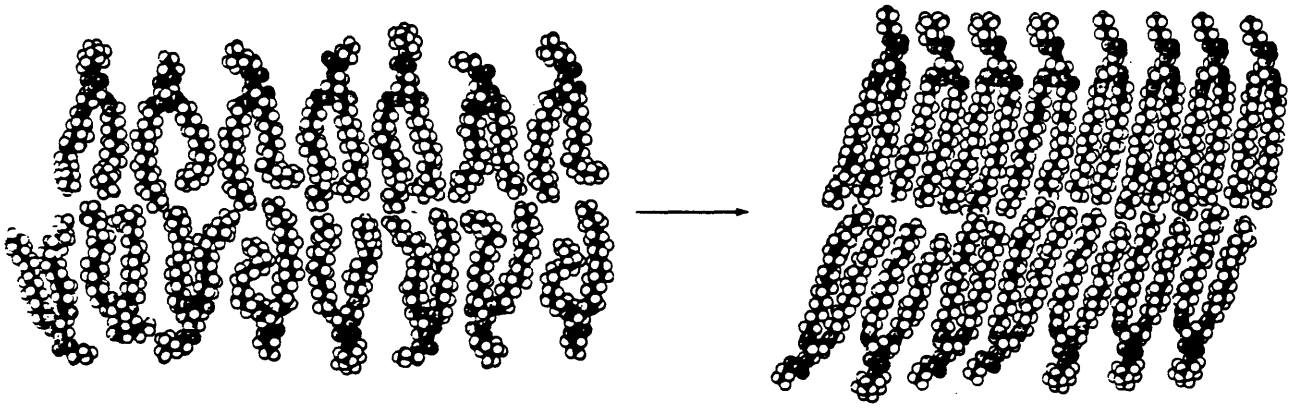

Figure 1.2b Spacefilling models of a lipid bilayer above and below the phase transition (from Voet and Voet, 1990). Note the change in bilayer thickness.

NMR spectrum. The hydrocarbon chains also becomes more disordered and shorter leading to a decrease in bilayer thickness (Figure 1.2b).

When cholesterol is added to the lipid bilayer, the existence of two distinct phases may be seen using deuterium NMR suggesting slow interchange between the two phases. This has not previously been observed in other lipid:cholesterol systems. These differences may be a consequence of hydrogen bonding between the amide groups found in NPGS. The effect of cholesterol on the bilayer is to broaden the transition between the two phases and lower the melting temperature. However spectra of the melted bilayer are somewhat broader than those observed for the liquid crystalline phase of the pure bilayer suggesting that the hydrocarbon chains are somewhat less motionally averaged. These observations have led to the assertion that the effect of cholesterol is to disorder the gel phase and increase order in the liquid crystalline phase.

1.2 Protein Folding

The elucidation of how a given DNA sequence determines the amino acid sequence of a protein and the demonstration that all the information needed to determine the three-dimensional structure of this protein is given by the amino acid sequence has led to one of the "great questions" of modern biology, physics, and chemistry--what forces determine the intricate, unique structure of a protein based solely on its amino acid sequence? In the last 40 years several experimental and theoretical studies have provided various levels of insight into possible kinetic pathways along which a protein might fold (Anfinsen & Scheraga, 1975; Chan & Dill, 1991; Kim & Baldwin, 1990), but there exists a dearth of information linking the two approaches at a molecular level---the longest molecular dynamics simulations last a few nanoseconds and the fastest stop-flow experiments fail to observe events in the first 10 msec of folding. It is estimated that key events in protein folding--helix-coil transitions and hinge motions --occur at rates of 10^5-10^7 and 10^8-10^{10} per second, respectively; These time scales severely restrict detailed analyses by either theoretical or standard experimental procedures. Deuterium nuclear magnetic

resonance spectroscopy (^{2}H NMR) is sensitive to motional rates on the order of 10^3-10^{10} per second and can distinguish between motional models at a molecular level; thus ^{2}H NMR is an ideal tool for studying protein folding and can provide a link between standard experiments and theory.

A global search of all possible conformations by a protein in order to determine its native structure is unreasonable. A protein 100 residues in length has well over 10^{100} possible conformations; given that conformational changes occur at a rate of 10^{13} per second or less, it could ~20 billion years for this protein to find a global minimum using a random search (Levinthal, 1968). However, some proteins have been shown to fold in a matter of minutes under *in vitro* conditions, and, *in vivo*, native conformations can be attained even more quickly (Anfinsen &Scheraga, 1975). These observations have lead to theories about folding pathways which a protein would follow in reaching its native three dimensional structure. The observation of various classes of secondary structure in proteins, namely α-helices, β-sheets, and β turns, has also lead to hierarchical approaches to protein folding

Currently, the generally accepted protein-folding process is that nascent secondary structure is formed (Figure 1.3), followed by tertiary interactions which stabilize secondary structure and determine the final conformation. Several experimental techniques, including exchange liquid NMR, oxidation and reformation of disulfide bonds between cysteine side chains, and peptide cleavage, have validated this viewpoint (Kim & Baldwin, 1990). What remains to be examined is what forces favor the formation of these secondary structures and whether the secondary structure of a given peptide sequence can be predicted.

From an empirical standpoint, based on known protein structures, one can predict the conformation of various amino acids in a given protein with 60-70% accuracy (Anfinsen &Scheraga, 1975); thus, it is surmised that short-range interactions play a major role. This has lead to the categorization of amino acids as helix-making, helix-

breaking, and indifferent. In addition, one can predict whether a given amino acid will be found more commonly at the surface of a protein or in the interior, by considering hydrophobic effects. However, calorimetric measurements have shown that the energetic differences between the random coil and native conformations of many proteins are quite small, and a majority of peptides, when removed from the context of a protein, fail to form identical secondary structure at observable levels in water (Anfinsen &Scheraga, 1975). Also, the hydrogen bonds which form with secondary structure do not contribute significantly to stability since they merely replace hydrogen bonds with water. What remains to counteract the loss of conformational entropy on folding is a gain in entropy from the release of water ordered by hydrophobic side chains and Van der Waals interactions in the protein interior. Given these considerations, it is possible that the formation of most secondary structure does not occur spontaneously in water, but that the protein initially undergoes a hydrophobic collapse which favors the subsequent formation of secondary structure due to the restriction of conformational space and the exclusion of water from the interior (Chan & Dill, 1991).

In spite of the above arguments, short peptides exist which form significant amounts of helical structure in water (Marqusee et al., 1989; Miick et al., 1992), although they are longer than the average helix found in proteins. Also, nascent helices and β-turns have been observed using NMR techniques (Wright et al., 1988). Thus ideal systems of manageable size do exist for studying helix-coil transitions and β-turn formations and quantifying the possible driving forces in protein folding. To date, these peptides have been studied by methods which allow only a macroscopic determination of their properties, namely the helix/coil ratio, the average helix propensities of some amino acids averaged over entire peptides, the change in enthalpy on melting, and the observation of a significant population of peptide in a β-turn conformation. Determination of helix-coil transition rates and elucidation of molecular dynamics have been precluded by the accessible time scales and specificity of the methods utilized.

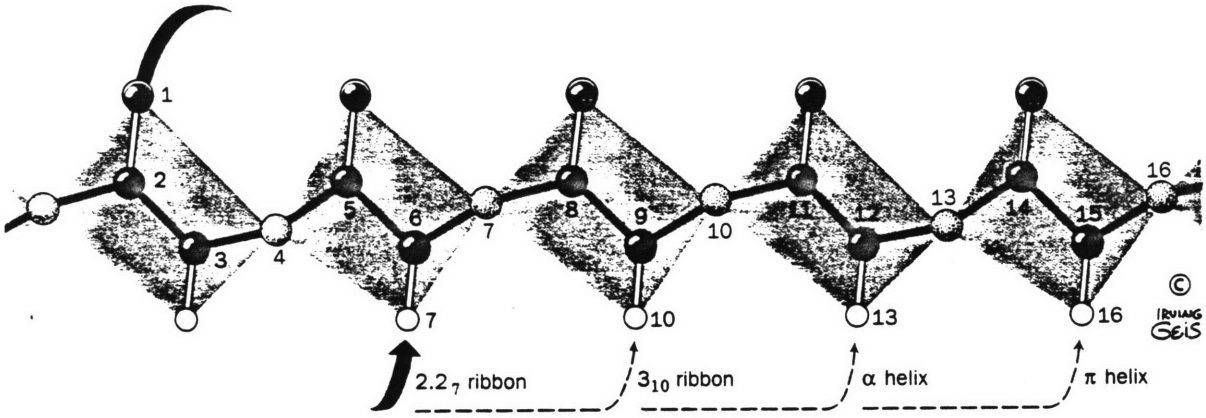

Figure 1.3a Peptide backbone showing possible hydrogen bonding and resulting secondary structure (from Voet and Voet, 1990).

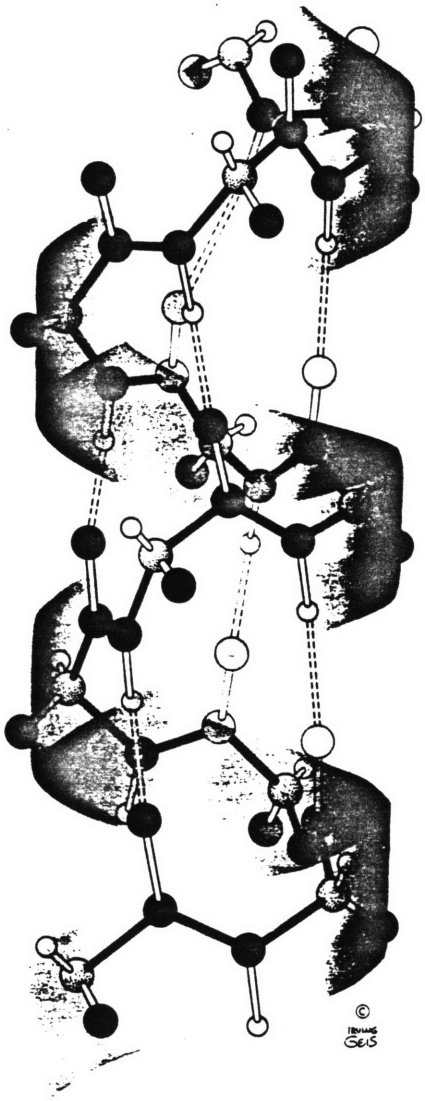

Figure 1.3b Peptide forming a right-handed α-helix (from Voet and Voet, 1990).

1.3 Solid State NMR

^2H NMR, given its wide dynamic range and spectroscopic detail, is a technique which could determine the dynamics of these systems and distinguish various energetic contributions. Deuterium has the additional advantage of having only 0.16% natural abundance, so only specifically labeled sites in a molecule are observed. Labeling with deuterium is also less invasive than using spin labels for ESR spectroscopy. Several specifically deuterated compounds are commercially available, making the experiments described in the following chapters feasible.

Chapter 2 gives a general description of the quadrupolar interaction and deuterium NMR spectroscopy. In addition, a short synopsis of computer simulations used to fit the experimental data is given.

To validate the use of quadrupole echo simulations in fitting echo lineshape and relaxation parameters, two model compounds were studied using deuterium NMR. In Chapter 3, the results of these studies are presented. The motion of the ammonium group of crystalline L-alanine was studied as an example of three-fold hopping. In addition, this model compound is ideal for demonstrating the effects of inequivalent sites due to hydrogen bonding. Experimental spectra were fit to computer simulations of quadrupole echo spectra at various kinetic rates using geometries obtained from neutron diffraction data and quadrupole coupling constants measured by single crystal experiments. In addition, inversion recovery experiments were carried out and simulated. Of interest in interpreting results of other solid state NMR techniques, the ammonium group is hopping at a rate of only 1.5×10^6 at 19° C; this explains why room temperature multiple pulse experiments fail to give a high resolution spectrum at the ammonium group resonance . In addition, nitrogen chemical shift spectra at various temperature demonstrate how motion on the order of 10^5-10^7 can affect the efficiency of proton decoupling in standard solid state NMR experiments. A second study was conducted on the water molecule in barium chlorate monohydrate. This system provides an ideal example of two-site flipping mo-

tion. Additionally, in a simple system such as this the effects of various assumptions made in doing deuterium NMR simulations may be explored. For example it was demonstrated that both small angle libration at high frequencies and slightly assymmetric quadrupolar couplings have small but measurable (5-10%) effects when determining rate constants using simulations of relaxation and powder lineshapes.

The level of detail obtained with deuterium NMR is not limited to simple motions in model compounds. Chapter four presents a comprehensive study of a side-chain labeled lipid in the L_α phase. This system demonstrates that it is possible to differentiate between simultaneous motions and determine independent rate constants; also, the populations of various molecular orientations can be determined. However, developing a complex model of motion and proving its validity requires obtaining an exhaustive amount of data and careful attention to matching variables with experimental measurements. Chapter five extends the study of this lipid to its interactions with cholesterol using both ^2H NMR and ^{13}C NMR.

Given the level of detail possible in ^2H NMR spectra, this technique is uniquely suited to a study peptide dynamics. Chapter 5 provides recent results in studying a peptide which forms appreciable amounts of alpha helix in water. In order to study the dynamics of such a system it is first necessary to understand the range of structures a specific peptide sequence may adapt in a given environment. To this end, solid state NMR techniques for measuring internuclear distances were applied. Of particular importance in obtaining spectral detail from ^2H NMR experiments is ensuring motion is primarily anisotropic. Since small peptides tumble isotropically on a time scale shorter than the ^2H NMR time scale when dissolved in water, they must be anchored to a support in order to make deuterium NMR experiments useful. Also, the interaction of the peptide with any support used to make it behave anisotropically must also be observed. Experiments addressing these questions are also presented in Chapter 5.

References

Anfinsen, C.B. & Scheraga, H.A. (1975) *Advances in Protein Chemistry 29*, 205-300.

Chan, H.S. & Dill, K.A. (1991) *Annual Review of Biophysical Chemistry 20*, 447-90.

Darnell, J., Lodish, H. & Baltimore, D. (1990) *Molecular Cell Biology*, Scientific American Books, New York.

Davis, J.H. (1993)

Kim, P.S. & Baldwin, R.L. (1990) *Annual Review of Biochemistry 59*, 631-60.

Levinthal, C. (1968) *Journal of Chemical Physics 65*, 44.

Marqusee, S., Robbins, V.H. & Baldwin, R.L. (1989) *Proceedings of the National Academy of Sciences 86*, 5286-90.

Meier, P., Ohmes, E. & Kothe, G. (1986) *Journal of Chemical Physics 85*, 3598-3614.

Miick, S.M., Martinez, G.V., Fiori, W.R., Todd, A.P. & Millhauser, G.L. (1992) *Nature 359*, 653-655.

Rothman, J. & Lenard, J. (1977) *Science 195*, 743-753.

Seelig, J. (1977) *Quarterly Reviews of Biophysics 10*, 353-418.

Seelig, J. & Seelig, A. (1980) *Quarterly Review of Biophysics 13*, 19-61.

Singer, S.J. & Nicholson, G.L. (1972) *Science 175*, 720-731.

Speyer, J.B., Weber, R.T., Das Gupta, S.K. & Griffin, R.G. (1989) *Biochemistry 28*, 9569-74.

Stryer, L. (1988) *Biochemistry*, W. H. Freeman and Company, New York.

Voet, D. & Voet, J. (1990) *Biochemistry*, John Wiley & Sons, New York.

Wright, P.E., Dyson, H.J. & Lerner, R.A. (1988) *Biochemistry 27*, 7167-75.

2. Solid State NMR

What follows is a brief discussion of deuterium NMR. It is a summary of the concepts presented in several works, especially the reviews of Davis, the Volds, and Spiess (Davis, 1983; Davis, 1991; Spiess, 1978; Vold & Vold, 1991). The reader is encouraged to go to these sources for a more indepth discussion.

Deuterium is a spin-1 nucleus, and therefore possesses a quadrupolar moment. The interaction of the nucleus with its surroundings in a magnetic field can be described by the Hamiltonian

H =	H_Z +	H_Q +	H_D +	H_{CS} +	H_J
Solid (^{2}H AT 11.7 T)	76.8 MHz	150-250 kHz	10 kHz	1 kHz	0.1 kHz
Liquid	76.8 MHz	0	0	1 kHz	0.1 kHz

where H_Z represents the Zeeman interaction with the magnetic field, H_Q the quadrupole coupling with the electric field gradient, H_D the dipole coupling between nuclei, H_{CS} the interaction with the electronic environment , and H_J the spin-spin coupling. Since $H_Z >> H_Q >> H_D, H_{CS}, H_J$, H_Q may be treated as a perturbation of H_Z and the other interactions ignored to first order. H_Q arises from the interaction of the electric quadrupole moment with the electric field gradient (Figure 1a); being an electrostatic interaction, it is independent of the magnetic field.

2.1 The Quadrupolar Interaction

The Hamiltonian for H_Q is

$$H_Q = \frac{eQ}{2I(2I-1)\hbar}\mathbf{I}\bullet\mathbf{V}\bullet\mathbf{I} \qquad (2\text{-}1)$$

where eQ is the quadrupole coupling constant, **I** is the spin vector, and **V** is the electric field gradient tensor. In the principle axis system, by definition the tensor is diagonal;

$$\mathbf{V}_{PAS} = \begin{bmatrix} V_{XX} & 0 & 0 \\ 0 & V_{YY} & 0 \\ 0 & 0 & V_{ZZ} \end{bmatrix} \qquad (2\text{-}2)$$

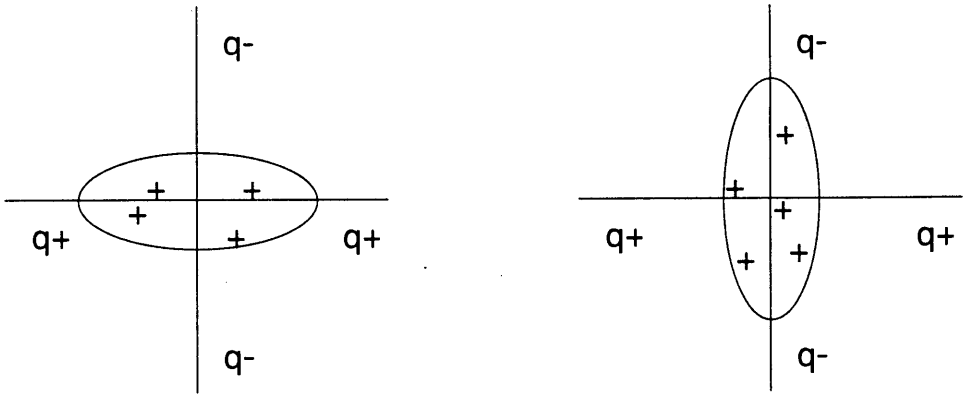

Figure 2.1a. Quadrupolar Interaction

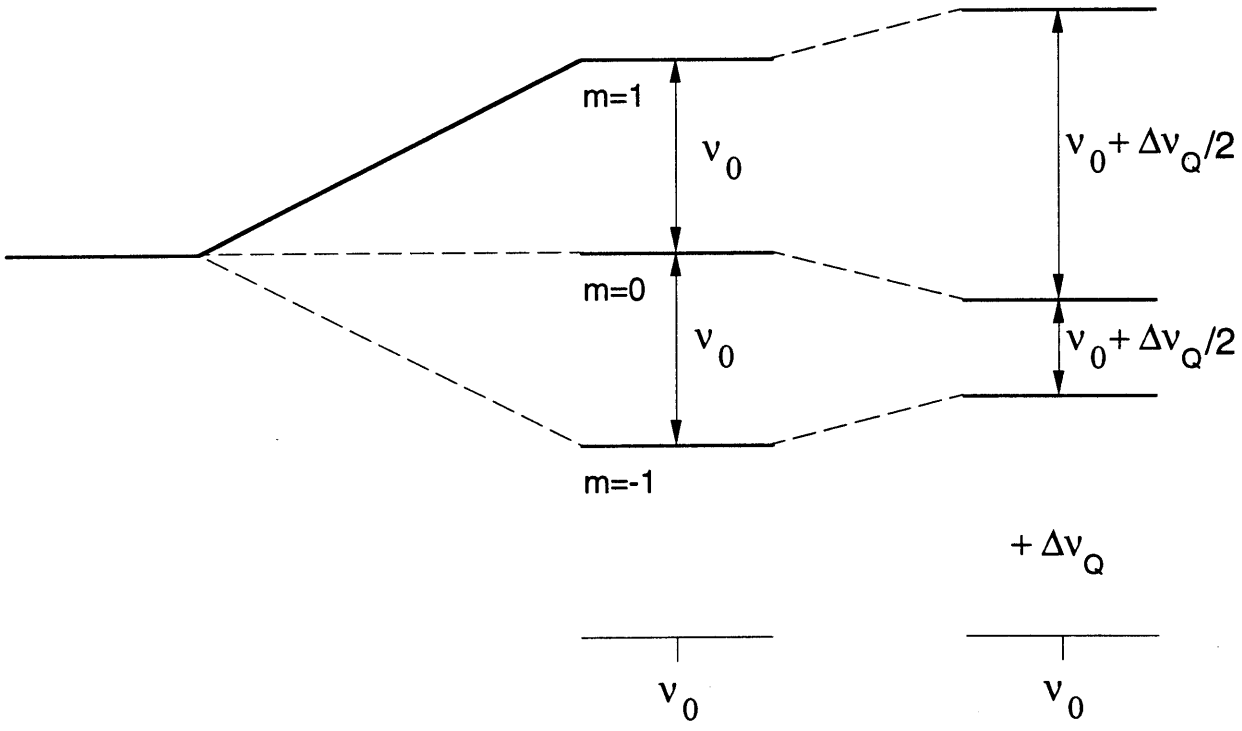

Figure 2.1b Energy level diagram for quadrupolar interaction

Since the electron density at the nucleus is zero, Laplace's equation must hold, so **V** is traceless,

$$V_{XX} + V_{YY} + V_{ZZ} = 0 \tag{2-3}$$

By convention,

$$V_{ZZ} > V_{XX} > V_{YY}, \qquad \eta = \frac{V_{XX} - V_{YY}}{V_{ZZ}}, \qquad V_{ZZ} = eq \tag{2-4}$$

where η is the asymmetry parameter. Using these definitions, for deuterium

$$H_Q = \frac{e^2 qQ}{4\hbar}\left[\left(3I_z^2 - \mathbf{I}\bullet\mathbf{I}\right) + \eta\left(I_x^2 - I_y^2\right)\right] \tag{2-5}$$

To convert this interaction from the principle axis system to the laboratory reference frame, it is convenient to introduce a spherical coordinate system and use irreducible spherical tensors, or

$$H_Q = \sum_{m=-2}^{2} (-1)^m A_{2,m} T_{2,-m}^{PAS} \tag{2-6}$$

Thus, the electric field gradient in the principal axis system is given by

$$\begin{aligned} T_{2,0}^{(PAS)} &= \frac{\sqrt{6}}{4}\left(e^2 qQ/\hbar\right) \\ T_{2,\pm1}^{(PAS)} &= 0 \\ T_{2,\pm2}^{(PAS)} &= \frac{1}{4}\eta\left(e^2 qQ/\hbar\right) \end{aligned} \tag{2-6}$$

and the spin variables are represented by the second rank spherical tensor elements

$$\begin{aligned} A_{2,0}^{(PAS)} &= \frac{1}{\sqrt{6}}\left(3I_Z^2 - \mathbf{I}\bullet\mathbf{I}\right) \\ A_{2,\pm1}^{(PAS)} &= \mp\frac{1}{2}\left(I_Z I_\pm + I_\pm I_Z\right) \\ A_{2,\pm2}^{(PAS)} &= \frac{1}{2} I_\pm^2 \end{aligned} \tag{2-7}$$

where $I_\pm = I_x \pm iI_y$. The electric field tensor elements in the principle axis system (P) can be related to those in the laboratory frame (L) via the Wigner rotation matrix elements,

$$T_{2,m}^{(LAB)} = \sum_{k=-2}^{2} D_{mk}^{(2)*}(\Omega_{LP}) T_{2,k}^{(PAS)} \tag{2-8}$$

This transformation may be accomplished via a series of rotations such as a rotation from the principle axis system to a molecule fixed axis system frame (M) via Ω_{MP} and a then a rotation to the laboratory coordinate system via Ω_{LM}, or

$$D^{(2)}_{mk}(\Omega_{LP}) = \sum_{l=-2}^{2} D^{(2)}_{ml}(\Omega_{LM}) D^{(2)}_{lk}(\Omega_{MP}) \tag{2-9}$$

Since deuterium NMR is normally done at high fields ($H_Z >> H_Q$), first order perturbation theory applies, so only the part of H_Q which commutes with H_Z needs to be kept. Using

$$\left[I_Z, A_{2,m}\right] = mA_{2,m} \tag{2-10}$$

only terms in $A_{2,0}$ remain. A second simplification results by choosing the laboratory frame such that the z-axes in both the laboratory and principle axis coordinate systems lie in a plane perpendicular to laboratory y-axis, or the Euler angle γ to be zero. This may be done since the magnetic field defining the laboratory coordinate system is axially symmetric. Thus, in the laboratory frame

$$H_Q = \frac{e^2qQ}{8\hbar}\left(3I_z^2 - I(I+1)\right)\left[\left(3\cos^2\beta - 1\right) + \left(\eta\sin^2\beta\cos 2\alpha\right)\right] \tag{2-11}$$

Evaluating the Hamiltonian ($H_Z + H_Q$),

$$E_m = -\gamma m\hbar\omega_0 + \frac{e^2qQ}{8}\left(3m^2 - 2\right)\left[\left(3\cos^2\beta - 1\right) + \left(\eta\sin^2\beta\cos 2\alpha\right)\right] \tag{2-12}$$

For spin 1,

$$E_1 = -\gamma\hbar\omega_0 + \frac{e^2qQ}{8}\left[\left(3\cos^2\beta - 1\right) + \left(\eta\sin^2\beta\cos 2\alpha\right)\right]$$

$$E_0 = -\frac{e^2qQ}{4}\left[\left(3\cos^2\beta - 1\right) + \left(\eta\sin^2\beta\cos 2\alpha\right)\right] \tag{2-13}$$

$$E_{-1} = \gamma\hbar\omega_0 + \frac{e^2qQ}{8}\left[\left(3\cos^2\beta - 1\right) + \left(\eta\sin^2\beta\cos 2\alpha\right)\right]$$

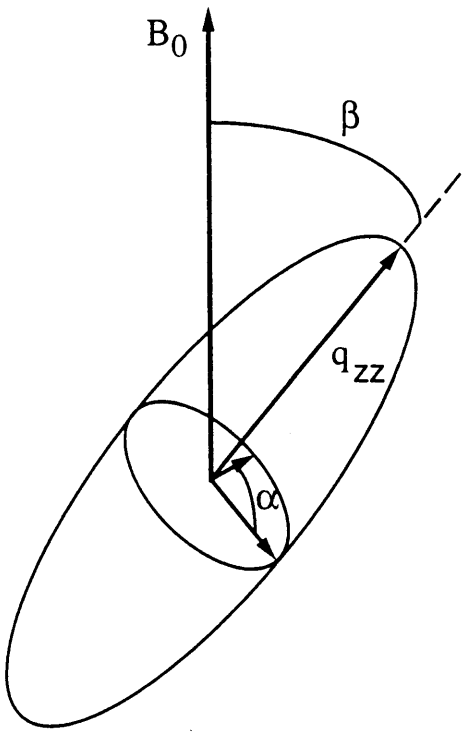

Figure 2.2a Angular dependence of the quadrupolar interaction

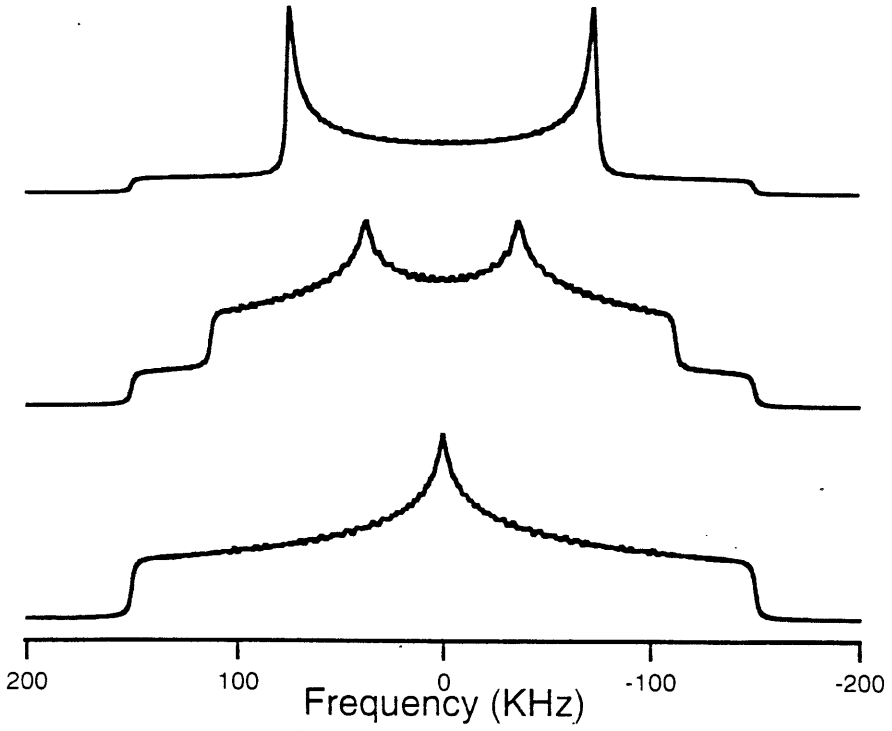

Figure 2.2b Characteristic powder patterns for eta =0 (top), eta = 0.5 (middle), and eta=1 (bottom)

Therefore the energy absorbed for each of the two transitions is:

$$E_{-1} - E_0 = \gamma\omega_0 + \frac{3e^2qQ}{8\hbar}\left[\left(3\cos^2\beta - 1\right) + \left(\eta\sin^2\gamma\cos 2\alpha\right)\right]$$
$$E_0 - E_1 = \gamma\omega_0 - \frac{3e^2qQ}{8\hbar}\left[\left(3\cos^2\beta - 1\right) + \left(\eta\sin^2\beta\cos 2\alpha\right)\right] \quad (2\text{-}14)$$

giving rise to a splitting (Figure 1b)

$$\Delta\nu_Q = \frac{3e^2qQ}{4h}\left[\left(3\cos^2\beta - 1\right) + \left(\eta\sin^2\beta\cos 2\alpha\right)\right] \quad (2\text{-}15)$$

However, this splitting relates to only one crystallite orientation (β, α). For a powdered sample, the sum over all possible orientations must be evaluated to determine the spectrum. This leads to the characteristic deuterium powder pattern (Figure 2a, b).

2.2 Relaxation

The ensemble averaged spin density operator, ρ, evolves according to the Stochastic Liouville equation,

$$\frac{d\rho(t)}{dt} = \frac{i}{\hbar}[\rho(t), H] - \Gamma(\rho(t) - \rho_0) \quad (2\text{-}16)$$

In the limit of the quadrupolar interaction being much larger than the dipolar couplings or chemical shift interaction, the Hamiltonian consists of only the Zeeman and quadrupolar interactions. This can be separated into time-independent , H_0, and varying, $H_1(t)$, parts. H_0 contains the Zeeman interaction and equilibrium quadrupole coupling. $H_1(t)$ is a second-rank tensor which describes relaxation via the quadrupole coupling; since this interaction is a function of orientation, molecular motion results in time dependence. These motions are not isotropic and depend on the system being observed; rather, they may consist of a random walk among well-defined, spatially unique sites. These leads to a nonzero average of H_Q over time, so it is convenient to split H_Q into an average Hamiltonian and a second Hamiltonian which contains time-dependent terms fluctuating about zero. Thus, the total Hamiltonian is

$$H = \underbrace{H_Z + \langle H_Q(t)\rangle}_{H_0} + \underbrace{\left(H_Q(t) - \langle H_Q(t)\rangle\right)}_{H_1(t)} \tag{2-17}$$

The fluctuations produce relaxation to the equilibrium states described by H_0. Using the notation introduced earlier in this chapter, the quadrupolar Hamiltonian may be written in terms of second-rank tensors, or

$$H_Q(t) = \sum_{m=-2}^{2} A_{2,m} T_{2,-m}(t)(-1)^m \tag{2-18}$$

Since relaxation of quadrupolar nuclei is primarily via spin-lattice relaxation, the time-dependence is due to spatial reorientations and hence the spin part of the Hamiltonian may be viewed as time-independent. In order to simplify the evolution of the spin density, one can convert to the interaction representation using $U = \exp\left[-i(H_Z + \langle H_Q(t)\rangle)t/\hbar\right]$ and take the ensemble average assuming $H_0 >> H_1(t)$. Thus

$$\frac{d\rho^*(t)}{dt} = -\frac{i}{\hbar}\left[H_1^*(t), \rho^*\right] \tag{2-19}$$

$$\frac{d\langle\rho\rangle^*}{dt} = -\frac{1}{\hbar^2}\int_0^\infty d\tau \left\langle\left[H_1^*(t), \left[H_1^*(t-\tau), \rho^*(t) - \rho_0^*\right]\right]\right\rangle \tag{2-20}$$

Where * indicates the unitary transformation $U\rho U^{-1}$ and $\rho_0 = \rho_0^*$ is the equilibrium spin density. In the rotating frame (rotating at ω_0), created by the unitary transformation $T = \exp\left[-iH_Z t/\hbar\right]$ the time evolution is

$$\frac{d\tilde{\rho}}{dt} = -\frac{i}{\hbar}\left[\langle H_Q\rangle, \tilde{\rho}\right] - \frac{1}{\hbar^2}\int_0^\infty dt \left\langle\left[\tilde{H}_1^*(t), \left[U\tilde{H}_1^*(t-\tau)U^{-1}, \tilde{\rho}(t) - \tilde{\rho}_0\right]\right]\right\rangle \tag{2-21}$$

where ~ indicates the rotating frame. Introducing the form of H_Q given in equation (2-18) and taking the secular approximation (i.e. keeping only m'=-m)

$$\frac{d\tilde{\rho}}{dt} = -\frac{i}{\hbar}\left[\langle H_Q\rangle, \tilde{\rho}\right] - \frac{e^2Q^2}{4\hbar^2}\sum_{m=-2}^{2}(-1)^m\left[A_{2,m}, \left[A_{2,-m}, \tilde{\rho}(t) - \tilde{\rho}_0\right]\right] \times (-1)^m \int_0^\infty d\tau \exp\{im\omega_0\tau\left\langle T_{2,-m}(t), T_{2,m}(t-\tau)\right\rangle \tag{2-22}$$

the evolution of the density operator can be separated into the spin and spatial parts. The

spin part may be treated quantum mechanically, and the spatial part may be treated classically as random fluctuations of the deuteron with respect to the magnetic field that cause relaxation. In order to simplify notation the definition of a correlation function

$$J_m(m\omega_0) = (-1)^m \int_{-\infty}^{\infty} d\tau \exp\{im\omega_0\tau\}\left\langle T_{2,-m}(t), T_{2,m}(t-\tau)\right\rangle \qquad (2\text{-}23)$$

is introduced and combined with equation (2-22) to yield the widely recognized equation

$$\Gamma(\rho(t)^* - \rho_0^*) = \frac{e^2Q^2}{8\hbar^2} \sum_{m=-2}^{2} (-1)^m \left[A_{2,m}, [A_{2,-m}, \tilde{\rho}(t) - \tilde{\rho}_0]\right] J_m(m\omega_0) \qquad (2\text{-}24)$$

Thus far our discussion of relaxation has been in term of the principle axis system. However, it is possible to calculate relaxation in the laboratory frame using a series of Wigner rotations as discussed previously. Using reduced Wigner rotation matrices and assuming η=0, the spatial interaction in the laboratory frame is

$$T_m^{(2)}(LAB) = \frac{4\pi}{5} T_0^{(2)}(PAS) \sum_{m'=-2}^{2} Y_{2,m'}^*(\theta,\varphi) d_{mm'}^{(2)}(\beta') \qquad (2\text{-}25)$$

and the correlation function may be calculated using

$$J_m(m\omega_0) = (-1)^m \left(\frac{4\pi}{5}\right)^2 (T_0^{(2),PAS})^2 \sum_{m'=-2}^{2} \sum_{m''=-2}^{2} d_{m',m}^{(2)}(\beta') d_{m'',-m}^{(2)}(\beta') \times \int_{-\infty}^{\infty} d\tau \exp\{im\omega_0\tau\}\left\langle Y_{2,m''}^*(\theta(t),\varphi(t)), Y_{2,m'}^*(\theta(t-\tau),\varphi(t-\tau))\right\rangle \qquad (2\text{-}26)$$

The numerical calculation of correlation functions will be discussed further in the section on computer simulations.

2.3 Calculation of pulse experiments

Following is a brief synopsis of pulse experiments commonly used when doing deuterium NMR. These sequences are shown in figure 2.3 This discussion describes the effects of pulses on the system quantum mechanically using density matrix formalism and is a summary of the excellent review article by Davis (1991). In order to understand

a) Quadrupole Echo

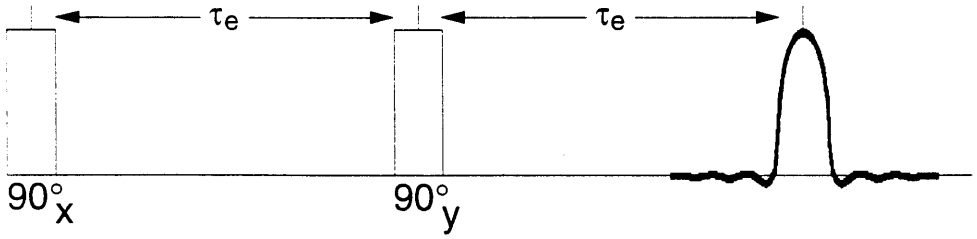

b) Standard Inversion Recovery

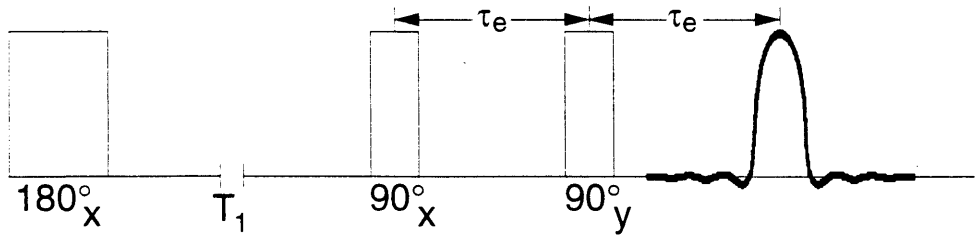

c) Frequency Dependent Jeener-Broekaert

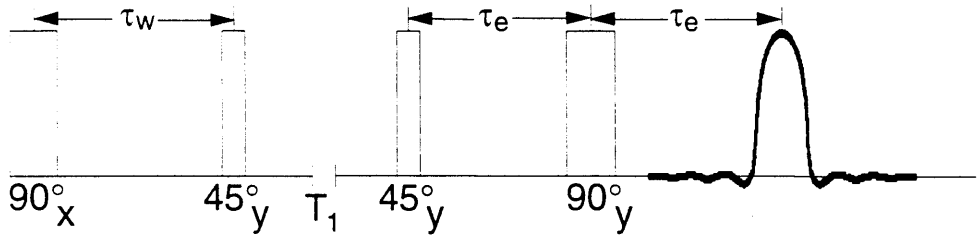

d) Broad-Banded Jeener-Broekaert

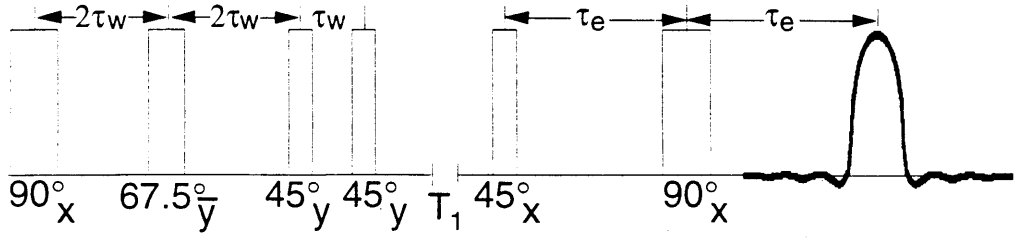

Figure 2.3 Pulse programs used in deuterium NMR

the consequence of various pulses and delays between pulses, it is convenient to introduce a basis set to describe the density operator

$$\rho(t) = \sum_k a_k(t) Q_k \qquad (2\text{-}27)$$

One especially tractable basis set for nuclei of spin 1 uses the following eigenvectors:

$$Q_1 = \frac{1}{\sqrt{2}} I_x = \frac{1}{2}\begin{pmatrix} 0 & 1 & 0 \\ 1 & 0 & 1 \\ 0 & 1 & 0 \end{pmatrix}, \qquad Q_2 = \frac{1}{\sqrt{2}} I_y = \frac{1}{2}\begin{pmatrix} 0 & -i & 0 \\ i & 0 & -i \\ 0 & i & 0 \end{pmatrix}$$

$$Q_3 = \frac{1}{\sqrt{2}} I_z = \frac{1}{2}\begin{pmatrix} 1 & 0 & 0 \\ 0 & 0 & 0 \\ 0 & 0 & -1 \end{pmatrix}, \qquad Q_4 = \frac{1}{\sqrt{6}}\left(3I_z^2 - 2\right) = \frac{1}{\sqrt{6}}\begin{pmatrix} 1 & 0 & 0 \\ 0 & -2 & 0 \\ 0 & 0 & 1 \end{pmatrix}$$

$$Q_5 = \frac{1}{\sqrt{2}}\left(I_x I_z + I_z I_x\right) = \frac{1}{2}\begin{pmatrix} 0 & 1 & 0 \\ 1 & 0 & -1 \\ 0 & -1 & 0 \end{pmatrix}, Q_6 = \frac{1}{\sqrt{2}}\left(I_y I_z + I_z I_y\right) = \frac{1}{2}\begin{pmatrix} 0 & -i & 0 \\ i & 0 & i \\ 0 & -i & 0 \end{pmatrix}$$

$$Q_7 = \frac{1}{\sqrt{2}}\left(I_x^2 - I_y^2\right) = \frac{1}{2}\begin{pmatrix} 0 & 0 & 1 \\ 0 & 0 & 0 \\ 1 & 0 & 0 \end{pmatrix}, Q_8 = \frac{1}{\sqrt{2}}\left(I_x I_y + I_y I_x\right) = \frac{1}{\sqrt{2}}\begin{pmatrix} 0 & 0 & -i \\ 0 & 0 & 0 \\ i & 0 & 0 \end{pmatrix}$$

$$Q_9 = \bar{\bar{1}} = \frac{1}{\sqrt{3}}\begin{pmatrix} 1 & 0 & 0 \\ 0 & 1 & 0 \\ 0 & 0 & 1 \end{pmatrix} \qquad (2\text{-}28)$$

Using this representation,

$$H_Q = \frac{e^2 qQ}{4}\left[3I_z^2 - 2\right] = \left(\frac{2}{3}\right)^{1/2} \hbar \omega_Q Q_4 \qquad (2\text{-}29)$$

and

$$H_0 = H_Z + H_Q = -\sqrt{2}\hbar\left(\omega_0 Q_3 + \frac{\omega_Q}{\sqrt{3}} Q_4\right) \qquad (2\text{-}30)$$

where

$$\omega_Q = \frac{3e^2 qQ}{4\hbar} \qquad (2\text{-}31)$$

A radiofrequency pulse of strength ω_1 along the x-axis may be represented

$$H_1 = -\hbar\omega_1 I_x = -\sqrt{2}\omega_1 Q_1 \qquad (2\text{-}32)$$

2.3a Quadrupole echo experiment

In the high temperature limit, the equilibrium density matrix for a sample placed in a magnet is defined by

$$\rho_0 = \frac{e^{-H_0/kT}}{Tr(e^{-H_0/kT})} \approx \frac{1-H_0/kT}{Tr(1-H_0/kT)} \approx \frac{-H_0}{3kT} \qquad (2\text{-}33)$$

The Zeeman magnetization is

$$\langle I_z \rangle = -Tr\{I_z \rho_0\} = \frac{2\hbar}{3kT} Tr\left[Q_3(\omega_0 Q_3 - \frac{1}{\sqrt{3}}\omega_Q Q_4) \right] = \frac{2\hbar\omega_0}{3kT} \qquad (2\text{-}34)$$

and similarly the degree of quadrupolar order is

$$\left\langle \frac{1}{2}(3I_z^2 - 2) \right\rangle = \frac{\hbar}{\sqrt{3}kT} Tr\left[Q_4(\omega_0 Q_3 - \frac{1}{\sqrt{3}}\omega_Q Q_4) \right] = -\frac{\hbar\omega_Q}{3kT} \qquad (2\text{-}35)$$

Since $\omega_0 >> \omega_Q$ the equilibrium quadrupolar order may be disregarded. In order to observe the decay of quadrupolar order, the Zeeman magnetization is transferred to quadrupolar order via rf pulses. This is covered in the section on Jeener-Broekaert sequences. In the quadrupole echo experiment, the system at equilibrium is subjected to a 90° pulse to create observable magnetization in the XY plane. Given the breadth of deuterium spectra, the power necessary to generate a short enough 90° pulse is quite sizable. If one tried to measure the deuterium spectrum immediately after this pulse, the receiver would be overloaded by the ringdown from the rf pulse and very little useful information would be gained. In the quadrupole echo, the system is allowed to evolve for a time τ after the initial pulse and then is refocussed using a second 90° pulse. Since the magnetization reaches a maximum at time τ after the second pulse, the various elements in the spectrometer have time to recover from the rf pulses and an undistorted spectrum may be measured. To understand how this works and set the groundwork for understanding relaxation experiments the following is a quantum mechanical description of the time evolution of the magnetization.

If we apply an rf pulse of frequency ω_1 to a system at equilibrium in a magnet, the time evolution of the magnetization is

$$\frac{dc_3(t)}{dt} = \frac{i}{\hbar}\sum_q c_Q(t)\mathrm{Tr}\left[Q_q\left[H_1,Q_3\right]\right] = -\omega_1\sum_q c_Q(t)\mathrm{Tr}\left[Q_qQ_2\right] = -\omega_1 c_2(t) \quad (2\text{-}36)$$

to evaluate this, we need the equation for $c_2(t)$

$$\frac{dc_2(t)}{dt} = \frac{i}{\hbar}\sum_q c_Q(t)\mathrm{Tr}\left[Q_q\left[H_1,Q_2\right]\right] = \omega_1\sum_q c_Q(t)\mathrm{Tr}\left[Q_qQ_3\right] = \omega_1 c_3(t) \quad (2\text{-}37)$$

Thus, we have a pair of coupled equations. All the other coefficients are zero during the pulse. This is generally true for simple pulse experiments; one need only evaluate the time evolution of those elements which were initially nonzero and the coefficients to which they are coupled by the pulse. The solution to these coupled equations is readily seen by taking the second derivative and has the well-known form

$$c_Q(t) = A_Q\cos(\omega_1 t) + B_Q\sin(\omega_1 t) \quad (2\text{-}38)$$

Using initial conditions, one obtains

$$c_3(t) = \frac{\sqrt{2}\hbar\omega_0}{3kT}\cos(\omega_1 t)$$
$$c_2(t) = \frac{\sqrt{2}\hbar\omega_0}{3kT}\sin(\omega_1 t) \quad (2\text{-}39)$$

If the pulse is of duration such that $\omega_1 t=90°$ then after the pulse $c_3(t)$ is 0 and $c_2(t)$ is maximized. After the pulse the system again evolves under the quadrupolar Hamiltonian for a time τ, but now the initial conditions are different so another set of coupled equations must be solved. Starting with the initial state,

$$\frac{dc_2(t)}{dt} = \frac{i}{\hbar}\sum_q c_Q(t)\mathrm{Tr}\left[Q_q\left[H_Q,Q_2\right]\right]$$
$$= -\omega_Q\sum_q c_Q(t)\mathrm{Tr}\left[Q_qQ_5\right] = -\omega_Q c_5(t) \quad (2\text{-}40)$$

Its complement is

$$\frac{dc_5(t)}{dt} = \frac{i}{\hbar}\sum_q c_Q(t)\mathrm{Tr}\left[Q_q\left[H_Q,Q_5\right]\right]$$
$$= \omega_Q\sum_q c_Q(t)\mathrm{Tr}\left[Q_qQ_2\right] = -\omega_Q c_2(t) \quad (2\text{-}41)$$

The solution again has the same form, namely

$$c_2(\tau) = \frac{\sqrt{2}\hbar\omega_0}{3kT}\cos(\omega_Q\tau) \qquad (2\text{-}42)$$
$$c_5(\tau) = \frac{\sqrt{2}\hbar\omega_0}{3kT}\sin(\omega_Q\tau)$$

After waiting a delay τ, a pulse along the y-axis of frequency ω_2 has the following effect:

$$\frac{dc_2(t)}{dt} = \frac{i}{\hbar}\sum_q c_Q(t)\mathrm{Tr}\left[Q_q\left[H_2, Q_2\right]\right] = 0 \qquad (2\text{-}43)$$

$$\frac{dc_5(t)}{dt} = \frac{i}{\hbar}\sum_q c_Q(t)\mathrm{Tr}\left[Q_q\left[H_2, Q_5\right]\right] = -2\omega_2\sum_q c_Q(t)\mathrm{Tr}\left[Q_q\frac{1}{2}(\sqrt{3}Q_4 - Q_7)\right]$$
$$= -2\omega_2\frac{1}{2}(\sqrt{3}c_4(t) - c_7(t)) \qquad (2\text{-}44)$$

and

$$\frac{d\left[\frac{1}{2}(\sqrt{3}c_4(t) - c_7(t))\right]}{dt} = \frac{i}{\hbar}\sum_q c_Q(t)\mathrm{Tr}\left[Q_q\left[H_2, \frac{1}{2}(\sqrt{3}Q_4 - Q_7)\right]\right]$$
$$= -2\omega_2\sum_q c_Q(t)\mathrm{Tr}\left[Q_q\frac{1}{2}(\sqrt{3}Q_4 - Q_7\right] = 2\omega_2 c_5(t) \qquad (2\text{-}45)$$

Using the conditions immediately before the pulse and choosing to make the pulse 90°,

$$c_5(t) = -\frac{\sqrt{2}\hbar\omega_0}{3kT}\sin(\omega_Q\tau)\cos(2\omega_2 t) = \frac{\sqrt{2}\hbar\omega_0}{3kT}\sin(\omega_Q\tau)$$
$$\frac{1}{2}(\sqrt{3}c_4(t) - c_7(t)) = -\frac{\sqrt{2}\hbar\omega_0}{3kT}\sin(\omega_Q\tau)\sin(2\omega_2 t) = 0 \qquad (2\text{-}46)$$

Now again the system evolves under a quadrupolar Hamiltonian. Assuming the pulses are short enough that no significant evolution other than that caused by the rf field occurs, the system immediately following the second pulse is characterized by

$$c_5(t) = \frac{\sqrt{2}\hbar\omega_0}{3kT}\sin(\omega_Q\tau) \qquad (2\text{-}47)$$

The time evolution is the same as that solved in eqns. (2-41) and (2-42) and the solution is again of the form in eqn.(2-38). Substituting in the initial conditions,

$$c_2(t) = \frac{\sqrt{2}\hbar\omega_0}{3kT}\left[\cos(\omega_Q\tau)\sin(\omega_Q t) + \sin(\omega_Q\tau)\sin(\omega_Q t)\right] \qquad (2\text{-}48)$$

$$c_5(t) = \frac{\sqrt{2}\hbar\omega_0}{3kT}\left[\sin(\omega_Q\tau)\sin(\omega_Q t) + \cos(\omega_Q\tau)\sin(\omega_Q t)\right] \quad (2\text{-}49)$$

If $t=\tau$ this simplifies to

$$c_2(t) = \frac{\sqrt{2}\hbar\omega_0}{3kT} \qquad c_5(t) = 0 \quad (2\text{-}50)$$

This can be detected along the y-axis or

$$\langle I_y \rangle = \sqrt{2}\mathrm{Tr}[Q_2\rho(t)] = \sqrt{2}c_2(t) = \frac{2\hbar\omega_0}{3kT} \quad (2\text{-}51)$$

In the analysis of the evolution of the system during the quadrupole echo pulse sequence we have assumed that no relaxation occurs. T_2 in deuterium is in general on the order of msec and τ is chosen to be on the order of 30 μsec, so this is usually a legitimate assumption. However, if molecular motion occurs during the two pulses so that a deuteron moves to an orientation with respect to the magnetic field that gives it a different frequency, it will not be effectively refocussed by the second pulse and observed at $t=2\tau$. This leads to an effective T_2 which can be quite short, and this phenomenon may be exploited in determining various motional mechanisms and rate constants. In order to calculate the effect of this motion on the spectrum observed at the echo maximum, it is necessary to introduce a more comprehensive Hamiltonian to describe the evolution of the spin system between the two pulses. Such a calculation is discussed in the section of this chapter devoted to computer simulations..

2.3b Inversion Recovery experiment

In the inversion recovery experiment, the z-magnetization is first inverted via a 180° pulse and then allowed to relax for an arbitrary period of time before a quadrupole echo sequence is applied in order to observe the magnetization. After the initial π pulse, the state of the system may be described by

$$\rho_0 = -I_z = -\sqrt{2}Q_3\frac{\hbar\omega_0}{3kT} \quad (2\text{-}52)$$

Since I_z commutes with both the quadrupolar and Zeeman Hamiltonians, the only effect on the magnetization after this pulse is spin lattice relaxation. If one evaluates the commutators

of I_z with the spin part of the Hamiltonian (see eq. 2-24), the end result is

$$\frac{1}{T_{1Z}} = \frac{e^2qQ}{8\hbar^2}[J_1(\omega_0) + 4J_2(2\omega_0)] \tag{2-53}$$

Thus, after a time, t_1, the magnetization is

$$\rho_0 = -\frac{\sqrt{2}\hbar\omega_0}{3kT}\left[1 - 2\exp\left(-\frac{t_1}{T_{1Z}}\right)\right]Q_3 \tag{2-54}$$

If one applies a quadrupole echo sequence after this delay, the result will be the same as described in the previous section except that the magnetization will be scaled by $\left[1 - 2\exp(-t_1/T_{1Z})\right]$.

2.3c Jeener-Broekaert and Broad-Banded Jeener-Broekaert sequences

Using the inversion recovery experiment, one may empirically determine the quantity $[J_1(\omega_0) + 4J_2(2\omega_0)]$, but it is more useful to know $J_1(\omega_0)$ and $J_2(2\omega_0)$ independently when evaluating complicated motional models since this increases the number of constraints one has. Taking the commuter of Q_4 with the spin parts of the quadrupolar Hamiltonian one obtains

$$\frac{1}{T_{1Q}} = \frac{e^2qQ}{8\hbar^2}[3J_1(\omega_0)] \tag{2-55}$$

which suggests a convenient method for independently measuring $J_1(\omega_0)$. Recall that in the quadrupole echo pulse sequence during the second pulse there was mixing with the Q_4 and Q_7 states (eq. 2-46), but that the buildup of magnetization was circumvented by choosing a 90° pulse. The set of coupled differential equations during this pulse are

$$\begin{aligned} \frac{dc_5(t)}{dt} &= -2\omega_2\frac{1}{2}(\sqrt{3}c_4(t) - c_7(t)) \\ \frac{dc_4(t)}{dt} &= \sqrt{3}\omega_2 c_5(t) \\ \frac{dc_7(t)}{dt} &= -\omega_2 c_5(t) \end{aligned} \tag{2-56}$$

The coefficients c_4 and c_7 describe the evolution of the quadrupole order and double quantum coherences respectively. If one makes the second pulse 45°, immediately following this pulse the magnetization will be described by

$$c_5(t) = -\frac{\sqrt{2}\hbar\omega_0}{3kT}\sin(\omega_Q t)\cos(2\omega_2 t) = 0$$

$$c_4(t) = -\frac{1}{2}\sqrt{\frac{2}{3}}\frac{\hbar\omega_0}{kT}\sin(\omega_Q t)\sin(2\omega_2 t) = -\frac{1}{2}\sqrt{\frac{2}{3}}\frac{\hbar\omega_0}{kT}\sin(\omega_Q t) \quad (2\text{-}57)$$

$$c_7(t) = \frac{\sqrt{2}}{6}\frac{\hbar\omega_0}{kT}\sin(\omega_Q t)\sin(2\omega_2 t) = \frac{\sqrt{2}}{6}\frac{\hbar\omega_0}{kT}\sin(\omega_Q t)$$

Both the quadrupolar order and the double quantum coherence are maximized if we choose τ such that $\omega_Q\tau$=90°, so the result of this experiment is frequency dependent. Some effort has been made to develop composite pulse sequences which are more broad-banded and has met with good success; such a sequence is shown in Figure 2.3d. It is beyond the scope of this discussion to describe these pulse sequences, and the reader is referred to Hoatson (1991). If one wishes to measure either of these quantities, they must be made observable or changed back to single quantum coherences via a second 45° pulse. If a time period , t_1, between the second and third pulses is introduced, the system is only subject to relaxation since both Q_4 and Q_7 commute with H_Q. The density matrix during this time evolves as

$$\rho_0 = -\frac{1}{\sqrt{2}}\frac{\hbar\omega_0}{3kT}\sin\omega_Q t\left[\sqrt{3}\exp\left(-\frac{t_1}{T_{1Q}}\right)Q_4 - \exp\left(-\frac{t_1}{T_{DQ}}\right)Q_7\right] \quad (2\text{-}58)$$

If the first two pulses are shifted by 90°, the resulting density matrix is

$$\rho_0 = \frac{1}{\sqrt{2}}\frac{\hbar\omega_0}{3kT}\sin\omega_Q t\left[\sqrt{3}\exp\left(-\frac{t_1}{T_{1Q}}\right)Q_4 + \exp\left(-\frac{t_1}{T_{DQ}}\right)Q_7\right] \quad (2\text{-}59)$$

Using a combination of these two pulse sequences it is possible to individually determine T_{1Q} and T_{DQ}. The broadbanded sequence shown in figure 2.3d results in only quadrupolar order. The final 90° pulse shown for both Jeener-Broekaert sequences accomplishes the same result as the second 90° pulse in the quadrupole echo experiment since after the other pulses in the Jeener-Broekaert sequences the magnetization is again described by the evolution of $c_2(t)$ and $c_5(t)$. However, the observed spectrum is scaled by the relaxation and inverted about zero due to the dependence of the magnetization on $\sin(\omega_Q\tau)$.

2.4 Turbopowder

With the large increases in speed and capability of computers over the past two decades, rapidly simulating NMR results has become more and more feasible. Deuterium NMR is no exception and relaxation calculations are particularly suited to numerical methods. Given the numerous orientations, frames of reference, summations, etc. which must be considered, the use of programs which accomplish successive rotations as well as matrix diagonalizations has become widespread. A brief summary follows for a program developed in the Griffin lab which I modified and used extensively for deuterium simulations presented in this thesis. A complete copy of the FORTRAN code is available.

The program is comprised of three parts. The first set of calculations converts the input parameters from the principle axis system to the lab frame via successive Wigner rotations, using Euler angles given in the input file to define the relationship between the various axes of motion and the principle axis system. A powder average is then performed to generate the complete spectrum.

The second major subdivision of the program derives the effective T_2 and frequency for each orientation in an unoriented system undergoing N-site hops. The details of this calculation are given in Wittebort, Olejniczak, and Griffin as well as Mehring and Spiess (Mehring, 1983; Spiess, 1978; Spiess & Sillescu, 1981; Wittebort et al., 1987). Following a 90° pulse, the magnetization is in the transverse (xy) plane. In the rotating frame, the equation of motion for this magnetization is

$$\frac{dM(\Omega)}{dt} = [i\omega(\Omega) + R(\Omega)]M(\Omega) \qquad (2\text{-}60)$$

where $R(\Omega)$ refers to the matrix of jump rates and $\omega(\Omega)$ is the frequency of the quadrupole interaction for that particular orientation. In the case of spin one there are of course both the -1-->0 and 0-->1 transitions. However, the frequencies for these transitions are mirror images of each other, so only the spectrum for one transition needs to be determined. For a system with jumps among N sites, this is expanded to

$$\frac{dM_i}{dt} = \sum_{j=1}^{N}\left[i\delta_{ij}\omega_{ij} + R_{ij}\right]M_i \qquad (2\text{-}61)$$

with R_{ij} being the jump rate between sites i and j and, assuming microscopic reversibility,

$$R_{ii} = -\sum_{j=1}^{N} R_{ij}(1-\delta_{ij}) \qquad (2\text{-}62)$$

The solution to this is

$$M(t) = \exp[(iw + R)t]A \qquad (2\text{-}63)$$

with A given by the equilibrium magnetization $A=M(0)=P_{eq}$.

The effect of the second pulse in the quadrupole echo is to interchange the magnetization of the two transitions, so after the delay τ, the system evolves as above except that now the initial condition is $A=M^*(\tau)$. Thus, at 2τ,

$$M(t) = \exp[(iw + R)(t+\tau)]\exp[(-iw + R)\tau]P_{eq} \qquad (2\text{-}64)$$

In deuterium NMR, it is generally assumed contributions to T_2 other than from (iw+R) are greater than 2τ and are neglected. The effective T_2 may then be calculated by diagonalizing iw+R and this result may be Fourier transformed to give the frequency spectrum or lineshape.

The final subroutine calculates the correlation functions for relaxation using the formalism of Torcia and Szabo (1982). If one assumes the motion occurs as discrete jumps between distinct sites, the time dependence in the crystal reference frame may be determined by sums over site orientations rather than integrals, and the correlation function given in eqn. 2-26 may be calculated using

$$J_m(m\omega_0) = \sum_{m'=-2}^{2}\sum_{m''=-2}^{2} d^{(2)}_{m',m}(\beta')\,d^{(2)}_{m'',-m}(\beta')\int_{-\infty}^{\infty} d\tau \exp\{im\omega_0\tau\}C_{LL'}(t) \qquad (2\text{-}65)$$

where $C_{LL'}$ is the correlation function for reorientation in the crystal fixed-axis system and is given by

$$C_{LL'}(t) = \sum_{KK'} \frac{T_K^{(2),pas} T_K^{(2),pas*}}{(T_0^{(2),pas})^2} \times \sum_{j=1}^{N}\sum_{i=1}^{N}\sum_{n=2}^{N} (p_i^{eq} p_j^{eq})^{1/2} U_{jn} U_{in} e^{\lambda_n t} D_{LK}^{(2)*}(\Omega_i) D_{L'K'}^{(2)}(\Omega_j) \quad (2\text{-}66)$$

In this equation, λ and U refer to the eigenvalues and eigenvectors of the rate matrix. Turbopowder takes the input rate matrix and site probabilities and calculates these variables. The multiple summations are performed using the geometries of the system provided. Finally a powder average over all orientations of the sample with respect to the magnet field is performed. It should be noted that for fast-limit spectra, it is only necessary to calculate the averaged quadrupole coupling and T_{2e} may also be neglected.

The program also includes corrections for experimental parameters such as finite pulse effects and linebroadening due to T_2. A series of experiments such as varying delays or motional rates may also be done.

2.5 Other NMR experiments

In addition to deuterium NMR, some other solid state NMR techniques were used to examine structure in the peptides discussed in chapter 6. There are already several excellent discussions of these techniques, and the reader is referred to two recent reviews (Bennett et al., 1994; Griffiths & Griffin, 1993). These experiments were done to reintroduce small (<1 kHz) dipolar couplings between homonuclear and heteronuclear spins in samples spinning at the magic angle at rates greater than the dipolar couplings. For measuring carbon-nitrogen distances, a standard REDOR experiment was employed. For carbon-carbon distances the complementary experiments R^2 and R^2 tickling were used. The use of both experiments allows the natural linewidths of the various resonances to be determined and thus gives some information on chemical shift dispersion as well.

REFERENCES

Bennett, A.E., Griffin, R.G. & Vega, S. (1994) in *Solid-State NMR IV: Methods and Applications of Solid-State NMR* (Blumich, B., Ed.) 1-77, Springer-Verlag, Berlin.

Davis, J.H. (1983) *Biochimica et Biophysica Acta 737*, 117-171.

Davis, J.H. (1991) in *Isotopes in the Pysical and Biomedical Science* (Buncel, E. & Jones, J.R., Ed.) 99-157, Elsevier Science Publishers B. V., Amsterdam.

Griffiths, J.M. & Griffin, R.G. (1993) *Analytica Chimica Acta 283*, 1081-1101.

Hoatson, G.L. (1991) *Journal of Magnetic Resonance 94*, 152-159.

Mehring, M. (1983) *Principles of High Resolution NMR in Solids*, Springer-Verlag, Berlin.

Spiess, H.W. (1978) in *Dynamic NMR Spectroscopy* (Diehl, P., Fluck, E. & Kosfeld, R., Ed.) 55-214, Springer-Verlag, Berlin.

Spiess, H.W. & Sillescu, H. (1981) *Journal of Magnetic Resonance 42*, 381-389.

Vold, R.R. & Vold, R.L. (1991) in *Advances in Magnetic and Optical Resonance* (Warren, W., Ed.) 85-171, Academic Press, Inc., San Diego, CA.

Wittebort, R.J., Olejniczak, E.T. & Griffin, R.G. (1987) *Journal of Chemical Physics 86*, 5411-5420.

3. Model Compound Studies

Acknowledgements: the work presented on alanine in the first half of this chapter was originally published as an article in Journal of the American Society **116**: 11950-11956. The ^{15}N simulations presented in figure 4-6 and 4-7 were performed by Boqin Sun using his simulation program NMRLAB®.

3.1. ND_3-L-Alanine

3.1.1 Introduction

Inter- and intramolecular dynamic processes can profoundly affect spectral features (lineshapes and relaxation times) when the rate of a process becomes equal to a characteristic frequency of the experiment. Several well known examples of these phenomena occur in solution NMR when the correlation times governed by chemical exchange processes reach a minimum (Spiess, 1978). The increased use of multiple pulse and multiple resonance experiments presents additional opportunities for these effects to occur. In particular, when the correlation times of the motional processes become comparable to the cycle time of a radiofrequency (RF) perturbation, spectral broadening is observed. For example, motion at a rate equal to the inverse of the size of a heteronuclear decoupling field or on the timescale of a homonuclear multiple pulse train will have deleterious effects on the applied RF field/pulse train. This interaction can severely reduce resolution, thus rendering certain resonances undetectable in chemical shift spectra. This phenomenon was used to explain the loss of resolution observed in ^{13}C CPMAS spectra of proteins and peptides in membranes (Sefcik et al., 1983; Lee, 1990); specifically, motional interference via diffusion in the membrane could explain the failure to observe several of the expected resonances. More recently, line intensities in chemical shift spectra of the tyrosine sidechain carbons in a cyclic hexapeptide, Gly-Tyr-Gly-Pro-Leu-Pro (Griffiths et al.,), and the coordinated methyl groups in $\{W(\eta^5\text{-}C_5Me_5)Me_4\}^+$ (Maus et al., 1996) have displayed strong temperature dependencies. Thus, it appears that the interference of molecular motion with RF fields is a widespread phenomenon.

In this chapter, this effect is demonstrated in detail using a combination of solid state NMR experiments. Namely, the kinetics of the ammonium group in L-alanine are investigated via deuterium NMR lineshape experiments and simulations. Using this data, it is possible to theoretically and experimentally investigate the interference between coherent spin motion, induced by a decoupling field, and incoherent hopping of the protons

of the ammonium group of L-alanine using two separate techniques: proton decoupling when observing ^{15}N and homonuclear decoupling when observing ^{1}H. As expected, the spectra exhibit dramatic lineshape and linewidth effects when the hopping rate is comparable to the decoupling field. This behavior is further confirmed by computer simulations which model the dependence of the lineshape and linewidth on hopping rates.

3.1.2. Materials and Methods

Sample preparation. L-alanine was purchased from Aldrich Chemical Co. (Milwaukee, Wisconsin). Deuterated samples were prepared by proton/deuteron exchange in D_2O purchased from CIL (Woburn, Massachusetts). The saturated solution was placed in a nitrogen atmosphere and ND_3-labeled L-alanine was recovered by slow evaporation at room temperature. Crystals were redissolved in D_2O and recrystallized a second time, dried, and then pulverized. The powder was dried over P_2O_5 to remove occluded D_2O molecules; nevertheless, the deuterium NMR spectra do show a residual D_2O peak. ^{15}N-labeled L-alanine, also purchased from CIL, was used without further purification.

Deuterium NMR measurements. Deuterium quadrupole NMR spectra of ND_3-labeled L-alanine were recorded at 61.05 MHz on a home built spectrometer. Pulse lengths and phases were optimized prior to recording spectra, and a quadrupole echo pulse sequence (Figure 3-1a) was used to record lineshapes. Quadrature detection with a dwell time of 2 μsec was used and 90° pulse lengths were typically ≤ 2.2 μsec. Pulses were phase cycled through a set of eight quadrupole echoes during signal averaging to eliminate DC offset and quadrature phase error artifacts. Recycle delays were greater than five times T_1, ranging from 0.5 sec at higher temperatures to 400 sec at lower temperatures. T_1 was measured using the inversion recovery method with a quadrupole echo sequence for observation, i.e., 180°--delay (msec)--$90°_x$--τ--$90°_y$--τ--echo.

Proton NMR measurements. Proton multiple-pulse NMR spectra (Mansfield, 1971; Rhim et al., 1973; Taylor et al., 1979) of natural abundance L-alanine were ob

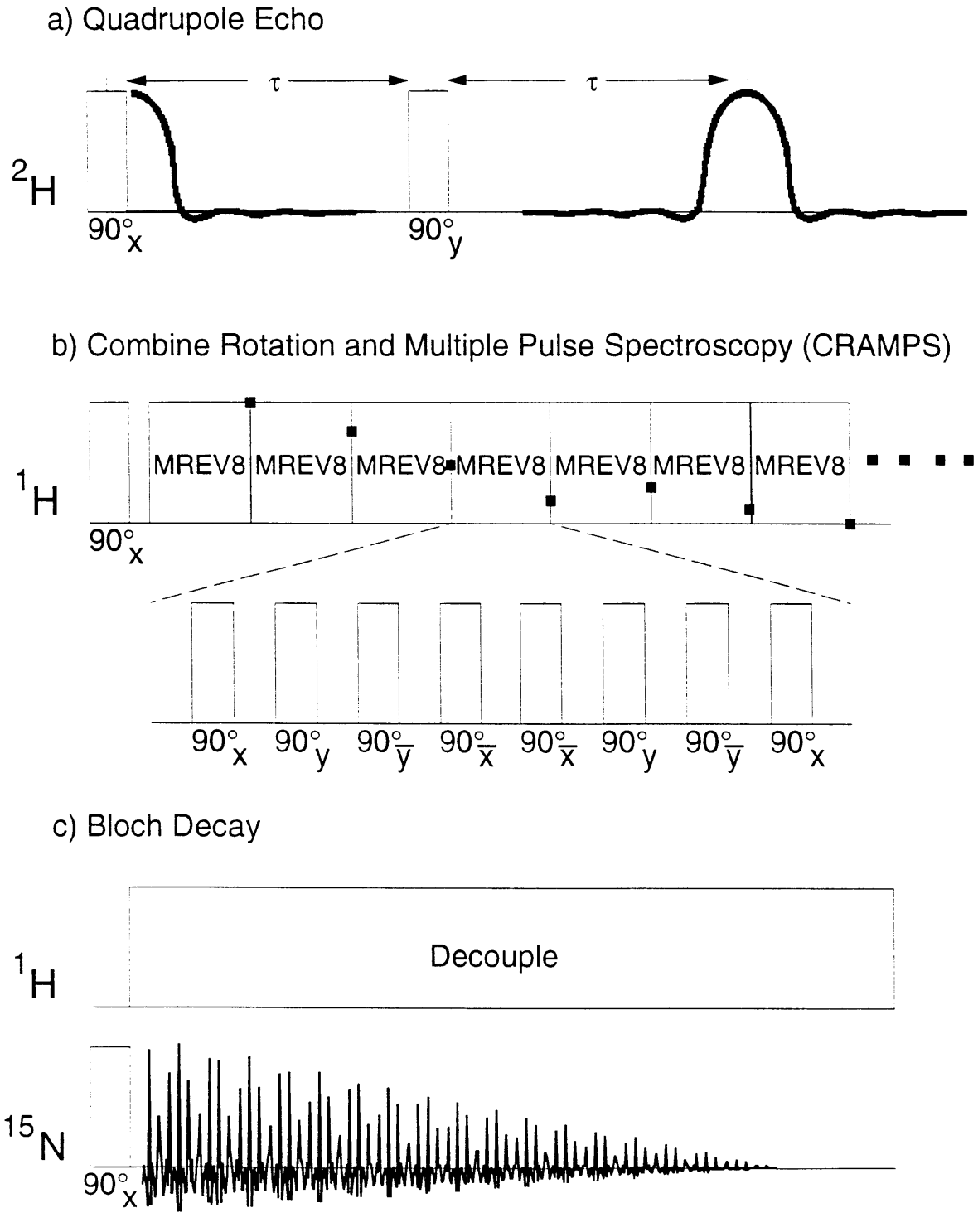

Figure 3-1. Schematics of NMR pulse sequences used to obtain spectra.

tained at 397.6 MHz on the same spectrometer. A standard double resonance probe was used with proton 90° pulse lengths ≤ 4 μsec. Multiple pulse parameters were optimized using malonic acid and cycle times for the MREV-8 sequence were typically 70 to 75 μsec (Figure 3-1b). Spectra of L-alanine were obtained at spinning speeds of 1.5 - 1.7 kHz, with recycle delays ranging from 3 sec at higher temperatures to 10 sec at lower temperatures. The resolution over the temperature range was independently monitored using malonic acid; lineshapes remained consistent with minimal increases in linewidth at lower and higher temperatures (data not shown). The extent of chemical shift scaling was measured using a standard comb of H_2O spectra with 2 kHz frequency intervals to ± 8 kHz off resonance. Spectra were collected at -4 kHz off resonance to avoid zero-frequency artifacts.

Nitrogen NMR measurements. Magic angle spinning ^{15}N Bloch decay spectra of ^{15}N-labeled L-alanine were acquired with ^{15}N and ^{1}H Larmor frequencies of 40.3 MHz and 397.6 MHz, respectively. The proton decoupling RF field was 67 kHz, corresponding to a ^{1}H 90° pulse length of 3.7 μsec. Spectra were acquired under proton continuous wave (CW) decoupling after a ^{15}N 5 μsec 90° pulse (Figure 3-1c). The sample spinning rate was 4.5 kHz and repetition times during data accumulation varied from 3 sec at higher temperatures to 300 sec at lower temperatures.

Lineshape Simulations: ^{2}H lineshapes. The details of the lineshape calculations are discussed elsewhere (Wittebort et al., 1987), but input to the program consists of molecular geometry, quadrupole coupling constant, pulse program parameters, site populations, and exchange rates. The molecular structure for L-alanine is shown in Figure 3-2a, and the angles between the ND bond vectors and the threefold C^{α}-N rotation axis were taken from the neutron diffraction data of Lehman *et al.*(Lehman et al., 1972) In all cases the equilibrium population for each site was assumed to be one-third and the exchange rates (k) between different sites were assumed to be equal. The rigid lattice quadrupole coupling constants of the three sites were taken from zero field quadrupole

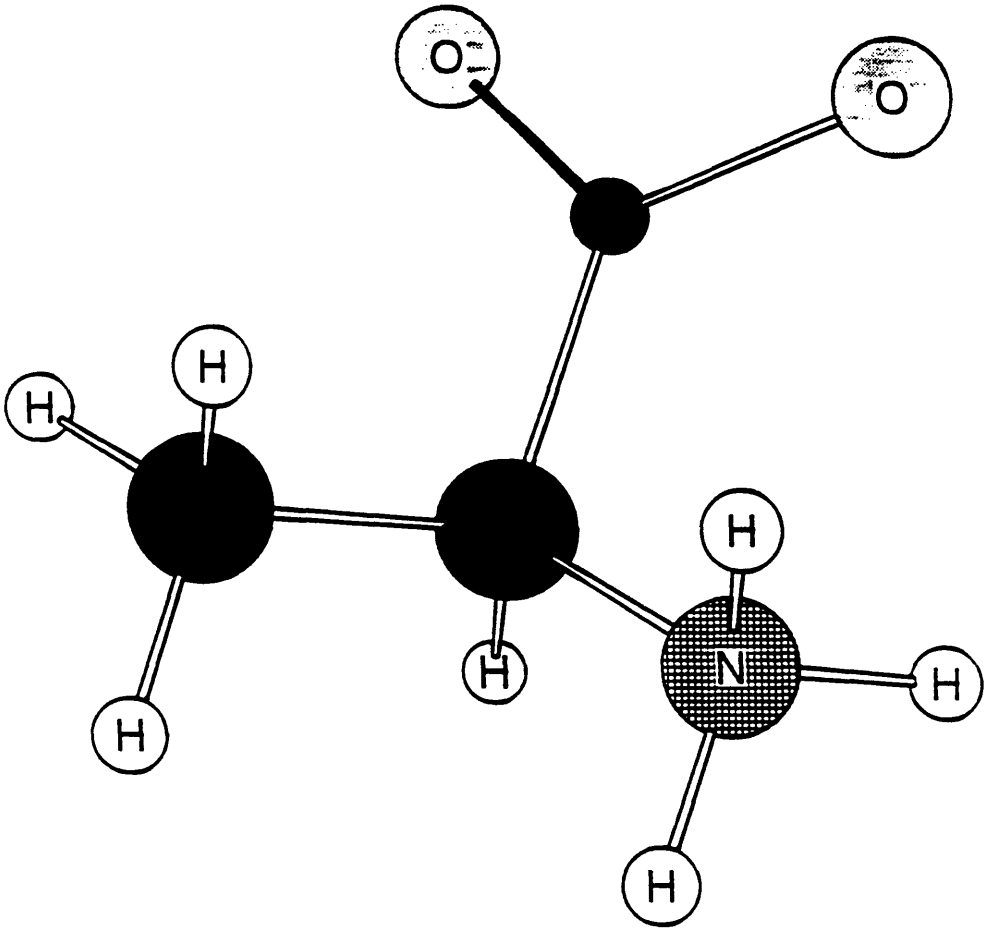

Figure 3-2a Molecular structure of L-alanine

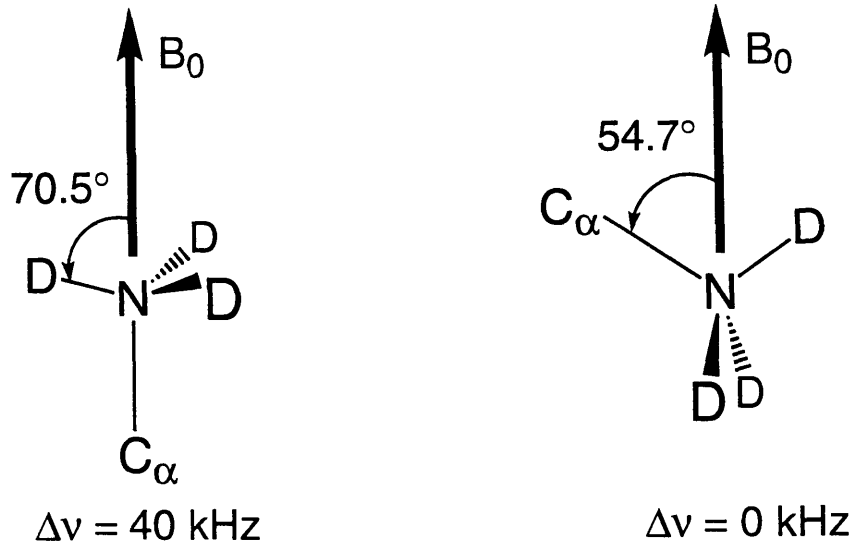

Figure 3-2b. two orientations of L-alanine in the magnetic field leading to characteristic triplet deuterium NMR powder pattern at intermediate hopping rates.

resonance data of Hunt *et al.* (Hunt & MacKay, 1974) Slight modifications to the lineshape calculation program were made to account for the different quadrupole coupling constants of the three sites due to hydrogen bonding; modifications were not made when calculating relaxation spectra since these experiments were performed at temperatures at which one can assume the quadrupole couplings were essentially averaged. (In this instance the average of the three quadrupole coupling constants was used.) Each simulation provides two pieces of information: the spectral lineshape and the relative integrated intensity of the spectrum. At lower temperatures, the rate for a rotational jump of the ammonium group at a given temperature was obtained by visual comparison of the experimental and theoretical lineshapes; T_1 data were more rigorously fit via direct comparison of theoretical and experimental relaxation values for various orientations. A correction for finite pulse effects is used in the simulations (Bloom et al., 1980), but this correction is minimal given the RF field employed and spectral widths in the experiments.

^{15}N Lineshapes. Simulations of ^{15}N spectra at different jumping rates were carried out using a program, NMRLAB®, written in FORTRAN. In NMRLAB, the spin system, consisting of a nitrogen and three protons is defined in the input file according to the neutron diffraction structure of L-alanine (Lehman et al., 1972). Zeeman interactions, hetero- and homonuclear dipolar couplings, and chemical shift anisotropies were taken into account in order to fit the experimental results. The homo- and heteronuclear dipolar coupling constants were calculated from the crystal structure using the gyromagnetic ratios of ^{1}H and ^{15}N nuclei, yielding an ^{15}N-^{1}H dipolar coupling constant of 10.9 kHz, based on the average NH bond length, and a ^{1}H-^{1}H dipolar coupling constant of 25 kHz. The chemical shift anisotropy (CSA) tensor parameter was estimated to be about 200 Hz based on static ^{15}N spectra under decoupling and should be symmetric according to the molecular structure. NMRLAB is also able to calculate the ^{15}N spectra with various approximate methods to be discussed elsewhere (Sun et al.,).

3.1.3 Results and Discussion

3.1.3a Quadrupole echo lineshapes

The essential features of quadrupole echo lineshapes are similar to those for a $-CD_3$ group (Beshah et al., 1987). However, it is interesting to note that in the rigid lattice spectrum for the ammonium group, two distinct quadrupole coupling constants may be seen due to the inequivalent environments of the deuterons arising from hydrogen bonding. As the hopping rate increases, the different quadrupole coupling constants are motionally averaged and the spectra then more closely resemble those of the methyl group. The shapes of these spectra result from the $-ND_3^+$ undergoing three-site hops and can be easily understood, especially in the intermediate exchange region, by considering the two special orientations with respect to the magnetic field shown in Figure 3-2b. In the slow-exchange limit each deuteron in the rigid lattice yields a separate resonance line in the spectrum. A spectrum of a single crystal would have three quadrupole doublets; one for each magnetically inequivalent deuteron. In the fast hopping limit, $k >> \omega_Q = (e^2Qq/h)$, the three ND tensors will be averaged to a single tensor with its unique axis collinear to the C^α-N bond, which is the hopping axis. This gives rise to a single quadrupole doublet for each crystallite in the fast limit spectrum . In both the rigid lattice and fast limit spectra of powders axially symmetric Pake patterns are observed; however, the fast limit spectrum is a factor of three narrower due to the motional averaging. In the intermediate exchange regime, $k \approx \omega_Q$, T_2 becomes comparable to the τ value in the echo experiment for certain orientations in the powder sample. For these orientations the second pulse does not refocus the magnetization and there is a corresponding spectral intensity loss. However, for other orientations, T_2 is long since the motion does not change the orientation of an ND vector with respect to the magnetic field. These orientations give rise to prominent singularities in the lineshapes, two such orientations being illustrated in Figure 3-2b. The effect of these two special orientations on intermediate ^2H lineshapes is apparent in Figure 3-3. These spectra are similar to lineshapes previously

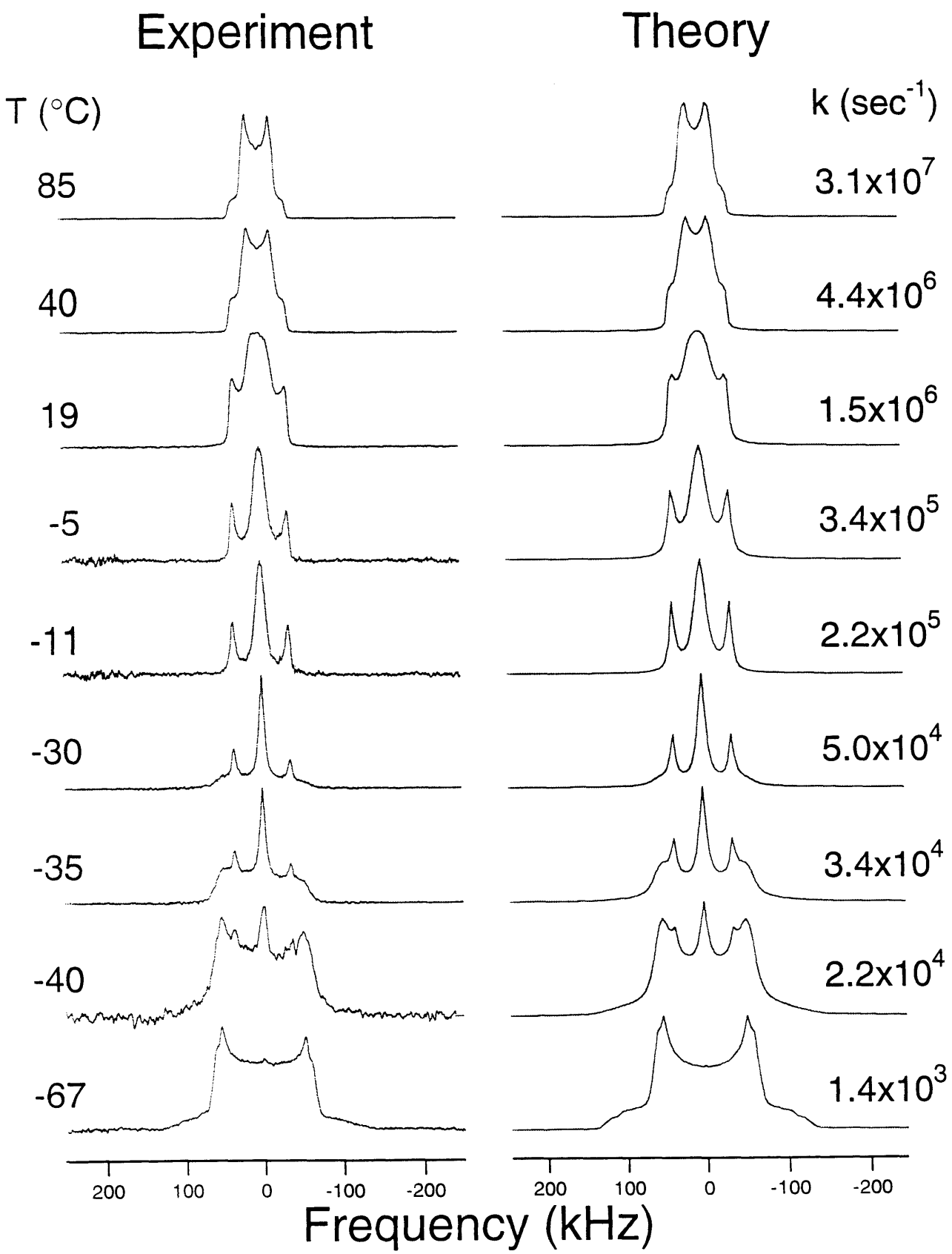

Figure 3-3. Experimental and simulated deuterium NMR spectra for ND_3-labeled L-alanine. Parameters for the simulations are given in the text.

observed in ^2H NMR studies of the methyl group in L-alanine (Beshah et al., 1987).

^2H quadrupole echo spectra of ND_3^+-labeled L-alanine were taken as a function of temperature in the range -70 to +85° C. Figure 3-3 contains typical experimental and simulated lineshapes at the indicated temperatures. At -67° C the rigid lattice $\eta \approx 0$ spectrum is obtained. This lineshape develops to the intermediate exchange spectrum, particularly in the range $-35 < T < -5$° C, where $3.5 \times 10^4 < k < 5.5 \times 10^5$ s^{-1}. At higher temperatures (> 30° C) a fast limit Pake pattern is observed. For 30° C < T < 70° C the lineshape remains essentially constant but the spectral intensity continues to increase with temperature. As seen in Figure 3-3, the simulations are in excellent agreement with the experimental results and provide a jump rate for each temperature. The simulations are based on a single correlation time motional model and their success indicates there is no significant distribution of correlation times present in ND_3-labeled L-alanine over the temperature range studied. Spectra similar to those shown in Figure 3-3 have been reported for the methyl group of L-alanine, although they occur at much lower temperatures (Beshah et al., 1987).

3.1.3b ^2H spectral intensities and anisotropic spin-lattice relaxation

In the intermediate exchange region, the quadrupole echo spectra show frequencies arising from the molecular orientations shown in Figure 3-2. As discussed above, these orientations have a relatively long T_2 and lead to the triplet lineshape observed, for example, in the -12°C spectrum. The remainder of the signal decays rapidly after the first pulse and cannot be refocused because the decay is due to the exchange process. Consequently, the intensities of the observed signals in the intermediate exchange region are only ~5% of the intensities observed in the slow and fast limit. In addition to the large intensity loss which occurs at log k ~ 5, there are significant intensity losses over a wide range of hopping rates. In particular, a 25% loss is observed for hopping rates between 10^4 and 10^8 s^{-1} and a 50% loss between 5×10^4 and 5×10^7 s^{-1}.

Three-site hops are particularly sensitive to intensity losses during intermediate exchange due to the high symmetry of the motion (Beshah et al., 1987). However, similar spectral intensity losses have been observed in other systems. For instance, aromatic rings in crystalline amino acids and peptides undergo twofold flips which transform the spectra to η=0.6 lineshapes in the fast limit (Rice et al., 1987). In the intermediate exchange region a minimum intensity value of ~20% is observed for this case, which is a factor of ~ 5 larger than the minimum value observed for three-site hops.

Anisotropic relaxation of lineshapes in T_1 experiments provides another means of determining kinetic rates of motions. A specific motional mechanism will lead to faster relaxation of certain portions of a powder lineshape than other models. In both the experimental and the simulated spectra of ND_3^+-labeled L-alanine, the parallel edges relax more quickly than the perpendicular edges. In addition, T_1 values may determined, leading to a more rigorous fit to experimental data.

3.1.3c Activation energy for the -ND_3^+ hopping

The rate constants obtained from spectra, such as those shown in Figure 3-4, can be used to calculate an activation energy, E_a, for the threefold motion of the ND_3^+ group; a plot of log k vs. 1/T is shown in Figure 3-4. The errors in fitting the simulations to the data are indicated by the vertical bars and the solid line represents a least-squares fit to the results. The slope of this line yields an activation energy of 40.5 kJ/mol (k_0= 2.52×10^{13}). The E_a for the ammonium group of L-alanine is comparable to activation energies obtained for other -NH_3^+ groups. For example, in other amino acids values ranging from 32.5 to 51.7 kJ/mol have been measured (Andrew et al., 1974; Andrew et al., 1976). These large activation energies for ammonium group motion in amino acids are easily understood given the steric hindrance and hydrogen bonding present in amino acid crystallites. Finally, the activation energy measured for the ammonium group in L-alanine agrees well with the value of 38.6 kJ/mol ($k_0=6.5 \times 10^{13}$) obtained from proton relaxation experiments (Andrew et al., 1976).

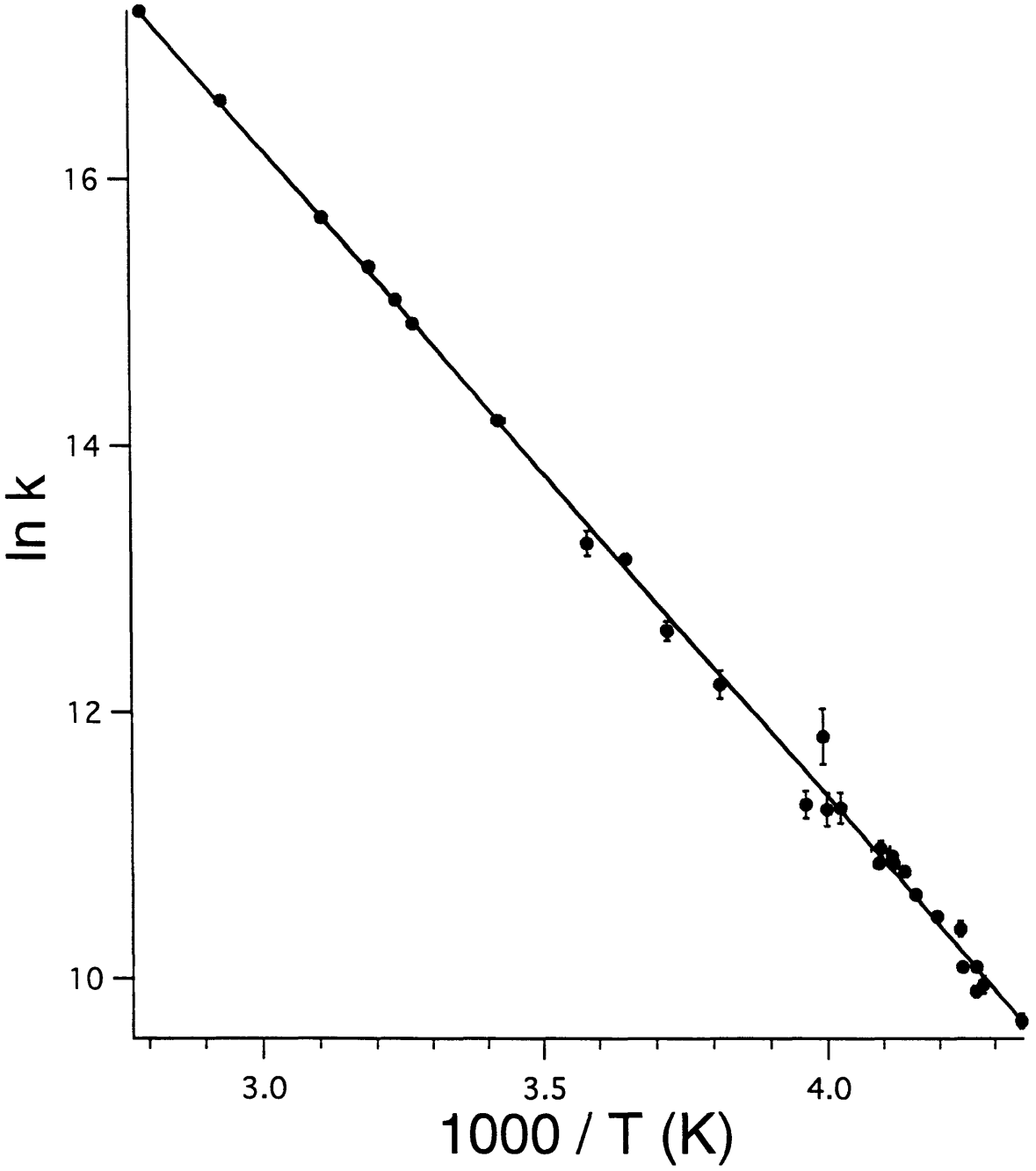

Figure 3-4. Arrhenius plot of hopping rates for the ammonium group of L-alanine obtained from deuterium NMR simulations. A best fit line yields an activation energy of 40.5 kJ/mol.

3.1.3d Molecular Motion Effects in Proton Multiple Pulse Spectra

Interestingly, at room temperature (25° C) the motional rate of the ammonium group in L-alanine is only 2 x 10^6 s^{-1}. This rate is close to the time scales involved in multiple pulse experiments and can explain the anomalous broadening observed in ^1H chemical shift spectra at the ammonium group resonance. As seen in Figure 3-5, increasing the temperature, and therefore the hopping rate, leads to significant narrowing of this resonance; lowering the temperature and decreasing the hopping rate to ~ 2 x 10^5 s^{-1} (on the timescale of the pulse spacings and the RF cycle time) leads to almost a complete loss of resolution, as previously predicted by Haeberlen and Waugh (Ellett et al., 1970; Ellett et al., 1974).

3.1.3e Molecular Motion Effects in Nitrogen Solid State MAS Spectra

^{15}N CPMAS spectra of L-alanine measured at different sample temperatures are shown in Figure 3-6A. As the sample temperature is lowered the intensity of the ^{15}N peak decreases and its linewidth increases, and at -30° C, the ^{15}N resonance becomes too broad to be observed. As the sample is cooled further, the ^{15}N resonance reappears and the linewidth decreases.

One possible explanation for the lineshape changes with temperature is the interference between the threefold hopping motion of the ND_3^+ group protons discussed above with the applied decoupling rf field. In order to simulate the effects of this interference on the lineshape, one may assume that the intermolecular dipolar coupling can be ignored and the -ND_3^+ group forms a isolated four spin system in which the total spin Hamiltonian includes the Zeeman interaction, hetero- and homonuclear dipolar couplings, and chemical shift anisotropy. Transferring the total spin Hamiltonian to the rotating frame yields the zero order average Hamiltonian

$$H = \sum_i (\omega_{0i}^I I_{iz} + \omega_{0i}^S S_{iz}) + H_{CS}^I + H_{CS}^S + H_{IS} + H_{II} \qquad (3\text{-}1)$$

where

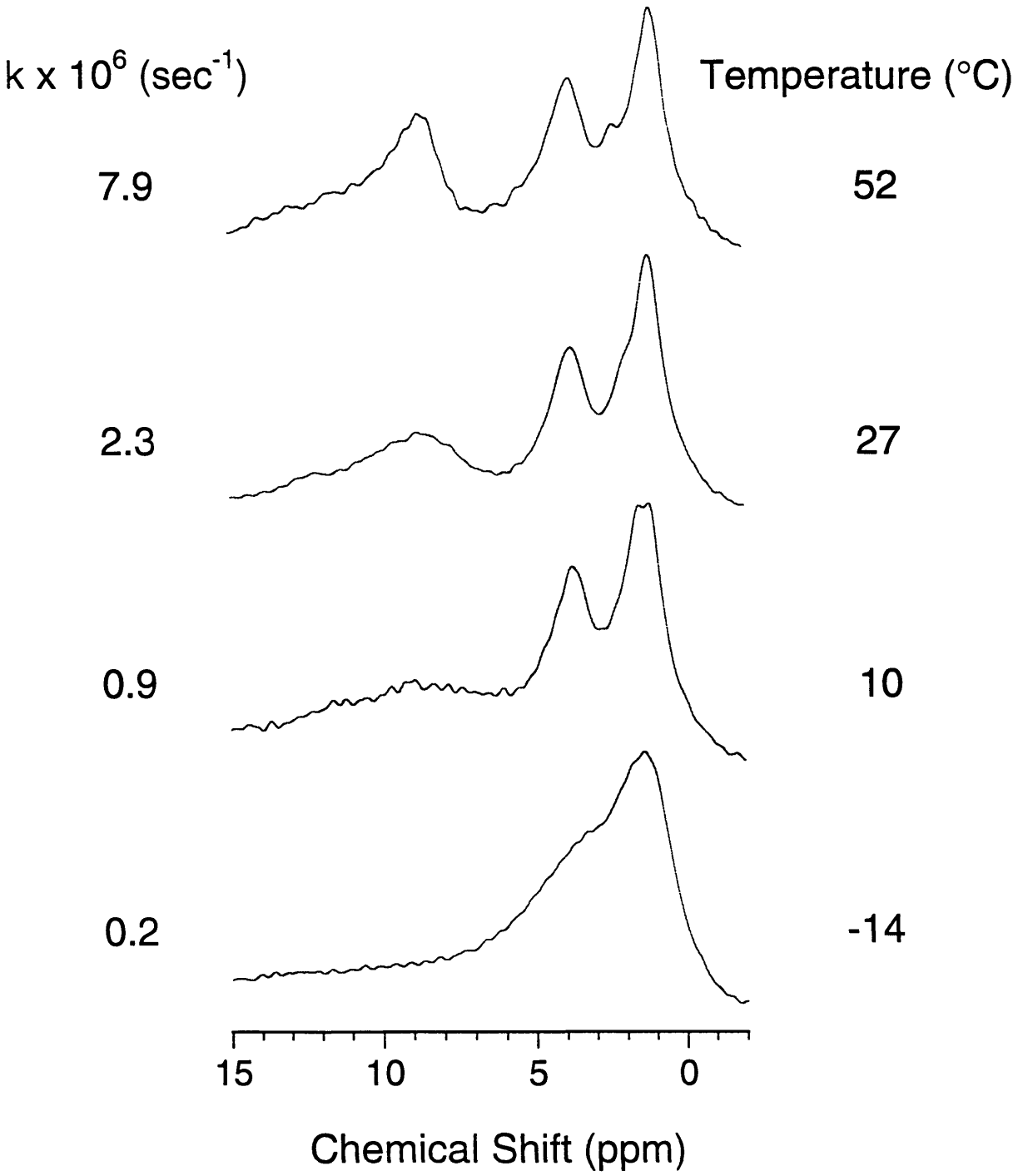

Figure 3-5. Multiple pulse spectra of L-alanine obtained using CRAMPS. Estimated hopping rates for the ammonium group extracted from deuterium NMR data. Note some broadening of the $-CH_3$ resonance (~1 ppm) also occurs at lower temperatures as the hopping rate of the methyl group approaches the frequency of the decoupling field.

$$H_{CS}^{I} = \sum_{i} \omega_{CS_i}^{I}(\Omega_i) I_{iz},$$
$$H_{CS}^{S} = \sum_{i} \omega_{CS_i}^{S}(\Omega_i) S_{iz}$$
$$H_{IS} = \sum_{i,j} 2\omega_{D_{i,j}}^{IS}(\Omega_{ij}) I_{iz} S_{jz}$$
$$H_{II} = \sum_{i,j} 2\omega_{D_{i,j}}^{II}(\Omega_{ij})(3I_{iz}I_{jz} - \mathbf{I}_i \bullet \mathbf{I}_j) \qquad (3\text{-}2)$$

the Ω_i are Euler angles between the principal axis system of an interaction and the laboratory frame, the H_{CS} represent the chemical shift interactions, and H_{II} and H_{IS} represent the homonuclear and heteronuclear dipolar interactions, respectively. The random threefold hop can be represented by a permutation matrix between all the spin states in the product Zeeman basis. After the total spin Hamiltonian and the permutation matrix are transferred into Liouville space, the spin density matrix may be solved by the master equation

$$\frac{d}{dt}\rho(t) = \hat{L}(t)\rho(t) + \hat{\Gamma}(t)\rho_0 \qquad (3\text{-}3)$$

where $\hat{\Gamma}$ is the relaxation super matrix, ρ_0 is the equilibrium density matrix, and $\hat{L}$ is the super Liouville operator given by

$$\hat{\mathrm{L}}(\mathrm{t}) = -\mathrm{i}\hat{\mathrm{H}}(\mathrm{t}) - \hat{\Gamma} - \hat{\mathrm{X}} \qquad (3\text{-}4)$$

and

$$\hat{\mathrm{H}} = \mathrm{H} \otimes \mathrm{E} - \mathrm{E} \otimes \mathrm{H}, \quad \hat{\mathrm{X}} = \mathrm{X} \otimes \mathrm{X} \qquad (3\text{-}5)$$

where $\hat{\mathrm{X}}$ is the exchange matrix. The formal solution of Eq.(3-3), if one ignores the T_1 relaxation, may be written as

$$\rho(t) = T\exp\left(\int_0^t dt' \hat{L}(t')\right)\rho(0) \qquad (3\text{-}6)$$

where T is the Dyson time ordering operator. Since the Liouvillian is time dependent and does not generally commute with itself at different times, the argument of the exponential cannot be integrated normally. To evaluate the exact evolution of the density matrix, NMRLAB divides the acquisition time into N steps. During each time step, the Liouvillian varies slightly, and can be assumed to be approximately equivalent to its

average. The density matrix at the end of the kth step can then be calculated by diagonalizing the time independent Liouvillian, and is given by

$$\rho(t_k)=\left\{\prod_{i=0}^{k-1}\exp\left[\hat{L}(t_i)\Delta t_i\right]\right\}\rho(0). \qquad (3\text{-}7)$$

The diagonalization of a 256 x 256 Liouvillian matrix to determine the propagator of the spin density matrix is usually very time consuming . In order to accelerate calculation of the spin density matrix, one can choose a random crystallite orientation and the look for block structure. Once the block structure of the Liouvillian is known, one needs only to focus on the blocks which relate the observable operator and initial density matrix. For L-alanine, the Liouvillian of the NH_3^+ group has only four such blocks, each 64 x 64. this is because the nitrogen nucleus in not involved in the chemical exchange process, and the heteronuclear dipolar coupling of the nitrogen to the protons is diagonal in the Zeeman basis. This block-diagonalized structure translates to the Zeeman basis with a spin Hamiltonian comprised of 8 x 8 blocks. The chemical exchange between protons only causes evolution within individual blocks. Since the observable of interest, I for the nitrogen nucleus, only has 8 nonzero elements in the Zeeman basis and becomes a vector with 64 elements in the Liouville apace, only one of the 64 x 64 blocks of the Liouvillian matrix propagates the evolution of the spin density matrix for the observable.

For calculational purposes, one can assume that the activation energy of the three-site hop is the same for protons and deuterons since the experimental data being fit was taken at relatively high temperatures. Thus, jumping rates of the protons in natural abundance L-alanine at various temperatures can be calculated from the deuterium data. With the calculated jumping rates, the ^{15}N spectra at various temperatures have been simulated, and the results are shown in Figure 3-6. The maximum linewidth is found when the jumping rate is comparable to the decoupling RF field. This evidence, together with the experimental and theoretical deuterium results described above, strongly supports the argument that loss of resolution observed in various L-alanine spectra arises from the

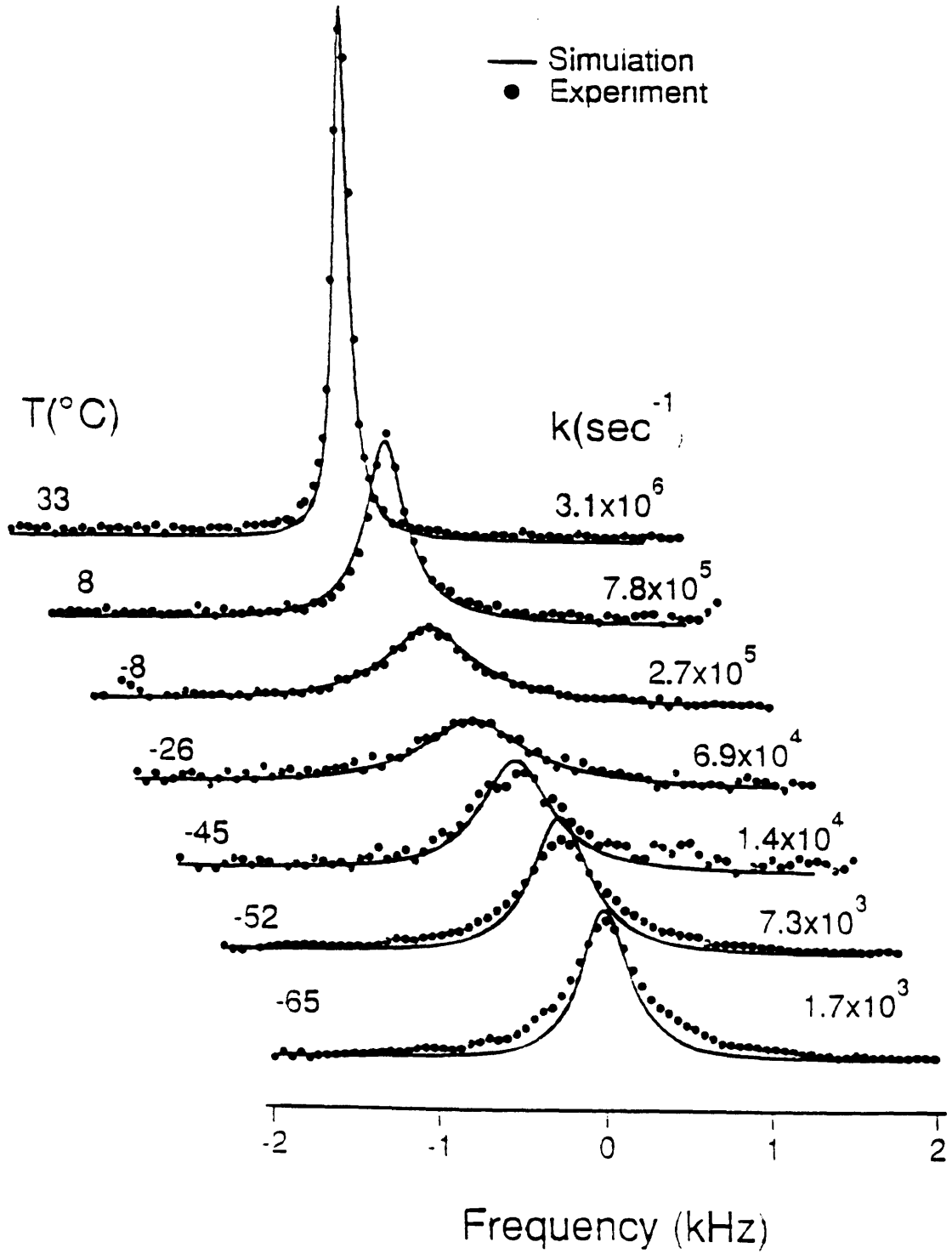

Figure 3-6. Comparison of experimental and simulated nitrogen NMR spectra. Simulations are exact solutions based on a three-fold hopping model using parameters given in the text.

motional interference between the decoupling RF field and random threefold hopping of the ammonium group.

The following is a brief discussion of previous works classified as three alternative methods to simulate the ^{15}N spectra shown in Figure 3-6. The first derivation calculates the transverse relaxation time of the observable using classical relaxation theory; the second approach uses the random walk model; and the third approximation uses average Hamiltonian theory.

Classic Relaxation Theory. The interference between an externally applied coherent perturbation and a random molecular motion was first explored by Maricq and Waugh for the case of a spin system undergoing molecular motion while the sample is spinning around the magic angle (Maricq & Waugh, 1979). Such an interference broadens the spectral lines due to a loss of efficiency in averaging the inhomogeneous and anisotropic interactions by MAS. Subsequently, this interaction was characterized as advantageous for studying slow motions in organic solids. VanderHart and co-workers first studied the interference occurring between random rotational diffusion and a continuous wave decoupling RF field using hexamethylbenzene (VanderHart et al., 1981). A theoretical description of this motional interference was presented by Rothwell and Waugh, using relaxation theory with a spin Hamiltonian consisting of the Zeeman interactions, RF terms, and the heteronuclear dipolar coupling of a lone-pair IS spin system (I spin denotes a proton and S spin refers to ^{15}N or ^{13}C) (Rothwell & Waugh, 1981). With this theory, the transverse relaxation time, T_2, under the high temperature approximation is given by

$$\frac{1}{T_2} = \frac{4\omega_d^2 I(I+1)}{15} J(\omega_1) \tag{3-8}$$

where ω_d is the amplitude of the I-S dipolar coupling, ω_1 is the amplitude of the applied CW decoupling RF field, $J(\omega_1)$ is the spectral density function,

$$J(\omega_1) = \frac{\tau_C}{1+\omega_1^2\tau_C^2} \tag{3-9}$$

and τ_C is the correlation time of the random rotational diffusion. The prefactor in Eqn. (3-8) is just the powder average of the I-S second moment, M_2^{IS}, as pointed out by the authors. From this equation, the linewidth (Δ) of the affected resonance can be calculated using $\Delta=(\pi T_2)^{-1}$. To calculate the linewidth of an I_NS spin system subjected to magic angle sample spinning, Eqn.(3-8) has to be modified, and the result is

$$\frac{1}{T_2}=\sum_{i=1}^{N}\frac{2\omega_{d_i}^2\, I(I+1)}{45}\left[2J(\omega_1+\omega_r)+2J(\omega_1-\omega_r)+J(\omega_1+2\omega_r)+J(\omega_1-2\omega_r)\right] \quad (3\text{-}10)$$

where ω_r is the sample spinning rate and N is number of I spins. When the sample spinning rate is small, the values of the four spectral density functions are nearly equal, and Eqn. (3-10) will reduce to Eqn. (3-8) for an IS spin system. In the other limit, where there is no decoupling RF field applied, even if the spinning speed is very fast, the interference between MAS and the random jumping motion results in residual linewidth, determined by Eqn. (3-10), which is similar to the equation derived by Suwelack (Suwelack et al., 1980).

In the derivation of Eqns. (3-8) and (3-10) two approximations have been made. First, only the secular terms in the master equation of the density matrix are included; since the homonuclear dipolar couplings between protons have no contribution to the transverse relaxation of the S spin, it is possible to ignore them. Secondly, no differentiation is made between discrete hopping and rotational diffusion. The cross-correlation terms which arise from the S spin being coupled to more than one I spin and the motion of the I spins being correlated, as in the case of the ammonium group in L-alanine, are also neglected. To include these effects, a higher order approximation has to take into account a more general treatment of the relaxation of the S spin.

When applying either Eqn.(3-8) or (3-10) to the analysis of experimental data, one usually measures the second moment from the lineshape, which already includes the contributions from the homonuclear dipolar coupling and cross relaxation effects. This may lead to an incorrect determination of the correlation time. In this study, since the

crystal structure of L-alanine is known, the dipolar coupling constant between ^{15}N and ^{1}H may be calculated. Using a coupling of 10.9 kHz, this analysis predicts an ^{15}N linewidth of about 990 Hz at a jumping rate of 290 kHz, decoupling field of 67 kHz, and spinning speed of 4.5 kHz, corresponding to experimental data at -8° C. However, the experimental result is 580 Hz (see Figure 3-7); obviously Eqn.(3-10) only qualitatively describes the interference effect.

Random Walk Model. Another approach to predicting the effects of the interference between the decoupling and random jumping motion in a molecule on the linewidth of the S spin is to use a random walk model described by Waugh. During a decoupling cycle, all the spin packets evolve through the trajectories which depend on individual orientation and anisotropic parameters, and have the same phase at the end of each decoupling cycle if there is no interruption. However, if the molecule or a group in the molecule jumps from one configuration to another, the spin packets will evolve following different trajectories, and therefore not all spin packets will return to their original positions. This behavior is similar to echo and de-echo process induced by applied π pulses under MAS (Olejniczak et al., 1984; Kolbert et al., 1989). The trajectory of each spin packet is determined by the spin Hamiltonian, and the interruption of the evolution of each spin packet is also equivalent to changing the spin Hamiltonian. In the simulation, as the spin packet evolves, the spin Hamiltonian changes randomly among all possible configurations specified by two variables, one indicating the configuration of the molecule and the other denoting how long the spin packet stays at any given configuration. For a single spin packet, the time evolution of the S spin calculated by this method will be discontinuous, so an ensemble average over all spin packets is necessary; an ensemble average is equivalent to a powder average, making a reduction in computation time possible. The lineshapes of S spin nuclei calculated by the random walk method are the same as those predicted by the classic relaxation model discussed earlier. In order to obtain a reasonably smooth time evolution of the observable, more than a few orienta

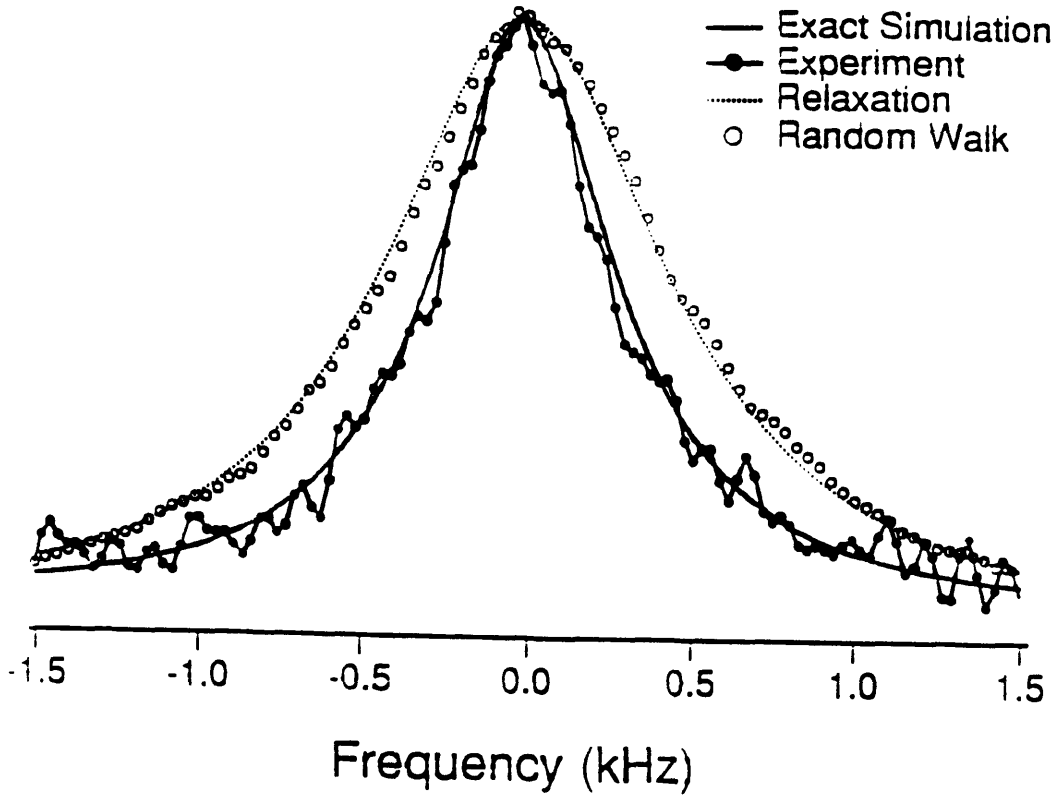

Figure 3-7. Comparison of nitrogen NMR spectra simulated using different approaches with experimental results obtained for L-alanine at -8° C.

tions have to be averaged. The number of jumps during the entire evolution depends on the jumping rate, and each jump involves at least one diagonalization of the spin Hamiltonian. When the jumping rate is very large, the number of diagonalizations increases dramatically, and the whole calculation becomes very time consuming even though this method avoids a diagonalization of a Liouvillian.

Average Hamiltonian Theory More recently, the interference between random discrete jumps and a CW decoupling RF field was investigated by Frydman and Frydman (Frydman & Frydman, 1990) for the static sample. In order to simulate the lineshape changes as sample temperature varied, they proposed an approximate method for a two site jump model. In this method, since the time dependent spin Hamiltonian in the tilted rotating frame defined by the unitary transformation operator $T=\exp\{-i\omega_1 I_x t\}$ has a period of $\tau_c=2\pi/\omega_1$, the effective dipolar coupling constant is positive during the first half of the decoupling cycle (relative to a positive dipolar coupling constant in the laboratory frame) and becomes negative during the second half of the decoupling cycle. The lineshape changes induced by molecular motions are different between the first and second half of the decoupling cycle; each half yields its own lineshape at a particular jumping rate. The overall lineshape will be the convolution of these two lineshapes assuming the lineshape changes due to the different splitting during each period are negligible. In other words, the following average spin Hamiltonian may be used to evaluate the density matrix of the spin during the first and the second halves of the decoupling period, respectively.

$$H=\begin{cases}\sum_i \omega^S_{CS_i}(\Omega_i)S_{iz}+\sum_{i,j}\omega^{IS}_{D_{i,j}}(\Omega_{ij})I_{iz}S_{jz} & 0\le t\le\dfrac{\pi}{\omega_1}\\ \sum_i \omega^S_{CS_i}(\Omega_i)S_{iz}-\sum_{i,j}\omega^{IS}_{D_{i,j}}(\Omega_{ij})I_{iz}S_{jz} & \text{for } \dfrac{\pi}{\omega_1}\le t\le\dfrac{2\pi}{\omega_1}\end{cases} \qquad (3\text{-}11)$$

The density matrix during the first half of the n+1 decoupling cycle is then given by

$$\rho[(n+1)\tau_c]=e^{\frac{1}{2}\hat{L}_2\tau_c}[\rho[(n+\tfrac{1}{2})\tau_c]-\hat{L}_2^{-1}\hat{X}\rho_0]+\hat{L}_2^{-1}\hat{X}\rho_0 \qquad (3\text{-}12a)$$

and during the second half by

$$\rho[(n+\frac{1}{2})\tau_c]=e^{\frac{1}{2}\hat{L}_1\tau_c}[\rho[(n\tau_c)]-\hat{L}_1^{-1}\hat{X}\rho_0]+\hat{L}_1^{-1}\hat{X}\rho_0 \qquad (3\text{-}12b)$$

where $\hat{L}_1$, and $\hat{L}_2$ are super operators. In this method, the cross-correlation terms are already included in the evolution of the density matrix. However, the homonuclear dipolar coupling effects are not included in this calculation, and the model only approximately works for a 2-fold hopping process.

3.1.4 Conclusions

The observed and calculated ^2H quadrupole echo lineshapes show good agreement using a threefold hopping model to describe the dynamics of the ammonium group in L-alanine. The Pake doublet observed in the slow exchange regime transforms to a triplet in the intermediate exchange region, and this in turn to a Pake spectrum of reduced width in the fast exchange limit. The shape of the intermediate exchange spectrum is due to the geometry of the ammonium group and the two special orientations which occur with respect to the laboratory field. In addition to the temperature dependence of the lineshapes, the observed spectral intensity dependencies and anisotropy in the spin-lattice relaxation have been simulated. It is also possible to observe the effects of hydrogen bonding on lineshapes at low temperatures and to include these effects in simulations. Simulations of all three sets of experimental data suggest that a threefold hopping model based on a single correlation time is an excellent representation of the dynamics of the $-NH_3^+$ group in L-alanine. The spectral lineshape simulations yield an activation energy of 40.5 kJ/mol in good agreement with previous measurements.

Using the deuterium results, kinetic rates at various temperatures can be calculated, and their effects on various decoupling schemes may be observed and simulated. For instance, the kinetic rate determined at room temperature provides an explanation for the broadening observed at the ammonium resonance in ^1H multiple pulse spectra of L-alanine.

In a more detailed analysis, the variation of the linewidth and intensity of the ^{15}N peak of the ammonium group in L-alanine with the sample temperature was observed. In these spectra, the ^{15}N peak becomes broad as the sample temperature approaches -30° C

and then narrows as the temperature decreases further. This linewidth change arises from the interference between the decoupling field and the threefold hopping of the protons in the ammonium group. Using the hopping rates calculated based on the deuterium results, one can simulate the ^{15}N L-alanine spectra at various temperatures by solving the master equation of the density matrix in Liouville space, and the results agree well with experimental spectra. Various other approximate methods have also been considered. Except for the random walk approach, all other methods cannot reproduce the experimental results. This is due to neglect of the homonuclear dipolar coupling between protons as well as the cross relaxation effects.

3.2. $Ba(ClO_3)\cdot D_2O$

3.2.1 Introduction

Pulsed deuterium NMR, in combination with lineshape simulations, is a powerful tool for investigating dynamic processes in solid and semi-solid materials (Griffin, 1981; Davis, 1983). With this technique details on the rate and mechanism of anisotropic molecular motion are available from studies of lineshapes which arise from the deuterium quadrupole interaction (Griffin et al., 1988). The size of this interaction is 170-250 kHz and therefore other anisotropic nuclear spin interactions, such as the dipole-dipole coupling and chemical shift, are relatively small and do not have to be considered explicitly in interpreting the spectral lineshapes or spin-lattice relaxation. To investigate processes with rates between 10^3 s^{-1} (slow exchange) and 10^8 s^{-1} (fast exchange), the temperature dependence of quadrupole echo spectra and the dependence on pulse spacing, τ, can be employed (Vega & Luz, 1987; Spiess & Sillescu, 1981; Spiess, 1978). Particularly dramatic changes in powder lineshapes and spectral intensities are observed when the rates of motion are on the order of the quadrupole coupling constant ~ 10^4-10^7 s^{-1}. For faster motions, in the regime 10^8-10^{11} s^{-1}, the anisotropy of the spin lattice relaxation observed in inversion recovery experiments can be used (Torchia & Szabo, 1982; Wittebort et al., 1987). This latter experiment overlaps with the upper end of the time scale of quadrupole echo measurements, and in addition permits observation of faster motions where the quadrupole echo lineshape is insensitive to changes in the rate of molecular reorientation. For both the quadrupole echo and inversion recovery techniques, information on the rate and mechanism of molecular motion is extracted by fitting experimental spectra with theoretical lineshapes.

Generally, the theoretical spectra are calculated on the basis of a dynamic model, assuming particular values for the number of sites involved in the motional process, their populations and relative EFG tensor orientations, and the exchange rates among the sites. A particular dynamic model should be consistent with all the spectroscopic lineshape data

that are available. Thus, testing the applicability of a model requires careful analysis of the lineshapes and intensity of quadrupole echo spectra as a function of temperature and of the solid echo pulse delay. Furthermore, one must be able to simulate the anisotropic spin lattice relaxation recorded by the inversion recovery experiment using this model.

In the last few years, there have been several ^{2}H-NMR studies of simple and complex molecules which have demonstrated many of the essential features expected in ^{2}H quadrupole echo lineshapes. For instance, phenylalanine and tyrosine aromatic side chains have been shown to exhibit two-site flips (Hiyama et al., 1986; Rice et al., 1987; Rice et al., 1981), proline ring motions have been observed (Sarkar et al., 1986), and spectra of methyl and ammonium groups display lineshapes consistent with three-fold motion (Batchelder et al., 1983; Beshah et al., 1987; Beshah & Griffin, 1989; Long et al., 1994; Maus et al., 1996). In addition, other applications have focused on more complex systems such as polymers (Jelinski, 1985; Spiess, 1985; Spiess, 1983; Ebelhauser & Spiess, 1985), proteins (Burke et al., 1993), and lipid bilayers (Speyer et al., 1989; Ruocco et al., 1996; Siminovitch et al., 1985; Huang et al., 1980) which, in general, exhibit complex lineshapes. For example, polymers commonly exhibit distributions of correlation times and proteins can have multiple sites which can display a range of dynamic behaviors. In lipid bilayers multiple motions can occur at different rates and therefore lead to complicated spectra. Thus, despite the relatively large number of ^{2}H-NMR studies of molecular dynamics, there is a paucity of cases where it has been possible to unambiguously confirm the correctness of the lineshape and T_1 calculations. It is this fact which provided the primary motivation for the experiments described here.

In order to test the lineshape calculations, we desired a molecule which would exhibit relatively simple molecular motions. In addition, the material should display a single phase, with a single dynamically distinct site. Finally, it is useful to have a system where the rates can be varied from 10^4-10^7 s^{-1}, for instance at low temperatures where the quadrupole echo lineshapes will be affected, to 10^8-10^{11} s^{-1} at higher temperatures

where T_1 and T_1 anisotropies will change. The simple hydrates are excellent candidates for this type of study. Many of these substances have been crystallized and their structure and phase behavior are well characterized (Holcomb & Pedersen, 1962; McGrath & Silvidi, 1963; Silvidi et al., 1964; Silvidi, 1966). In addition, the H_2O molecules of hydration exhibit two-fold flips about the HOH bisector at rates which can be varied by controlling the temperature. Thus, at low temperatures the motion can be in the regime appropriate for quadrupole echo experiments, and, since the molecules are relatively small and can therefore move rapidly at higher temperatures, the anisotropy of the T_1 will be affected. Finally hydrates are easily labeled simply by recrystallization from D_2O.

3.2.2 Materials and Methods

Sample Preparation. Single crystals of $Ba(ClO_3)_2 \cdot {}^2H_2O$ were grown by slow evaporation of a saturated solution of barium chlorate in D_2O at room temperature. The dried crystals were crushed to form a powder which was sealed in a 5 mm sample tube.

NMR Spectroscopy. The NMR measurements were performed on a home-built spectrometer operating at a deuterium frequency of 61.05 MHz using quadrature detection and a dwell time of 0.5 μs. The $\pi/2$ pulse length was 1.6-2.0 μs. A phase-cycled quadrupole echo sequence was employed to observe τ-dependent and temperature-dependent spectra. The quadrupole echo pulse spacing varied between 30 μs and 200 μs. Partially relaxed spectra were recorded with an inversion recovery sequence, where Zeeman magnetization was inverted with a π pulse. After a recovery delay of time t_1, Z-magnetization was monitored by a quadrupole echo sequence. To guarantee the fidelity of the ^2H NMR lineshapes, the recycle delays employed were typically six times T_1 for the quadrupole echo experiments and twelve times T_1 for the inversion recovery sequence.

Powder Lineshape Calculations. The lineshape calculations discussed below account for anisotropic transverse and longitudinal relaxation, as well as finite pulse width effects. The details of the simulations are explained elsewhere (Wittebort et al.,

1987). Given the simplicity of this system, correlation functions for $\eta \neq 0$ were also included in the relaxation calculation. In the rigid lattice limit (T~-120°C), deuterons in $Ba(ClO_3)_2 \cdot {}^2H_2O$ exhibit a quadrupole coupling constant (e^2qQ/h) = 244 kHz and an asymmetry parameter η = 0.074 (Chiba, 1963). As the temperature is increased, vibration attenuates the quadrupole coupling constant and averages the asymmetry. If the water molecule is not flipping, it vibrates with frequencies on the order of 10^{13} s^{-1}. (Ericksson et al., 1979) However, this is much higher than the Larmor frequency employed in our experiments and should have little direct effect upon the observed spin-lattice relaxation, but as stated above, an oscillatory motion of the water molecule about the bisector leads to a decrease of the quadrupole coupling constant proportional to the amplitude of angular oscillation. Both the quadrupole coupling constant and assymetry parameter were studied as a function of temperature in the single crystal experiments of Chiba and coworkers. Their values were used in the present study. Since the deuteron sites are identical, the equilibrium population of each is one-half. A jump angle of 110.7° was used in close agreement with neutron diffraction analysis (Sikka et al., 1968). The spectra discussed below demonstrate that deviations in the D-O-D angle from the tetrahedral angle and the asymmetry of the static **EFG** tensor compensate for one another to yield an $\eta \equiv 1$ spectrum in the fast exchange limit.

The pulse widths, quadrupole echo pulse spacing, and the delay in the inversion recovery sequence are input parameters dictated by the experiment. To account for other relaxation mechanisms, a homogeneous transverse relaxation time was introduced in the calculation by exponentially broadening the line from each crystallite sub-spectrum by $1/\pi T_2^* = 1$ kHz. This value is based on the measurement of T_2 in the fast motion limit (data not shown). This is somewhat shorter than usually observed in deuterium spectra and can be attributed to the dipole coupling between the deuteriums in the water molecule which is unattenuated by 180° flips. Thus, the only unknown parameter in this simula-

tion was the exchange rate, which was adjusted to provide satisfactory agreement between experimental and calculated spectra.

3.2.3 Results and Discussion

3.2.3a Quadrupole Echo Lineshapes

In Figure 3-8 ^{2}H-NMR quadrupole echo spectra of $Ba(ClO_3)_2 \cdot ^2H_2O$ are shown as a function of temperature between -119 and 18°C, together with simulated spectra for a tetrahedral jump between two sites of equal population. In a manner which will be described below, the rate constants for some of these simulations were obtained from the inversion recovery experiment (except for the low temperature spectrum at -119°C), where the exchange rates can be determined with high accuracy. In particular, at each temperature an entire series of partially relaxed lineshapes is available for simulation rather than a single spectrum.

The spectra displayed in Figure 3-8 are typical for the rigid, intermediate, and fast exchange limits, and demonstrate the excellent agreement which can be achieved between the experimental and calculated lineshapes. At -119°C, using a recycle delay of 200 sec, we obtain an almost rigid lattice lineshape displaying an asymmetry parameter $\eta = 0.074$. In contrast, spectra recorded between -83 and -58°C are characteristic of the intermediate exchange regime where the rigid lattice tensors of the water molecule are transformed to an averaged field gradient tensor by the twofold flipping motion. In comparison to the rigid lattice spectrum, the intermediate exchange lineshapes show no parallel edges and concurrently a spike appears in the middle of the spectrum which develops with increasing temperature. The components of the rigid lattice electric field gradient perpendicular to the plane of the water molecule ($V_\perp$) are not affected by the twofold flipping motion, but the averaged tensor element lying along the axis of motion (the bisector of the water molecule) is approximately zero and corresponds to the center of the spectrum. Since $Tr(H_Q)=0$, the third tensor element must be the negative of the element of the static field gradient ($-V_\perp$) that is not averaged by the jump process. Thus, $V_\perp$ and $-V_\perp$ correspond

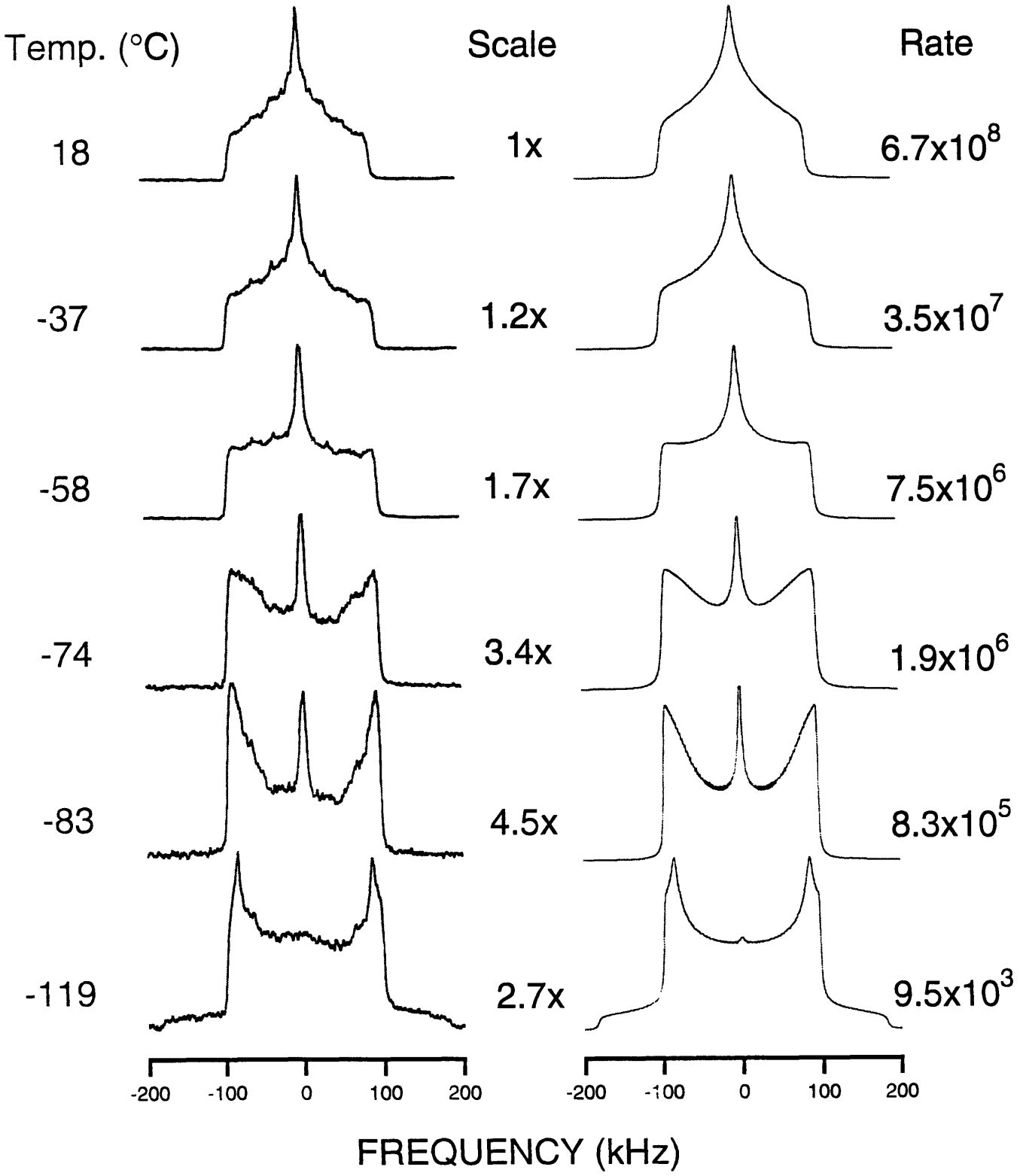

Figure 3-8. Temperature dependence of the experimental quadrupole echo spectra of $Ba(ClO_3)_2 \cdot {}^2H_2O$ and corresponding simulations for a pulse delay of $\tau = 30$ μs.

to the outer edges of the averaged spectrum. Between -37 and 18°C the rates are in the rapid exchange limit for the quadrupole echoes and the lineshapes show no changes at higher temperature except that the width of the spectra decreases slightly, reflecting further averaging of the electric field gradient tensor via vibration. (Ericksson et al., 1979)

To illustrate the τ-dependent quadrupole echo spectra, lineshapes recorded for a pulse spacing of 30 , 100, and 200 μsec at a temperature of -74°C are presented in Figure 3-9. Despite a large change in pulse spacing, the alterations in lineshapes due to anisotropic dephasing of transverse magnetization (in the intermediate exchange regime) are relatively minor. However, it can be readily observed that T_2 is longest if the magnetic field orientation is perpendicular (outer edges) or parallel (spike) to the HOH bisector, while other orientations relax more quickly. The calculated lineshapes in Figure 3-9 are in good agreement with the experimental spectra and describe the observed anisotropy. In a similar manner, the exchange-induced τ-dependence of the spectra can be interpreted.

3.2.3b Quadrupole Echo Spectral Intensities

In Figure 3-9, all spectra have been scaled to the same intensity to ensure that details of the lineshape can be observed. However, the tetrahedral jump model should not only account for changes in the lineshape with τ and jump rate, but it should also predict the variation of signal intensity with temperature. For this reason we must compare experimental and calculated integrated signal intensities for a given value of τ at each temperature. The measurement of absolute signal intensities is complicated by the fact that a value for $\tau = 0$ is required, and this cannot be obtained because of the finite recovery time of the spectrometer components following the RF pulses. However, the absolute signal intensity can be measured in the rapid exchange limit where the echo intensity has an almost exponential dependence on τ; there, extrapolation of the points to $\tau = 0$ is possible. By correcting these intensities for temperature variations through use of the Boltzmann factor, $e^{-h\omega/kT}$, the desired fast limit echo intensities of the FID can be

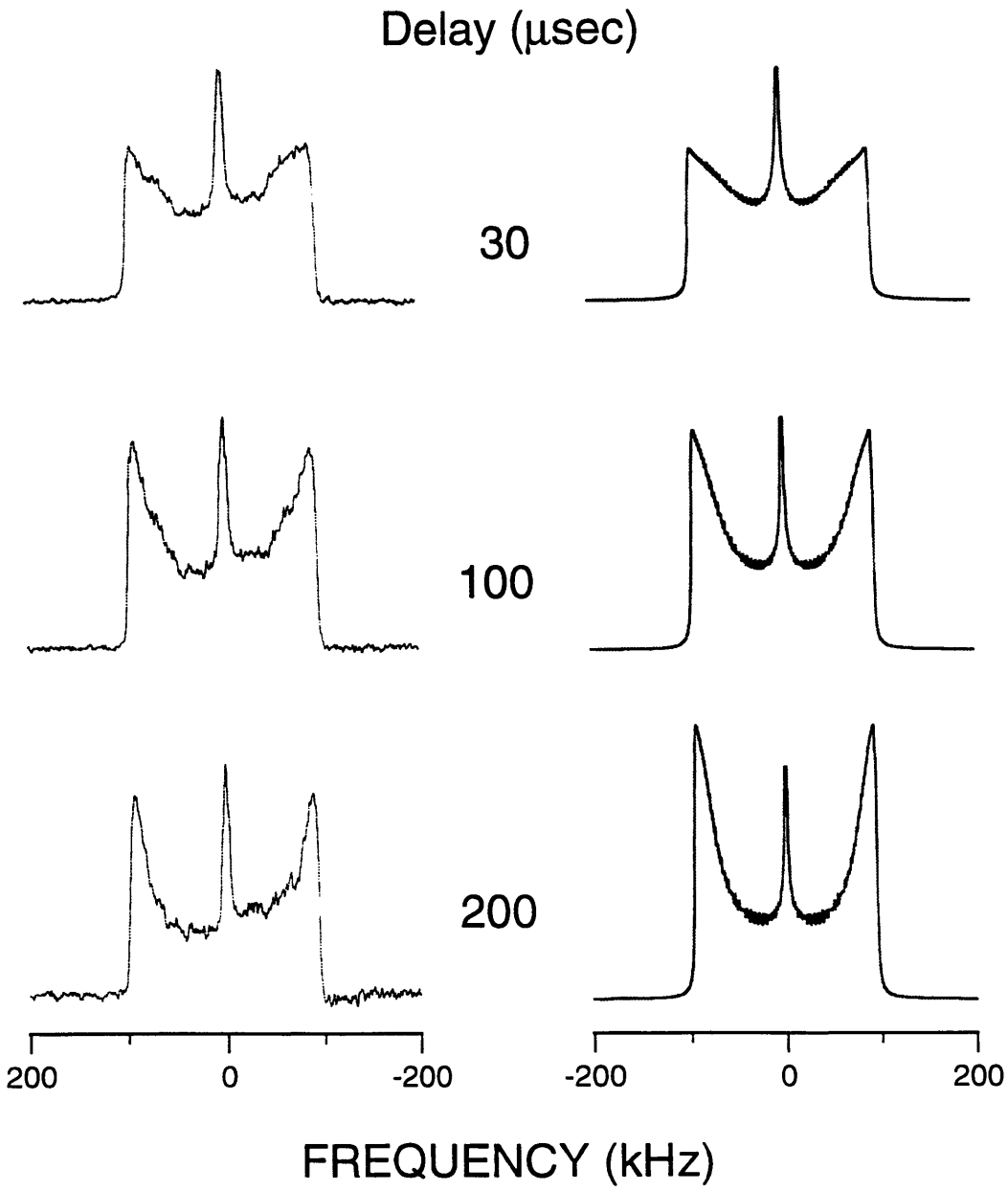

Figure 3-9. τ-dependence of quadrupole echo spectra at a temperature of -74°C.

calculated. For the intermediate exchange regime, where relaxation is strongly orientation-dependent, this extrapolation of data points is not possible, as the transverse relaxation is very non-exponential. An additional consideration in calculating absolute echo intensities is the fact that finite pulse width effects are larger for a rigid lattice than for motionally averaged spectra, which may result in excessively low echo intensity measurements for $\tau_c^{-1} << \omega_Q$.

The solid lines in Figure 3-10 are calculated signal intensities for pulse spacings of 30, 100, and 200 μsec on the basis of the two-site jump model for the water molecule assuming a fast-limit T_2 of 320 μsec. While this relaxation parameter does not change the lineshape profile, it largely determines the echo intensity in the rigid and rapid exchange cases, since transverse relaxation in these limits is no longer dominated by modulation of the quadrupole interaction. This is particularly significant for longer pulse delays. In addition, finite pulse width effects lead to signal intensities of less than one, since broadband excitation of the spectra is limited. For short pulse spacing this contribution to the reduction of signal intensities may overshadow losses due to transverse relaxation, and losses are larger for the rigid exchange limit than for the fast exchange limit because of the broader spectral width for the static case. The jump rates for the experimental points were obtained by analyzing the corresponding inversion recovery spectra as discussed in the next section. The variation of the signal intensities shows that, in the rigid and fast limit regimes for the quadrupole echo experiment, significant attenuation of the echo is observed even though the lineshapes are no longer dependent on the jump rates. Interestingly, the curves are asymmetric with a minimum that is dependent on the pulse spacing. It is shifted to slower exchange rates with increasing pulse spacing. In particular, for a delay of 30 μsec the minimum occurs at log (k) = 5, with a signal intensity of about 11% of the FID intensity. The corresponding minima for the pulse spacings 100 and 200 μsec occur at log (k) = 4.5 and 4.2, with signal intensities of 3% and less than 1%, respectively. The comparison of experimental and calculated signal

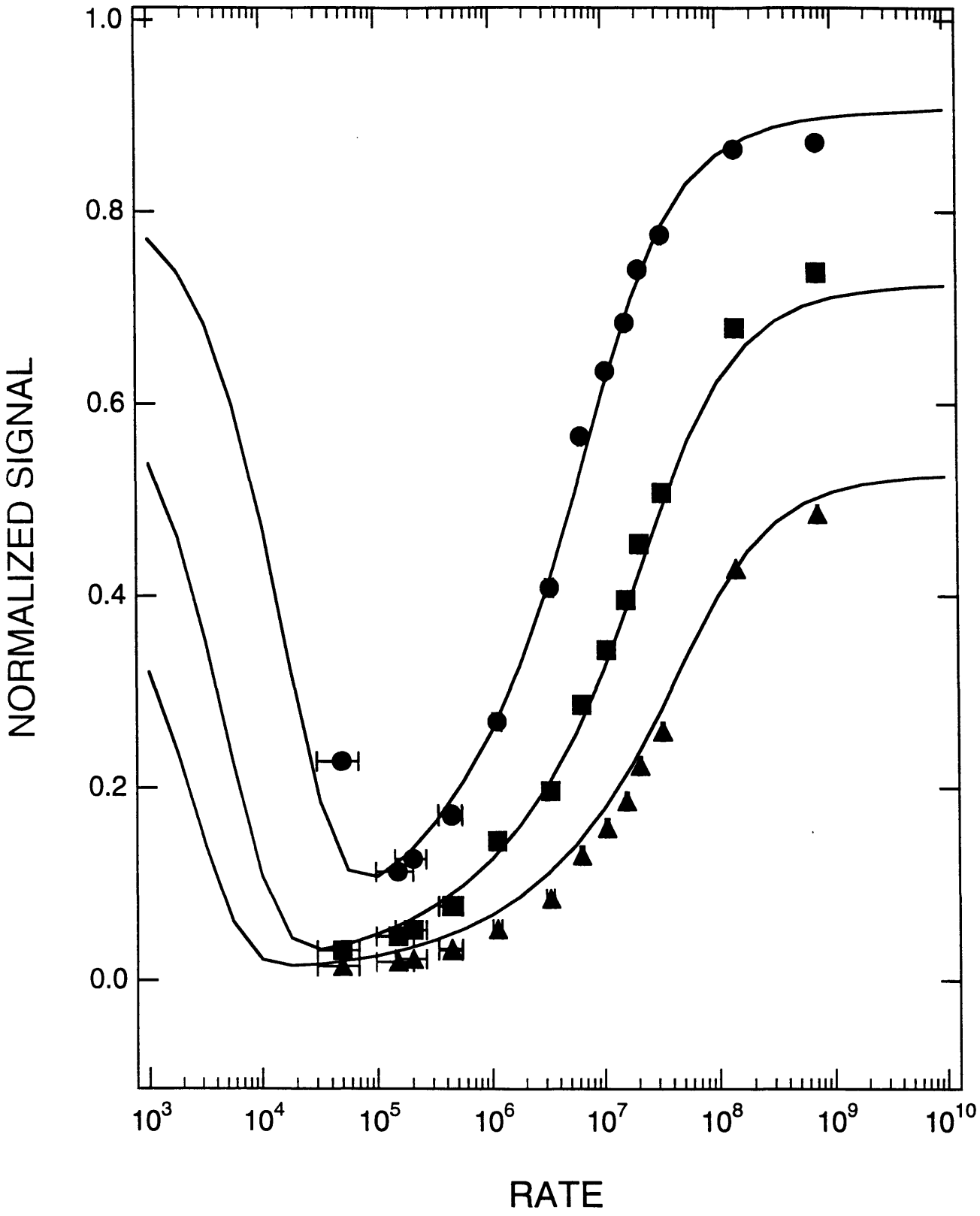

Figure 3-10. Calculated (solid lines) and experimental signal intensities for three different pulse spacings: τ= 30 μsec (●), τ= 100 μsec (■) and τ= 200 μsec (▲).

intensities shows good agreement. We did not measure signal intensities for rates below log (k) = 4.5 since the relaxation time T_1 becomes prohibitively long.

3.2.3c Anisotropic Spin-Lattice Relaxation

In addition to quadrupole echo lineshapes, we have employed the anisotropy of the deuteron spin lattice relaxation to determine the rates of motion. Before discussing lineshapes for partially recovered spectra recorded as a function of temperature, we examine the orientation dependence of T_1 (Figure 3-11). As usual, the spherical polar angles, θ and ϕ, define the orientation of the external magnetic field in the molecular frame. Note that the orientations with longer T_1's are shown by dotted contours, while the faster relaxing orientations are indicated by solid lines. These contours were generated using correlation functions for two-site 180° flips (Vold & Vold, 1991). The Zeeman relaxation is dominated by motions of the quadrupole nucleus on the order of the Larmor frequency and twice the Larmor frequency,

$$\frac{1}{T_{1z}} = \frac{3\pi^2}{2}\left(e^2qQ/h\right)^2\left[J_1(\omega_0) + 4J_2(2\omega_0)\right] \tag{3-13}$$

For two equivalent sites, the correlation functions, assuming η=0, are

$$J_1(\omega_0) = \frac{1}{2}\frac{3k}{4k^2+\omega_0^2}\sin^2\beta\cos^2\beta[1-3\cos^2\theta+4\cos^4\theta+$$

$$(4\cos^4\theta-5\cos^2\theta+1)\cos 2\phi] \tag{3-14}$$

$$J_2(2\omega_0) = \frac{1}{2}\frac{3k}{4k^2+4\omega_0^2}\sin^2\beta\cos^2\beta\left[1-\cos^4\theta-\sin^4\theta\cos 2\phi\right] \tag{3-15}$$

where β is the angle between the O-D bond and the flipping axis. For tetrahedral geometry, this angle is near the magic angle (54.75°). In the top plot of Figure 3-11, $k << \omega_0$, so the expression for the correlation functions reduces to

$$J_1(\omega_0) + 4J_2(2\omega_0) = \frac{3k}{2\omega_0^2}\left[1-\frac{3}{2}\cos^2\theta(1-\cos^2\theta)(1+\cos 2\phi)\right] \tag{3-16}$$

If the hopping rate is equivalent to the Larmor frequency,

$$J_1(\omega_0) + 4J_2(2\omega_0) = \frac{5}{6k}\left[1-\frac{3}{5}\cos^2\theta+\frac{3}{10}(\cos^4\theta-1)(1+\cos 2\phi)\right] \tag{3-17}$$

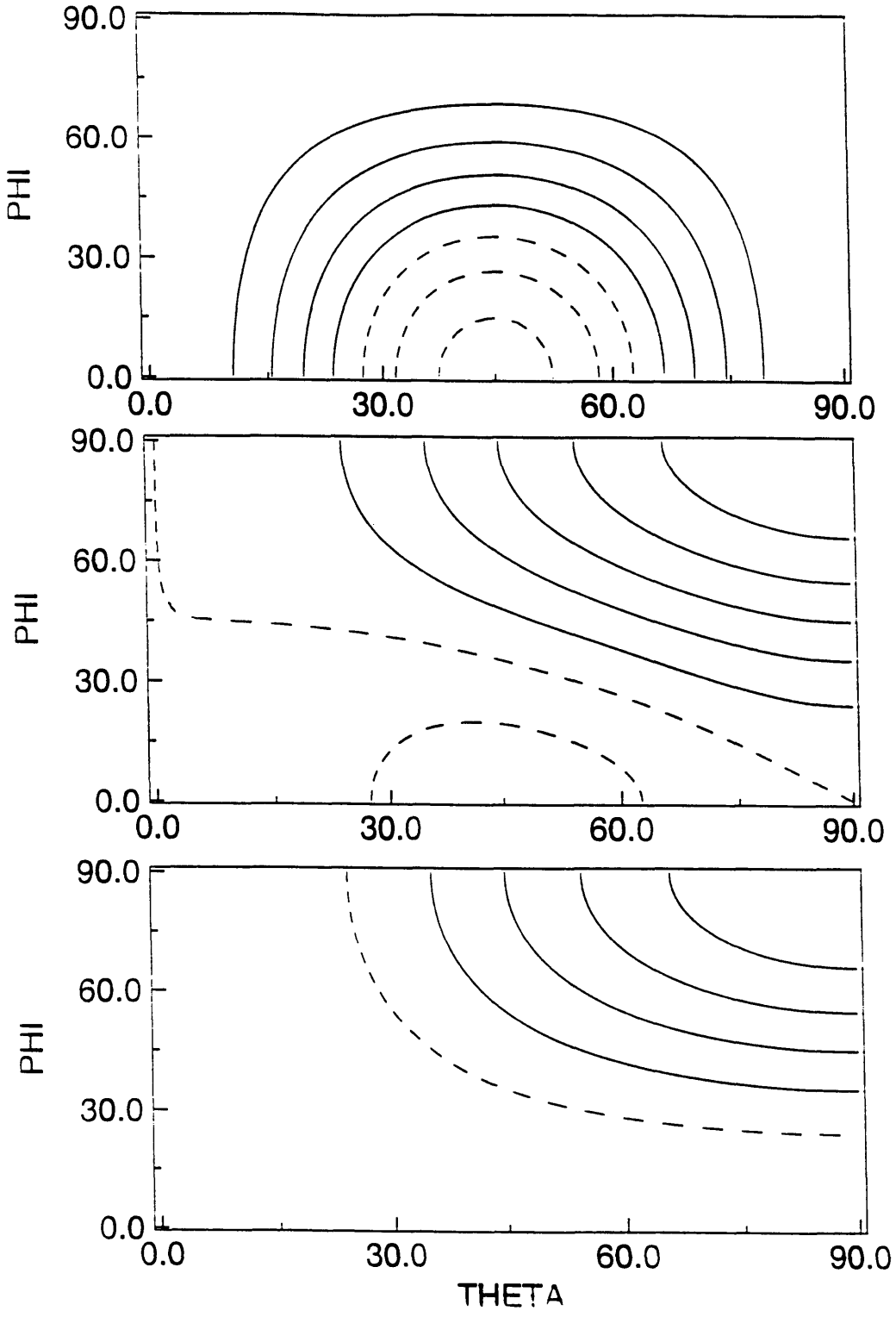

Figure 3-11. Contour plots representing the anisotropy of T_1. The angles θ and ϕ specify the magnetic field orientation in the molecular frame. (Top) $k << \omega_0$; (Middle) $k \approx \omega_0$; (Bottom) $k >> \omega_0$.

This result is plotted in the middle of Figure 3-11. As the rate increases until it is much greater than the Larmor frequency, the relaxation follows

$$J_1(\omega_0) + 4J_2(2\omega_0) = \frac{3}{8k}\left[1 - \frac{3}{2}\sin^2\theta(1 - \cos 2\phi)\right] \qquad (3\text{-}18)$$

as shown in the bottom plot of Figure 3-11.

In order to understand the effect of orientation-dependent T_1's on the partially relaxed lineshapes, it is necessary to relate the tensor elements $V_{\parallel}$ and $V_{\perp}$ to their spectral frequencies. In the case of the motionally averaged asymmetric $\eta = 1$ spectrum, the elements $\pm V_{\perp}$ ($\theta = 90°$, $\phi = 0°, 90°$) define the outer portion of the spectrum, while $V_{\parallel}$ ($\theta = 0°$) generates the center of the spectrum. Next, we consider the T_1 anisotropy for three cases with jump rate $k << \omega_0$ (Figure 3-11 top), $k = \omega_0$ (middle) and $k >> \omega_0$ (bottom). For jump rates much slower than the Larmor frequency, T_1 is longest if $\theta = 45°$ and $\phi = 0°$, while the shortest T_1 is given by orientations where $\theta = 0°$ or $\theta = 90°$. Thus the portions of the spectrum determined by $\pm V_{\perp}$ and $V_{\parallel}$ should recover first. In the middle frame of Figure 3-11 the jump rate is comparable to the Larmor frequency and characteristics of the T_1 anisotropy of the slow and fast regime are superimposed. Examining the bottom contour plot we see that the T_1 anisotropy is distinctly different for jump rates faster than the Larmor frequency. Again, T_1 is shortest if $\theta = 90°$, $\phi = 90°$, reflecting the tensor element $V_{\perp}$ that is not averaged by the molecular motion. However, in this regime T_1 is longest for $V_{\parallel}$ (center of the spectrum). Consequently, a reversal in the anisotropy of the powder pattern will be observed upon going from $k << \omega_0$ to $k >> \omega_0$.

We now examine the experimental and calculated T_1's measured via inversion recovery experiments at several different temperatures. The T_1's in Figure 3-12 were measured between -90 and -60°C where $k << \omega_0$. Discounting finite pulse width effects (discussed below), little anisotropy is seen in the frequency profile. However, if individual spectra taken near the zero-crossing are examined, it is still possible to see significant anisotropy. Such a spectrum is plotted at the bottom of Figure 3-12. In Figures 3-13 and 3-14 T_1's were measured in the ranges -45 to -8°C and 1 to 55°C, respectively. These

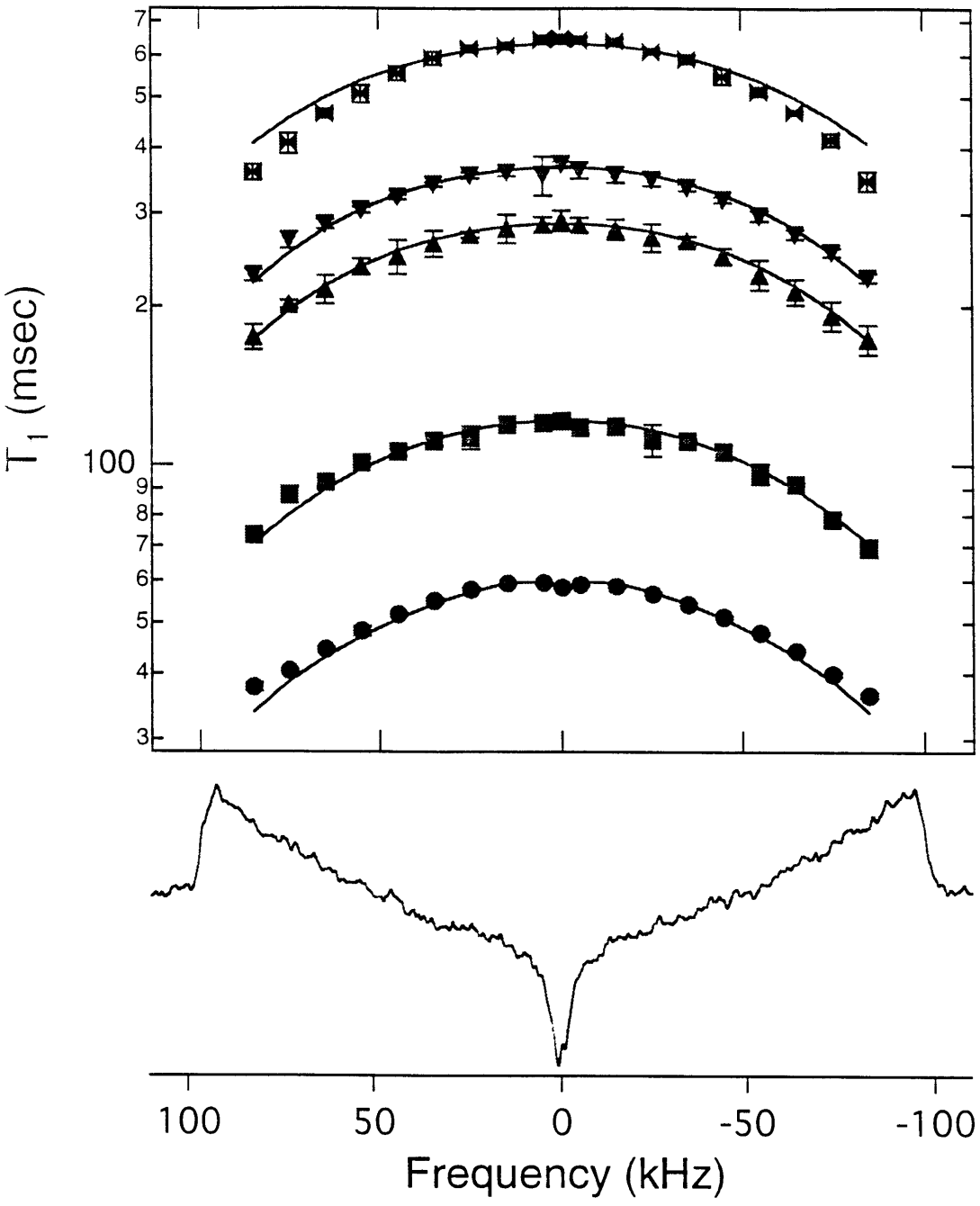

Figure 3-12. Experimental and calculated T_1 anisotropy profiles at five different temperatures between -90 and -60°C ($k<<\omega_0$): (✖) -89°C, $k=4.3\times10^5$, (▼) -83°C, $k=7.6\times10^5$, (▲) -81°C, $k=9.65\times10^5$, (■) -71°C, $k=2.4\times10^6$, (●) -62°C, $k=5.2\times10^6$. A spectrum taken near the T_1 zero crossing (230 msec) at -83°C is also plotted.

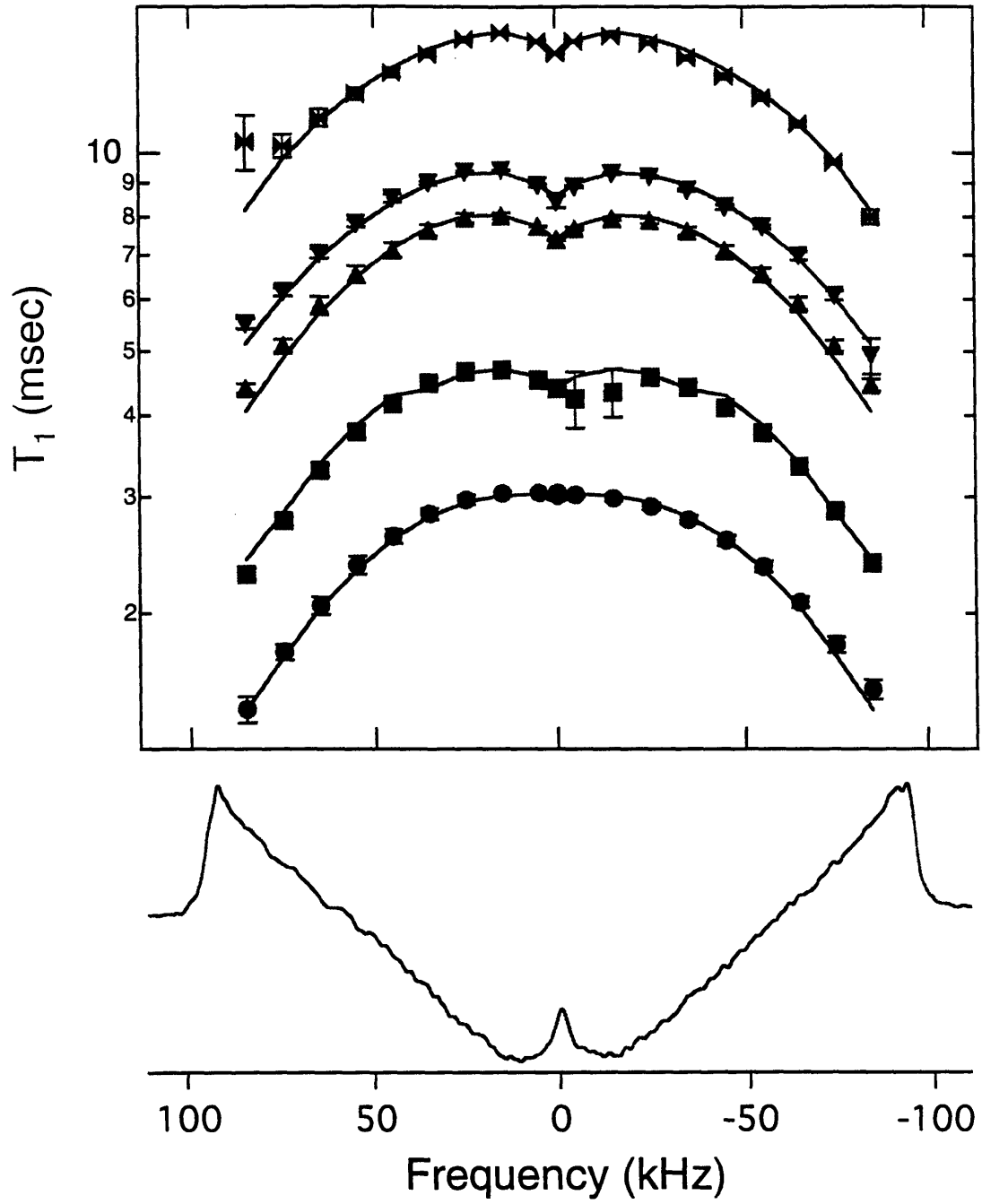

Figure 3-13. Experimental and calculated T_1 anisotropy profiles at five different temperatures between -45 and -8°C ($k \sim \omega_0$): (⋈) -44°C, $k=2.30 \times 10^7$, (▼) -37°C, $k=3.98 \times 10^7$, (▲) -34°C, $k=4.66 \times 10^7$, (■) -23.5°C, $k=8.75 \times 10^7$, (●) -8.4°C, $k=2.10 \times 10^8$. A spectrum taken near the T_1 zero crossing (5.5 msec) at -37°C is also plotted .

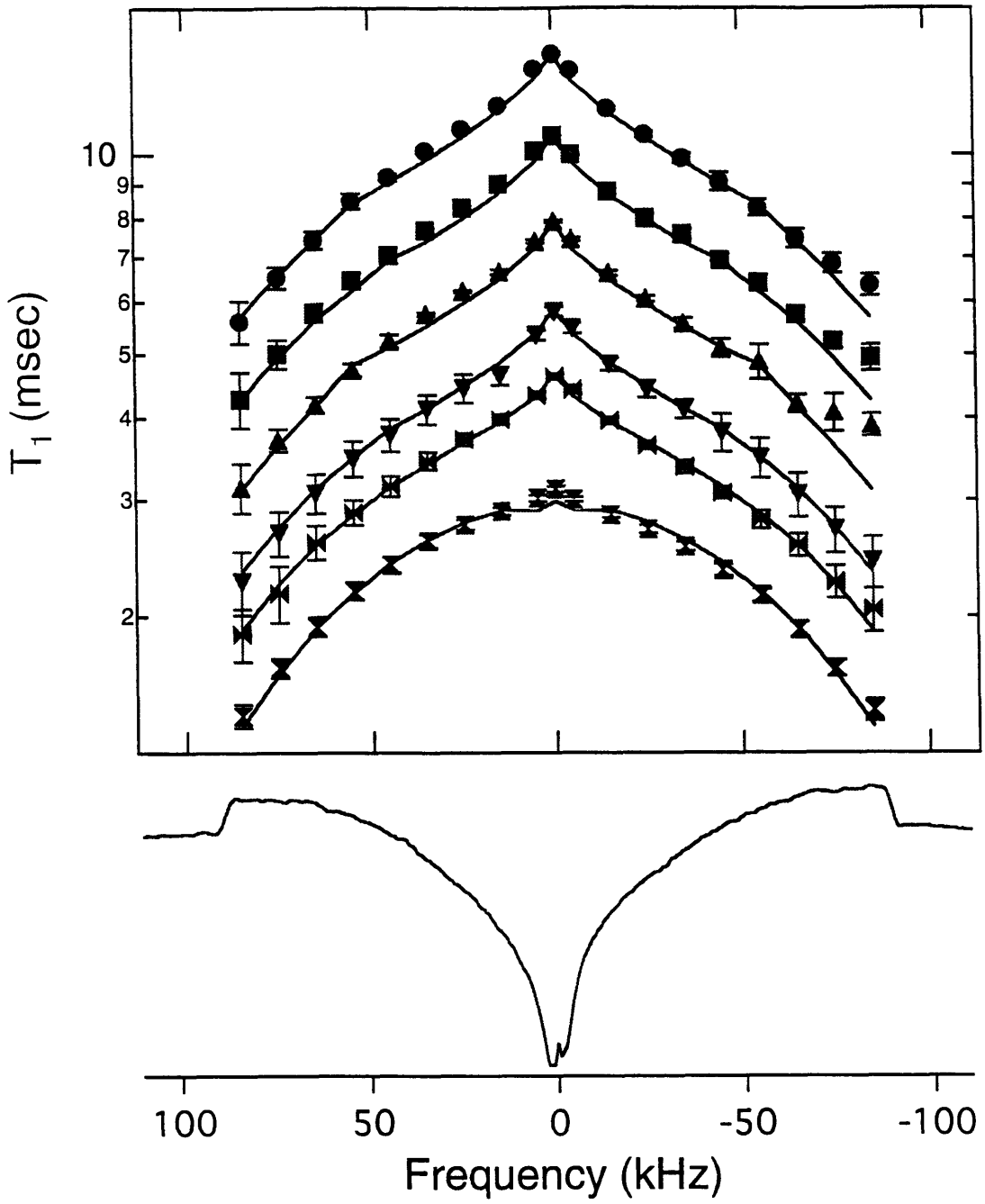

Figure 3-14. Experimental and calculated T_1 anisotropy profiles at six different temperatures between 0 and 55°C ($k>>\omega_0$): (⧗) 1.0°C, $k=3.20\times10^8$, (■) 20.5°C, $k=6.92\times10^8$, (▼) 27.3°C, $k=9.45\times10^8$, (▲) 36.2°C, $k=1.34\times10^9$, (■) 45.6°C, $k=1.85\times10^9$, (●) 54.9°C, $k=2.48\times10^9$. A spectrum taken near the T_1 zero crossing (3.6 msec) at 36.2°C is also plotted.

correspond to jump rates with $k \sim \omega_0$ and $k >> \omega_0$. Observed and simulated relaxation rates are in excellent agreement for all temperatures. In particular, it is possible to see the reversal in the anisotropy at the center of the spectra as the hopping rate increases, and for the rapid exchange limit $k >> \omega_0$, the center of the spectrum exhibits a relatively long T_1 in accordance with our predictions from the anisotropic relaxation profiles in Figure 3-11. Spectra taken near the zero-crossing at -37°C and 36.2°C (Figures 3-13 and 3-14, respectively) also demonstrate this reversal of anisotropy at the center frequency.

Finally, in this section we will discuss the dependence of the relaxation simulations on vibrational averaging of the quadrupole coupling constant and eta as well as finite pulse width corrections. In Figure 3-15a the relaxation observed at room temperature is plotted along with best-fit simulations using the rigid-lattice and vibrationally averaged quadrupole coupling constants both including and neglecting the contributions of $\eta \neq 0$ to the correlation functions. Within experimental error these simulations are indistinguishable. However, the hopping rates vary significantly from 9.45×10^8 using the vibrationally averaged constants to 1.14×10^9 using the rigid lattice quadrupole coupling and $\eta = 0$. In fact neglecting either of these parameters, the averaging of the quadrupole coupling or the inclusion of $\eta \neq 0$ in the calculation of the correlation function, can lead to a 5% error in the determination of the activation energy for the hopping, and their effects are additive (data not shown). Figure 3-15b demonstrates the effect of incomplete inversion due to finite pulse widths. Experimental data for inversion pulse lengths of 4.0 and 4.4 μsec agree well with simulation. In addition, the expected results for 3.6 μsec and complete inversion are shown.

3.2.3d Activation Energy for Reorientation of the Hydrate Molecule

The rates of chemical exchange obtained by simulating the inversion recovery profiles are plotted in the form of ln k versus 1/T in order to obtain the activation energy for the rotation of the water molecule about its C_2 axis. The points fall almost on a straight line between rates of 4.3×10^5 and 2.48×10^9 s^{-1}. (Note that the point at a temp

Figure 3-15a. Experimental and calculated T_1 anisotropy profiles at 27.3°: (O) experimental data, (.....) $k=9.45x10^8$, $e^2qQ/h=231.4$ kHz, $\eta=0.040$, (-----) $k=9.76x10^8$, $e^2qQ/h=231.4$ kHz, $\eta=0$, (- - - -) $k=1.07x10^9$, $e^2qQ/h=243.5$ kHz, $\eta=0.074$, (-- -- --) $k=1.14x10^9$, $e^2qQ/h=243.5$ kHz, $\eta=0$.

Figure 3-15b. Experimental and calculated T_1 anisotropy profiles at 27.3°: (◐) experimental data with inversion pulse length 4.0 μsec, (▲) experimental data with inversion pulse length 4.4 μsec, (.....) $k=9.45x10^8$, pulse width correction 4.4 μsec, (------) $k=9.45x10^8$, pulse width correction 4.0 μsec, (- - - -) $k=9.45x10^8$, pulse width correction 3.6 μsec, (-- -- --) $k=9.45x10^8$, no pulse width correction.

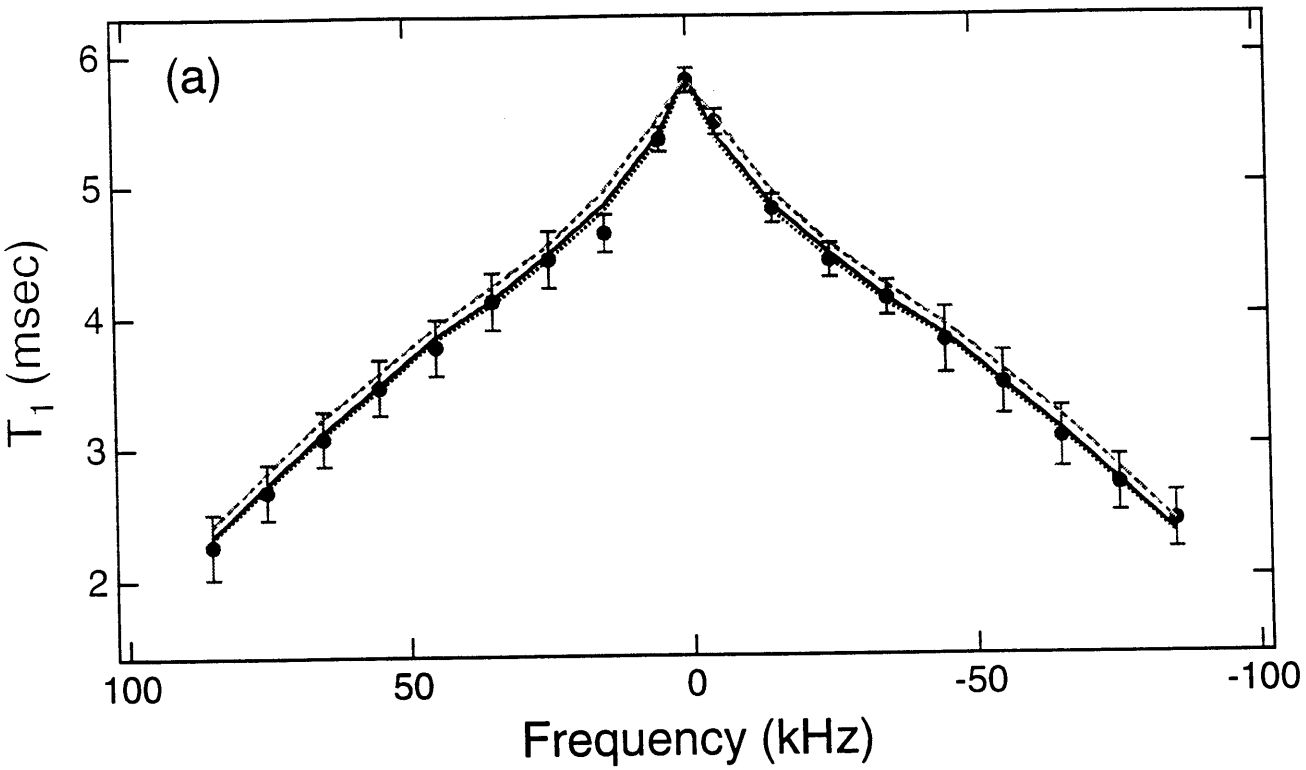
(a)
6
5
4
3
2
T_1 (msec)
100
50
0
-50
-100
Frequency (kHz)

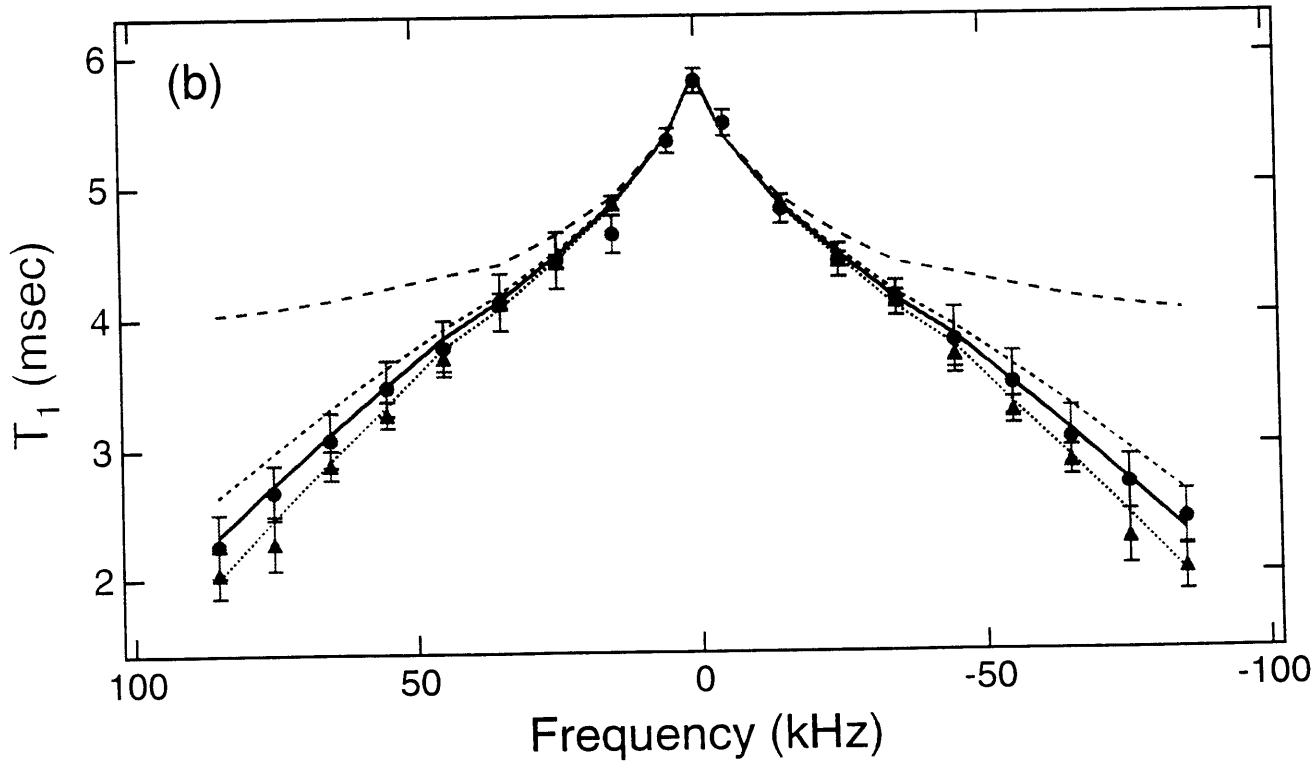
(b)
6
5
4
3
2
T_1 (msec)
100
50
0
-50
-100
Frequency (kHz)

erature of -119°C was obtained by extrapolation, yielding the jump rate that was used to simulate the low temperature spectrum in Figure 3-8.) The plot presented in Figure 3-16 is consistent with an activation energy of 29.9±0.9 kJ/mol. If we assume that each water deuteron is linked by a hydrogen bond to the nearest oxygen atom of the chlorate anion, then the 180° flip motion involves breaking two hydrogen bonds. The activation energy calculated for $Ba(ClO_3)_2 \cdot H_2O$ is typical for hydrates with hydrogen bonds of moderate strength if crossing the rotational barrier is associated with breaking the hydrogen bonds (Holcomb et al., 1962; Silvidi, 1966). In barium chlorate monohydrate the hydrogen bond has a length of 1.991 Å as measured by neutron scattering, which is typical for an N-D···O bond (Sikka et al., 1968). In further support of our measurement, the activation energy reported here is in good agreement with values reported by other NMR techniques. In particular, proton spin lattice relaxation time measurements on single crystals of $Ba(ClO_3)_2 \cdot H_2O$ provided an activation energy of 19.2±2.1 kJ/mol (Silvidi, 1966) (the isotope effect due to the substitution of deuterium predicts a ratio of 1.4 for the activation energies.), while CW deuteron lineshape analysis performed on single crystals of $Ba(ClO_3)_2 \cdot D_2O$ yielded an activation energy of 27.2 kJ/mol (Chiba, 1963).

3.2.4 Conclusions

Deuterium NMR spectroscopy has been employed to investigate the motion of the water molecule in barium chlorate monohydrate. A simple two-site jump model describing exchange between degenerate orientations has been demonstrated to provide excellent agreement between experimental and simulated quadrupole echo and inversion recovery spectra. In the temperature range considered in this work, lattice vibration and internal vibratory motions of the water molecule need not be explicitly included in the calculation of the longitudinal relaxation time T_1, but they do lead to averaging of the quadrupolar coupling and eta.

Motions with rates higher than the quadrupole coupling constant can be studied conveniently by the inversion recovery sequence, while motions with rates on the order

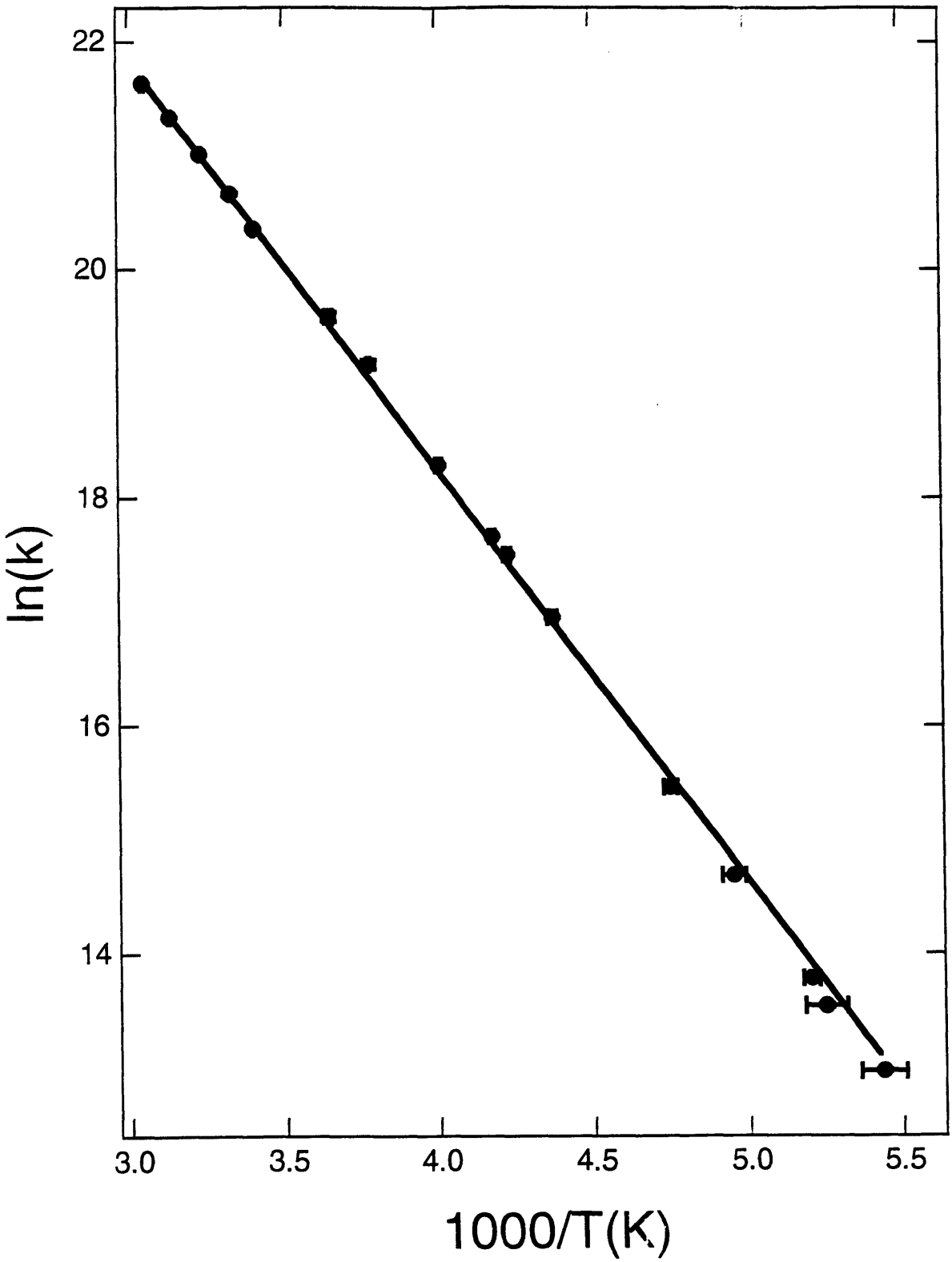

Figure 3-16. Observed temperature dependence of the jump rate for the 180° flipping motion of the water molecule. A least squares fit of the data yields an activation energy of 29.9±0.9 kJ/mol

of or slower than the coupling constant may also be determined using the τ-dependence technique. Thus, the combination of quadrupole echo and inversion recovery measurements, with iterative simulations of the data, provides an excellent tool for probing the mechanism and time scale of molecular motions in solids.

References

Andrew, E.R., Hinshaw, W.S. & Hutchins, M.G. (1974) *J. Mag. Res. 15*, 196-200.

Andrew, E.R., Hinshaw, W.S., Hutchins, M.G., Sjöblom, R.O.I. & Canepa, P.C. (1976) *Mol. Phys. 32*, 795-806.

Batchelder, L.S., Niu, C.H. & Torchia, D.A. (1983) *J. Amer. Chem. Soc. 105*, 2228-2231.

Beshah, K. & Griffin, R.G. (1989) *J. Mag. Res. 84*, 268-274.

Beshah, K., Olejniczak, E.T. & Griffin, R.G. (1987) *J. Chem. Phys. 86*, 4730-4736.

Bloom, M., Davis, J.H. & Valic, M.I. (1980) *Can. J. Phys. 58*, 1510.

Burke, P.A., Griffin, R.G. & Klibanov, A.M. (1993) *Biotechn. Bioeng. 42*, 87-94.

Chiba, T. (1963) *J. Chem. Phys. 39*, 947-953.

Davis, J.H. (1983) *Biochim. Biophys. Acta 737*, 117-171.

Ebelhauser, R. & Spiess, H.W. (1985) *Ber. Bunsenges. Phys. Chem. 89*, 1208-1214.

Ellett, D., Griffin, R.G. & Waugh, J.S. (1974) *J. Amer. Chem. So. 96*, 345.

Ellett, D., Haeberlen, U. & Waugh, J.S. (1970) *J. Amer. Chem. Soc. 92*, 411.

Ericksson, A., Hussein, N.A., Berglund, B., Tegenfeldt, J. & Lindren, J. (1979) *J. Mol. Struct. 52*, 95-105.

Frydman, L. & Frydman, B. (1990) *J. Chem. Phys. 92*, 1620.

Griffiths, J., Hall, M. & Griffin, R.G. Private Communication.

Griffin, R.G. (1981) *Meth. Enzymol. 72*, 108-174,

Griffin, R.G., Beshah, K., Ebelhauser, R., Huang, T.H., Olejniczak, E.T., Rice, D.M., Siminovitch, D.J. & Wittebort, R.J. (1988) in *The Time Domain in Surface and Structural Dynamics* (Long, G.J. & Grandjean, F., Ed.) , Kluwer Academic Publishers, 81-105.

Hiyama, Y., Silverton, J.V., Torchia, D.A., Gerig, J.T. & Hammond, S.J. (1986) *J. Ame. Chem. Soc. 108*, 2715-2723.

Holcomb, D.F. & Pedersen, B. (1962) *J. Chem. Phys. 36*, 3270.

Huang, T.H., Skarjune, R.P., Wittebort, R.J., Griffin, R.G. & Oldfield, E. (1980) *J. Amer. Chem. Soc. 102*, 7377-7379.

Hunt, M.J. & MacKay, A.L. (1974) *J. Mag. Res.15*, 402-414.

Jelinski, L.W. (1985) *Ann. Rev. Mater. Sci. 15*, 359-377.

Kolbert, A.C., Raleigh, D.P. & Griffin, R.G. (1989) *J. Mag. Res. 82*, 483-491.

Lee, C.W.B. (1990) Massachusetts Institute of Technology.

Lehman, M.S., Koetzle, T.F. & Hamilton, W.C. (1972) *J. Amer. Chem. Soc.* 2657-2660.

Long, J.R., Sun, B., Bowen, A.E. & Griffin.R.G. (1994) *J. Amer. Chem. So. 116*, 11950-11956.

Mansfield, P. (1971) *J. Phys. Chem. C 4*, 1444.

Maricq, M.M. & Waugh, J.S. (1979) *J. Chem. Phys. 70*, 3300.

Maus, D.C., Copie, V., Sun, B., Griffiths, J.M., Griffin, R.G., Luo, S., Schrock, R.R., Liu, A.H., Seidel, S.W., Davis, W.M. & Grohmann, A. (1996) *J. Amer. Chem. Soc. 109*, 4282-4291.

McGrath, J.W. & Silvidi, A.A. (1963) *J. Chem. Phys. 39*, 3017-3021.

Olejniczak, E.T., Vega, S. & Griffin, R.G. (1984) *J. Chem. Phys. 81*, 4804-4817.

Rhim, W.-K., Elleman, D.D. & Vaugn, R.W. (1973) *J. Chem. Phys. 58*, 1772.

Rice, D.M., Meinwald, Y.C., Scheraga, H.A. & Griffin, R.G. (1987) *J. Amer. Chem. Soc. 109*, 1636-1640.

Rice, D.M., Wittebort, R.J., Griffin, R.G., Meirovitch, E., Stimson, E.R., Meinwald, Y.C., Freed, J.H. & Scheraga, H.A. (1981) *J. Amer. Chem. Soc. 103*, 7707-7710.

Rothwell, W.P. & Waugh, J.S. (1981) *J. Chem. Phys. 74*, 2721.

Ruocco, M.J., Siminovitch, D.J., Long, J.R., Das Gupta, S.K. & Griffin, R.G. (1996) *Biophys. J. 71*, In Press.

Sarkar, S.K., Young, P.E. & Torchia, D.A. (1986) *J. Amer. Chem. Soc. 108*, 6459-6464.

Sefcik, M.D., Schaefer, J., Stejskal, E.O., Ellena, J.F., Dodd, S.W. & Brown, M.F. (1983) *Biochem. Biophys. Res. Comm. 114*, 1048-1055.

Sikka, S.K., Momin, S.N., Rajagopal, H. & Chidambaram, R. (1968) *J. Chem. Phys. 48*, 1883-1890.

Silvidi, A.A. (1966) *J. Chem. Phys. 45*, 3892-3895.

Silvidi, A.A., McGrath, J.W. & Holcomb, D.F. (1964) *J. Chem. Phys. 41*, 105-111.

Siminovitch, D.J., Ruocco, M.J., Olejniczak, E.T., Das Gupta, S.K. & Griffin, R.G. (1985) *Chem. Phys. Lett. 119*, 251-255.

Speyer, J.B., Weber, R.T., Das Gupta, S.K. & Griffin, R.G. (1989) *Biochem. 28*, 9569-9574.

Spiess, H.W. (1978) *Dynamic NMR Spectroscopy*, Springer-Verlag, New York.

Spiess, H.W. (1983) *Colloid Polym. Sci. 261*, 193-209.

Spiess, H.W. (1985) in Advances in Polymer Science (H. H. Kausch and H.G. Zachmann, Ed.), Springer-Verlag, Berlin, *66*, 23-58.

Spiess, H.W. & Sillescu, H. (1981) *J. Mag. Res. 42*, 381-389.

Sun, B.Q. & Griffin, R.G. *In preparation*

Suwelack, D., Rothwell, W.P. & Waugh, J.S. (1980) *J. Chem. Phys. 73*, 2559.

Taylor, R.E., Pembleton, R.G., Ryan, L.M. & Gerstein, B.C. (1979) *J. Chem. Phys. 71*, 4541.

Torchia, D.A. & Szabo, A. (1982) *J. Mag. Res. 49*, 107-121.

VanderHart, D.L., Earl, W.L. & Garroway, A.N. (1981) *J. Mag. Res. 44*, 361.

Vega, A.J. & Luz, Z. (1987) *J. Chem. Phys. 86*, 1803-1813.

Vold, R.R. & Vold, R.L. (1991) in *Advances in Magnetic and Optical Resonance* (Warren, W., Ed.) , Academic Press, Inc., San Diego, CA, 85-171.

Wittebort, R.J., Olejniczak, E.T. & Griffin, R.G. (1987) *J. Chem. Phys. 86*, 5411-20.

4. Order and Dynamics in L_α Phase Cerebroside Bilayers

The past few years have seen the increased use of ^2H NMR to study lipid bilayers in the biologically relevant liquid-crystalline (L_α) phase (Bonmatin et al., 1990; Brown et al., 1979; Mayer et al., 1988; Meier et al., 1986; Speyer et al., 1989; Trouard et al., 1992; Weisz et al., 1992; Winsborrow et al., 1991). Through the use of both lineshapes and relaxation measurements a picture of lipid structure and dynamics in the L_α phase has begun to emerge. With the increased speed and capability of computing that has become available, it is now possible to use quite elaborate models of motion to fit experimental results. The problems which can arise at this stage of matching experiment to theory are twofold: first it is all too easy to start fitting data with more parameters than one has variables and second when fitting many parameters to a complex set of data the search for a best fit can become quite time consuming. To date, the studies and simulations performed have given a consistent picture for each individual study, but a systematic study of every segment along the polymethylene chain in a given molecule has not been reported. What follows is a systematic evaluation of motional models to give some insight into how one may go about addressing these issues. The first half of this chapter focuses on the measurement of quadrupole splittings, or order parameters, in lipids; the second half investigates relaxation.

4.1 ^2H NMR Lineshape Spectra of Lipid Bilayers

In discussing lipids and their motions it is helpful to first examine what is universal about the spectroscopic features of lipids as diverse as phosphatidylcholines (PCs) and cerebrosides. Namely, the behavior of the polymethylene chains in lipids just above their melting temperatures is remarkably similar even though the temperatures are not (Seelig & Seelig, 1980). These systems, when specifically deuterated along the polymethylene chain, exhibit axially symmetric powder patterns with residual quadrupole splittings of ~30 kHz for the first 8-10 segments and then following this plateau region the splittings decrease approximately monotonically. This behavior has also been observed in soaps such as K-palmitate when they are incorporated into phospholipid bilayers. It is common to

describe these axially symmetric spectra in terms of order parameters which relate the scaling of the quadrupole coupling to the average orientation of a particular C-D vector with respect to the axis of diffusion in the membrane. This axis is generally coincident with the molecular long axis. Mapping these order parameters (S) as a function of the of the position in the polymethylene chain yields a physically appealing picture of the increase in disorder toward the center of the bilayer. However, they fail to describe the molecular mechanisms which lead to these spectra. For example, if S is approximately zero it could either be a result of isotropic tumbling of the molecule, axial diffusion of the molecule with the C-D vector at the magic angle, or symmetric four-fold hops of the C-D vector on a tetrahedral lattice. This type of reasoning may be extended to spectra observed for lipid chain spectra. The order parameters or quadrupole splittings and spectral lineshapes have been measured for a number of compounds and systems, but only recently has a physical model accounting for the mechanisms which gives rise to these parameters been suggested.

Before describing a motional model which we feel is the most comprehensive to date, we first review some experimental results which suggest constraints any model must satisfy. As mentioned above, ^2H spectra of chain-labelled lipids in their L_α phase are axially symmetric powder patterns. Additionally, a proton decoupled spectrum of a chain containing a -CHD- segment does not differ significantly from a spectrum obtained when the decoupling fields is removed. Thus, the dipolar coupling is less than about 100 Hz. This fact has also been measured directly (Bloom et al., 1978; Seiter & Chan, 1973). In addition, if a methylene segment is labelled with two deuterons instead of one, its spectrum is not altered; the averaged quadrupolar couplings for each deuteron are identical. This is generally true for all sites along the chain except for the 2- and, in some cases, 3-positions (Seelig & Browning, 1978). At this segment, two magnetically inequivalent deuterons have been observed and it has been conclusively shown that this is due to the two deuterons in a single molecule being inequivalent rather than two conformations of the

molecule (Engel & Cowburn, 1981). Therefore, any model for lipid motion must provide for this equivalence at all positions along the chain except for the 2-position.

A second feature of lipid spectra which must be accounted for is the similarity of the splittings in the first 8-10 segments of the chain or plateau region. This feature is illustrated in greater detail in Figure 4-1 where the data for 1,2-dipalmitoyl-*sn*-glycero-3-phosphocholine (DPPC), 1,2-dimyristoyl-*sn*-glycero-3-phosphocholine (DMPC), 1,2-dipalmitoyl-*sn*-glycero-3-phosphoserine (DPPS), and NPGS at roughly their respective melting temperatures are plotted as a function of chain position. It is clear that all these lipids have splittings on the order of 30 kHz in the plateau region and then the order parameters decrease monotonically further down the chain. Also there are local oscillatory variations of the order parameters for the first few positions in the chains. However, the sign of the oscillation is dependent on the lipid being studied.

Thirdly, the chain splittings for pure lipid bilayers show a negative temperature dependence. In PC's and PS this amounts to about -400 Hz/°C, while in glycolipids it is slightly smaller, about -300 Hz/°C. If cholesterol is added to a system, at a given temperature the quadrupolar coupling will increase. For example, pure (7,7-d_2)NPGS exhibits a splitting of 30 kHz just above T_c=82°C; adding 50 mol% CHOL increases the splitting to 50 kHz. However, neither temperature nor CHOL concentration has much effect on the coupling for glycerol backbone labelled lipids or NPGS. Typically the effects are less than 5 % in comparison to a change of 200% for the chains. This difference points to an important constraint. Namely, it suggests that motion perpendicular to the long axis of diffusion is not significantly altered. If it was, the backbone splittings would show the same temperature and cholesterol dependence as the chain splittings. For these reasons we believe that large angular excursions (>30°) perpendicular to this axis may be neglected.

4.1a Motional model

The dynamics of the polymethylene chains in a lipid molecule may be modeled as a combination of gauche-trans isomerizations and overall lipid motions consisting of axial

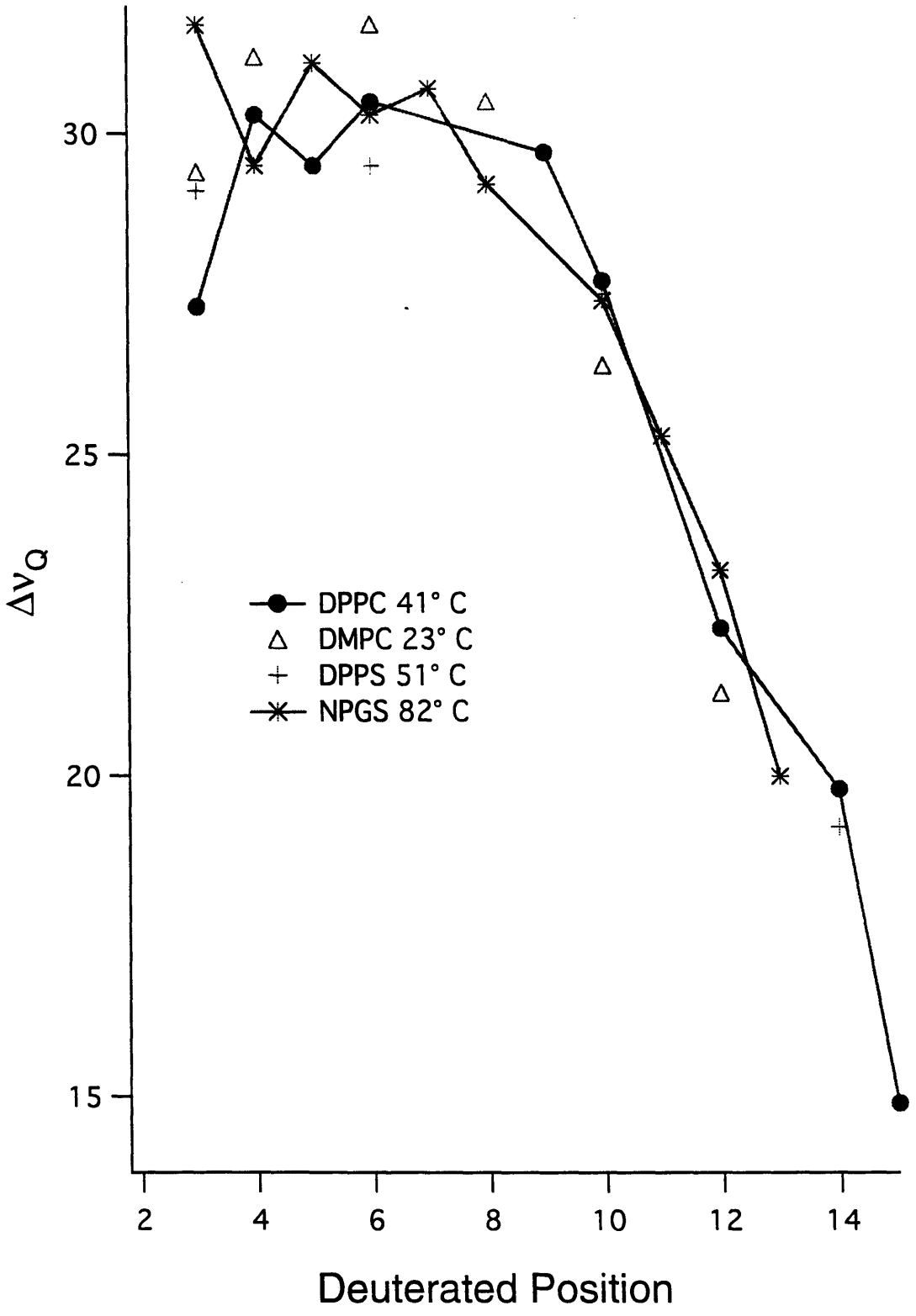

Figure 4-1 Quadrupole splittings as a function of chain position in selectively deuterated lipid bilayers.

diffusion about the long axis and reorientation of the director for a particular molecule with respect to the bilayer normal. The powder pattern for a lipid molecule in the L_α phase is axially symmetric and can be characterized by an order parameter

$$S_{zz} = \frac{1}{2}\left\langle 3\cos^2\theta - 1 \right\rangle \tag{4-1}$$

which describes the splitting as a function of the average angle between the deuteron and long axis of rotation or

$$\Delta\upsilon = \frac{3}{4}\frac{e^2qQ}{h}S_{zz} \tag{4-2}$$

The averaging of this interaction may be separated into two components representing the averaging due to director fluctuations and molecular motions, respectively (Peterson & Chan, 1977).

$$S_{zz} = \frac{1}{2}\left\langle 3\cos^2\beta - 1 \right\rangle \frac{1}{2}\left\langle 3\cos^2\alpha - 1 \right\rangle = S_{D\perp}S_{mol} \tag{4-3}$$

If the reorientation of the director relative to the bilayer normal is under the influence of an orienting potential such that its probability function is described by

$$f(\beta) = N\exp[A(3\cos^2\beta - 1)] \tag{4-4}$$

then the diffusional order parameter may be related to the strength of the orienting potential, A, by

$$S_{D\perp} = N\int_0^\pi (3\cos^2\beta - 1)\exp[A(3\cos^2\beta - 1)]\sin\beta d\beta \tag{4-5}$$

In the limit of a strong potential, $S_{D\perp}$ approaches 1 and director fluctuations do not contribute to the averaging of the quadrupole coupling. In an infinitely weak potential, $S_{D\perp}$ approaches 0 and a singles line characteristic of isotropic tumbling is observed.

Molecular motion can be restricted by the nature of the compound which results in hops between specific sites rather than continuous diffusion. The order parameter for this motion may than be calculated using

$$S_{mol,i} = \frac{1}{2}(3\cos^2 \alpha_i - 1)$$
$$S_{mol} = \sum_i p_i S_{mol,i} \qquad (4\text{-}6)$$

where p_i represents the population of a particular orientation and α_i describes the orientation. For a polymethylene chain, tetrahedral geometry may be assigned to each segment with gauche-trans isomerization resulting in hops between various sites on a diamond-type lattice (Huang et al., 1980). For a particularly labelled segment in the trans conformation, if the plane defined by the CD_2 group (and the C_2 axis) is perpendicular to the director of the molecule, both C-D bonds will lie at an angle of 90° with the axis of diffusion (Figure 4-2a). Two gauche isomerizations are possible as indicated in Figure 4-2a. In either of the gauche conformations, one C-D bond makes an angle of 144.75° with the director and the other C-D bond is at an angle of 90° with the axis of rotation. Thus the angle of the principle values (V_{zz}) of the quadrupole couplings of the deuterons with respect to the director for these two orientations is also 144.75° and 90°, respectively. In one isomer the quadrupole interaction of a specific deuteron is scaled by +1/2 and in the other conformation it is scaled by -1/2. The only difference between the two gauche conformations is the positions of the two deuterons are exchanged. If the two conformations are equally populated their net contribution to the observed quadrupole splitting is zero; this phenomenon is identical for both the deuterons. The trans conformer also scales by +1/2 while the fourth conformation scales by a factor of -1/2. Thus these two conformations may cancel each other as well to the extent that the fourth conformation is populated. This results in the well-known equality (Peterson et al., 1977)

$$S_{mol} = -\frac{1}{2}(p_1 - p_4) \qquad (4\text{-}7)$$

In general there is not significant occupation of the fourth orientation until a large amount of disorder is already present and it may neglected for most positions in the chain.

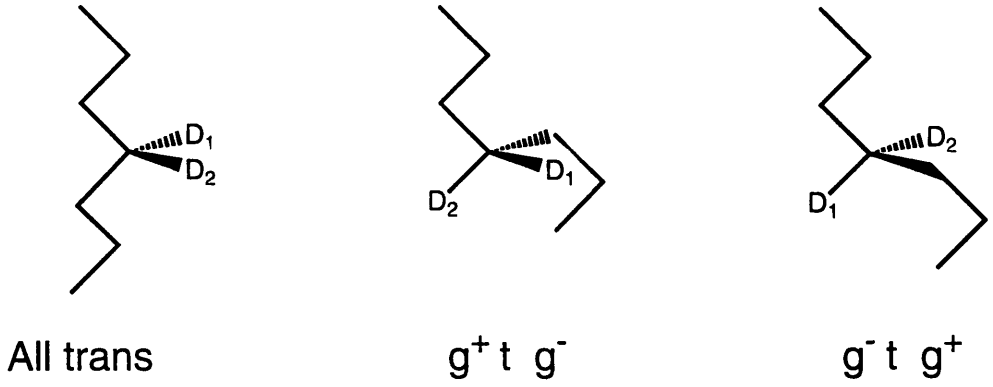

Figure 4-2a Possible orientations in gauche-trans isomerization

Figure 4-2b Effect of tilt angle on relative orientations

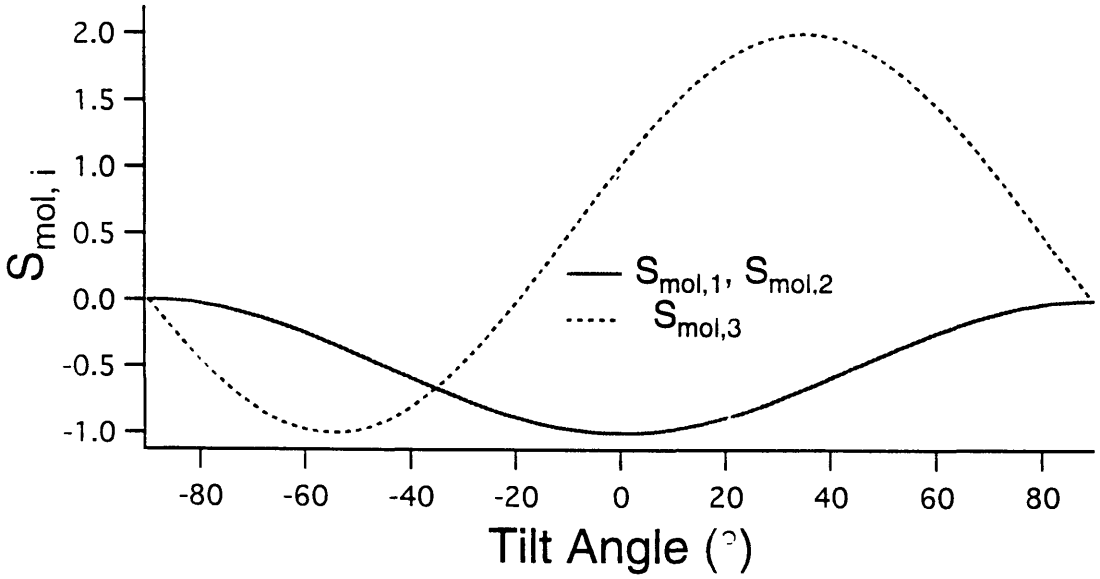

Figure 4-2c Influences of tile on molecular order parameters

Suppose, however, that the headgroup of a lipid molecule distorts the initial methylene segments so the planes of the CD_2 groups are not perpendicular to the director. A tilt of 10° would lead to an angle of 154.75° between the director and one of the gauche conformers and a subsequent scaling factor of 1.45 (Figure 4-2b). However, the other gauche conformer would not of course be shifted to an orientation with a solution to $(3\cos^2\theta-1)$ of -1.45 since its minimum value is -1. Additionally, the trans conformer would give a slightly less negative contribution. The net effect of this "tilt" of the axis is to make the molecular order parameter less negative and thus decrease the observed splitting. If one rotates the axis in the other direction by 10° a slight decrease in the order parameter is effected and the splitting is increased. If the two gauche conformations are equally populated, the two deuterons will still exhibit the same splitting.

If one considers how this tilt perpetuates down the polymethylene chains one can see that if the plane containing the CD_2 group for the 3 position is tilted up by the distortion the plane defined by the CD_2 group at the 4 position will be tilted down since it is rotated 180° around the chain axis with respect to the 3 position. Thus a molecular distortion which decreases the quadrupolar splitting at position 3 would increase the splitting observed at position 4. It is reasonable to assume that distortions of the polymethylene chain from ideal geometry caused by the headgroup will be progressively relaxed by torsional adjustments as one proceeds down the chain. Thus, the effects seen at position 8 would be somewhat damped or nonexistent in comparison to position 3.

At most positions along the polymethylene chain the two deuterons give identical splittings, so one can only estimate the distortions from ideal geometry based on the oscillations of the splittings observed at various positions along the chain. However, for the 2 position it is possible to determine both the degree of tilt and the populations p_2 and p_3 independently if one has already determined $S_{D\perp}$. This is possible since the trans conformation is not significantly populated and the two gauche orientations are unequally populated, giving rise to two splittings whose ratio and magnitude are only dependent on two

variables: the tilt angle and the proportion of p_2 to p_3. The magnitudes of the splittings are determined by $S_{D\perp}$ and

$$S_{mol}^{D1} = \frac{1}{2}[p_2(3\cos^2\alpha_2 - 1) + (1 - p_2)(3\cos^2\alpha_3 - 1)]$$
$$S_{mol}^{D2} = \frac{1}{2}[(1 - p_2)(3\cos^2\alpha_2 - 1) + p_2(3\cos^2\alpha_3 - 1)] \quad (4\text{-}8)$$

where D1 and D2 refer to the two deuterons and α_2 and α_3 refer to the angles between the two possible orientations and the director. The ratio of the splittings is given by the ratio of the order parameters. The two angles are also related since the tetrahedral geometry of the methylene group is maintained.

Unfortunately, it is not possible to determine $S_{D\perp}$ solely via quadrupole echo spectra of unoriented bilayers. Several approaches to determining the degree of wobble have been reported, including the use of proton and deuterium dipolar couplings (Peterson et al., 1977), incorporation of rigid probes (Oldfield et al., 1978), and the measurement of T_1 anisotropy (Meier et al., 1986). The use of T_1 anisotropy is somewhat questionable since relaxation in these systems is highly dependent on many parameters, including the trans populations, degree of director fluctuations, and three to four independent motional rates. Using a rigid probe such as cholesterol to measure orientational order is more straightforward, but the results must be extrapolated to infinite dilution for pure lipid systems. Assumptions about the equilibrium orientation of the cholesterol molecule and its rigidity must also be made, and thus this method can only place a lower limit on $S_{D\perp}$. Measuring dipole couplings takes advantage of the relation between the two order parameters if the director and the axis perpendicular to the CD_2 plane are coincident. In this case,

$$S_{mol}^{CD} = -\frac{1}{2}p_t$$
$$S_{mol}^{DD} = -\frac{3}{8}p_t - \frac{1}{8} \quad (4\text{-}9)$$

Use of these techniques on phospholipids have led to estimates of $S_{D\perp}$ between 0.5 and 0.8 just above the melting temperature.

In this present work, we examine the quadrupolar interactions of a glycolipid, N-palmitoylgalactosylsphingosince (NPGS), specifically labelled at several positions along the polymethylene chain. Our results are considered in light of the model presented and compared to the phenomena previously observed in phospholipids.

4.1b Materials and Methods

Sample preparation: NPGS was synthesized by Sunil DasGupta using palmitic acids specifically labelled at the 2, 3, 4, 5, 6, 7, 8, 10, 11, 12, or 13-position (DasGupta, 1982). All samples consisted of about 50 mg of lipid dispersed in deuterium-depleted water in a 1:2 lipid:water ratio. The mixture was flame-sealed under vacuum in 5-mm glass tubes. Homogenization of the samples was accomplished by heating the lipid to above T_c (82°C) for about 2 hours.

^{2}H NMR spectroscopy: Experiments were performed on a homebuilt spectrometer with a deuterium frequency of 61.0 MHz using a standard quadrupole echo sequence (90_x-τ-90_y-τ–ACQ). The $\pi/2$ pulse length was typically 1.8-2.4 μsec and the pulse spacing for the echo was set at 30 μsec. A recycle delay greater than 8 times the T_1 of the portion of the spectrum with the longest relaxation time was used. The number of acquisitions varied from 1024 to 24,000 depending on the spectral intensity. The temperature was regulated to within 0.5°C by blowing heated air through the insulated chamber containing the rf sample coil.

4.1c Results and Discussion

Typical quadrupole echo spectra of NPGS in the L_α phase are shown in Figure 4-3 for deuterium labels at the 2 and 3 positions. Samples labelled at other sites displayed axially symmetric lineshapes similar to those observed for the 3,3-d_2 sample with only a single splitting. Figure 4-4 summarizes the dependence of the quadrupolar splittings of the various samples on temperature. As expected, the quadrupolar interaction was further motionally averaged as the temperature was increased. The dependence of the splittings on chain position are illustrated in Figure 4-5. As previously seen in phospholipid systems

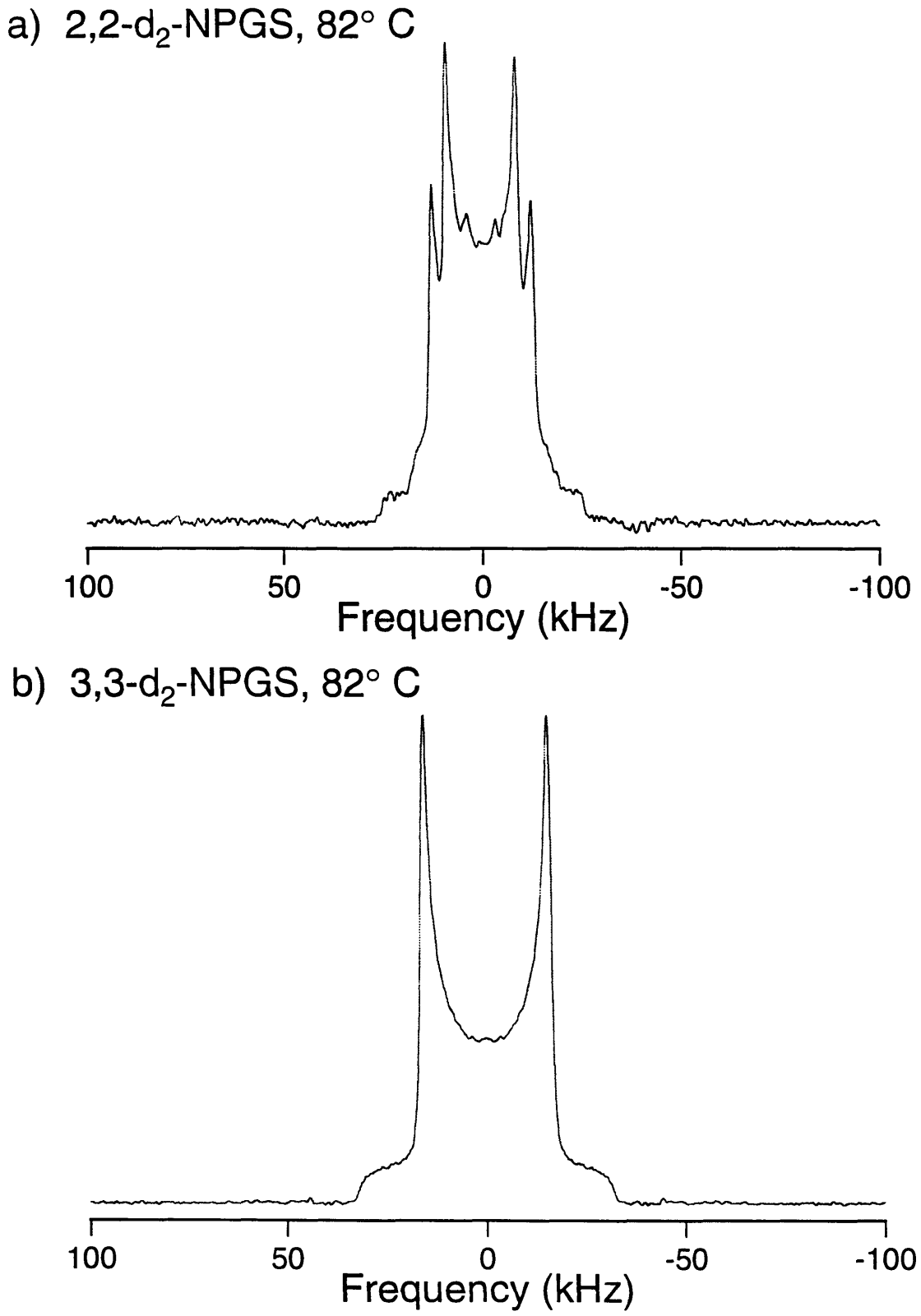

Figure 4-3 Quadrupole echo spectra of NPGS labelled at the 2- and 3-postions.

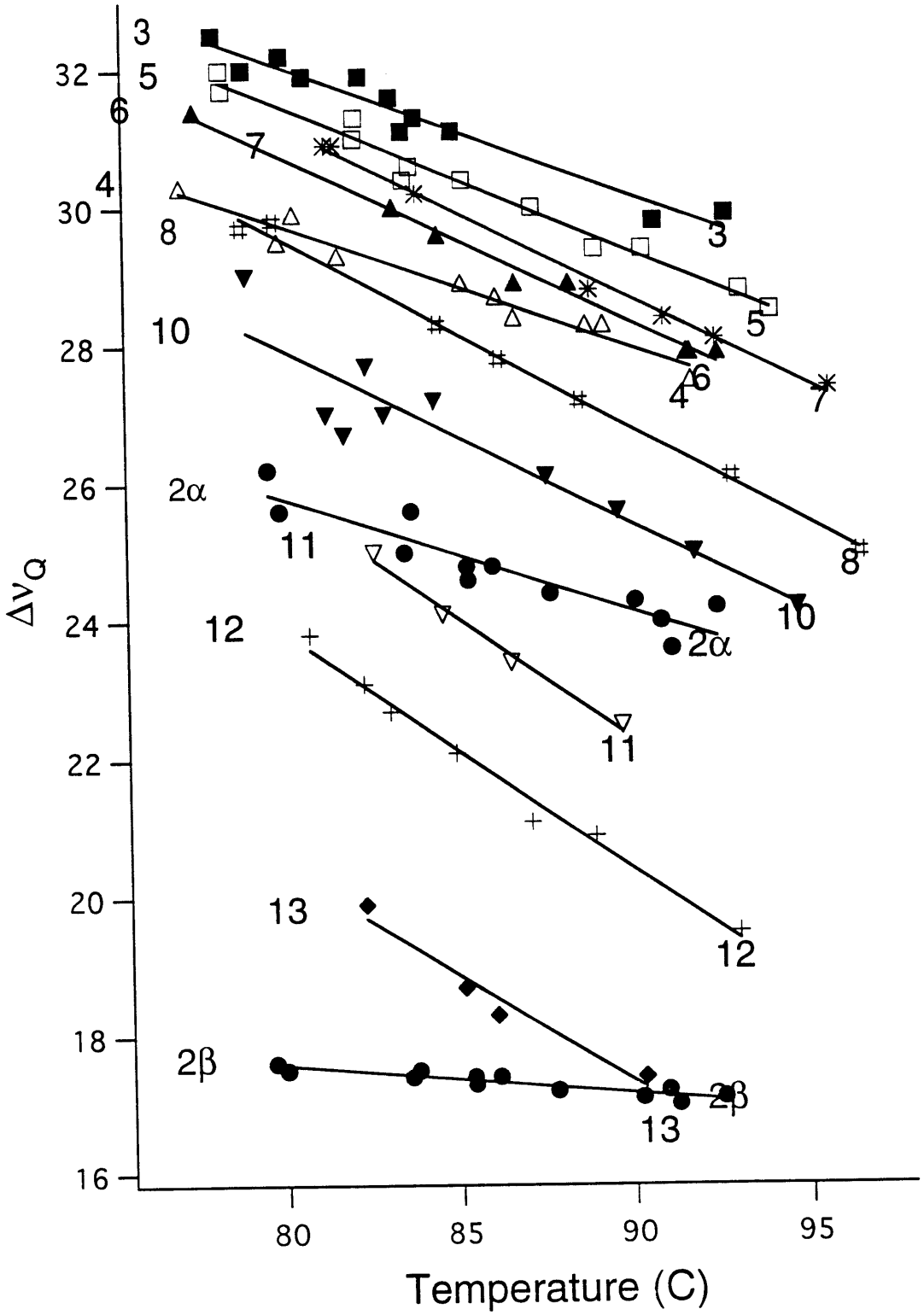

Figure 4-4 Quadrupole splitting as a function of temperature in NPGS

(Seelig et al., 1980), there is a plateau region for the first several segments of the chain, and then the averaging increases rapidly toward the end of the chain. In the plateau region, there are oscillations of the averaged quadrupole couplings. This was also seen in phospholipids and was explained to be a consequence of the headgroup holding one end of the chain in place during gauche-trans isomerization (Meraldi & Schlitter, 1981). However, the oscillation seen in NPGS is opposite to that seen in the phospholipids (i.e. the splitting at the 3 position is greater rather than less than the splitting at the 4 position), and would therefore not conform to this explanation.

A possible explanation for the divergent character of the NPGS order profile emerges if one considers the conformations of the lipids at the bilayer surface, especially the carbonyl carbon adjacent to the 2-position in each of the lipids. It has been appreciated for quite some time that the first part on the *sn*-2 chain in phospholipids adopts a bent conformation even in the L_α phase and is oriented parallel to the bilayer surface (i.e. the plane of the methylene group at the 2 position is at an angle of less than 90° with the molecular director) (Fuson & Prestegard, 1983; Seelig & Seelig, 1975; Zaccai et al., 1979). It has been assumed that by the 3 position the chain is oriented perpendicular to the bilayer surface, and the plane of this methylene group is perpendicular to the molecular director. This is plausible given that labels on the *sn*-1 chain and *sn*-2 chain have nearly identical splittings by the 3 position. However, if the distortion were to still be affecting the orientation of the chain even at the third methylene, this would result in the plane of the methylene inclining slightly downward with respect to the director and would lead to a net increase in the molecular order parameter. This would explain the slight divergence in splittings at the 3 position of the two chains observed at some temperatures (Seelig & Seelig, 1974).

Recent investigations of NPGS carbon labelled at the carbonyl position have indicated that the plane described by the amide bond is inclined at an angle of 35-52° with respect to the bilayer surface (Ruocco et al., 1996). The effect of this orientation on the 2 position of the polymethylene chain would be to decrease the angle between the plane of the

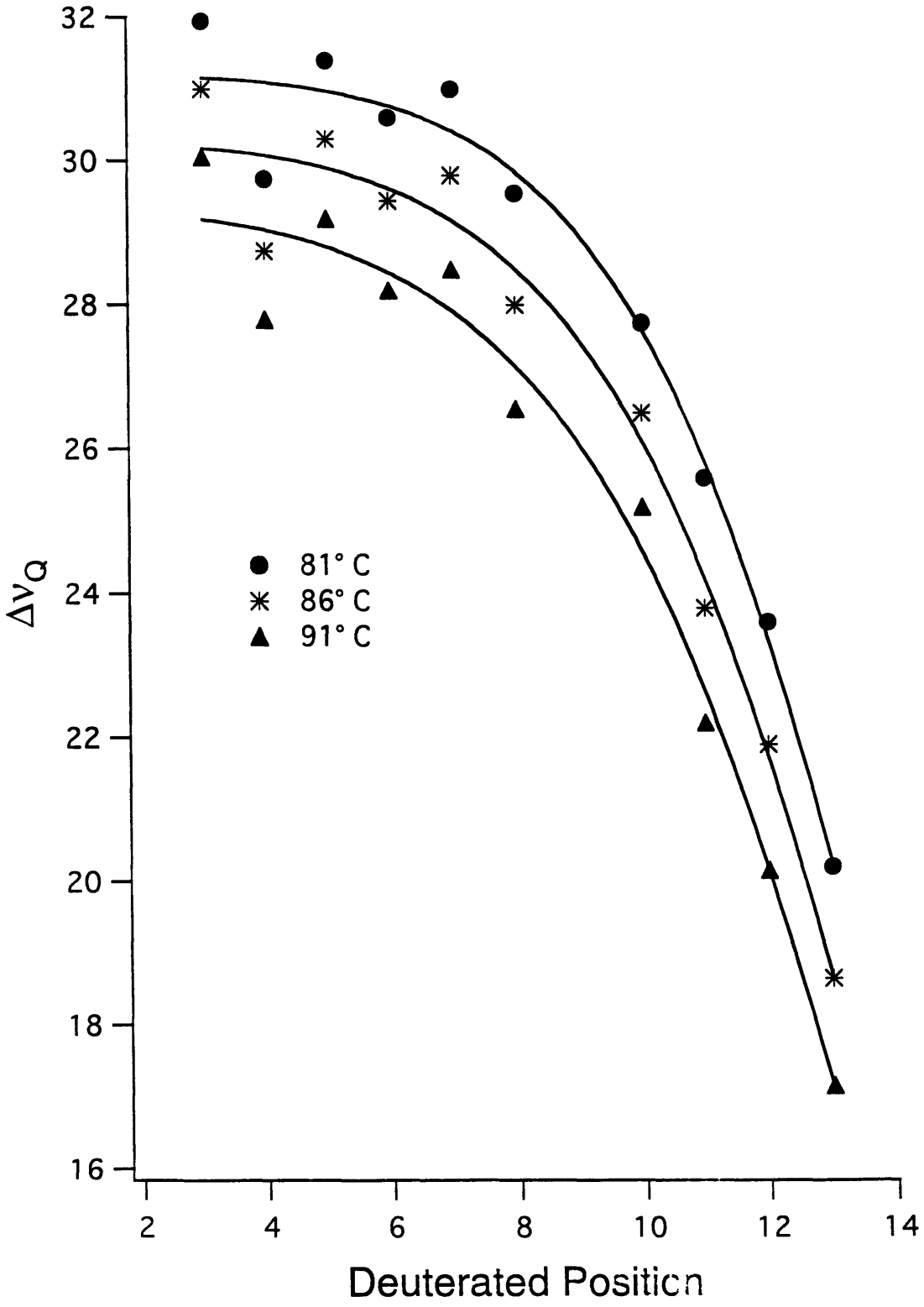

Figure 4-5 Quadrupole splitting as a function of chain position in NPGS.

CH_2 group and the molecular director. If the distortion continues down the chain, the plane of the methylene at the 3 position would incline slightly downward and lead to a net increase in the splitting measured at this position. Further propagation would decrease the splitting at the 4 position and increase the splitting at the 5 position. The distortions introduced by the orientation of the amide plane might be further exacerbated by the double bond between carbons 4 and 5 in the sphingosine base on adjacent molecules.

In light of the above discussion of motional averaging, the splittings observed in NPGS may result from several combinations of the available parameters. Table 4-1 gives the site populations, tilt angle, and degree of director fluctuations for three different models. The first assumes no director fluctuations or tilt; only gauche-trans isomerization determines the observed splittings. The second derivation assumes director fluctuations and isomerization. The third approach includes all three parameters, using three different values of $S_{D\perp}$ given the wide range of values reported in the literature. In light of the wide range of possible fits, more experiments should be performed to independently measure these parameters. Namely, the deuterium dipolar couplings could be measured in specifically labeled NPGS to determine the degree of director fluctuation. A position near the middle or end of the chain, combined with the deuterium data, would directly yield this value, and then values obtained further up the chain could be compared and used to determine tilt angles.

A: No tilt of polymethylene chain

Position	Splitting (82° C)	$S_{D\perp}=1$ p_{trans}	$S_{D\perp}=0.75$ p_{trans}	$S_{D\perp}=0.55$ p_{trans}
2_α	17.3	0.06	0.08	0.11
2_β	24.7	0.64[a]	0.68[a]	0.75[a]
3	31.0	0.49	0.65	0.88
4	28.8	0.45	0.60	0.82
5	30.3	0.48	0.63	0.86
6	29.4	0.46	0.61	0.84
7	29.8	0.47	0.62	0.85
8	28.0	0.44	0.59	0.80
10	26.5	0.42	0.55	0.76
11	23.8	0.37	0.50	0.68
12	21.9	0.34	0.46	0.62
13	18.6	0.29	0.39	0.53

B: Chain tilted[b] to obtain smooth splitting profile

Position	Smoothed Splitting	$S_{D\perp}=1$ tilt, p_{trans}	$S_{D\perp}=0.75$ tilt, p_{trans}	$S_{D\perp}=0.55$ tilt, p_{trans}
2_α	17.3	0	0	0
2_β	24.7	+2.4, 0.66[a]	+3.1, 0.70[a]	+4.3, 0.77[a]
3	30.2	- 0.5, 0.47	- 1.0, 0.63	- 3.8, 0.86
4	30.0	+0.8, 0.47	+1.4, 0.63	+4.5, 0.86
5	29.9	- 0.2, 0.47	- 0.4, 0.63	- 1.7, 0.85
6	29.6	+0.1, 0.46	+0.2, 0.62	+0.7, 0.84
7	29.2	- 0.4, 0.46	- 0.6, 0.61	- 2.2, 0.83
8	28.5	+0.3, 0.45	+0.6, 0.60	+1.5, 0.81

C: Chain tilted[b] to obtain splittings observed in DPPC at T_m (41° C)

Position	DPPC Splitting	$S_{D\perp}=1$ tilt, p_{trans}	$S_{D\perp}=0.75$ tilt, p_{trans}	$S_{D\perp}=0.55$ tilt, p_{trans}
3	26.7	- 2.4, 0.42	- 4.3, 0.56	-16.6, 0.76
4	29.5	+0.4, 0.46	+0.8, 0.62	+2.5, 0.84
5	28.7	- 1.0, 0.45	- 1.8, 0.60	- 6.2, 0.82
6	29.6	+0.1, 0.46	+0.2, 0.62	+0.5, 0.84

[a] p_{g+}
[b] tilt in degrees as indicated in figure 4-2

Table 4-1 Trans Population Dependence on Position in NPGS

4.2 ^{2}H NMR Relaxation in NPGS Lipid Bilayers

Deuterium relaxation experiments provide an ideal method of measuring molecular dynamics in lipids. Through the use of both inversion recovery and broadbanded Jeener-Broekaert sequences on unoriented samples, one can measure several variables. Proposed models may then be tested in light of these results and allow estimates of various kinetic rates and their temperature dependence.

Models of lipid motion generally incorporate two or more modes of motion. The most basic model employs 3-site gauche-trans isomerization with 3-site hops around the long axis of diffusion. This is the simplest model which can take into account the gauche-trans isomerization known to exist from lineshape experiments in the gel phase (Huang et al., 1980) and produce an axially symmetric lineshape (Speyer et al., 1989). The combination of these two types of motion leads to nine distinct sites and a 9 x 9 rate matrix. If one assumes continuous diffusion instead of three-site hops around the director, more sites must be incorporated; generally around 20 sites are chosen to approximate continuous diffusion (Meier et al., 1986). This leads to 60 sites and a 60 x 60 rate matrix. More complicated models also add director fluctuations perpendicular to the axis of diffusion (usually modeled by 10 sites) and lateral translation due to the gauche-gauche isomerizations at the two position (Mayer et al., 1988). Thus, one can easily have a 1200 site problem! In addition to being computationally difficult, such an approach does not lend itself to analytic solutions and gaining insight into which parameters most affect T_{1Z} and T_{1Q} at a particular orientation is difficult.

4.2a Development of Correlation Functions

Fortunately, if the motions in lipids are uncorrelated, the calculation of the correlation functions may be significantly simplified. Such an assumption allows time-averaging of the tensor components to be done successively (Hoatson et al., 1994). Recall that the correlation function is given by

$$J_M(M\omega_0) = \sum_{LL'} D^{(2)*}_{ML}(\Omega) D^{(2)}_{ML'}(\Omega) \tilde{C}_{L.L'}(M\omega_0)$$
$$\tilde{C}_{LL'}(M\omega_0) = \int_0^\infty d\tau \exp\{im\omega_0\tau\} C_{LL'}(t) \tag{4-10}$$

where $C_{LL'}$ is the correlation function for reorientation in the crystal fixed-axis system and is given by

$$C_{LL'}(t) = \sum_{KK'} \frac{T_K^{(2),pas} T_K^{(2),pas*}}{(T_0^{(2),pas})^2} \times \sum_{j=1}^{N}\sum_{i=1}^{N}\sum_{n=2}^{N} (p_i^{eq} p_j^{eq})^{1/2} U_{jn} U_{in} e^{\lambda_n t} D^{(2)*}_{LK}(\Omega_i) D^{(2)}_{L'K'}(\Omega_j) \tag{4-11}$$

For two uncorrelated motions this calculation may me broken up into two parts using

$$C_{LL'}(t) = \sum_{KK'} C_{LKL'K'}(t, A) \sum_{NN'} C_{KNK'N'}(t, B) \tag{4-12}$$

where

$$C_{KNK'N'}(t, A) = \sum_{NN'} \frac{T_K^{(2),pas} T_K^{(2),pas*}}{(T_0^{(2),pas})^2} \times \sum_{j=1}^{N}\sum_{i=1}^{N}\sum_{n=2}^{N} (p_i^{eq} p_j^{eq})^{1/2} U_{jn} U_{in} e^{\lambda_n t} D^{(2)*}_{KN}(\Omega_i) D^{(2)}_{K'N'}(\Omega_j) \tag{4-13}$$

and A and B refer to the two kinds of motion. If there are three or four uncorrelated motions, this may be expanded further. Thus, the problem of calculating spectral densities for lipids may be solved by solving the correlation functions for the individual motions, namely gauche-trans isomerization, 3-site hops, continuous diffusion, and diffusion in an orienting potential. This is further simplified since the latter three problems have already been solved (Torchia & Szabo, 1982; Vold & Vold, 1988).

Gauche-trans isomerization. For gauche-trans isomerization with the two gauche conformations equally probable, the sites are described by

$$p_t^{eq} + p_{g^+}^{eq} + p_{g^+}^{eq} = 1$$

$$p_{g^+}^{eq} = p_{g^+}^{eq} = \frac{1 - p_t^{eq}}{2}$$

$$\alpha_t = 0 \qquad \alpha_{g^+} = 120 \qquad \alpha_{g^-} = 240$$

$$\beta_t = \beta_{g^+} = \beta_{g^-} = 109.5$$

$$\gamma_t = \gamma_{g^+} = \gamma_{g^-} = 0 \tag{4-14}$$

Assuming isomerization only occurs between the trans conformer and each gauche conformer, the rate matrix is

$$\mathbf{k} = \begin{bmatrix} -2k & k & k \\ \frac{1-p_t}{2p_t}k & -\frac{1-p_t}{2p_t}k & 0 \\ \frac{1-p_t}{2p_t}k & 0 & -\frac{1-p_t}{2p_t}k \end{bmatrix} \tag{4-15}$$

Solving this problem yields

$$C_{K0K'0}(t) = \begin{bmatrix} \frac{8}{27}z & -\frac{4\sqrt{2}}{27}y & -\frac{2\sqrt{2}}{9\sqrt{3}}x & \frac{4\sqrt{2}}{27}z & \frac{8}{27}y \\ -\frac{4\sqrt{2}}{27}y & \frac{4}{27}z & \frac{2}{9\sqrt{3}}x & -\frac{4}{27}y & -\frac{4\sqrt{2}}{27}z \\ -\frac{2\sqrt{2}}{9\sqrt{3}}x & \frac{2}{9\sqrt{3}}x & \frac{1}{9}w & -\frac{2}{9\sqrt{3}}x & -\frac{2\sqrt{2}}{9\sqrt{3}}x \\ \frac{4\sqrt{2}}{27}z & -\frac{4}{27}y & -\frac{2}{9\sqrt{3}}x & \frac{4}{27}z & \frac{4\sqrt{2}}{27}y \\ \frac{8}{27}y & -\frac{4\sqrt{2}}{27}z & -\frac{2\sqrt{2}}{9\sqrt{3}}x & \frac{4\sqrt{2}}{27}y & \frac{8}{27}z \end{bmatrix} \tag{4-16}$$

where

$$w = 1 + \frac{(3p_t - 1)^2}{3p_t + 1} \exp\left[-\left(\frac{3p_t + 1}{2p_t} \right) k_{gt} t \right]$$

$$x = \frac{(3p_t - 1)}{2} + \frac{(3p_t - 1)}{2} \exp\left[-\left(\frac{3p_t + 1}{2p_t} \right) k_{gt} t \right]$$

$$y = \frac{(3p_t - 1)^2}{4} - \frac{3(1-p_t)}{4} \exp\left[-\left(\frac{1-p_t}{2p_t} \right) k_{gt} t \right] + \frac{(3p_t + 1)}{4} \exp\left[-\left(\frac{3p_t + 1}{2p_t} \right) k_{gt} t \right]$$

$$z = \frac{(3p_t - 1)^2}{4} + \frac{3(1-p_t)}{4} \exp\left[-\left(\frac{1-p_t}{2p_t} \right) k_{gt} t \right] + \frac{(3p_t + 1)}{4} \exp\left[-\left(\frac{3p_t + 1}{2p_t} \right) k_{gt} t \right]$$

(4-17)

(Since one can choose the crystal z-axis to be coincident with the axis of motion, it is only necessary to solve the correlation function for N, N' = 0.)

Gauche-trans isomerization with continuous diffusion. To approximate lipid motion as a combination of gauche-trans isomerization and continuous diffusion about the molecular director, the correlation function for continuous diffusion,

$$C_{LKL'K'}(t) = \delta_{LL'} d_{LK}(\beta) d_{L'K'}(\beta) \exp\left[-\frac{4k_{ax} L^2 \pi^2 t}{N^2} \right] \qquad (4\text{-}18)$$

may be combined with the result for gauche-trans isomerization. β is the <u>average</u> angle between the C-D vector and the diffusion axis, so it is dependent on the site populations and tilt angle. However, it may be directly determined from the observed splitting and $S_{D\perp}$. Given the high degree of symmetry in the solution for gauche-trans isomerization and the number of zero terms in the diffusion result one expects the final solution to be some-what simple as well. Using equation (4-12) yields

$$C_{00}(t) = \frac{1}{36}(3\cos^2\beta - 1)^2 w -$$

$$\frac{2}{9}(3\cos^2\beta - 1)(\sin^2\beta + \sqrt{2}\cos\beta\sin\beta)x +$$

$$\frac{2}{9}(1 + \cos^2\beta + 2\sqrt{2}\cos\beta\sin\beta)\sin^2\beta(y + z)$$

$$C_{11}(t) = C_{-1-1}(t) = \exp\left(\frac{-4k_{ax}\pi^2 t}{N^2}\right)\times\left[\frac{w}{6}\cos^2\beta\sin^2\beta + \right.$$
$$\frac{2x}{9}\left[2\cos^2\beta\sin^2\beta - \sqrt{2}\cos\beta\sin\beta(1-2\cos^2\beta)\right] +$$
$$\frac{2y}{27}\left[-\sin^2\beta(1+2\cos^2\beta) + 4\sqrt{2}\cos^3\beta\sin\beta\right] +$$
$$\left.\frac{2z}{27}\left[3\sin^2\beta + 2\cos^4\beta - 4\sqrt{2}\cos\beta\sin\beta\right]\right]$$
$$C_{22}(t) = C_{-2-2}(t) = \exp\left(\frac{-16k_{ax}\pi^2 t}{N^2}\right)\times\left[\frac{w}{24}\sin^4\beta + \right.$$
$$\frac{x}{9}\left[\sqrt{2}\sin^3\beta\cos\beta - \sin^2\beta(1+\cos^2\beta)\right] -$$
$$\frac{y}{27}\left[\sin^4\beta + 2\sqrt{2}\sin\beta\cos\beta(3+\cos^2\beta)\right] + \qquad (4\text{-}19)$$
$$\left.\frac{z}{27}\left[3 + 5\cos^2\beta + \cos^2\beta\sin^2\beta + 2\sqrt{2}\sin^3\beta\cos\beta\right]\right]$$

Of particular interest is the fact that C_{00} depends only on the rate of gauche-trans isomerization, β, and the trans population. Only these three correlation functions are nonzero, so the spectral densities in the laboratory frame are simply

$$J_0(0) = \frac{1}{4}\left(9\cos^4\beta_x - 6\cos^2\beta_x + 1\right)\tilde{C}_{00}(0)$$
$$+3\cos^2\beta_x\sin^2\beta_x\tilde{C}_{11}(0) + \frac{3}{4}\sin^4\beta_x\tilde{C}_{22}(0)$$
$$J_1(\omega_0) = \frac{3}{2}\cos^2\beta_x\sin^2\beta_x\tilde{C}_{00}(\omega_0)$$
$$+\frac{1}{2}\left(4\cos^4\beta_x - 3\cos^2\beta_x + 1\right)\tilde{C}_{11}(\omega_0) + \frac{1}{2}\left(1-\cos^4\beta_x\right)\tilde{C}_{22}(\omega_0)$$
$$J_2(2\omega_0) = \frac{3}{8}\sin^4\beta_x\tilde{C}_{00}(2\omega_0) + \frac{1}{2}\left(1-\cos^4\beta_x\right)\tilde{C}_{11}(2\omega_0)$$
$$+\frac{1}{8}\left(\cos^4\beta_x + 6\cos^2\beta_x + 1\right)\tilde{C}_{22}(2\omega_0)$$

(4-20)

where β_x refers to the angle between the magnetic field and the averaged V_{zz}. T_{1Z} and T_{1Q} at the parallel and perpendicular edges as well as the magic angle, assuming $k_{gt}>>\omega_0$, are

$$\begin{aligned}
\frac{1}{T_{1Z}}(0°) &= \tilde{C}_{11} + 4\tilde{C}_{22} \\
\frac{1}{T_{1Z}}(90°) &= \frac{3}{2}\tilde{C}_{00} + \frac{5}{2}\tilde{C}_{11} + \tilde{C}_{22} \\
\frac{1}{T_{1Z}}(MA) &= \tilde{C}_{00} + 2\tilde{C}_{11} + 2\tilde{C}_{22} \\
\frac{1}{T_{1Q}}(0°) &= 3\tilde{C}_{11} \\
\frac{1}{T_{1Q}}(90°) &= \frac{3}{2}\left(\tilde{C}_{11} + \tilde{C}_{22}\right) \\
\frac{1}{T_{1Q}}(MA) &= \tilde{C}_{00} + \frac{2}{3}\tilde{C}_{11} + \frac{4}{3}\tilde{C}_{22}
\end{aligned} \qquad (4\text{-}21)$$

If one measures T_{1Z} and T_{1Q} at the magic angle and 90°, respectively, it is possible to determine C_{00} and thus the rate of gauche-trans isomerization if the splitting and tilt angle are known. Subsequently, C_{11} and C_{22} may also be calculated and the rate of diffusion extracted.

Gauche-trans isomerization with 3-site hopping about the director. Crystallized cerebroside hydrocarbon chains pack in a hexagonal lattice with the fatty acid and sphingosine chains forming alternating pleated sheets (Pascher & Sundell, 1977), so the possibility that axial diffusion is not continuous but is instead characterized by three-fold hopping arises. Three-site hopping has also been found to fit relaxation data more closely than continuous diffusion in deuterated cholesterol incorporated into PC bilayers (Bonmatin et al., 1990). The correlation function for three-site hopping is

$$C_{LKL'K'}(t) = d_{LK}(\beta)d_{L'K'}(\beta)\exp\left[-3k_{hop}t\right] \qquad K = K' \bmod 3 \qquad (4\text{-}22)$$

There are two important differences between this mode of motion and continuous diffusion: the diagonal elements decay at the same rate, and there are nonzero off-diagonal elements (Torchia et al., 1982). The overall correlation functions are:

$$C_{00}(t) = \frac{1}{36}(3\cos^2\beta - 1)^2 w -$$
$$\frac{2}{9}(3\cos^2\beta - 1)(\sin^2\beta + \sqrt{2}\cos\beta\sin\beta)x +$$
$$\frac{2}{9}(1 + \cos^2\beta + 2\sqrt{2}\cos\beta\sin\beta)\sin^2\beta(y + z)$$

$$C_{11}(t) = C_{-1-1}(t) = \exp(-3k_{hop}t) \times \left[\frac{w}{6}\cos^2\beta\sin^2\beta + \right.$$
$$\frac{2x}{9}\left[2\cos^2\beta\sin^2\beta - \sqrt{2}\cos\beta\sin\beta(1 - 2\cos^2\beta)\right] +$$
$$\frac{2y}{27}\left[-\sin^2\beta(1 + 2\cos^2\beta) + 4\sqrt{2}\cos^3\beta\sin\beta\right] +$$
$$\left.\frac{2z}{27}\left[3\sin^2\beta + 2\cos^4\beta - 4\sqrt{2}\cos\beta\sin\beta\right]\right]$$

$$C_{22}(t) = C_{-2-2}(t) = \exp(-3k_{hop}t) \times \left[\frac{w}{24}\sin^4\beta + \right.$$
$$\frac{x}{9}\left[\sqrt{2}\sin^3\beta\cos\beta - \sin^2\beta(1 + \cos^2\beta)\right] -$$
$$\frac{y}{27}\left[\sin^4\beta + 2\sqrt{2}\sin\beta\cos\beta(3 + \cos^2\beta)\right] +$$
$$\left.\frac{z}{27}\left[3 + 5\cos^2\beta + \cos^2\beta\sin^2\beta + 2\sqrt{2}\sin^3\beta\cos\beta\right]\right]$$

$$C_{-21}(t) = C_{1-2}(t) = -C_{2-1}(t) = -C_{-12}(t) = \exp(-3k_{hop}t) \times$$
$$\left[-\frac{w}{12}\cos\beta\sin^3\beta + \frac{x}{18}\left[4\cos^3\beta\sin\beta - \sqrt{2}\sin^2\beta(4\cos^2\beta - 1)\right] +\right.$$
$$\frac{y}{27}\left[2\cos\beta\sin\beta(3 - \cos^2\beta) - \sqrt{2}\sin^2\beta(4\cos^2\beta - 1))\right] +$$
$$\left.\frac{z}{27}\left[2\cos\beta\sin^3\beta + \sqrt{2}(4\cos^4\beta - 3\sin^2\beta)\right]\right]$$

(4-23)

Again, C_{00} depends only on the rate of gauche-trans isomerization, β, and the trans population. However the relaxation behavior is complicated by the fact that the off-diagonal cor-

relation functions contribute to the spectral densities and are dependent on both the angles theta and phi relating the crystallite orientation to the laboratory frame.

Gauche-trans isomerization with axial diffusion and reorientation of the director in a Maier-Saupe potential. The frames of reference for axial diffusion and reorientation of the director are coincident, so the composite correlation functions may be found by simple multiplication of the correlation functions calculated above with the correlation functions for restricted diffusion, $G_{LL'}$, developed by Vold & Vold (Vold et al., 1988), or

$$C_{LL'}(t) = G_{LL'}(t) \sum_{KK'} C_{LKL'K'}(t, A) \sum_{NN'} C_{KNK'N'}(t, B) \qquad (4\text{-}24)$$

This is of course true for both the continuous diffusion and axial hopping models. There is not an analytic solution for diffusion in a cone, but numerical values consisting of polynomials of the order parameter $S_{D\perp}$ have been tabulated (Vold et al., 1988). Typically, these correlation functions are dominated by a single exponential.

4.2b Materials and Methods

Sample preparation: NPGS was synthesized by Sunil DasGupta using palmitic acids specifically labelled at the 2, 3, 4, 5, 6, 7, 8, 10, 11, 12, or 13-position (DasGupta, 1982). All samples consisted of about 50 mg of lipid dispersed in deuterium-depleted water in a 1:2 lipid:water ratio. The mixture was flame-sealed under vacuum in 5-mm glass tubes. Homogenization of the samples was accomplished by heating the lipid to above T_c (82°C) for about 2 hours.

^{2}H NMR spectroscopy: Experiments were performed on a homebuilt spectrometer with a deuterium frequency of 61.0 MHz using either a standard inversion recovery sequence (180_x-t_1-90_x-τ-90_y-τ–ACQ) or broad-banded Jeener-Broekaert sequence (Hoatson, 1991). The $\pi/2$ pulse length was 1.8-2.4 μsec and the pulse spacing for the echo was set at 30 μsec. For the Jeener-Broekaert sequence a window delay of 2 μsec was used to achieve a bandwidth of ±250 kHz. The recycle delay was typically 8 times the T_1 of the portion of the spectrum with the longest relaxation time. The number of acquisi-

tions varied from 1024 to 24,000 depending on the spectral intensity. The temperature was regulated to within 0.5°C by blowing heated air through an insulated chamber containing the rf sample coil.

4.2b Results and Discussion

Figures 4-6-4-18 summarize the temperature and frequency dependence of T_{1Z} and T_{1Q} for the various labelled methylene segments. T_{1Z} is plotted for the entire width of the powder pattern. However, due to poor signal-to-noise and the frequency dependence of the experiment, T_{1Q} may not be measured as accurately. Consequently values are only plotted near the perpendicular edges. The relaxation times increase with temperature at all positions along the polymethylene chain implying motion is considerably faster than ω_0. Examination of these plots yield several insights:

1) As seen previously in DPPC (Brown et al., 1979) T_1 values increase progressively down the chain including in the plateau region. This is strong evidence that gauche-trans isomerization at all positions is greater than the Larmor frequency and increases significantly toward the center of the bilayer.

2) The anisotropy of T_{1Z} changes sign near the 4 position while T_{1Q} shows little variation with frequency at the 3- and 4- positions, but shows increasing anisotropy down the chain. This occurs even in the plateau region where the splittings, and consequently the trans populations, are essentially constant. The dependence of T_{1Q} at the parallel and perpendicular edges is due entirely to the correlation functions $\tilde{C}_{11}(\omega_0)$ and $\tilde{C}_{22}(\omega_0)$. At the 3 position $\tilde{C}_{11}(\omega_0)$ and $\tilde{C}_{22}(\omega_0)$ are approximately equal, but as gauche-trans isomerization increases $\tilde{C}_{11}(\omega_0)$ becomes significantly larger than $\tilde{C}_{22}(\omega_0)$. Simulations of $\tilde{C}_{11}(\omega_0)$ - $\tilde{C}_{22}(\omega_0)$ for increasing gauche-trans isomerization, while holding all other variables constant, are shown in Figure 4-19 for both the models containing only isomerization and axial diffusion. As is evident in the figure, neither of these models properly predicts this trend, regardless of the diffusion rate. Clearly some other motion must be contributing to the relaxation.

3) At the perpendicular edges, T_{1Q} is only slightly greater than T_{1Z} for all positions. At the parallel edges, T_{1Q} is slightly greater than T_{1Z} at the 3 position and then becomes significantly smaller than T_{1Z} further down the chain. Thus, $\tilde{C}_{11}(\omega_0) > 2\tilde{C}_{22}(2\omega_0)$ at the 3 position. However, at this position, $\tilde{C}_{11}(\omega_0)$ and $\tilde{C}_{22}(\omega_0)$ are approximately equal. This implies a strong dependence of $\tilde{C}_{22}$ on the frequency and thus there must be some motion occurring at rates on the order of the Larmor frequency.

Given that models containing only gauche-trans isomerization and axial diffusion are unable to fit all of the data, other models must be considered. The most likely approach is to add some type of motion to account for reorientation of the director in a restoring potential. As stated previously, solutions for such motion have been calculated (Vold & Vold, 1988). Interestingly, the $\tilde{C}_{11}$ and $\tilde{C}_{22}$ correlation functions are somewhat independent of the choice of potential and simulations are currently being done to add this type of motion to the model for lipid dynamics.

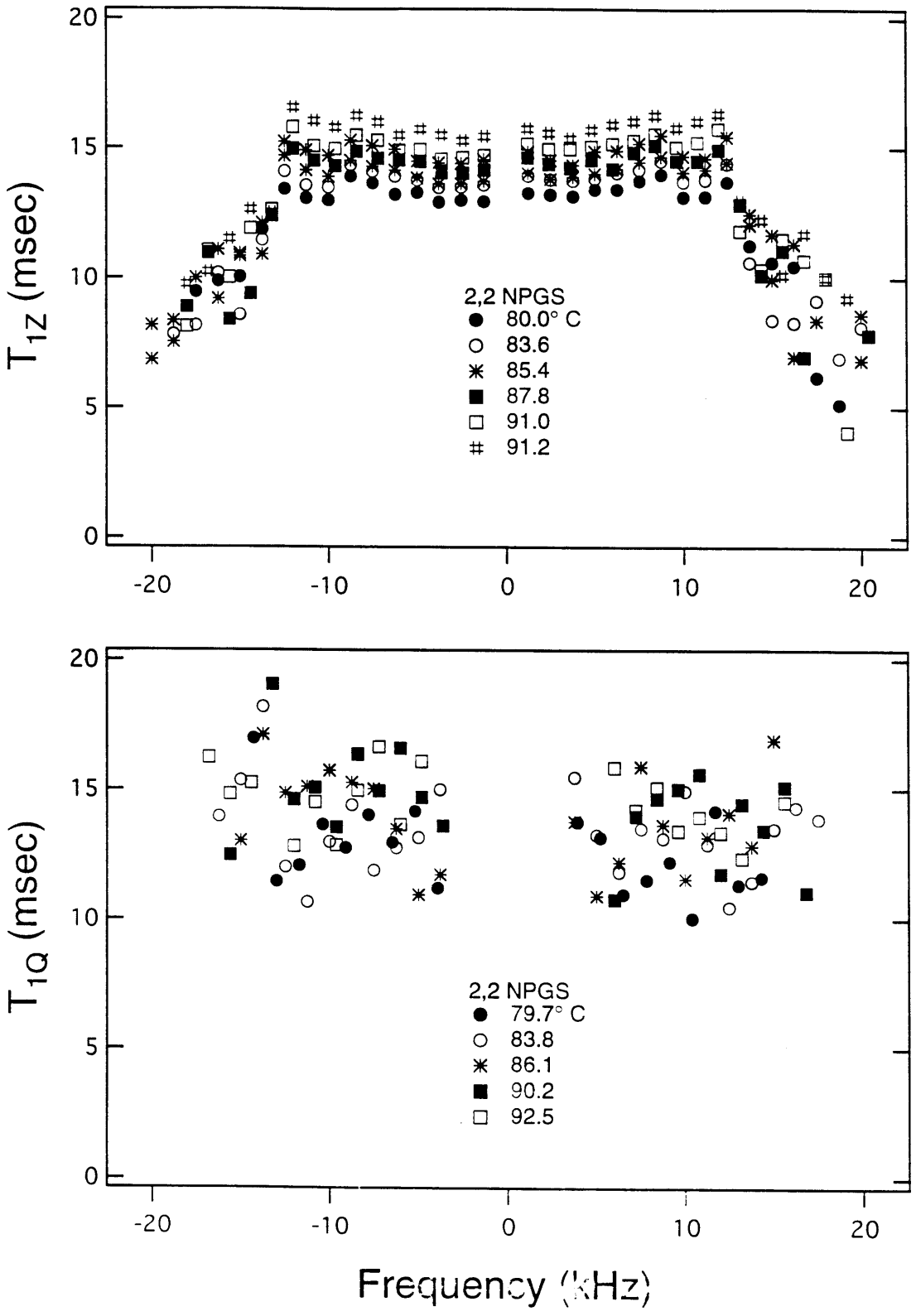

Figure 4-6. Temperature dependence of T_{1Z} and T_{1Q} in L_α phase 2,2-d_2-NPGS

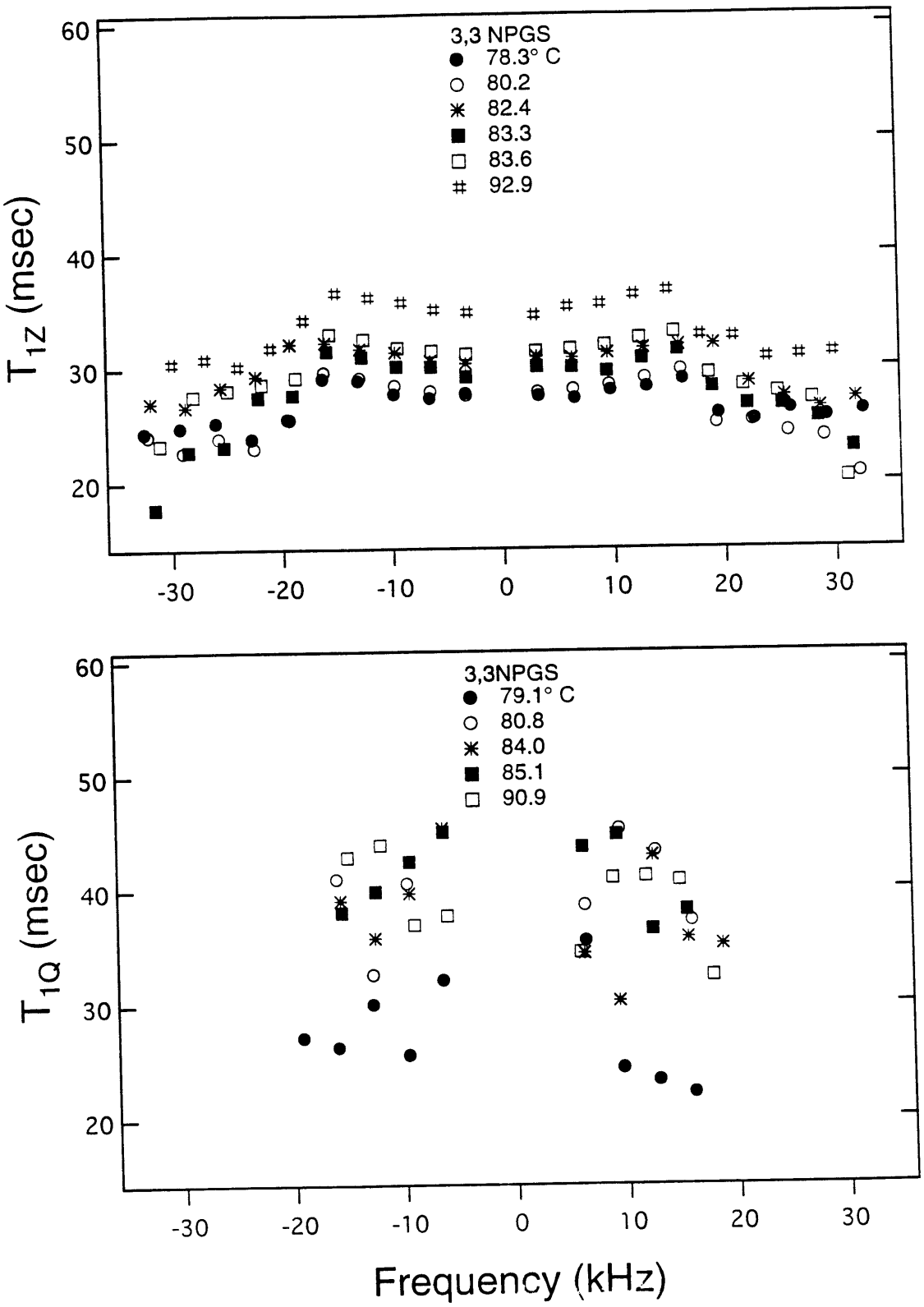

Figure 4-7. Temperature dependence of T_{1Z} and T_{1Q} in L_α phase 3,3-d_2-NPGS

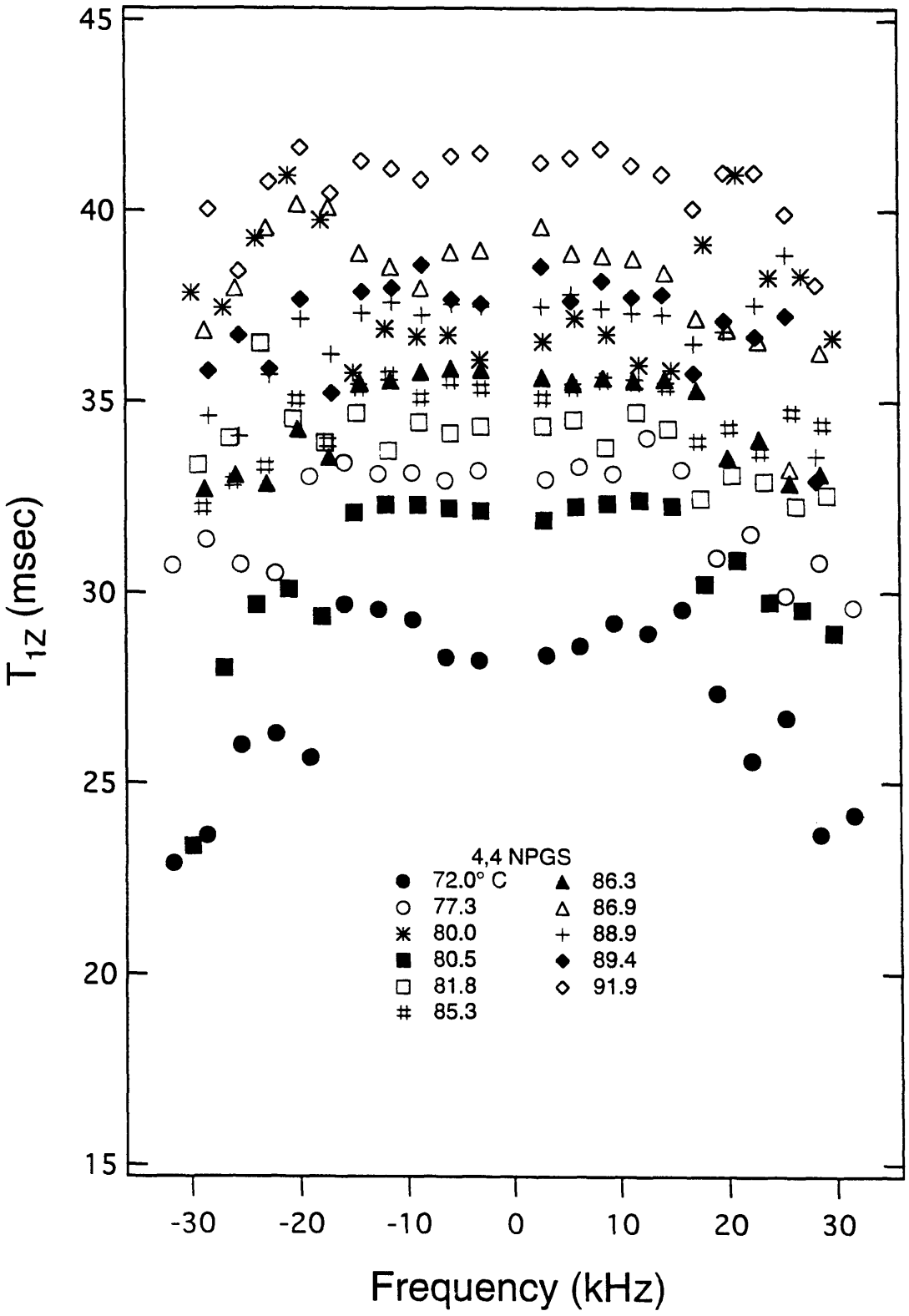

Figure 4-8. Temperature dependence of T_{1Z} in L_α phase 4,4-d_2-NPGS

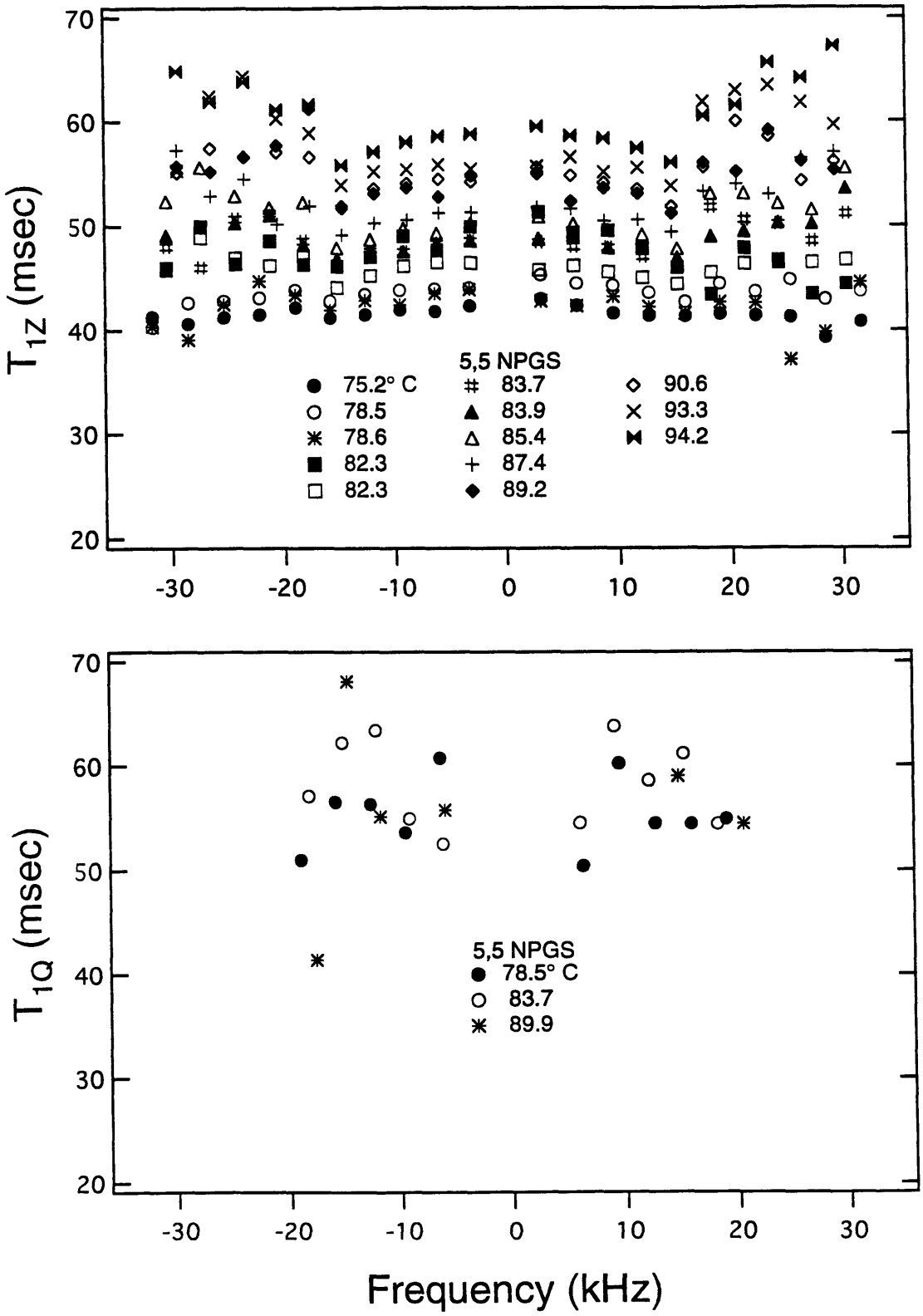

Figure 4-9. Temperature dependence of T_{1Z} and T_{1Q} in L_α phase 5,5-d_2-NPGS

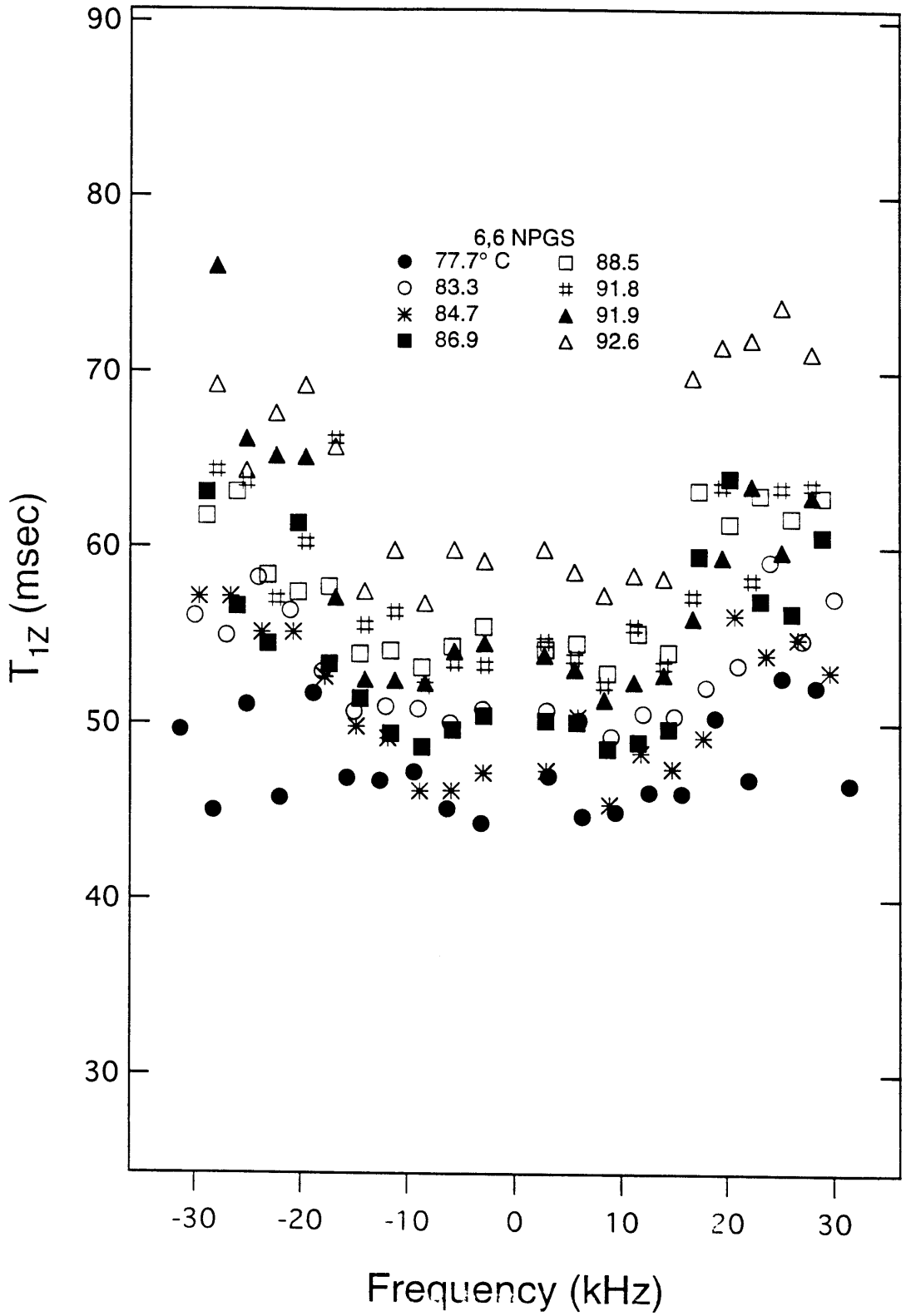

Figure 4-10. Temperature dependence of T_{1Z} in L_α phase 6,6-d_2-NPGS

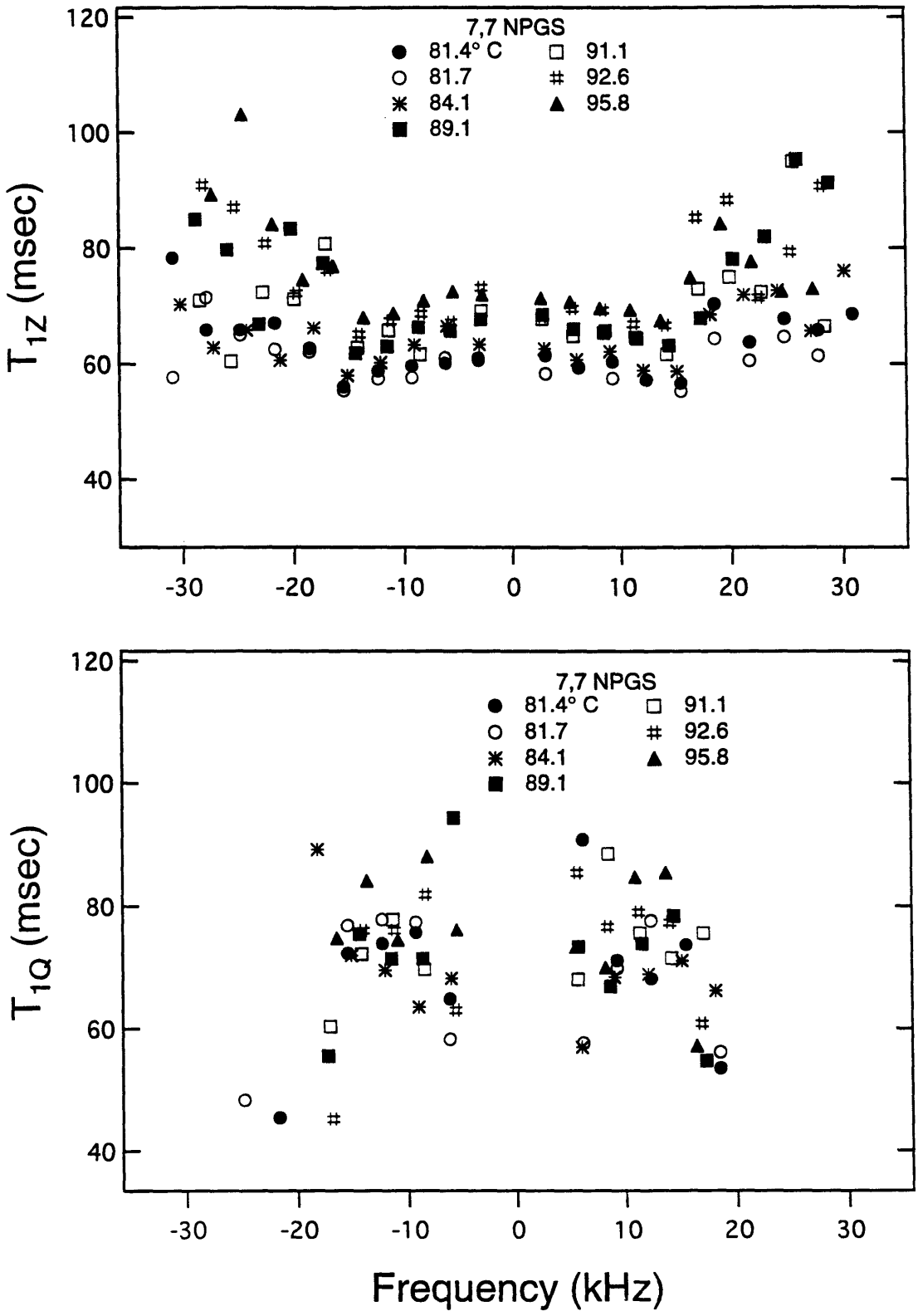

Figure 4-11. Temperature dependence of T_{1Z} and T_{1Q} in L_α phase 7,7-d_2-NPGS

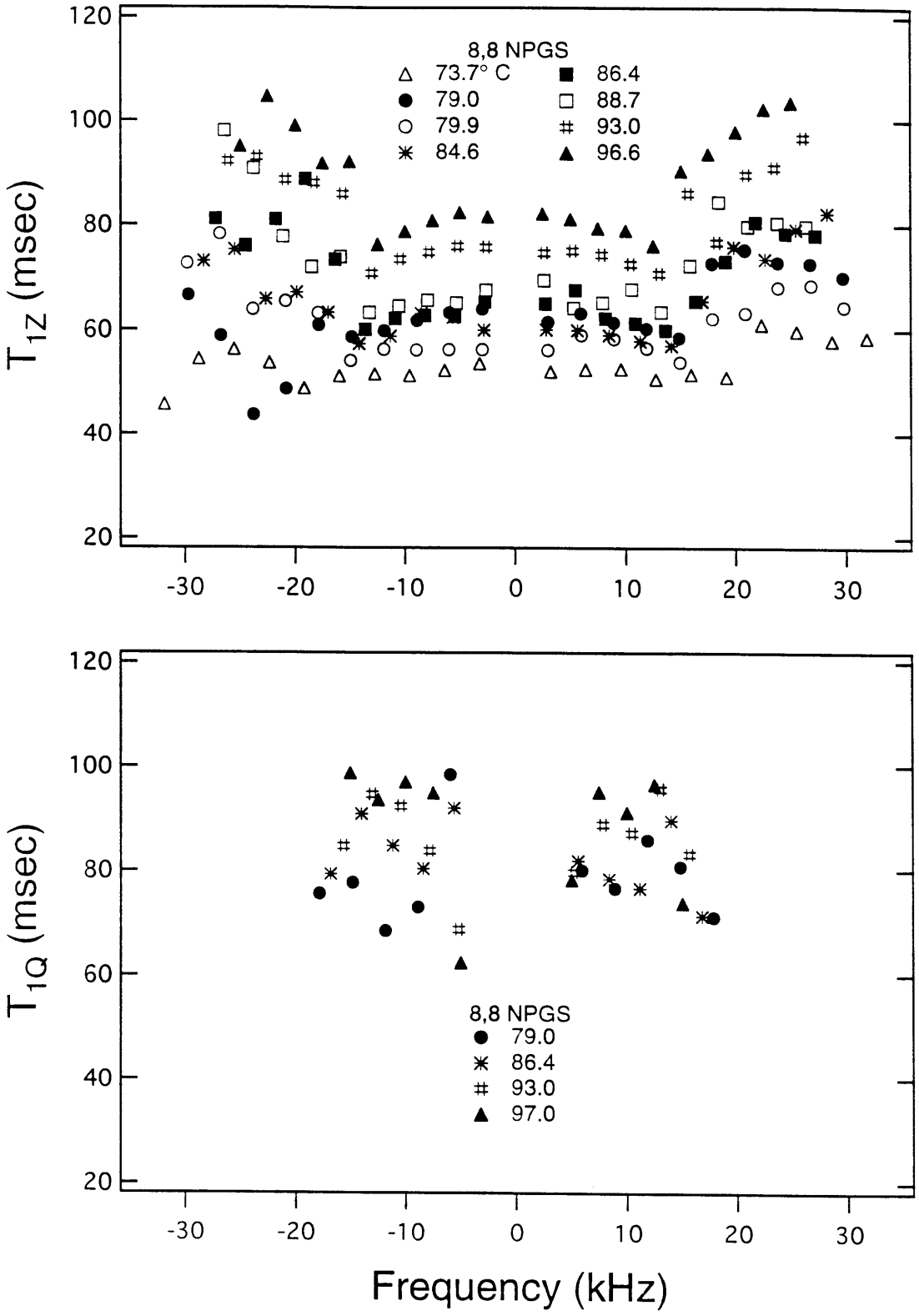

Figure 4-12. Temperature dependence of T_{1Z} and T_{1Q} in L_α phase 8,8-d_2-NPGS

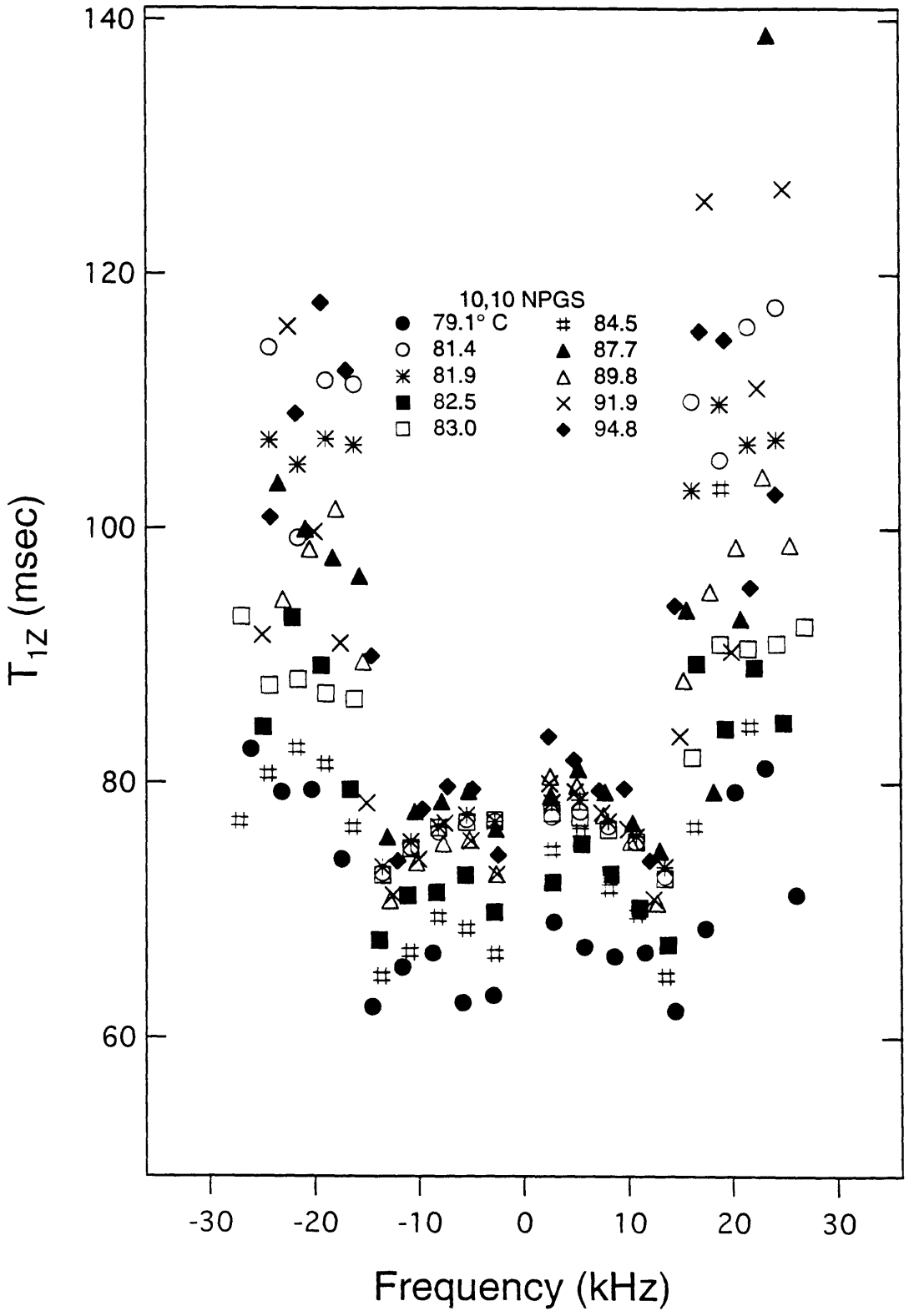

Figure 4-13. Temperature dependence of T_{1Z} in L_α phase 10.10-d_2-NPGS

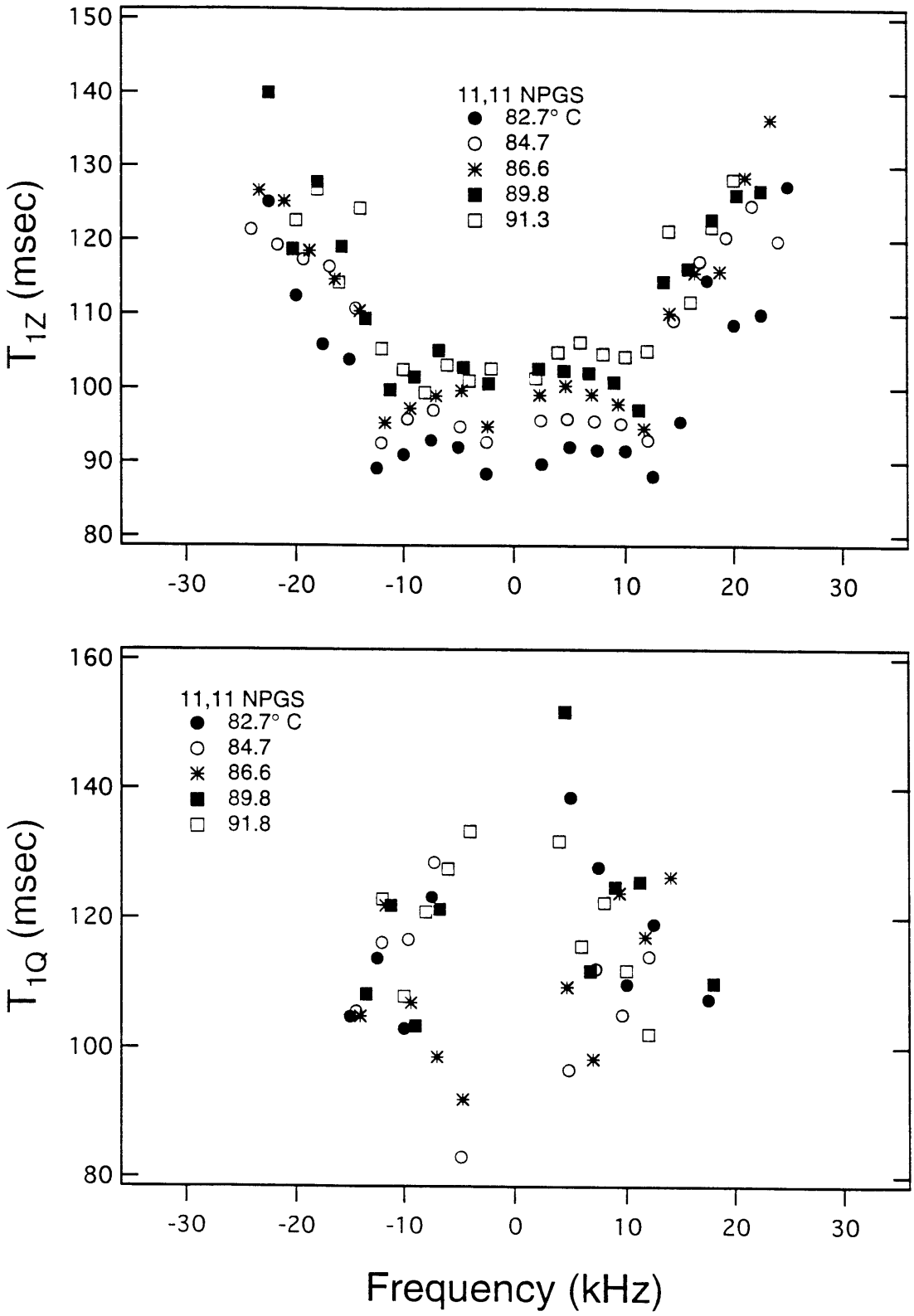

Figure 4-14. Temperature dependence of T_{1Z} and T_{1Q} in L_α phase 11,11-d_2-NPGS

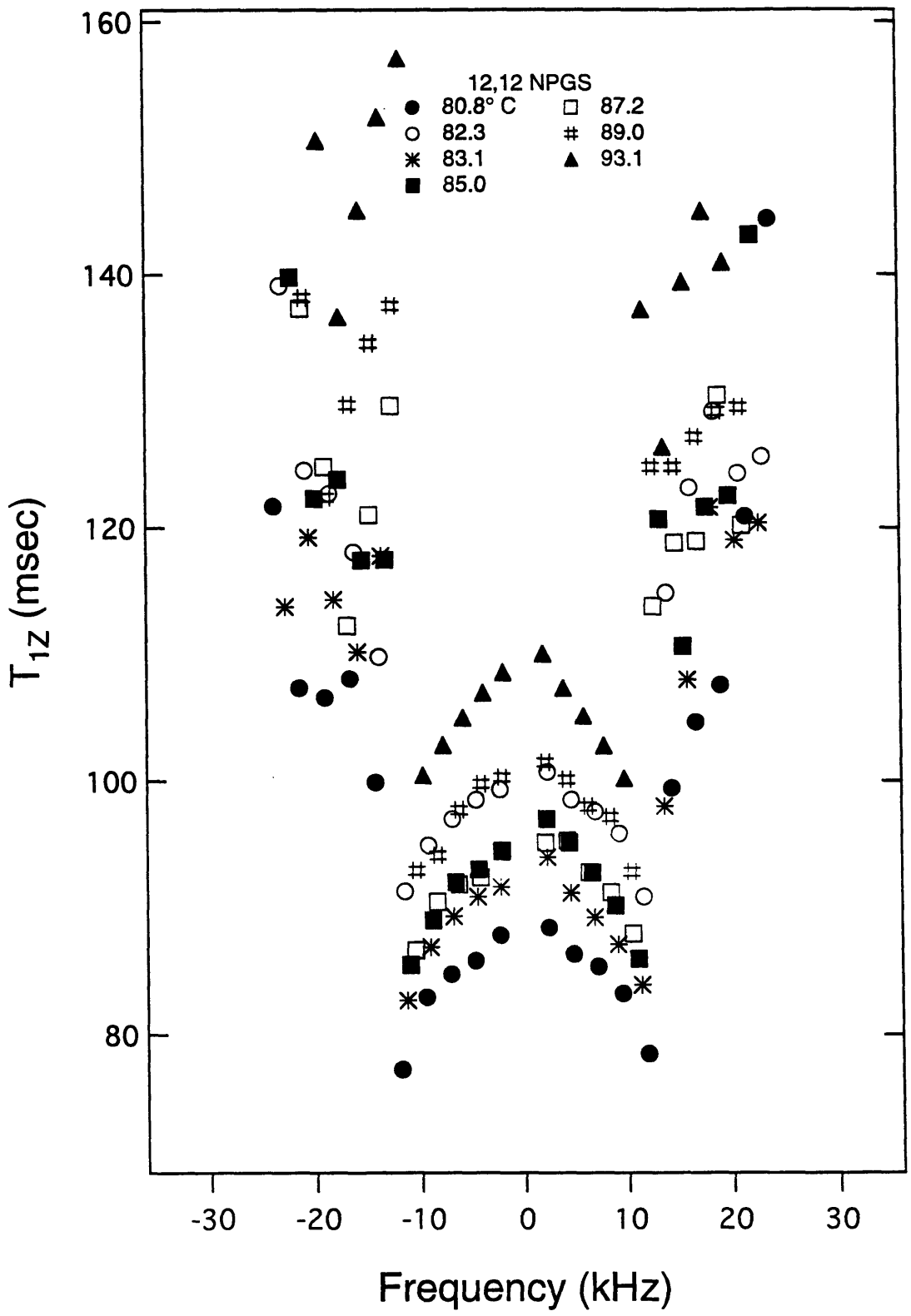

Figure 4-15. Temperature dependence of T_{1Z} in L_α phase 12,12-d_2-NPGS

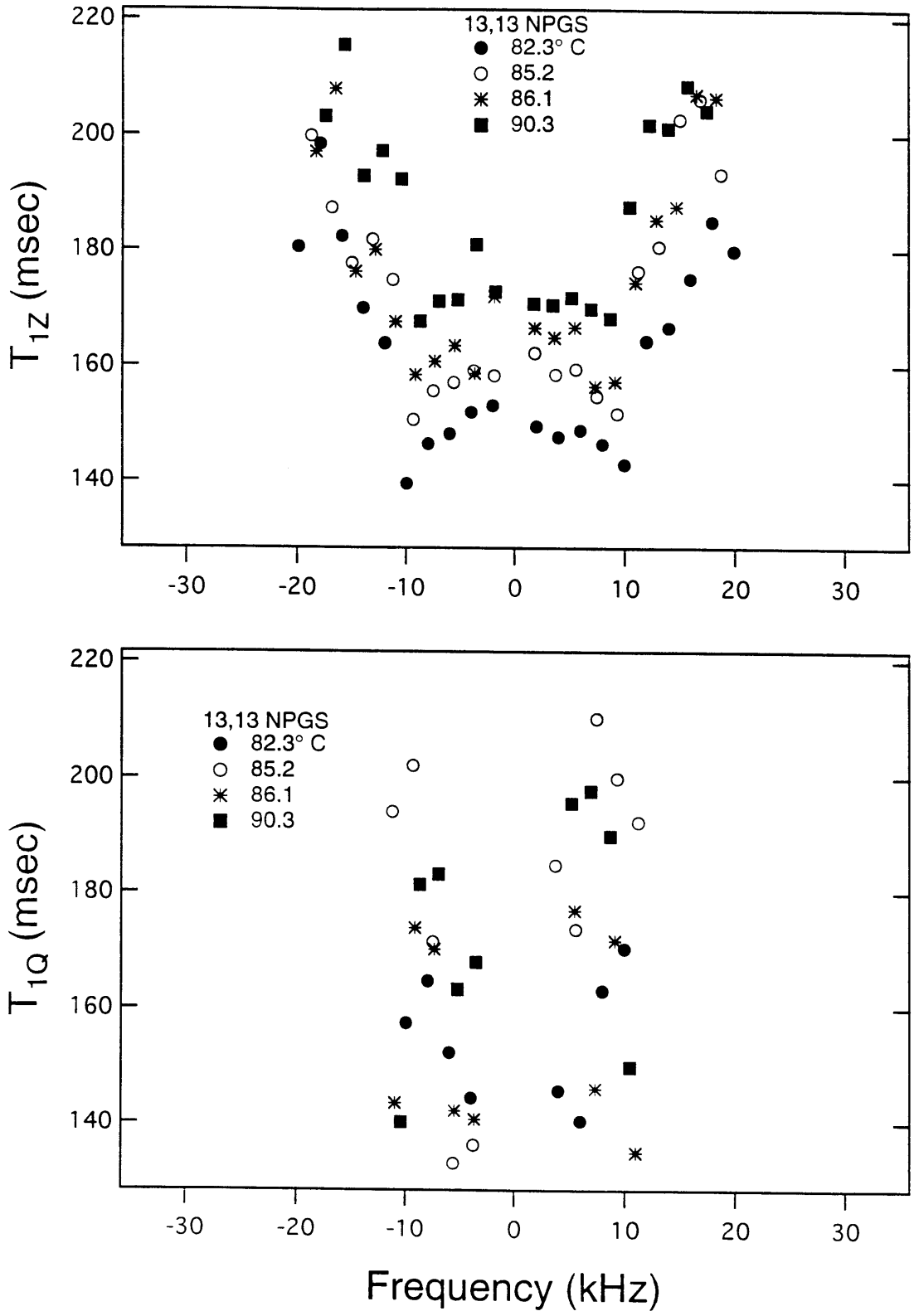

Figure 4.6. Temperature dependence of T_{1Z} and T_{1Q} in L_α phase 13,13-d_2-NPGS

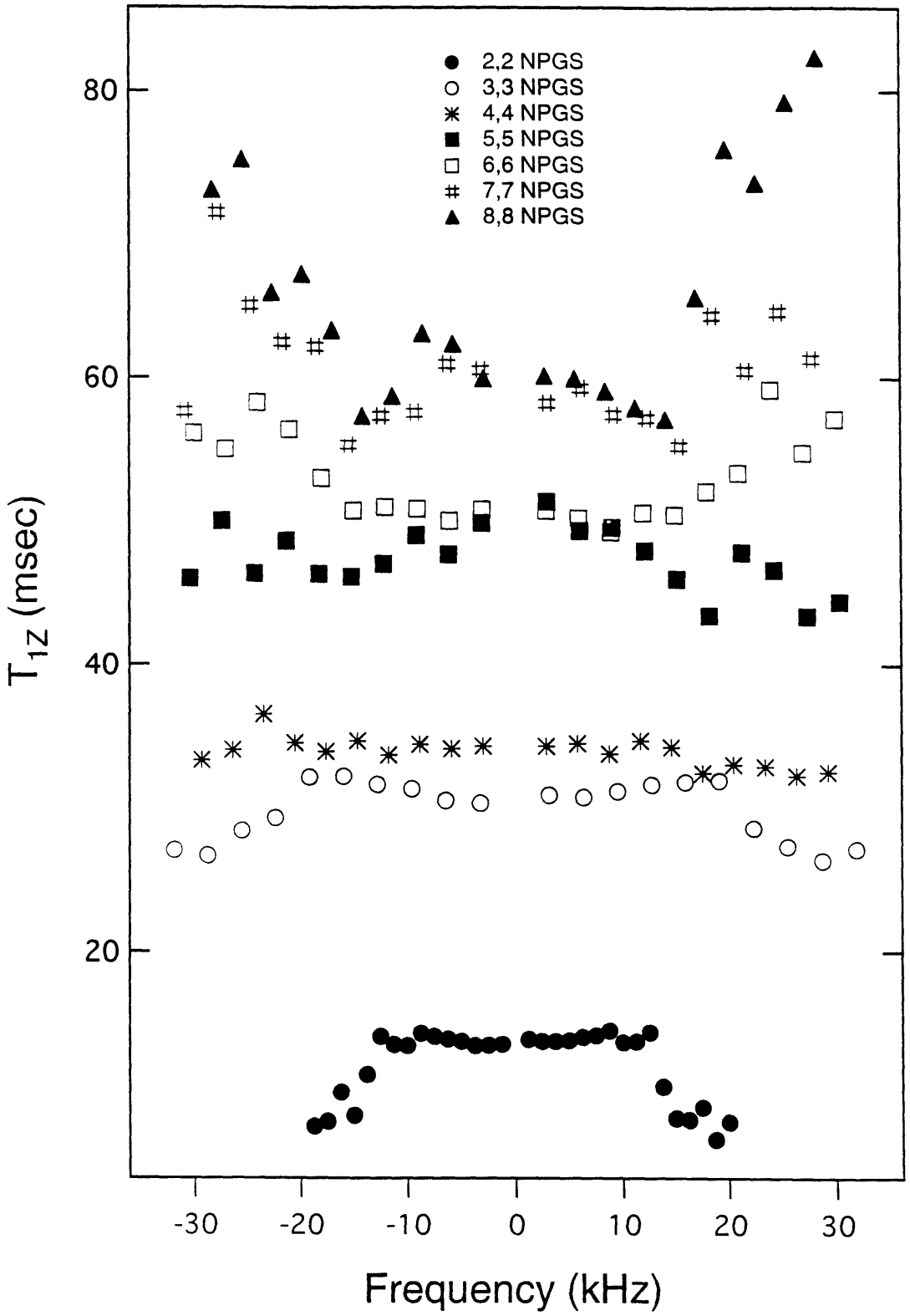

Figure 4-17. Dependence of T_{1Z} on position in L_α phase NPGS at 82° C.

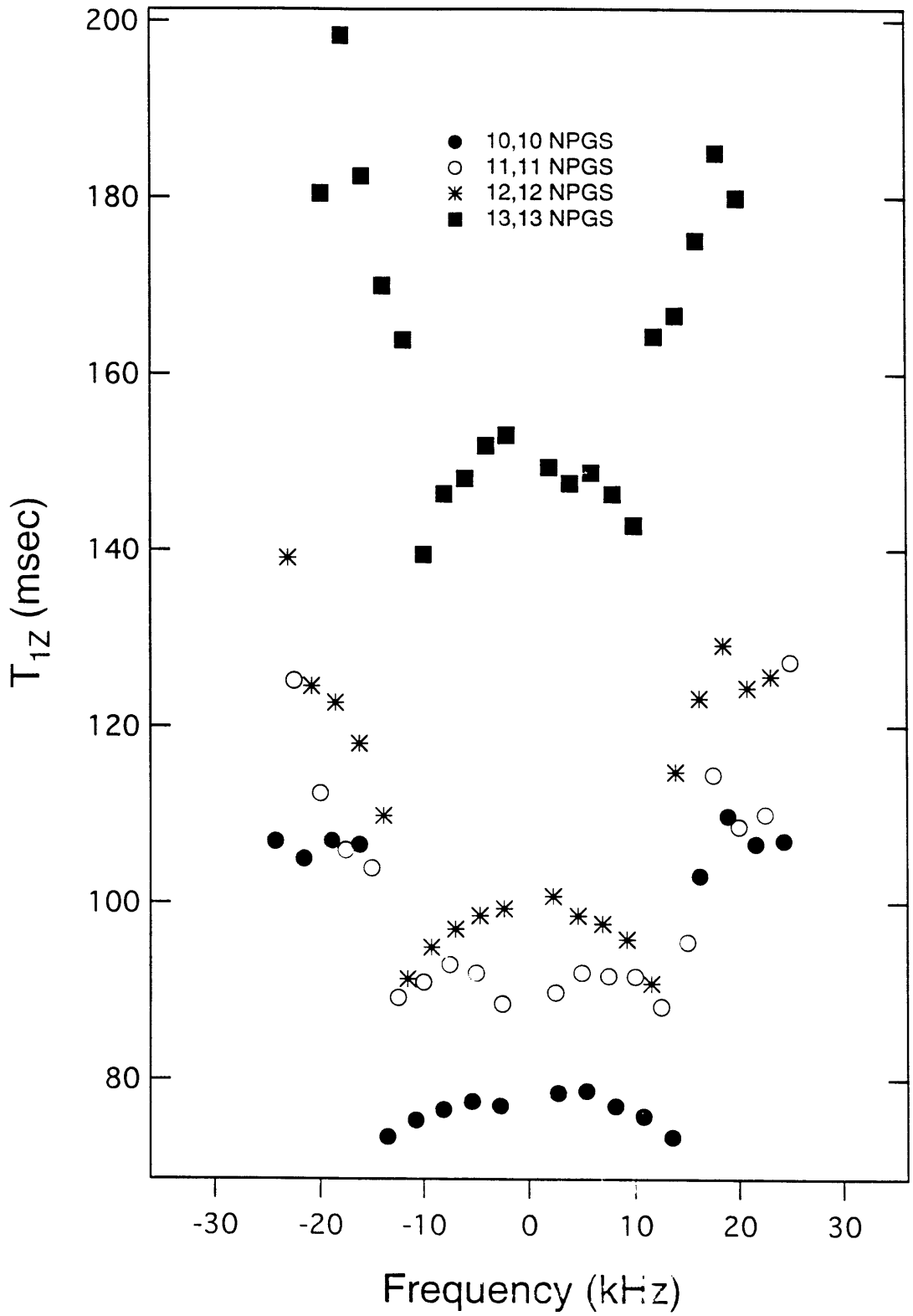

Figure 4-18. Dependence of T_{1Z} on position in L_α phase NPGS at 82° C.

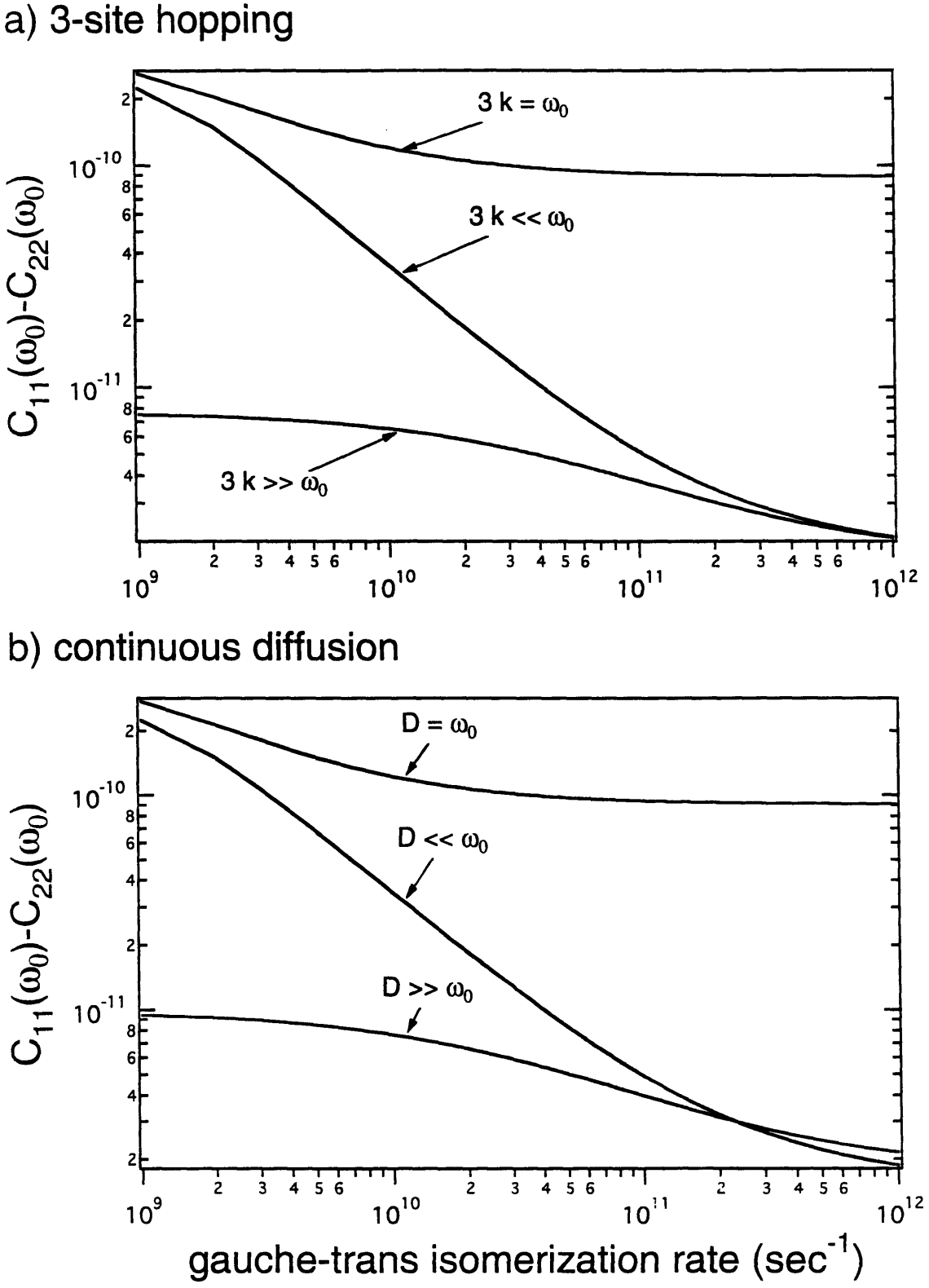

Figure 4-19. Correlation functions for gauche-trans isomerization with axial diffusion via a) 3-site hops or b) continuous diffusion. For all simulations p_{trans} = 0.5, tilt = 0°.

References

Bloom, M., Burnell, E.E., MacKay, A.L., P., N.C., Valic, M.I. & Weeks, G. (1978) *Biochem. 17*, 5750-5762.

Bonmatin, J.-M., Smith, I.C.P., Jarrell, H.C. & Siminovitch, D.J. (1990) *J. Amer. Chem. Soc. 112*, 1697-1704.

Brown, M.F., Seelig, J. & Haberlen, U. (1979) *J. Chem. Phys. 70*, 5045-5053.

Engel, A.K. & Cowburn, D. (1981) *FEBS Lett. 126*, 169-171.

Fuson, M.M. & Prestegard, J.H. (1983) *Biochem. 22*, 1311-1316.

Hoatson, G.L., Vold, R.L. & Tse, T.Y. (1994) *J. Chem.Phys. 100*, 4756-4765.

Huang, T.H., Skarjune, r.P., Wittebort, R.J. & Griffin, R.G. (1980) *J. Amer. Chem. Soc. 102*, 7377-7379.

Mayer, C., Muller, K., Weisz, K. & Kothe, G. (1988) *Liq. Cryst. 3*, 797-806.

Meier, P., Ohmes, E. & Kothe, G. (1986) *J. Chem. Phys. 85*, 3598-3614.

Meraldi, J.-P. & Schlitter, J. (1981) *Biochim. Biophys. Acta 645*, 193-210.

Oldfield, E., Meadows, M., Rice, D. & Jacobs, R. (1978) *Biochem. 17*, 2727-2740.

Pascher, I. & Sundell, S. (1977) *Chem. Phys. Lipids 20*, 175-191.

Peterson, N. & Chan, S.I. (1977) *Biochem. 16*, 2657-2667.

Ruocco, M.J., Siminovitch, D.J., Long, J.R., DasGupta, S. & Griffin, R. G. (1996) *Biophys. J.* In press.

Seelig, A. & Seelig, J. (1974) *Biochem. 13*, 4839-4845.

Seelig, A. & Seelig, J. (1975) *Biochim. Biophys. Acta 406*, 1-5.

Seelig, J. & Browning, J.L. (1978) *FEBS Lett. 92*, 41-44.

Seelig, J. & Seelig, A. (1980) *Q. Rev. Biophys. 13*, 19-61.

Seiter, C.H.A. & Chan, S.I. (1973) *J. Amer. Chem. Soc. 95*, 7541.

Speyer, J.B., Weber, R.T., Das Gupta, S.K. & Griffin, R.G. (1989) *Biochem. 28*, 9569-74.

Torchia, D.A. & Szabo, A. (1982) *J. Mag. Res. 49*, 107-21.

Trouard, T.P., Alan, T.M., Zajicek, J. & Brown, M.F. (1992) *Chem. Phys. Lett. 189*, 67-75.

Vold, R. & Vold, R. (1988) *J. Chem. Phys. 88*, 1443-1457.

Weisz, K., Grobner, G., Mayer, C., Stohrer, J. & Kothe, G. (1992) *Biochem. 31*, 1100-1112.

Winsborrow, B.G., Smith, I.C.P. & Jarrell, H.C. (1991) *Biophys. J. 59*, 729-741.

Zaccai, G., Buldt, G., Seelig, A. & Seelig, J. (1979) *J. Mol. Bio. 134*, 693-706.

5. Interaction of Cholesterol with Cerebroside

Acknowledgments: This chapter is excerpted from a manuscript currently in press (Biophysical Journal). The work was done in collaboration with Marty Ruocco, Dave Siminovitch, and Sunil DasGupta. The ^{13}C spectra and simulations, the spectra of deuterated cholesterol and their interpretation as well as much of the writing were done by Marty and Dave, however I have included the manuscript in its entirety to provide context.

5.1 Introduction

Cerebroside of the central nervous system myelin membrane has been the subject of many biochemical, immunological and biophysical studies over the past two decades. Fundamental studies characterizing the abundance and type of naturally occurring cerebrosides from normal and pathological mammalian myelin have established that (1) myelin cerebroside occurs almost exclusively as galactocerebroside; (2) galactocerebroside occurs almost exclusively in myelin membrane in a relatively high concentration (~20 weight %) and (3) mammalian CNS myelin membrane lipid composition ranges from 2/1.5/1 to 2/2/1 (cholesterol/phospholipid/ galactocerebroside) mol ratio (Norton and Cammer, 1984; Norton, 1981). Recognition of the preponderance and specific localization of galactocerebroside in myelin stimulated a number of initial biophysical studies of natural lipid extract membranes and monolayers to characterize the thermal behavior (Ladbrook et al., 1968; Linington and Rumsby, 1981), electric field effects (Clowes et al., 1971), surface potential (Quinn and Sherman, 1971), and surface viscosity (Poss et al., 1979) of galactocerebroside-containing membranes. Crystallographic studies of Abrahamsson et al. (1972) and Pascher and Sundell (1977) elucidated the structure and molecular conformation of cerebroside molecules in crystalline lamellae and showed that intermolecular hydrogen bonds were an important feature of the association between cerebroside molecules. The importance of intra- and intermolecular hydrogen bonding to hydrated cerebroside bilayer membrane stability-metastability was underscored by thermal and X-ray diffraction studies (Ruocco et al., 1981) on homogeneously acylated cerebroside and again by subsequent thermal studies on natural extracted whole fraction, non-hydroxylated and hydroxylated cerebrosides (Curatolo, 1982; Ruocco et al., 1983; Ruocco and Shipley, 1986; Jackson et al., 1988; Johnston and Chapman, 1988). It has been suggested that cerebrosides play a role in regulating the structure and properties of myelin as an insulating membrane (Ruocco and Shipley, 1984; Johnston and Chapman, 1988). Interestingly, neurochemical studies of pathological states of brain and PNS

myelin (Bologa-Sandru et al., 1981) indicate that cerebroside is a necessary component for normal myelination and nerve impulse conduction.

In order to better characterize the importance of the molecular structure and mode of intermolecular associations of cerebroside in myelin membrane, systematic thermal (DSC) and structural (X-ray diffraction and NMR) studies of the phase behavior of galactocerebroside in its pure form and in the presence of other major myelin lipids (phospholipid and cholesterol) have been undertaken (Skarjune and Oldfield, 1979a, b, 1982; Huang et al., 1980; Ruocco et al., 1983; Ruocco and Shipley, 1984; Jackson et al., 1988; Johnston and Chapman, 1988). It was shown that cerebroside exhibits a limited solubility in DPPC gel bilayers (20 mol % NPGS) and liquid crystal bilayers at $T \sim T_m$ (DPPC) (Ruocco et al., 1983). Furthermore, even though cholesterol exhibits gel phase immiscibility in cerebroside gel bilayers, the sterol can be incorporated to the extent of 50 mol % into melted liquid crystal NPGS bilayers (Ruocco and Shipley, 1984). In these studies preferential association of cerebroside molecules involving intermolecular hydrogen bonding among the galactosyl headgroups, sphingosine bases and amide linkages was suggested to explain the observed phase behavior, particularly at low temperatures (Ruocco and Shipley, 1984). These interactions also may affect cerebroside clustering in membranes (Suzuki et al., 1981) and lateral phase separation (Barenholz et al., 1983). Recent thermal and NMR studies of ceramides interacting with cholesterol and phospholipids also indicate they may play a similar role in regulating phase behavior (Florio et al., 1990; Abraham & Downing, 1991; Wiedmann & Salmon, 1991; Hamilton et al., 1993)

Although the structure and phase behavior of cerebroside in natural and model bilayer membranes have been studied extensively, the dynamic properties (e.g. molecular fluctuations and the time scale of such fluctuations), have not been studied in mixed lipid bilayers. Solid state NMR spectra of specifically labeled lipids allow a detailed examination of the motion and conformation of virtually any position in the molecule. In such a microscopic approach details of particular molecular events can be associated with

thermotropic and/or lyotropic transitions (Wittebort et al., 1981). In general, the NMR technique used in the investigation of labeled lipid compounds has been more sensitive to the onset of thermal phase transitions than DSC; however, to date, the correspondence of NMR data and a macroscopic technique such as DSC has been good (Blume etal., 1982a,b; Blume and Griffin, 1982, Vist and Davis, 1990, Huang et. al., 1993).

The unique dynamic characteristics of cerebroside in bilayers were originally reported in a study of chain-labeled cerebroside, N-[6,6-$^2H_2$]palmitoylgalactosyl-sphingosine, by Huang et al. (1980) (see also Griffin, 1981). It was observed that long axis diffusion of NPGS was slow for $T < T_c$. Further evidence in support of this contention is derived from ^{13}C=O spectra of [1-^{13}C]NPGS, which show an axially asymmetric rigid lattice powder pattern (Huang et al., to be published). In addition, ^2H-NMR spectra of headgroup-labeled cerebroside have spectral widths of ~100 kHz and demonstrate that the -CHDOH group of the galactose headgroups is restricted in its motion (Huang and Griffin, to be published). The rigid lattice ^{13}C=O spectrum and the unusually wide ^2H-labeled headgroup spectrum are attributed to the hydrogen bonding capability of the galactose residue and amide group (Huang et al., 1980). The only mode of motion in the acyl chains is then *trans-gauche* isomerization and this leads to the $\eta \sim 1$ spectra observed for N-[6,6-$^2H_2$]NPGS. This behavior is in contrast to that seen in phospholipid spectra where other modes of motion (e.g. molecular long axis rotation) contribute to the observed spectral narrowing (Huang et. al., 1993; Blume et al., 1982a,b).

Recently, the interactions of cholesterol in phospholipid (PE and PC) bilayers have been extensively characterized by ^{13}C- and ^2H-NMR (Blume and Griffin, 1982; Siminovitch et. al., 1987; Vist and Davis, 1990; Bonmatin et. al., 1990; Huang et. al., 1993). ^{13}C- and ^2H-NMR spectra were used to define the phase behavior and to distinguish various temperature-composition regions of DPPE/CHOL, DPPC/CHOL, DHPC/CHOL, DSPC/CHOL, and DAPC/CHOL bilayers. Whereas ^{13}C=O spectra of 2[1-^{13}C]DPPE/CHOL bilayers indicated a region in which there is a coexistence of two

conformationally and dynamically inequivalent DPPE molecules, the ^{2}H-NMR spectra of chain and headgroup-labeled DPPE did not clearly exhibit two components. This phenomenon was attributed to the intermolecular exchange of DPPE between gel and "liquid gelatin" bilayer phases in the two-phase composition region. The effect of cholesterol on the chain-labeled phospholipid ^{2}H spectra has resulted in a more specific interpretation of the molecular interaction of the sterol with phospholipid (Huang et. al., 1993; Blume and Griffin, 1982). Specifically, cholesterol is viewed as an intercalating spacer which disrupts the gel bilayer lattice to allow fast axial diffusion (long axis rotation) and it induces the conformational change in the glycerol backbone region characteristic of the gel $\rightarrow$ liquid crystal bilayer phase transition. At the same time, the sterol maintains, in large part, the acyl chain conformation characteristic of the gel state (i.e. a high *trans* population) (see Blume et al., 1982a). These effects upon cholesterol incorporation into phospholipid bilayers have led to an operational definition of the "liquid gelatin" (LG) phase in which conformational and dynamic properties characteristic of both gel and liquid crystalline phospholipids are present. What distinguishes "liquid gelatin" bilayers from the conventional "melted" liquid crystalline (LC) bilayers observed at high temperatures and/or in pure phospholipid systems is that the former contains greater conformational regularity or order in the acyl chain moieties than the latter. ^{2}H and ^{13}C spectra of the LG and LC bilayers are concurrently axially symmetric due to the presence of rapid axial diffusion, although spectral widths of the LG bilayers are larger. Disordering of the liquid gelatin to "melted" liquid crystalline bilayers is observed, for example, with increasing temperatures as a decrease of the deuterium quadrupole splitting, $\Delta\nu_Q$, in a sigmoidal fashion (see Blume and Griffin, 1982; Huang et. al., 1993). The sigmoidal change in $\Delta\nu_Q$ is associated with the cooperative nature of this transition from the LG to the LC bilayer phase.

The present study addresses the dynamic and conformational effects of cholesterol on a chain-linked cerebroside, N-[7,7-$^2H_2$]palmitoylgalactosylsphingosine and cerebro-

side labeled at the amide carbonyl position, N[1-^{13}C]palmitoylgalactosylsphingosine. Very different behavior is observed for the cerebroside/CHOL dispersions when compared to that reported for phospholipid/CHOL dispersions (Skarjune and Oldfield, 1979; 1982; Blume and Griffin, 1982; Vist And Davis, 1990; Huang et. al., 1993). In particular, two components are present in both ^{13}C- and ^{2}H-NMR spectra. In contradistinction to ^{13}C and ^{2}H spectra of phospholipid/CHOL bilayers, these results indicate that intermolecular exchange between the cerebroside gel and LG phases is <u>slow</u> on both the ^{13}C- and ^{2}H-NMR time scales. This slow intermolecular exchange facilitates both the simulation and quantitation of the ^{2}H-NMR lineshapes and lipid bilayer phases, respectively. Complementary ^{2}H-NMR studies of 3α-$^{2}H_1$-CHOL containing cerebroside bilayers are used to corroborate an X-ray diffraction investigation (Ruocco and Shipley, 1984) in which it is indicated that two separate lamellar phases, cholesterol monohydrate and NPGS "crystal" bilayers, may exist at low temperatures (< 40° C). Finally, the NMR results are compared and discussed in terms of observed calorimetric and structural behavior. Molecular interpretations of these results are discussed further in light of the molecular composition of myelin membrane.

5.2 Materials and Methods

Lipid Synthesis. [7,7-$^{2}H_2$]-N-palmitoylgalactosylsphingosine and [1-^{13}C]-N-palmitoylgalactosylsphingo-sine were synthesized using the method of Radin (1972). [7,7-$^{2}H_2$]palmitic acid and 1-^{13}C]palmitic acid were synthesized by the methods described in Das Gupta et al. (1982) and Wittebort et al. (1982), respectively. [7,7-$^{2}H_2$]NPGS and 1-^{13}C]NPGS were purified by silicic acid column chromatography with an elution solvent of $CHCl_3$/MeOH (9/1; V/V) and shown to be chromatographically pure by TLC, using CH_2Cl_2/MeOH/water (65/25/4; V/V) as elution solvent. The synthesis of 3α-$^{2}H_1$-CHOL required bromination, CrO_3 oxidation and zinc debromination of unlabeled cholesterol according to Feiser (1963) to form cholest-5-en-3-one. Cholestenone was then reduced with lithium aluminum deuteride in diethyl ether according to

Rosenfeld et al. (1954). 3α-$^2H_1$-CHOL was shown to be pure by TLC using an elution solvent. Cholesterol purchased from Nu-Chek Prep (Elysian, MN) also gave a single spot by TLC.

Sample Preparation. Samples consisted of 60-120 mg of lipid. NPGS and cholesterol were mixed in dichloromethane and methanol in a small vial; the solvent evaporated under N_2 at $40 < T < 50C$ and the final traces of solvent removed under vacuum for 16-24 hours. The lipid mixtures were then transferred to an NMR sample tube (7 mm OD) having a narrow constriction, ^2H-depleted water (Aldrich Chemicals, Milwaukee, WI) added (~70 wt % H_2O) and the tube flame sealed. Sample equilibrium was achieved by centrifuging the lipid-water sample through the narrow constriction at $T > T_c$ of the lipid mixture (typically 70-80°C). After equilibration, the portion of the NMR sample tube to be placed in the NMR coil was flame-sealed under vacuum. Prepared samples were then heated to $T > T_c$ (NPGS), cooled to room temperature and equilibrated at room temperature for $\geq$ 12 hours prior to recording spectra. This protocol is similar to that used in a recent X-ray diffraction and calorimetric study of NPGS/CHOL bilayers (see Ruocco and Shipley, 1984).

NMR Spectroscopy. ^2H- and ^{13}C-NMR spectra were obtained on two different home-built solid state pulse spectrometers operating at 45.3 MHz for ^2H and 79.9 MHz for ^{13}C, respectively. ^{13}C spectra were recorded with Hahn spin-echo or cross-polarization with a 180° refocusing pulse (Pines et al., 1973; Griffin, 1981). The ^{13}C $\pi/2$ pulse was 6.5 μsec and 3 msec mixing times were used for cross-polarization. Full phase cycling with quadrature detection was used (Griffin, 1981). In order to minimize radiofrequency heating, low ^1H decoupling power and long recycle delays ($\geq$ 5 sec) were used. ^2H-NMR spectra were obtained using a two-pulse quadrupole echo sequence, $\pi/2_x$-τ-$\pi/2_y$, with a typical pulse spacing of 50-60 μsec. The ^2H $\pi/2$ pulse was typically 2.2 to 2.5 μsec. Full phase cycling and quadrature detection were used. Between 500 and 4100 echo signals were accumulated per spectrum. The recycle delay was 0.2 s for all spectra

of [7,7-$^{2}H_2$]NPGS-containing samples; however, delays as long as 7 sec were used for spectra of 3α-$^{2}H_1$-CHOL-containing samples.

5.3 Results

The ^{13}C-NMR Spectra of [1-^{13}C]NPGS/CHOL mixtures are shown in Figure 5-1 as a function of cholesterol concentration over the 27°C to 86°C temperature range. The rigid lattice ^{13}C=O spectra of pure NPGS bilayers at temperatures below the gel bilayer → liquid crystal bilayer transition (T_c = 82°C) demonstrate an axially asymmetric line-shape which is indicative of a rigid, immobile carbonyl group that is situated at the water headgroup interfacial region of the bilayer (Figure 5-1a). These spectra are identical to those obtained for cerebroside bilayers in the absence of water (Griffin, 1981). Above the gel bilayer → liquid crystal transition at 86°C, an axially symmetric spectrum indicative of rapid molecular long axis diffusion is observed.

Notably, the addition of 10 to 50 mol % cholesterol results in no significant line-shape or spectral width changes at T ≤ 40°C (Figure 5-1b-f). In contrast, at higher temperatures (i.e. 60 ≤ T ≤ 75°C), a second spectral component is observed which corresponds to a melted cerebroside bilayer phase (see Figure 5-1). Furthermore, the appearance of this melted component occurs at progressively lower temperatures with increasing cholesterol concentrations (compare Figure 5-1a with 1b-f).

The coexistence of both gel and melted components is conclusively demonstrated by the complementary utilization of ^{13}C cross-polarization and Hahn spin-echo pulse experiments. The ^{13}C=O T_1 for [1-^{13}C]NPGS in the gel phase bilayers is long (> 1 min) and necessitates the use of ^{13}C cross-polarization experiments to obtain a ^{13}C-NMR spectrum (see Pines et al., 1973; Griffin, 1981). In contrast, [1-^{13}C]NPGS in melted bilayers exhibit a relatively short ^{13}C=O T_1 and allow the use of a simple Hahn spin-echo with relatively short recycle delay times (RD ~5 s). The large difference between the gel ^{13}C T_1 and the liquid crystal ^{13}C T_1 can be exploited in the two-phase region of the [1-^{13}C]NPGS/CHOL bilayer system (as defined in Ruocco and Shipley, 1984) to selectively

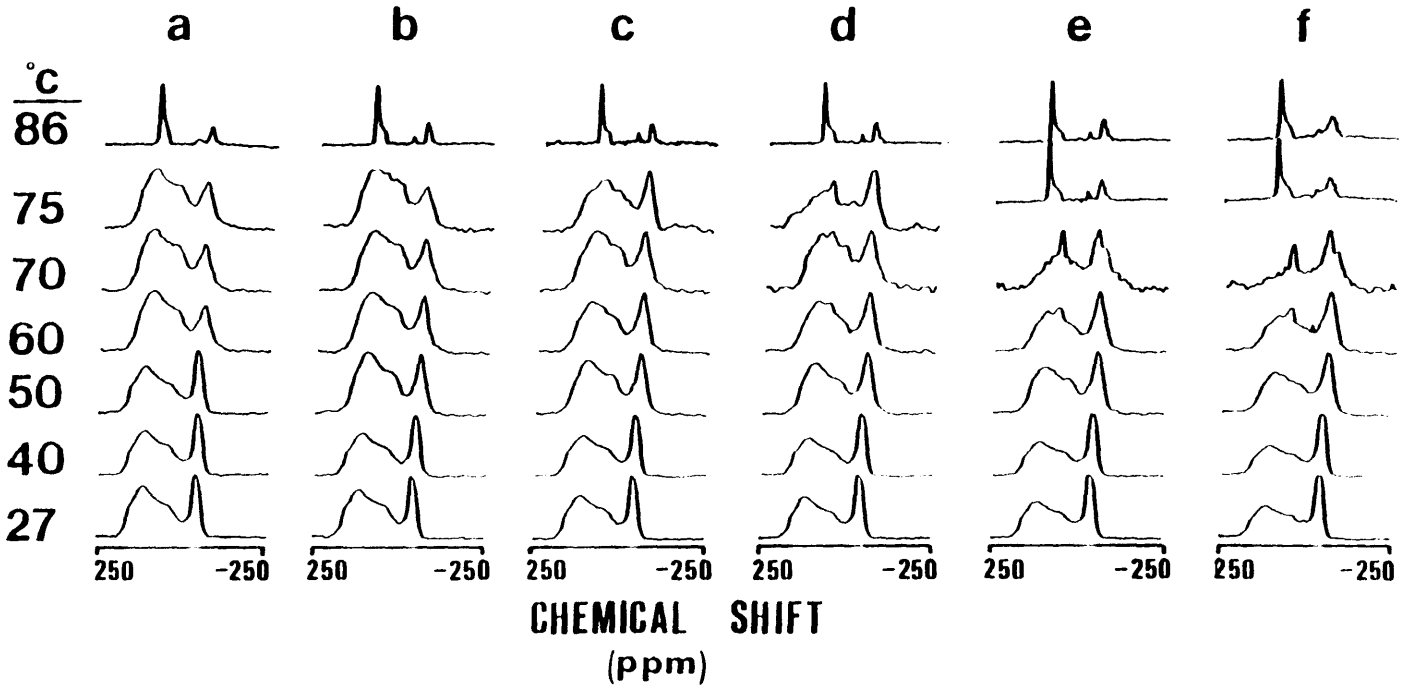

Figure 5-1. Proton decoupled ^{13} C-NMR spectra of [1-^{13}C]NPGS and [1-^{13}C]-NPGS/CHOL mixtures as a function of temperature (°C): (a) 0, (b) 10, (c) 20, (d) 30, (e) 40, and (f) 50 mol % CHOL, respectively.

observe the spectrum of the melted bilayer component. Figure 5-2 depicts spectra obtained in the two-phase region (T= 70°C) of NPGS mixtures containing 10 to 50 mol % cholesterol using either a ^{13}C cross-polarization spin-echo which is sensitive to both gel and liquid crystal [1-^{13}C]NPGS components (Figure 5-2a), or a spin-echo experiment using a short recycle delay, (RD = 5 s <<< T_1 (gel[1-^{13}C]NPGS)) which detects only the melted spectral component (Figure 5-2b). As would be expected for a given temperature with increasing cholesterol concentration, an increasing proportion of liquid crystal bilayer spectral component is observed. In complementary fashion, the gel spectra component diminishes progressively with increasing cholesterol concentration (compare gel spectral component in Figure 5-2a with liquid crystal spectra in Figures 5-2a and 5-2b).

The study of the linewidth dependence of the axially symmetric ^{13}C powder spectra of the NPGS/CHOL liquid crystal bilayers is facilitated by the tendency of cerebroside and cerebroside/CHOL bilayers to supercool to approximately 73°C (Ruocco et al., 1981; Ruocco, 1983). Figure 5-3 shows the axially symmetric spectra of melted cerebroside bilayers containing 0, 30 and 50 mol % cholesterol. The residual CSA, $\Delta\sigma_R$ (where $\Delta\sigma_R = \sigma_{||} - \sigma_{\perp}$), is plotted as a function of temperature at a constant cholesterol concentration (see Figure 5-4). For a given CHOL concentration the chemical shielding anisotropy decreases as a function of increasing temperature. However, for a given temperature it increases with increasing cholesterol concentration.

Figure 5-5 shows the ^2H-NMR spectra of [7,7-$^2H_2$]NPGS in bilayers containing 0-50 mol % CHOL as a function of temperature. In pure NPGS bilayers ^2H-NMR lineshapes similar to those reported previously by Huang et al. (1980) are observed. However, the NPGS/CHOL spectra in Figure 5-5b through 5e at 50°C ≤ T < 86°C are quite different from ^2H-NMR spectra obtained for deuterium chain-labeled phospholipid/CHOL bilayers at similar temperatures (i.e. $T < T_c$) (e.g. see Skarjune and Oldfield, 1979; 1982; Huang et. al., 1993). In particular, for temperatures below T_c of NPGS the spectra are a superposition of NPGS gel and melted NPGS liquid crystal spectral line

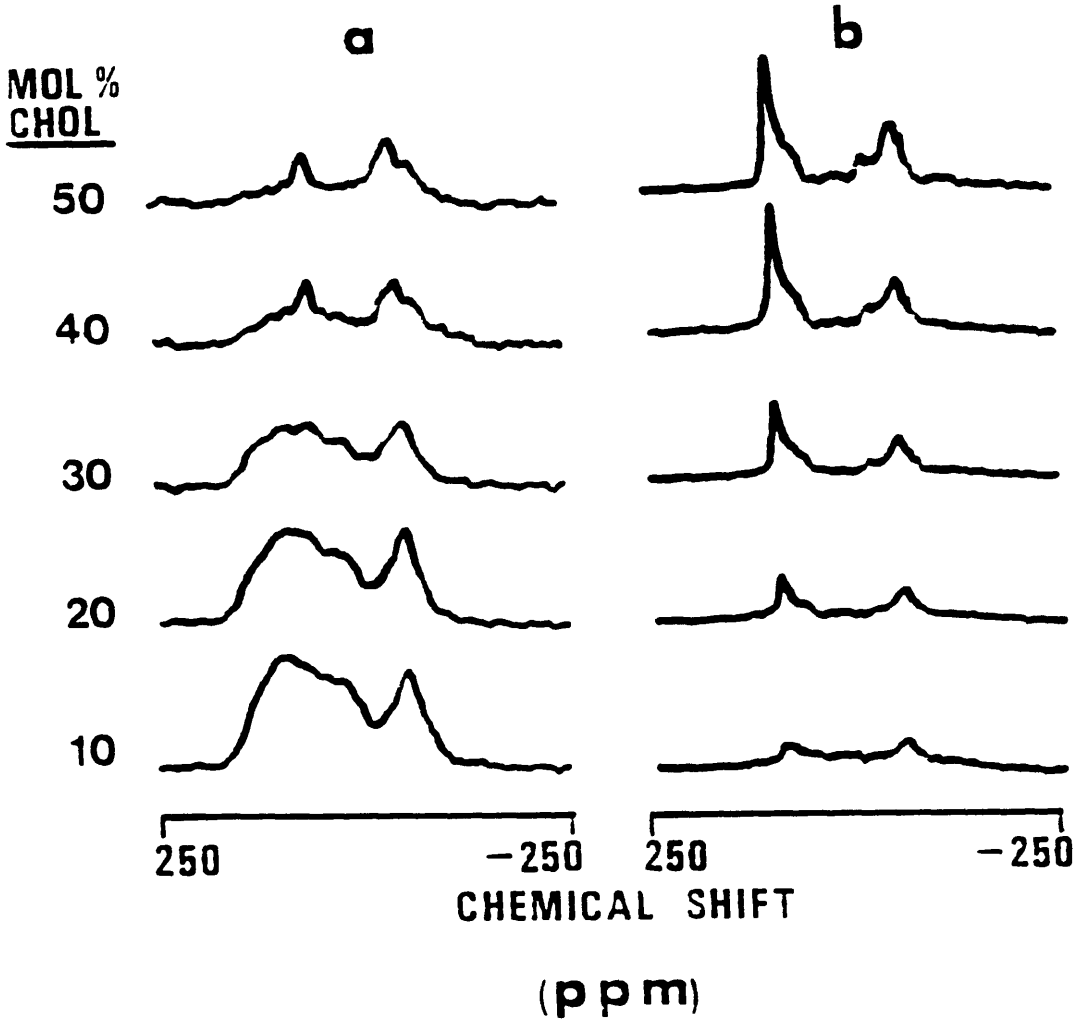

Figure 5-2. Proton decoupled ^{13}C-NMR spectra of [1-^{13}C]-NPGS/CHOL mixtures (T = 70°C) using (a) cross-polarization with a refocusing pulse or (b) simple Hahn echo pulse sequence.

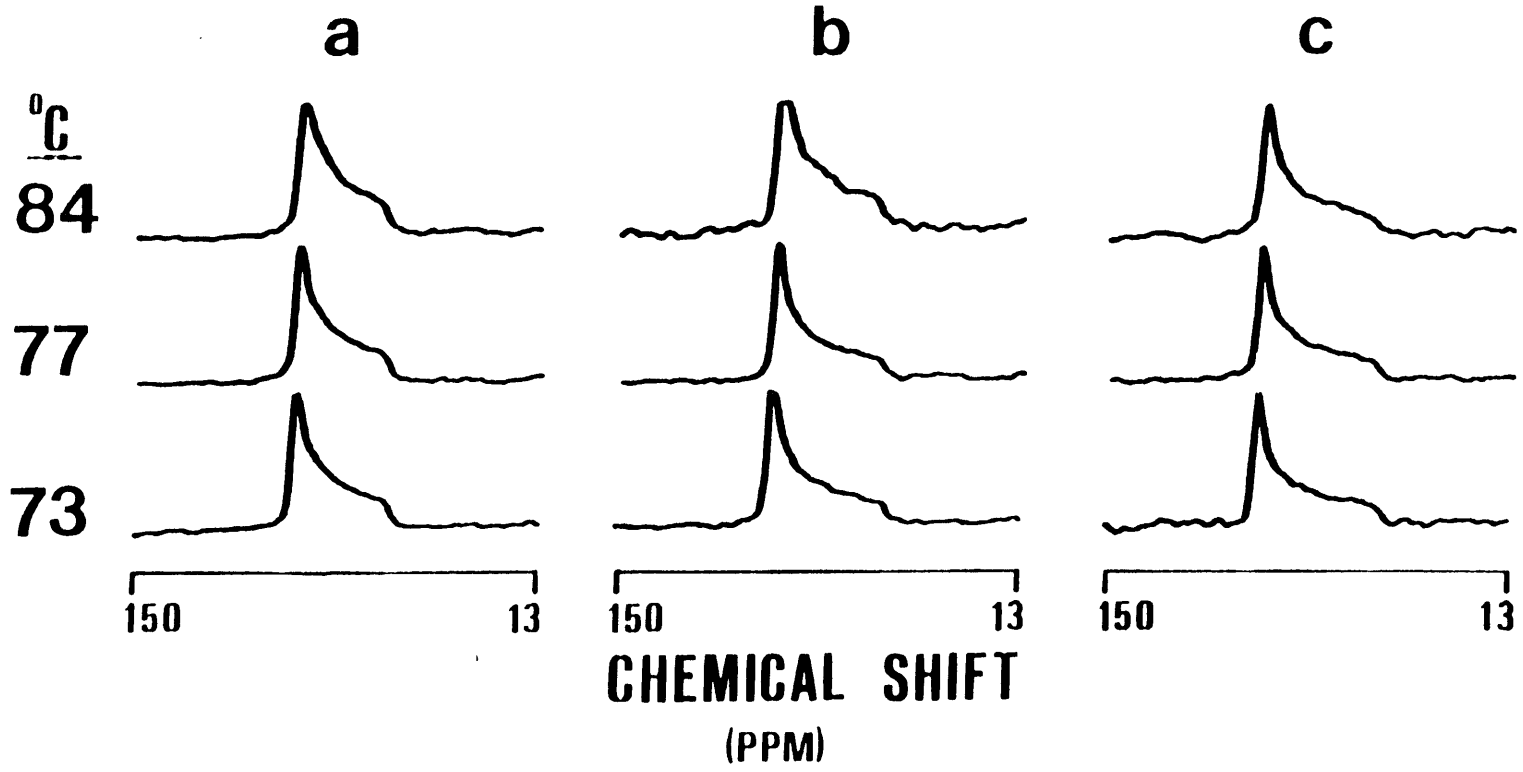

Figure 5-3. Proton decoupled ^{13}C-NMR spectra of [1-^{13}C]NPGS/CHOL bilayers as a function of temperature in the melted state: (a) 0, (b) 30, and (c) 50 mol % CHOL, respectively.

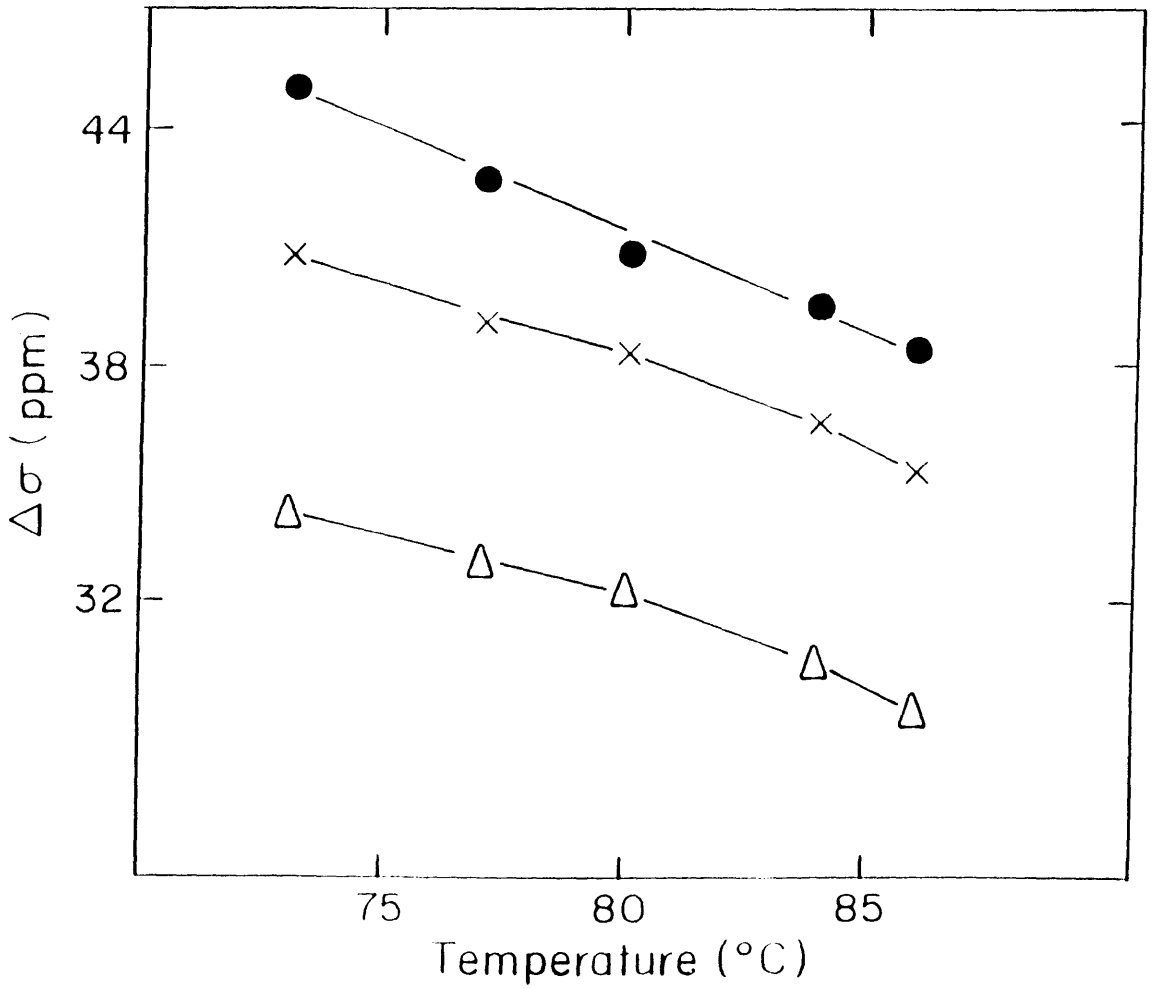

Figure 5-4. Chemical shift anisotropy, $\Delta\sigma$, for [1-^{13}C]NPGS/CHOL melted bilayers (also see Figure 5-3) as a function of temperature and CHOL concentration: (Δ) 0, (X) 30, and (O) 50 mol % CHOL, respectively.

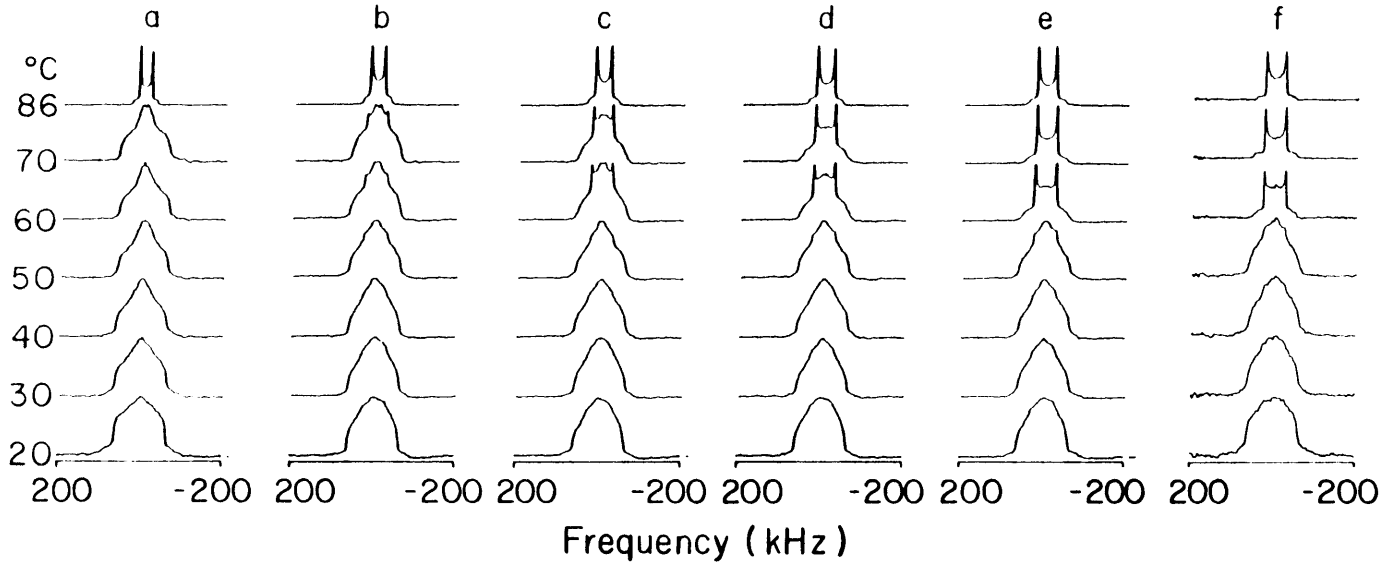

Figure 5-5. ^{2}H-NMR spectra of [7,7-$^{2}H_2$]NPGS as a function of temperature: (a) 0, (b) 10, (c) 20, (d) 30, (e) 40, and (f) 50 mol % CHOL, respectively.

shapes, indicating that exchange between the liquid crystal and gel phases is slow on the ^{2}H-NMR time scale. The residual quadrupole splittings, $\Delta\nu_Q$, of the axially symmetric liquid gelatin (liquid crystal) spectral component are plotted as a function of temperature at a constant cholesterol concentration (Figure 5-6a). Interestingly, the $\Delta\nu_Q$ is independent of cholesterol concentration in a limited temperature range (50°C $\leq$ T $\leq$ 65°C) beyond which the $\Delta\nu_Q$ disperse as a function of cholesterol. For example, the increase in magnitude of the quadrupole splitting as a function of cholesterol concentration is readily apparent near the transition temperature of NPGS (i.e. 80 to 86°C). Figure 5-6b better illustrates that $\Delta\nu_Q$ is constant over the 10 to 50 mol % cholesterol concentration range between 50 to 65°C. Changes in $\Delta\nu_Q$ as a function of cholesterol at a given temperature are observed at temperatures $\geq$ 65°C and are further accentuated at higher temperatures (see T = 70° to 86°C in Figure 5-6b). A second notable feature in Figures 5-6a and 5-6b is the magnitude of the $\Delta\nu_Q$ in the presence of cholesterol at 50°C $\leq$ T $\leq$ 65°C ($\Delta\nu_Q$ = 50-54 kHz) which indicates spectral widths, Δ, where 96 $\leq \Delta <$ 102 kHz, similar to or slightly less than that observed for cerebroside in gel bilayers without cholesterol (i.e. $\Delta \approx$ 125 kHz). As pointed out previously, these spectral parameters are characteristic of liquid gelatin bilayers (see Huang et. al., 1993).

The spectra and phase behavior of deuterium-labeled 3α-^{2}H$_1$-CHOL in NPGS bilayers are summarized in Figure 5-7. The NPGS 3α-^{2}H$_1$-CHOL (50 mol %) mixture was prepared as described in Ruocco and Shipley (1984). In brief, the dispersion was equilibrated in the presence of deuterium-depleted water at 70° to 86°C, slowly cooled to room temperature (~25°C) and equilibrated for $\geq$ 12 hours at this temperature. The ^{2}H-NMR lineshape observed at 19.5 °C after this particular regimen is depicted in Figure 5-7b. This lineshape exhibits two sharp peaks corresponding to the perpendicular edges of a rigid lattice spectrum ($\Delta\nu_Q \cong$ 122 kHz). The spectral width and lineshape in Figure 5-7b for the hydrated NPGS/3α-^{2}H$_1$-CHOL dispersion are identical to that observed for dry NPGS/3α-^{2}H$_1$-CHOL powder at 19.5°C (compare Figure 5-7a) with the exception that in

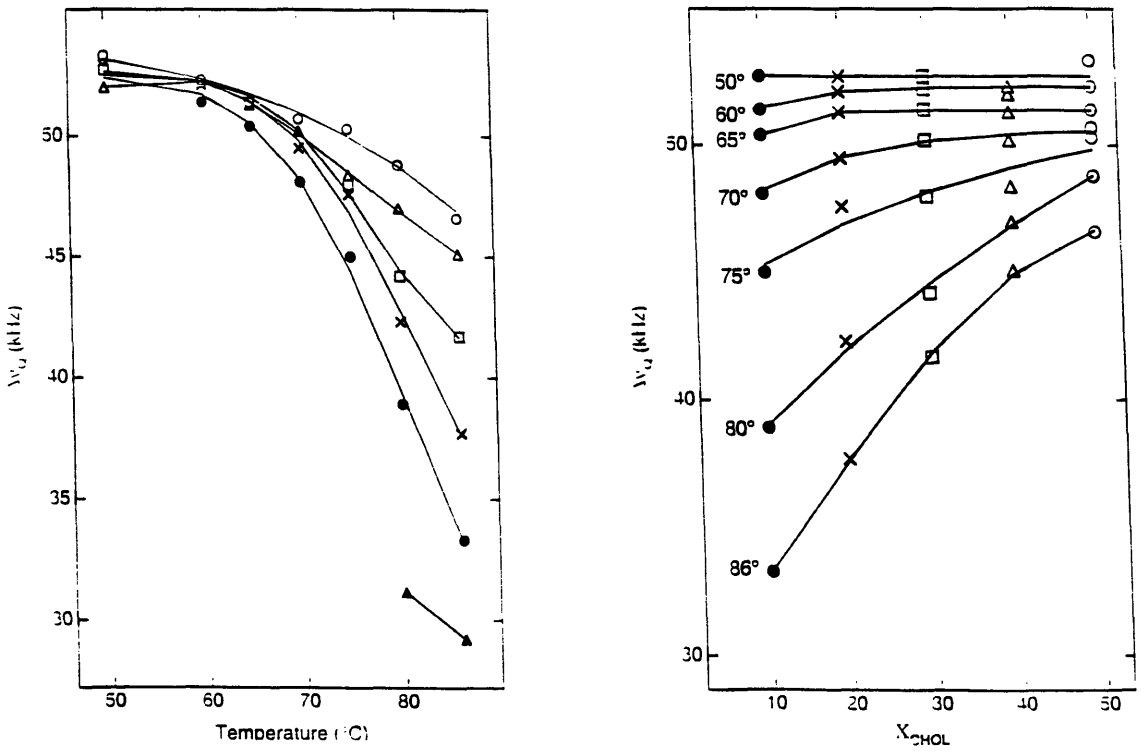

Figure 5-6. Residual quadrupole splitting, $\Delta\nu_Q$, for [7,7-$^2H_2$]NPGS/CHOL mixtures. (a) Vs. temperature (▲) 0; (●) 10, (X) 20, (□) 30, (Δ) 40, and (O) 50 mol % CHOL, respectively. (b) Vs. CHOL concentration.

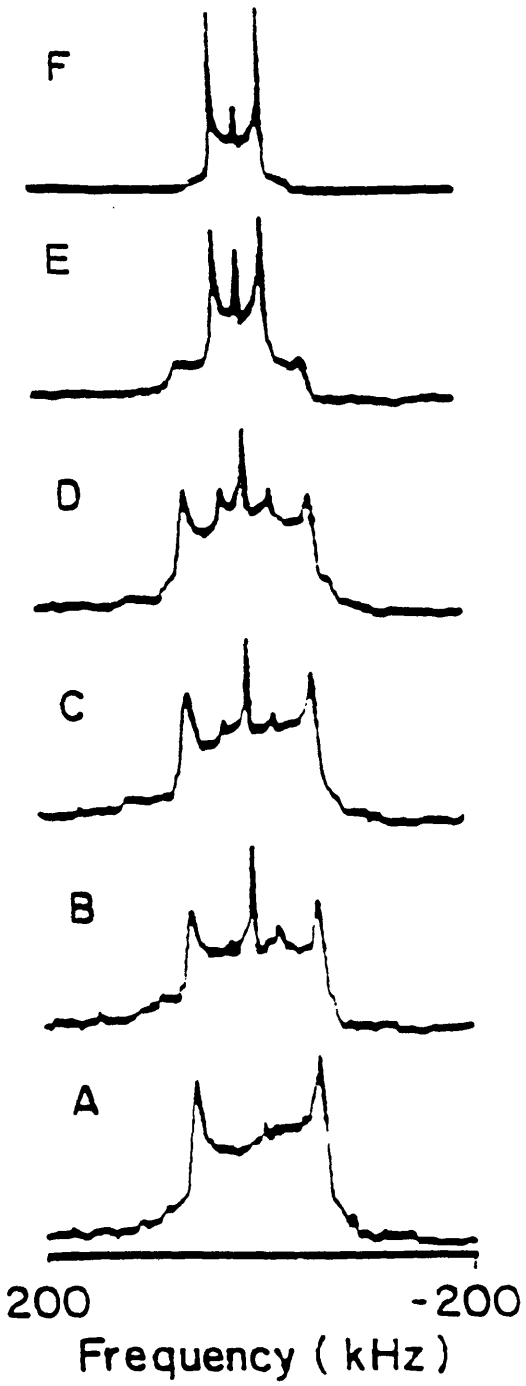

Figure 5-7. ^{2}H-NMR spectra of NPGS/3α-$^{2}H_{1}$-CHOL (50/50 mol ratio) dispersion as a function of temperature: (a) 19.5 °C, dry powder; (b) 19.5 °C, hydrated dispersion; (c) 39.5°C, hydrated dispersion; (d) 49.5°C, hydrated dispersion; (e) 53°C, hydrated dispersion, and (f) 66°C, hydrated dispersion, respectively.

Figure 5-7b, a pair of sharp spectral features at ± 22.5 kHz and a central resonance due to ^2H_2O are observed. The rigid lattice spectra observed in Figures 5-7a and 5-7b are identical to that observed for "dry" crystalline cholesterol at 19.5°C (unpublished data, M.J. Ruocco and R.G. Griffin)[2].

As the temperature is increased from 19.5°C to 49.5°C, the central peaks at ± 22.5 kHz are enhanced relative to the rigid lattice spectral component (see Figures 5-7c and 5-7d). At still higher temperatures (see T = 63°C, Figure 5-7e) a motionally narrowed component with $\Delta\nu_Q$ = 46.8 kHz dominates the spectrum until at T > 56°C, where a single, motionally narrowed, axially symmetric powder pattern is observed (see Figure 5-7f; T = 66°C). The spectrum depicted in Figure 5-7f is characteristic of cholesterol that has been totally incorporated into the melted liquid crystal cerebroside bilayers.

X-ray diffraction experiments indicate that cholesterol remains completely incorporated into the liquid-gel phase cerebroside bilayers only at temperatures ≥ 56°C. For T < ~56°C (Transition I)[3], the sterol gradually separates from the cerebroside bilayer to form a cholesterol monohydrate lamellar phase (Ruocco and Shipley, 1984). In the NMR experiment, this phase separation process can again be studied by taking advantage of the large difference in T_1 between cholesterol in melted bilayers and in cholesterol monohydrate crystals. With a short (0.2 sec) recycle delay, one selectively monitors the motionally averaged ^2H signal arising from cholesterol incorporated in the LG phase cerebroside bilayer (see Figure 5-8). However, when the cholesterol monohydrate lamellae form, the sterol exhibits a long T_1 characteristic of rigid crystalline solids and spectra of this species necessitates a much longer recycle delay time (7 sec). As shown in Figure 5-8, the spectral intensity decreases as the cerebroside/CHOL bilayers are cooled below Transition I until at T = 41°C essentially all but a residual intensity due to cholesterol remaining in cerebroside bilayers is observed. By simply lengthening the recycle delay to ~7 sec, following equilibration conditions as described in the Materials and Methods

section, one can obtain the broad, axially symmetric rigid lattice spectrum as observed in Figure 5-7b.

5.4 Discussion

5.4a ^{13}C Spectra of NPGS/CHOL Mixtures

The ^{13}C spectra of NPGS gel bilayers at 25°C yield an axially asymmetric powder pattern of spectral width ~130 ppm which is indicative of a rigid, relatively immobile $^{13}C{=}O$ chemical shift tensor on the ^{13}C-NMR time scale ($< 10^{-3}$ sec). On a molecular level the persistance of this spectrum at higher temperatures and with increasing amounts of cholesterol suggests the presence of headgroup and/or amide group inter- and intramolecular hydrogen bonding. As a result of these intimate, specifically directed molecular associations, two separate lipid phases, NPGS "crystal" bilayers and cholesterol monohydrate lamellae, are observed by X-ray diffraction at low temperatures (e.g. T = 20°C) (Ruocco and Shipley, 1984). Because these two phases are non-interacting, relatively little change in the gel ^{13}C spectra of NPGS/CHOL dispersions, compared to pure NPGS dispersions, is observed at low temperatures (see Figure 5-1 (a-f); T = 27°C).

At intermediate temperatures (i.e. 40°C ≤ T < 70°C) a second spectral component arises which, under all conditions used for the cross-polarization pulse sequence, gives rise to a distorted signal corresponding to a melted NPGS/CHOL liquid gelatin fraction superimposed on the rigid ^{13}C gel spectrum (see Figure 5-1 (d-f); T = 70°C and Figure 5-2 (c-e), for example). The liquid gelatin component, which is observed in the two-phase region through the use of the simple spin-echo, arises due to the incorporation of cholesterol into the cerebroside bilayer (*vide infra*). The incorporation of steroid disrupts the highly-ordered, two-dimensional lattice of the cerebroside bilayer, allowing axial diffusion of the cerebroside molecules which leads to the fast limit, motionally averaged, axially symmetric ^{13}C powder patterns (see Figure 5-2b). The appearance of the rotationally averaged spectral component for all cholesterol-containing mixtures at T ≥ 60°C

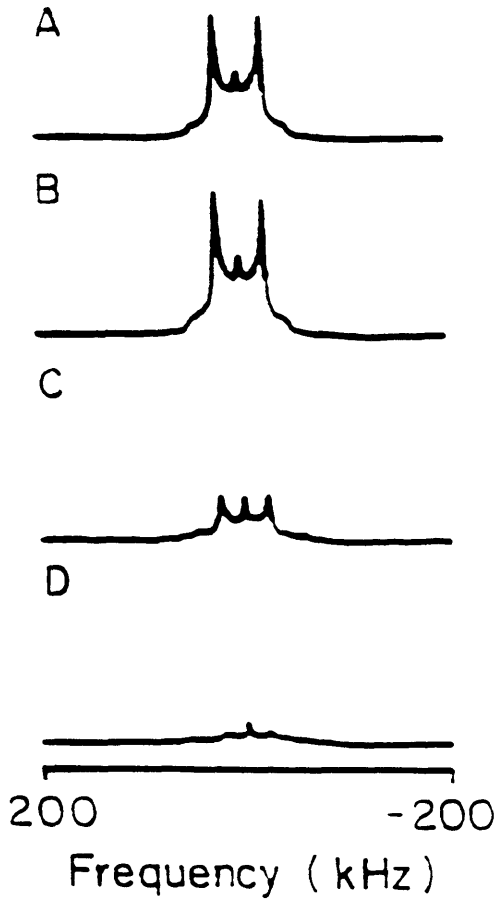

Figure 5-8. ^{2}H-NMR spectra of cerebroside/3α-$^{2}H_{1}$-CHOL (50/50 mol ratio) dispersion upon cooling from 66°C: (a) 66, (b) 56, (c) 46, and (d) 41°C, respectively.

corresponds to the occurrence of Transition I, as described in detail in a calorimetric study of NPGS/CHOL dispersions (Ruocco and Shipley, 1984).

At temperatures beyond Transition II for each mixture, a single component, axially symmetric ^{13}C powder pattern is observed. There are two interesting features to note concerning the spectra shown in Figure 5-1 (a-f), T = 86°C, and Figure 5-2. First, the spectra are not collapsed narrow lines as described for *sn*-2[1-^{13}C]acyl-labeled phospholipids studied to date (see Wittebort et al., 1981; 1982; Blume et al., 1982a, b; Blume and Griffin, 1982; Lewis et al., 1984). In the case of DPPE, DMPC, DSPC, MPPC and MSPC narrow *sn*-2 ^{13}C=O spectra characteristic of the melted L_α-bilayer phase are observed. This narrow spectrum has been discussed in detail and shown to result from rapid long axis diffusion of a carbonyl tensor which has its unique axis, $\sigma_{||}$, oriented at or near the "magic angle" (η = 54.7°C) with respect to the axis of motional averaging (i.e. the molecular long axis) (Wittebort et al., 1981; 1982). Since the ^{13}C and ^{2}H spectra of [1-^{13}C]NPGS/CHOL bilayers are in the fast limit regime (see above and below), the breadth of the powder pattern depends on the orientation of the carbonyl group with respect to the molecular long axis. Secondly, the breadth of the melted LG and/or LC single component spectra (Figure 5-1 (a-f), T = 86°C, and Figure 5-4) varies between ~5 and ~10 ppm as a function of temperature and cholesterol concentration, respectively. Again, because fast limit spectra are observed, the variation of the LC CSA with temperature and composition results primarily from minor changes in orientation of the amide carbonyl group. Spectral broadening of the ^{13}C=O spectrum has also been observed for phospholipid/CHOL LG/LC bilayer phases (Wittebort et al., 1982), although not to the extent observed for cerebroside/CHOL bilayers.

The conformation space of the amide carbonyl group of palmitoylcerebroside in the liquid crystal bilayer phase can be determined from the expression for rapid rotational averaging of the chemical shielding tensor. The breadth of a motionally averaged tensor, $\Delta\sigma^R$, is calculated using

$$\Delta\sigma^R = \left[\sigma_{33} - \frac{1}{2}(\sigma_{11}+\sigma_{22})\right]\left[\frac{1}{2}\left(3\cos^2\beta-1\right)\right] + \frac{3}{4}(\sigma_{11}-\sigma_{22})\sin^2\beta\cos 2\alpha \qquad (5\text{-}1)$$

where σ_{ii} values are the rigid lattice tensor elements, and α and β are Euler angles which specify the tensor orientation relative to the director (i.e. the axis about which the motional averaging occurs). Note that α and β correspond to the azimuthal and polar angles, respectively. For an axially symmetric rigid lattice tensor, the second term in Eq.(1) vanishes and therefore a measurement of $\Delta\sigma^R$ leads to a single value of β. However, for an axially asymmetric rigid lattice tensor, a given $\Delta\sigma^R$ will be consistent with a range of Euler angles α and β. Nevertheless, it is possible to exclude a large range of orientations. The conformation space for NPGS in the absence and presence of cholesterol in liquid crystal bilayers was calculated by assuming that the principal axes of the chemical shift tensor of the amide carbonyl have the same orientations as found in the dipeptide crystal, GlyGly·HCl·H_2O (Stark et al., 1983). The principal component, σ_{33}, is orthogonal to the amide plane in which the coplanar principal components σ_{22} and σ_{11} form angles of 13° and 77° to the C=O bond, respectively (see Figure 5-9a). Using the principal values of the rigid lattice chemical shift tensor obtained from [1-^{13}C]NPGS, the $\Delta\sigma^R$ (see Figure 5-4) has been calculated by co-varying the Euler angles α and β. The range of α's and β's which yield the experimental chemical shift anisotropy are listed in Table 1 for pure NPGS and equimolar NPGS/CHOL liquid crystal bilayers at T = 73°C and 86°C. Although β is constrained to a relatively narrow range of angles ($\leq 20°$) the value of α is considerably less restricted. This type of behavior has been observed previously (Skarjune and Oldfield, 1979; 1982).

For pure NPGS liquid crystal bilayers, β ranges from 38° to 55° (Table 1). Because β is analogous to the polar angle, θ, the results indicate that σ_{33}, the principal tensor component orthogonal to the amide plane, is between 38° and 55° from the director axis at T = 86°C. Assuming the director axis is coincident with the molecular long (chain) axis and, furthermore, that this axis is orthogonal to the bilayer interface in the

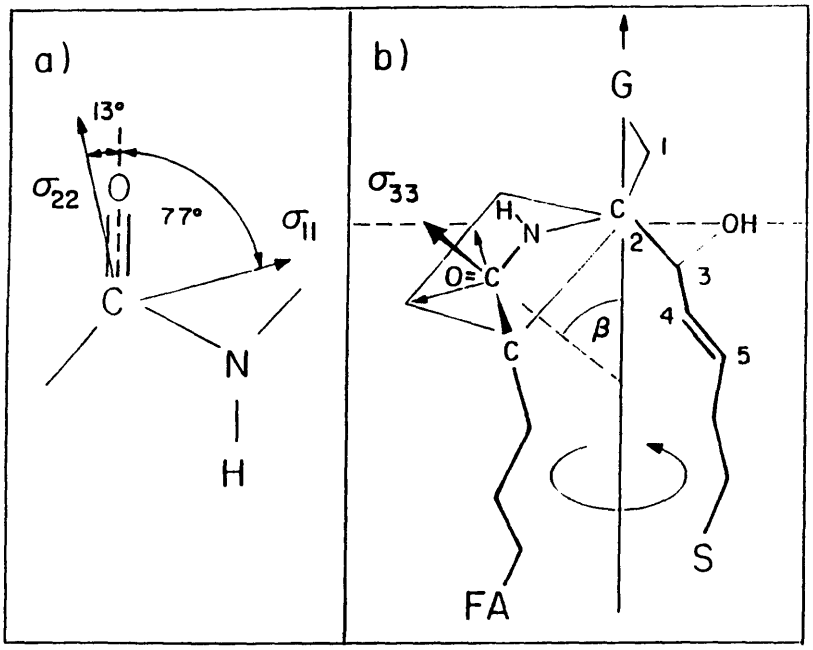

Figure 5-9. (a) Orientation of principal components of C=O chemical shielding tensor in amide group of Gly·Gly·HCl·H_2O (from Stark et al., 1983). Note σ_{33} is orthogonal to the amide plane. (b) Proposed conformation of amide group in palmitoylcerebroside. Principal components of chemical shielding tensor are shown in amide plane. The amide plane contains carbon-2 of both the sphingosine base and acyl chain. The angle β is described in the text. G = galactose headgroup, F = acyl chain, S = sphingosine base. Bilayer interfacial plane (dashed line) is shown normal to the molecular long axis (arrow). Sphingoid chain carbons are numbered.

TABLE 1

Chemical Shift Anisotropy of Axially Symmetric Powder Patterns for NPGS/CHOL L_α-Bilayers at the Indicated Temperatures.

	0 Mol % CHOL		50 Mol % CHOL	
T(°C)	**$\Delta\sigma$ (ppm)**	**β (degrees)**	**$\Delta\sigma$ (ppm)**	**β (degrees)**
73	34.3	$37 \leq \beta \leq 53$	45.2	$34 \leq \beta \leq 47$
86	29.3	$38 \leq \beta \leq 55$	38.5	$36 \leq \beta \leq 51$

L_α-phase (Tardieu et al., 1973; Luzzati and Tardieu, 1974), the average conformation shown in Figure 5-9b is proposed. The striking feature of this conformation is that the amide plane lies at an inclination to the bilayer interface rather than parallel to the surface. This inclination is between 35° and 52° with respect to the bilayer surface. Interestingly, the amide plane in the crystal structure of hydroxystearoylcerebroside (Pascher and Sundell, 1977) is inclined at 58° with respect to the director axis. The director in the crystallized form of cerebroside is described by a line parallel to the acyl and sphingoid chains and intersects carbon-2 of the sphingosine base. The bilayer interfacial plane is orthogonal to this axis. The greater inclination of the amide plane in the crystal form of hydroxystearoylcerebroside may be explained by the tighter intermolecular packing achieved in the crystal and/or the presence of the α-hydroxyl group of the acyl chain (see Pascher and Sundell, 1977). In either case, it is likely that the expanded in-plane lattice achieved in hydrated cerebroside bilayers is accommodated by moving the amide plane toward the bilayer surface (i.e. decreasing the angle of inclination). This conformational alteration would be consistent with the range of β's describing the conformation space of the L_α-phase.

The good agreement between the orientation of the amide plane relative to the bilayer interface for the L_α-bilayers and the crystal structure of cerebroside may suggest that the overall crystallographic conformation at the bilayer interface is preserved to a large degree in hydrated bilayers (Hamilton et. al., 1993). If this assumption holds true, then a second interesting structural feature shown in Figure 5-9b should be remarked upon. That is, the plane describing the initial segment of the sphingosine base between carbon-1 and carbon-5 would lie roughly orthogonal to the amide plane such that the hydroxyl group on carbon-3 orients toward the hydrated interface. Such an orientation favors intra- and intermolecular associations (e.g. hydrogen bonding) between adjacent amide groups, hydroxyl groups of the galactose and sphingosine moieties and interfacial water. To unequivocally determine the average orientation of the (C-3)-OH group rela-

tive to the bilayer interface, similar solid state ^{13}C-NMR methodology may be employed on cerebroside bilayers in which the carbon-3 of sphingosine is isotopically labeled.

Table 1 indicates that the average orientation of the amide plane in L_α-bilayers varies slightly as the temperature is increased from 73° to 86°C. Although the change in $\Delta\sigma^R$ is small, as cholesterol concentration is increased from 0 to 50 mol %, the observed changes are evidence for the molecular interaction of cholesterol with cerebroside affecting the orientation of the amide linkage. X-ray diffraction studies show an increased bilayer periodicity as a function of cholesterol concentration at 86°C. Such a structural change at constant hydration (70 wt% H_2O) is observed as a result of the "condensation" effect, which is imparted by the sterol to lipid bilayers (Lecuyer and Dervichian, 1969) and may be consistent with molecular interaction between cerebroside and cholesterol at the amide groups, which results in a small conformational change of the carbonyl group at the interface.

5.4b ^2H Spectra of NPGS/CHOL Mixtures

The most distinctive features of the ^2H spectra of the NPGS/CHOL mixtures are the two clearly distinguishable spectral components observed at $T \geq 50°C$, indicating that exchange between the gel and liquid crystal phases is slow. Furthermore, the loss of spectral intensity is less than 20% over the entire temperature range (20°C to 86°C) in which two transitions, each involving equilibrium between two lipid phases, are present. Significant spectral intensity losses are expected for intermediate exchange rates and have been observed in small molecules (Beshah et al., 1986) and when exchange occurs between two lipid phases (Skarjune and Oldfield, 1979; 1982; Wittebort et al., 1981; Blume and Griffin, 1982; Ruocco et al., 1985a, b). The distinct, sharp spectral features of the ^2H spectra presented here are to be contrasted with the broadened two-component ^2H spectra observed for chain-labeled lecithins in the pre-transition region (D.J. Siminovitch, S.K. Das Gupta, and R.G. Griffin, unpublished results) and 2-[4'4'-$^2H_2$]DPPE/CHOL dispersions (Blume and Griffin, 1982). In these cases, the lateral diffusion constants are high

and the domain sizes are small, leading to intermediate exchange spectra. Spectra of NPGS/CHOL mixtures are more similar to spectra of DPPE/DPPC mixtures, which show a clear superposition of gel and liquid crystal spectra in the two-phase regime (Blume et al., 1982b). Observation of the slow exchange ^2H spectra is not surprising, however, because X-ray diffraction data indicate two separate lipid phases coexist at these temperatures: a melted NPGS/CHOL bilayer phase and an NPGS gel bilayer phase (Ruocco and Shipley, 1984). Therefore, molecular exchange between these three-dimensionally distinct phases is expected to be slow on the ^2H-NMR time scales ($\tau_c > 10^{-5}$ sec).

The slow exchange between the lipid phases at $50°C \leq T \leq 75°C$ facilitates the interpretation of these composite spectra. The ^2H spectra for chain-labeled NPGS bilayers are distinct from phospholipid spectra in that the lineshapes can be simulated using a *trans-gauche* chain isomerization hopping model (Huang et al., 1980) at temperatures below the high enthalpy (17.5 kcal/mol NPGS) transition at 82°C (Ruocco et al., 1981). Above this transition, the axially symmetric fast limit spectrum can be simulated using a nine-site jump model which includes three chain isomerization sites (*trans*, (±)-*gauche*) upon which a three-site large amplitude long axis hopping motion is superimposed (Siminovitch et al., 1985). A combination of these two motional models, one for a gel bilayer phase, the other for a melted bilayer phase, is used to describe the experimental spectra observed for the NPGS/CHOL dispersions. Representative simulations are shown in Figure 5-10 (right) along with the experimental lineshapes (left) for an NPGS/CHOL dispersion containing 30 mol % CHOL. At 20°C the ^2H spectrum is simulated using a three-site (chain isomerization) hopping model where the three sites corresponding to *trans*, (+)-*gauche* and (-)-*gauche* conformations are assigned to three lattice sites of a tetrahedron as described by Siminovitch et al. (1985). The input parameters used for the simulation are listed in the caption of Figure 5-10. Note that there is no axial hop imposed for this simulated lineshape. The good spectral fit would be expected since cholesterol forms a separate lamellar phase independent of the cerebroside gel at this

Figure 5-10. ^{2}H-NMR spectra of a dispersion of [7,7-$^2H_2$]NPGS containing 30 mol % CHOL as a function of temperature. (Right) Lineshape simulations obtained by an appropriately weighted summation (see Figure 5-11) of an axially asymmetric gel spectral component at given temperature with an axially symmetric melted spectral component.

Gel Spectral Parameters:

(20°C) P_1=0.74, P_2=0.23, P_3=0.03

R_{12}=2.7 x 10^6 s^{-1}, R_{13}=3.2 x 10^5 s^{-1};

(30°C) P_1=0.70, P_2=0.27, P_3=0.03;

R_{12}=4.0 x 10^6 s^{-1}, R_{13}=3.2 x 10^5 s^{-1};

(50°C) P_1=0.64, P_2=0.30, P_3=0.06;

R_{12}=6.3 x 10^6 s^{-1}, R_{13}=3.2 x 10^5 s^{-1};

where R_{12} and R_{13} are the exchange rates between Sites 1 and 2 and Sites 1 and 3, respectively.

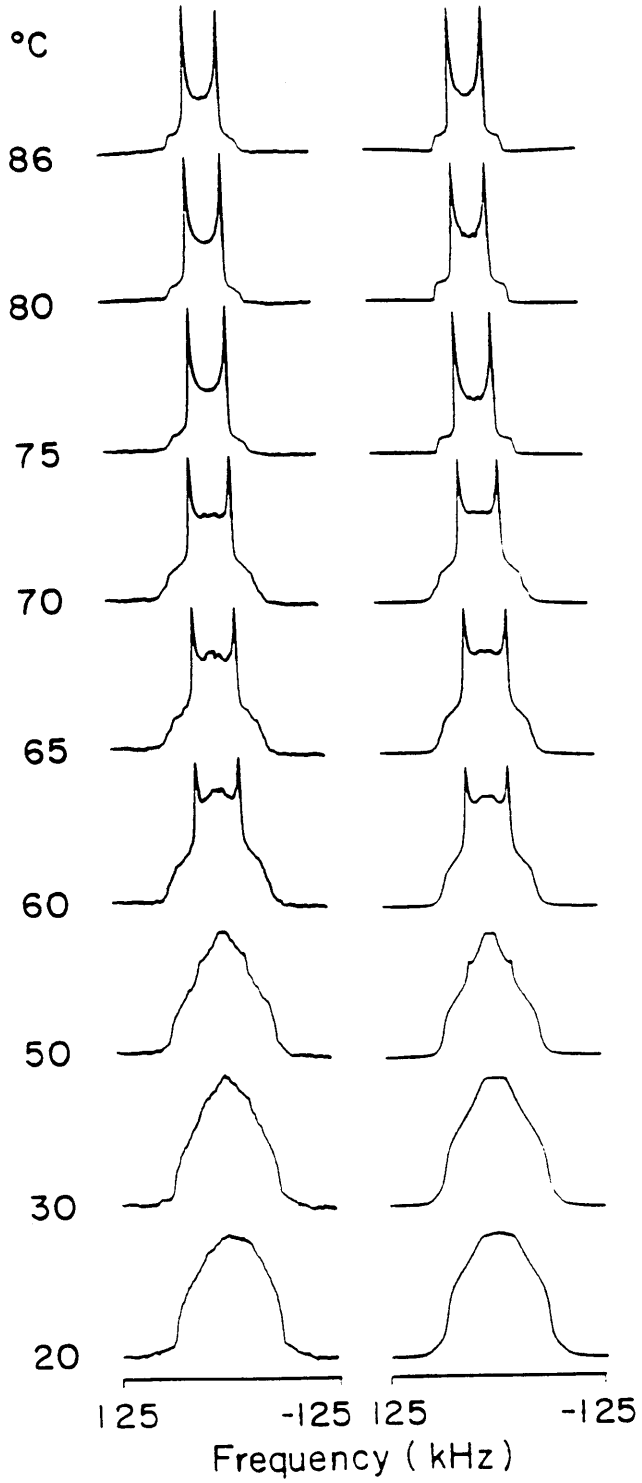
°C
86
80
75
70
65
60
50
30
20
125
-125
125
-125
Frequency (kHz)

temperature (Ruocco and Shipley, 1984), making the simulation analogous to a chain-labeled cerebroside spectral simulation (Huang et al., 1980). Corrections for power roll-off (Bloom et al., 1980) and distortions due to use of the quadrupole echo (Spiess and Sillescu, 1981) are included in performing the simulations. At higher temperatures (see spectra at T = 30°C and 50°C), narrowing of the top of the spectrum can be accounted for by a relative increase in both the (±) - *gauche* conformations and exchange rates between the conformations (see caption in Figure 5-10). At 50°C, however, the hint of a second, sharply defined component arises which can be simulated by using the nine-site jump model, which imposes fast limit long axis rotation (Siminovitch et al., 1985). For the spectral lineshape at 50°C, approximately 5% of the spectral lineshape is attributed to an LG bilayer phase. The quadrupole splitting in the 50°C ≤ T ≤ 65°C range is relatively constant for this phase regardless of the original stoichiometric ratio of NPGS and CHOL. The significance of this observation will be discussed below. At high temperatures (i.e. T > 50°C) the fraction of the LG component progressively increases (see T = 60°C, 65°C and 70°C in Figure 5-10) until a single, fast limit, axially symmetric powder pattern is observed at 86°C. The fidelity with which the experimental lineshapes are simulated is particularly encouraging for the models employed.

Simulation of the ^2H spectra shown in Figures 5-5 and 5-10, as described above, permits a determination of the fraction of the melted bilayer component over the entire temperature range. These results are summarized in Figure 5-11 where the melted lipid fraction, f_m, is plotted as a function of temperature. For greater clarity and in order to interpret these spectral data in terms of the reported thermal behavior of NPGS/CHOL dispersions (Ruocco and Shipley, 1984), an idealized DSC trace representative of NPGS/CHOL mixtures containing < 50 mol % CHOL is drawn to the temperature scale in Figure 5-11.

For the equimolar NPGS/CHOL dispersion a cooperative order-disorder transition (Transition I) centered at approximately 56°C is observed. The presence of a relatively

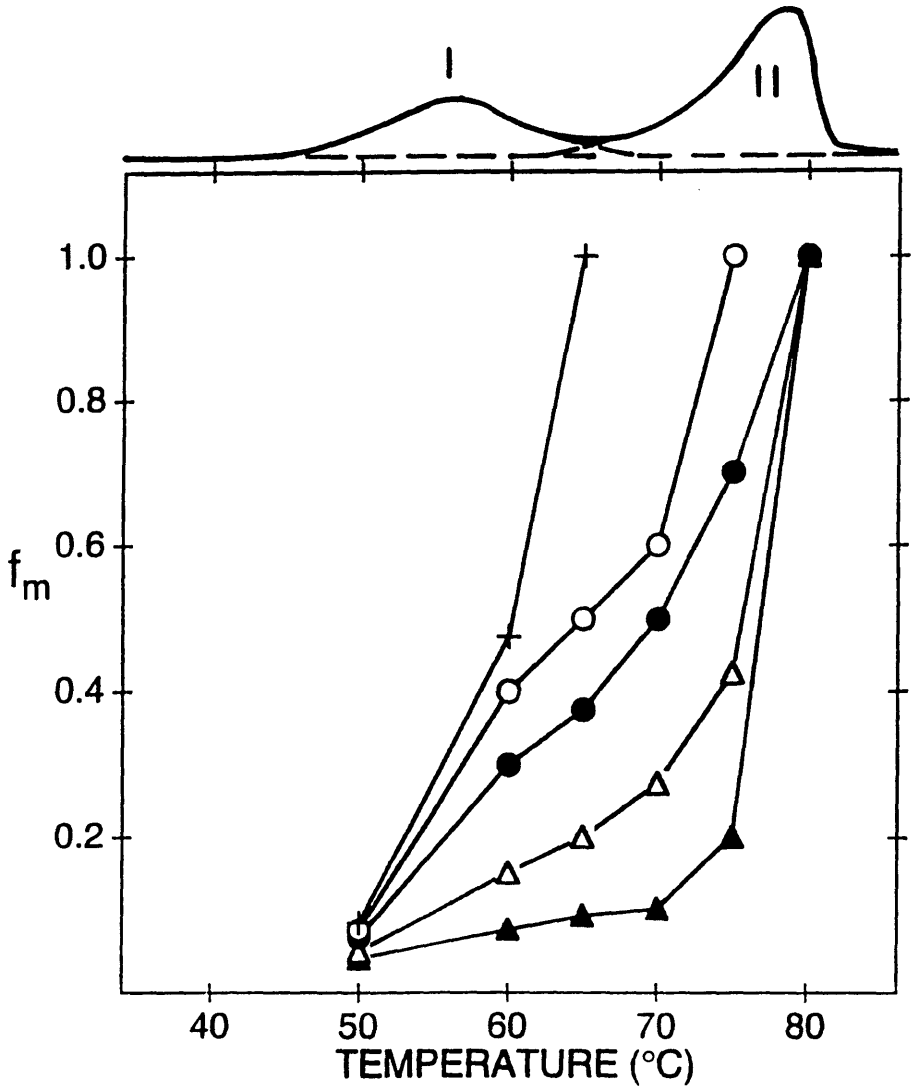

Figure 5-11. Fraction of melted lipid, f_m, obtained from lineshape simulations of the ^2H-NMR spectra in Figure 5-5 vs. temperature: (▲) 10, (Δ) 20, (●) 30, (O) 40, and (+) 50 mol % CHOL, respectively. Representative DSC traces are scaled to the temperature axis for NPGS/CHOL dispersions containing (a) 50 mol % CHOL and (b) < 50 mol % CHOL (also, see Ruocco and Shipley, 1984).

cooperative transition for equimolar cerebroside/CHOL dispersion is in contradistinction to the relatively low cooperative transition for equimolar phospholipid/CHOL dispersions (Huang et al., 1993). The nature of this transition can be better understood in light of the ^2H spectra observed for both [7,7-$^2H_2$]NPGS and 3α-$^2H_1$-CHOL in NPGS/CHOL dispersions (see Figures 5-5, 5-7 and 5-8). ^2H spectra of 3α-$^2H_1$-CHOL, which exists in a rigid, highly ordered lamellar monohydrate crystal form (Loomis et al., 1979) at 20°C, indicate that the sterol is gradually incorporated into a more mobile lattice (i.e. the NPGS LG bilayer) as the temperature is increased over the 20°C to 53°C temperature range. Here one observes the motionally averaged ^2H spectrum characteristic of the LG phase. Interestingly, the intercalation of cholesterol into the NPGS bilayer lattice begins at temperatures below or slightly into the relatively cooperative Transition I observed by DSC. Thus, the NMR experiment appears to report the presence of this transition before it appears in the DSC trace. A similar behavior was observed in ^{13}C-NMR studies of the pretransition in PC's (Wittebort et al., 1981). This suggests that the enthalpy of Transition I is partially associated with the incorporation of cholesterol into the cerebroside bilayer. Moreover, the [7,7-$^2H_2$]NPGS and the [^{13}C=O]NPGS spectra show an axially symmetric component in this temperature range, indicating that the NPGS molecule is also beginning to execute axial diffusion. With increasing temperature the gel-like component in these spectra decreases in intensity and the lineshape transforms to an axially symmetric component characteristic of an LG phase. Note that at 50% CHOL the chains do not significantly disorder with increasing temperature and thus the enthalpy of Transition I (ΔH ~9 kcal/mole) must be associated with the onset of axial diffusion. Thus, the NMR data permit a microscopic interpretation of the endotherm observed in the DSC experiment.

At lower cholesterol concentrations the low temperature Transition I is also observed. The proportion of melted cerebroside component at temperatures immediately above Transition I indicate a fractional melted component similar to the molar percentage

of cholesterol added to the original dispersion (Figure 5-11). It is known from X-ray diffraction studies over the 0.6 to 50 mol % CHOL concentration range at 66°C, a temperature just above Transition I, that cholesterol monohydrate reflections are no longer observed, indicating that all cholesterol present has been incorporated into the NPGS bilayers. Based on the fraction of melted component in Figure 5-11 and the discussion above, one can conclude that cholesterol intercalates into the NPGS bilayer forming a LG phase bilayer with NPGS/CHOL in a 1:1 stoichiometry above transition I. The similarity of the residual quadrupole splitting for NPGS/CHOL dispersions containing 10 to 40 mol % CHOL at temperatures in the region of Transition I (50°C ≤ T ≤ 65°C) with the quadrupole splitting of the equimolar NPGS/CHOL dispersions is consistent with the existence of an equimolar NPGS/CHOL bilayer phase for these NPGS/CHOL mixtures (see Figures 5-6a and 5-6b). This is in contrast to the change in quadrupolar splitting observed on addition of cholesterol in DPPC/Chol systems (see Figure 5-6, Huang et. al. 1993).

The LG phase equimolar NPGS/CHOL bilayers coexist with an unmelted NPGS gel bilayer in NPGS/CHOL mixtures containing < 50 mole % CHOL at temperatures intermediate to Transitions I and II. This bilayer phase gives rise to the axially asymmetric ^2H spectrum in the two component experimental lineshapes at T_c (Transition I) ≤ T ≤ T_c (Transition II) (see T = 60°C, 70°C in Figures 5-5c - 5-5e, for example). Transition II which is associated with the pure NPGS gel → liquid crystal transition is asymmetrically skewed to lower temperatures in the presence of cholesterol. As this pure NPGS gel fraction melts at temperatures > 65°C, the quadrupolar splitting decreases in a divergent manner depending on the original cholesterol concentrations in the dispersions. This divergence occurs as the residual NPGS is incorporated into the pre-existing LG NPGS/CHOL bilayer phase (Figure 5-6a). Thus, the quadrupolar splitting is modulated by both temperature (see $\Delta\nu_Q$ for 50 mol % CHOL dispersion in Figure 5-6a) and cholesterol concentration (see Figure 5-6b).

5.5 Conclusions

Although the NPGS/CHOL binary lipid system is complex, an understanding of the thermal, structural and dynamic features of the system is an important first step to understanding the physical properties and function of myelin. First, it should be recognized that cholesterol and cerebroside form the major proportion of lipid in the extracytoplasmic monolayer of the myelin sheath (Norton and Cammer, 1984; Norton, 1981). Although NPGS is not the major type of cerebroside in myelin, it is nevertheless the best characterized by a number of biophysical techniques; therefore, it is the most likely candidate to further understanding of the molecular interaction between cholesterol and cerebroside at the present time. The ^{13}C- and ^{2}H-NMR experiments described here have elucidated a number of features of the phase behavior, structure and dynamics of this system.

The ^{13}C=O spectra of the gel state show the rigid lattice behavior of the lipid in this phase, but with increasing CHOL concentration and temperature, long axis diffusion initiates and the spectrum narrows. A comparison of spectra obtained with cross-polarization and a Bloch decay clearly shows the coexistence of gel and liquid crystalline-like phases. Above T_c the width of the ^{13} C spectrum can be used to determine the average orientation of the amide C=O and to a good approximation the conformation is that found in crystals. However the observed temperature and CHOL concentration dependence indicate that this conformation changes slightly with these variables.

^{2}H spectra of 7,7-NPGS/CHOL mixtures share certain features with the ^{13}C=O spectra. In particular, over a rather large range of temperatures and CHOL concentrations the spectra can be accurately simulated with a simple superposition of gel and liquid gelatin phase spectra. This indicates that exchange between these two types of lipid phases is slow on the ^{2}H-NMR time scale, probably either because the domains are large and/or the lateral diffusion constants in the gel state domain is very slow. In addition, the ^{2}H spectra show that the liquid gelatin component disorders to form a component with ^{2}H

spectra similar to those observed in liquid crystalline phases. Spectra of 3α-$^{2}H_{2}$-CHOL indicate the presence of a rigid lattice CHOL molecule which converts to a diffusing molecule at higher temperatures as it becomes part of the NPGS bilayer. The observation of these changes in the ^{13}C and ^{2}H spectra correlate well with the DSC results and provide a microscopic picture of the changes which occur at the thermal transition.

References

Abraham, W., and D.T. Downing. 1991. *Biochim. Biophys. Acta* 1068:189-194.

Abrahamsson, S., I. Pascher, K. Larsson, and K.-A. Karlsson. 1972. *Chem. Phys. Lipids* 8:152-179.

Barenholtz, Y., E. Freire, T.E. Thompson, M.C. Correa-Freire, D. Bach, and I.R. Miller. 1983. *Biochem.* 22:3497-3501.

Beshah, K., E.T. Olejniczak, and R.G. Griffin. 1987. *J. Chem. Phys.* 86:4730-4736.

Blume, A., D.M. Rice, R.J. Wittebort, and R.G. Griffin. 1982a. *Biochem.* 21:6220-6230.

Blume, A. and R.G. Griffin. 1982. *Biochem.* 21:6230-6242.

Blume, A., R.J. Wittebort, S.K. Das Gupta, and R.G. Griffin. 1982b. *Biochem.* 21:6243-6253.

Bloom, M., J.H. Davis, and M.I. Valic. 1980. *Can. J. Phys.* 58:1510-1517.

Bologa-Sandru, L., B. Zalc, N. Herschkowitz, and N. Baumann. 1981. *Brain Res.* 225:425-430.

Bonmatin, J.-M., I.C.P. Smith, H.C. Jarrell, and D. J. Siminovitch. 1990. *J. Am. Chem. Soc.* 112:1697-1704.

Clowes, A.W., R.J. Cherry, and D. Chapman. 1971. *Biochim. Biophys. Acta* 249:301-317.

Curatolo, W.. 1983. *Biochemistry* 21:1761-1764.

Das Gupta, S.K., D.M. Rice, and R.G. Griffin. 1982. *J. Lipid Res.* 23:197-200.

Fieser, L.F. 1983. *Organic Syntheses, Collect. 4* pp. 195-201, Wiley, New York.

Florio, E., H.C. Jarrell, D.B. Fenske, K.R. Barber, and C.W.M. Grant. 1990. *Biochim.Biophy. Acta* 1025:157-163.

Griffin, R.G. 1981. *Methods Enzymol.* 72:108-174.

Hamilton, K.S., H.C. Jarrell, K.M. Brière, and C.W.M. Grant. 1993. *Biochem.* 32.4022-4028.

Huang, T.H., R.P. Skarjune, R.J. Wittebort, R.G. Griffin, and E. Oldfield. 1980. *J. Am. Chem. Soc.* 102:7377-7379.

Huang, T.H., C.W.B. Lee, S.K. Das Gupta, A. Blume, and R.G. Griffin. 1993. *Biochem.* 32:13277-13287.

Jackson, M., D.S. Johnston, and D. Chapman. 1988. *Biochim. Biophys. Acta* 944:497-506.

Johnston, D.S. and D. Chapman. 1988. *Biochim. Biophys. Acta* 939:603-614.

Ladbrooke, B.D., T.J. Jenkinson, V.B. Kamat, and D. Chapman. 1968. *Biochim. Biophys. Acta* 164:101-109.

Lecuyer, H. and D.G. Dervichian. 1969. *J. Mol. Biol.* 45:39-57.

Lewis, B.A., S.K. Das Gupta, and R.G. Griffin. 1984. *Biochem.* 23:1988-1993.

Linington, C. and M.G. Rumsby. 1981. *Neurochem. Int.* 3:211-218.

Loomis, C.R., G.G. Shipley, and D.M. Small. 1979. *J. Lipid Res.* 20:525-535.

Luzzati, V. and A. Tardieu. 1974. *Ann. Rev. Phys. Chem.* 25:79-94.

Norton, W.T. 1981. *Adv. in Neurology* 31:93-121.

Norton, W.T. and W. Cammer. 1984. in *Myelin* (P. Morell, ed.). Plenum Press,New York. 147-195.

Pascher, I. and S. Sundell. 1977. *Chem. Phys. Lipids* 20:175-191.

Pines, A., M.G. Gibby, and J.S. Waugh. 1973. *J. Chem. Phys.* 59:569-590.

Poss, A., C. Vancraenbroeck, C. Berliner, and J.M. Ruysschaert. 1979. *J. Coll. Interface Sci.* 70:124-129.

Quinn, P.J. and W.R. Sherman. 1971. *Biochim. Biophys. Acta* 233:734-752.

Radin, N.S. 1972. *Methods Enzymol.* 28:300-306.

Rosenfeld, R.S., D.K. Fukushima, L. Hellman, and T.F. Gallagher. 1954. *J. Biol. Chem.* 211:301-311.

Ruocco, M.J., D. Atkinson, D.M. Small, R.P. Skarjune, E. Oldfield, and G.G. Shipley. 1981. *Biochem.* 20:5957-5966.

Ruocco, M.J., G.G. Shipley, and E. Oldfield.1983. *Biophys. J.* 43:91-101.

Ruocco, M.J. and G.G. Shipley. 1984. *Biophys. J.* 46:695-707.

Ruocco, M.J., D.J. Siminovitch, and R.G. Griffin. 1985. *Biochem.* 24:2406-2411.

Ruocco, M.J., A. Makriyannis, D.J. Siminovitch, and R.G. Griffin. 1985. *Biochem.* 24:4844-4851.

Ruocco, M.J. and G.G. Shipley. 1986. *Biochim. Biophys. Acta* 859:246-256.

Siminovitch, D.J., M.J. Ruocco, E.T. Olejniczak, S.K. Das Gupta, and R.G. Griffin. 1985. *Chem. Phys. Letters* 119:251-255.

Siminovitch, D.J., M.J. Ruocco, A. Makriyannis, and R.G. Griffin. 1987. *Biochim. Biophys. Acta* 901:191-200.

Skarjune, R. and E. Oldfield. 1979a. *Biochim. Biophys. Acta* 556:208-218.

Skarjune, R. and E. Oldfield. 1979b. *Biochem.* 18:5903-5909.

Skarjune, R. and E. Oldfield. 1982. *Biochem.* 21:3154-3160.

Spiess, H.W. and H. Sillescu. 1981. *J. Magn. Reson.* 42:381-389.

Stark, R.E., L.W. Jelinski, D.J. Ruben, D.A. Torchia, and R.G. Griffin. 1983. *J. Magn. Reson.* 55:266-273.

Suzuki, T., H. Utsumi, K. Inoue, and S. Nojima. 1981. *Biochim. Biophys. Acta* 644:183-191.

Tardieu, A., V. Luzzati, and F.C. Reman. 1973. *J. Mol. Biol.* 75:711-733.

Vist, M.R. and J.H. Davis. 1990. *Biochem.* 29:451-464.

Wiedmann, T.S. and A. Salmon. 1991. *Lipids* 26:364-368.

Wittebort, R.J., C.F. Schmidt, and R.G. Griffin. 1981. *Biochem.* 20:4223-4228.

Wittebort, R.J., A. Blume, T.H. Huang, S.K. Das Gupta, and R.G. Griffin. 1982. *Biochem.* 21:3487-3502.

6. Secondary Structure and Dynamics in Helical Peptides

For many years, the α-helix has been recognized as the most prevalent secondary structure found in proteins. A quick survey of the literature shows that proteins with widely varying roles and environments--everything from hemoglobin and BPTI to bacteriorhodopsin--rely on α–helices to provide a framework to which the active sites of the protein are attached (Voet & Voet, 1990). Until recently, however, short peptide sequences were thought to be incapable of forming measurable amounts of α–helical structure in water. Extensive host-guest experiments combined with Zimm-Bragg helix-coil transition theory predicted that peptides less than 20 residues in length would not exhibit appreciable amounts of helical structure in water (Shoemaker et al., 1985). However there exist exceptions in which short peptides, such as the C- and S- fragments of ribonuclease A, do form helices in water (Brown & Klee, 1971). It was originally hypothesized that this was made possible by salt bridges formed between various side chains in the peptides (Bierzynski et al., 1982), but a model compound study designed to prove this point ultimately showed that instead it was possible to form helices with short peptides containing only alanine and a charged amino acid (to make the peptide water-soluble) (Marqusee et al., 1989). Several theoretical treatments of how this is possible have since been advanced, but they have been further complicated by the recent indication that some of these peptides might actually be forming 3_{10}-helices (Miick et al., 1992). This has led to further revisions of Zimm-Bragg theory and much debate is going on in the protein-folding community as to what the actual structural composition of these systems is and the energetics of forming these structures. Several solid state NMR experiments exist which would shed some light on both the structure and dynamics of these peptides.

6.1 Structure

The problem of conducting solid state NMR experiments on peptides which form helices in water is of course trapping these transient structures in the solid state. One possible way of accomplishing this is to quickly freeze the sample so that the water does not have time to freeze in an ordered manner and disrupt the peptide interactions. The water

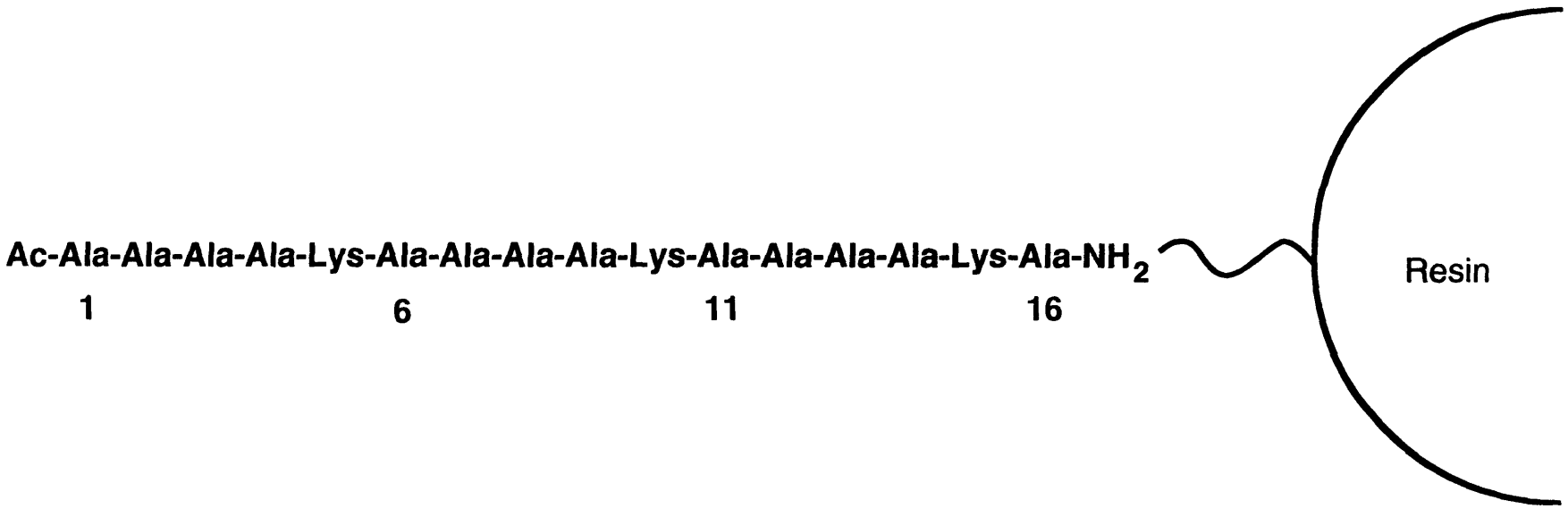

Figure 6-1. Sequence of model peptide and schematic for synthesis.

may then be removed by lyophilization. This sort of treatment has met with good success in looking at various lipid and proteins and as well as peptides which form fibrils. However, whether this approach would prove successful with simple peptides forming transient helical structure in water is open to debate. Thus the first aim of this project was to obtain samples suitable for solid state NMR and determine whether after sample preparation they retained their secondary structure.

6.1.a Chemical Shift Experiments

The simplest way to determine whether a peptide is helical or not is to take a chemical shift spectrum. Polycrystalline peptides in the solid state exhibit specific carbon chemical shifts which are dependent on their secondary structure (Saito et al., 1983). The C-α, C-β, and C=O resonances show resolvable changes in chemical shift on going from β-sheet to α-helix or 3_{10}-helix. The α-carbons are shifted downfield by 4.2 ppm from between 48 and 49 to between 52 and 53 ppm. The carbonyl resonances also shift downfield, from around 172 ppm to between 176 and 177 ppm. In contrast, the β-carbons shift upfield from around 20 ppm to near 15 ppm. Figure 6-1 shows the peptide Ac-AKAAAA-KAAAAKAAAA-NH_2 (3K(II)) which has demonstrated high amounts of helical structure (Marqusee et al., 1989). Estimates of almost 80% helical content have been made for a buffered solution of 3K(II) at neutral pH and 1° C; even at high concentrations, no aggregation has been observed to account for the formation of secondary structure. A sample of this peptide was made under similar conditions and allowed to equilibrate at 0°C; it was then quickly frozen by spraying the solution into cold isopentane and subsequently lyophilized. The chemical shift spectrum is shown in Figure 6-2a. The spectrum exhibits chemical shifts which are consistent with both helical and non-helical structures. This variation may be due to a combination of peptides, some which are helical and some which are not helical. Another possibility is that to only a portion of each peptide is helical with some "fraying" of the ends. Figure 6-2b shows a spectrum obtained from a sample which was slowly frozen and then lyophilized. Surprisingly, it also shows chemicals shifts consistent

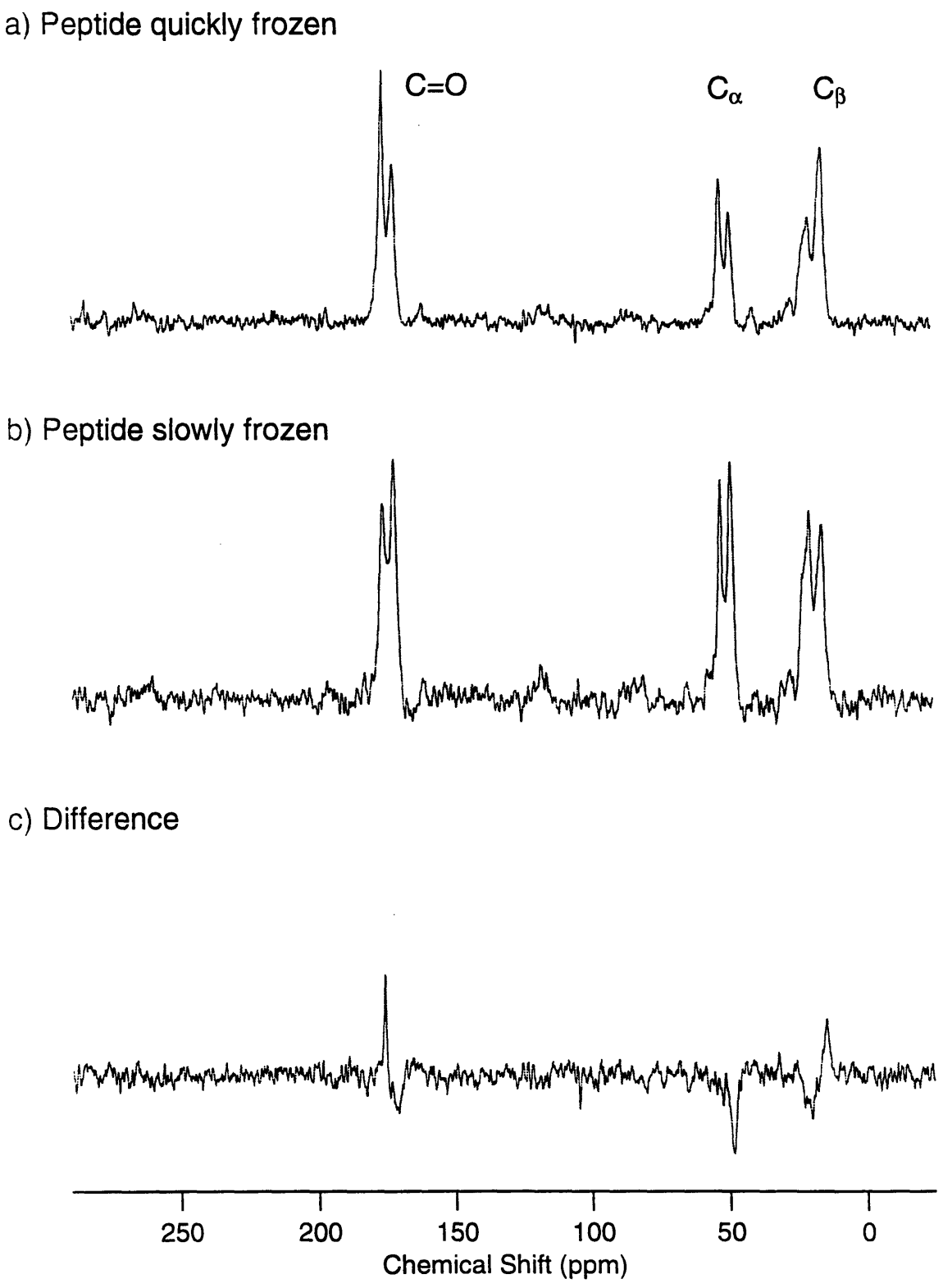

Figure 6-2 Chemical shift spectra of natural abundance peptides.

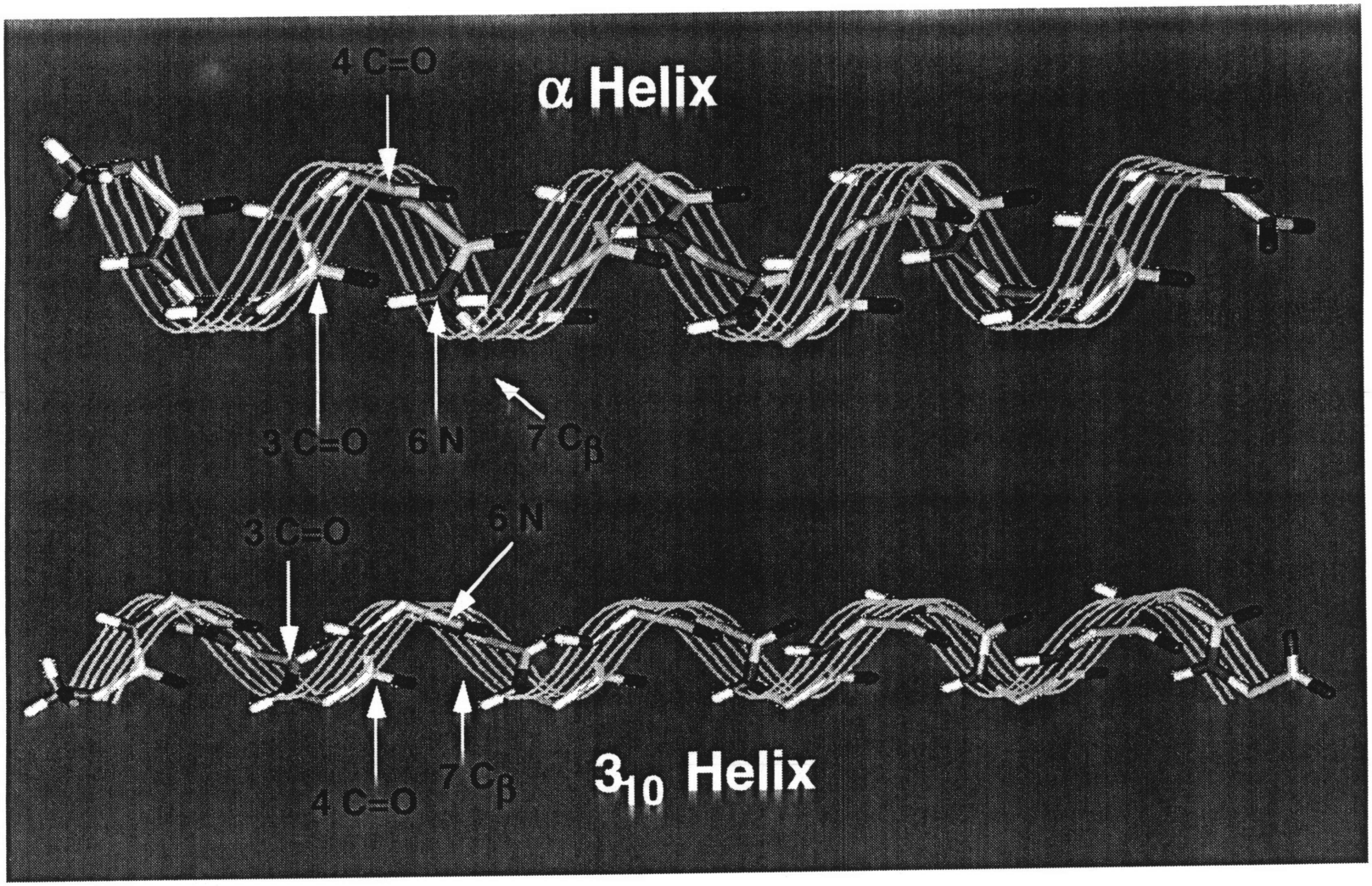

Figure 6-3. Labelling scheme for dipolar recoupling experiments

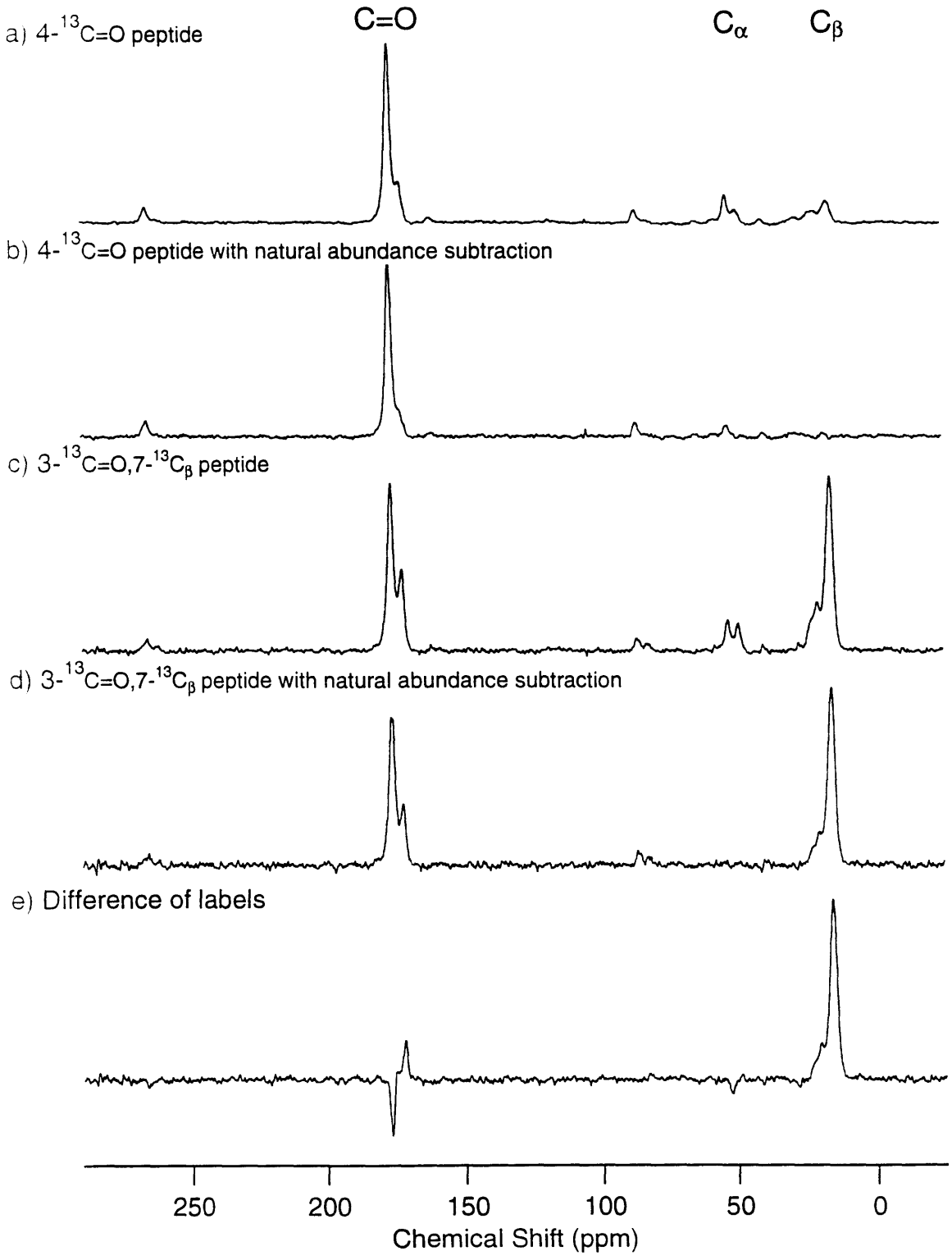
a) 4-^{13}C=O peptide
C=O
C_α
C_β
b) 4-^{13}C=O peptide with natural abundance subtraction
c) 3-^{13}C=O,7-$^{13}C_\beta$ peptide
d) 3-^{13}C=O,7-$^{13}C_\beta$ peptide with natural abundance subtraction
e) Difference of labels
250
200
150
100
50
0
Chemical Shift (ppm)

with some degree of helix formation, although their intensity is somewhat less than that seen in the sample that was frozen quickly. In order to gain more insight into the structure of these peptides, it is possible to isotopically label various amino acids at specific sites in the peptide (Figure 6-3). A spectrum of 3K(II) labelled at the carbonyl on the fourth amino acid from the amino terminus is shown in figure 6-4a. After natural abundance subtraction (Figure 6-4b), it appears that over 85% of the peptide sample is helical at this position. This would suggest that the nonhelical resonances observed in the natural abundance spectrum are more likely due to disorder at specific amino acids in all of the peptides rather than some peptides being helical and other peptides being disordered. Figures 6-4c and 6-4d show the spectrum with and without natural abundance subtraction for a peptide with the carbonyl carbon on the third amino acid from the amino terminus being labelled and a β-carbon label on the seventh amino acid. The 3-C=O resonance shows a significant amount of disorder; a gaussian fit of the resonances shows that at this amino acid about 75% of the sample is helical while the other 25% is not. Figure 6-4e shows a subtraction of the spectrum of the 4-C=O labelled peptide from the 3-C=O, 7-C_β labelled peptide to demonstrate the increase in disorder at the 3 position. The 7-C_β resonance displays more order, but a small shoulder resulting from about 15% of the peptides not being helical exists. Based on these two samples, it appears that for the center of the peptide about 85% of the sample is helical; however at the ends, a measurable amount of fraying does occur. Further studies of peptides labelled at other positions may yield further insight into the equilibria between helix and coil structures at each of the amino acids in the peptide.

6.1.b Dipolar Recoupling Experiments

In order to determine the exact nature of the helices formed by this peptide, homo- and heteronuclear dipolar recoupling experiments such as R^2, R^2 tickling, and REDOR may be carried out to determine key distances in the peptide and provide structural constraints (Bennett et al., 1994; Griffiths & Griffin, 1993). Possible distance measurements which may be made to distinguish between α– and 3_{10}-helices are given in Table 6-1. The

atom-atom distances for:	3_{10}-helix	α-helix
(i) $^{13}C{=}O$ --> (i+2) ^{15}N	3.0 Å	3.3 Å
(i) $^{13}C{=}O$ --> (i+3) $^{13}C_\beta$	4.8	4.2

Table 6-1 Calculated distances between peptide labels.

distances listed in Table 6-1 are based on a peptide with standard bond lengths and phi, psi angles of (-65°, -40°) and (-74°, -4°) for α– and 3_{10}-helices, respectively. The values implemented for phi and psi are based on a search of the protein data bank for average values found in α– and 3_{10}-helices. (Glenn Millhauser, private communication). As indicated by the table, large differences in distance exist between key nuclei and make it possible to distinguish between the two structures.

R^2, R^2 tickling, and REDOR experiments are used to measure dipolar couplings and thus measure internuclear distances. In the high magnetic field limit, for 2 unlike spins or two spins of the same type whose dipolar coupling is smaller than their chemical shift difference, the dipolar coupling is determined by both the gyromagnetic ratios of the nuclei and the distance between them, or

$$H_D^{IS} = \frac{\gamma_I \gamma_S \hbar}{r^3}(1 - 3\cos^2\theta) I_Z S_Z \qquad (6\text{-}1)$$

where θ refers to the angle between the dipolar interaction and the magnetic field. Due to this angular dependence, the dipolar coupling would give rise to a powder pattern in a simple static NMR experiment. However, the dipolar coupling would be obscured by chemical shift anisotropies, especially for the size of couplings (<200 Hz) which are typical for the internuclear distances being measured. Magic angle spinning gets rid of the chemical shift anisotropy, but it also averages the dipolar coupling. However, the dipolar Hamiltonian may be reintroduced either through the use of rf pulses (REDOR for heteronuclear spins), or in the case of homonuclear spins through judicious choice of the sample spinning rate (R^2), or a combination of the two (R^2 tickling).

The pulse sequences for R^2, R^2 tickling, and REDOR are shown in Figure 6-5. In R^2, the sample is spun at a rate where the difference in the isotropic chemical shift frequencies between the two spins is a small integer multiple of the spinning speed. At this frequency, the energy difference between the two spins is matched, and exchange of energy between the two homonuclear spins occurs via the dipole coupling. If one of the resonances is inverted, this exchange can be monitored and the rate at which it occurs can be measured to determine the dipole coupling. In the R^2 experiment the protons are initially prepared and the polarization is then transferred to the carbons to enhance the magnetization. The magnetization is then returned to the z-axis via a carbon $\pi/2$ pulse and one resonance is selectively inverted using a long, soft pulse. Alternatively, the carrier frequency may be placed such that the two spins are offset from the center frequency in equal, but opposite directions. A delay, equal to a quarter of the offsets, introduced before the carbon $\pi/2$ pulse will result in the spins having magnetizations opposite in sign when they are shifted back to the z-axis, thus circumventing the need for selective inversion. A mixing period follows in which the two spins exchange before the magnetization is made observable by a final $\pi/2$ pulse. To first order the rate of magnetization exchange is dependent on the dipolar coupling, but it is also governed by several other parameters such as the relative orientations of the chemical shift tensors with respect to the dipolar coupling, the principle values of the chemical shift tensors, the isotropic J-couplings between the spins, and the zero-quantum relaxation time (T_2^{ZQ}). The principle values of the chemical shift tensors may be determined by measuring sideband intensities at slow spinning speeds. A number of single crystal studies on model compounds give reasonable estimates of the orientations of the chemical shift tensors; if the spinning speed matches the chemical shift difference exactly, the spinning speed is generally fast enough that the exchange is insensitive to the relative orientations. Liquid spectra yield a measure of the J-couplings. The T_2^{ZQ} may be measured using standard echo experiments. An idea of the contributions to the linewidths from T_2^{ZQ} and chemical shift dispersion may also be estimated by varying the spinning

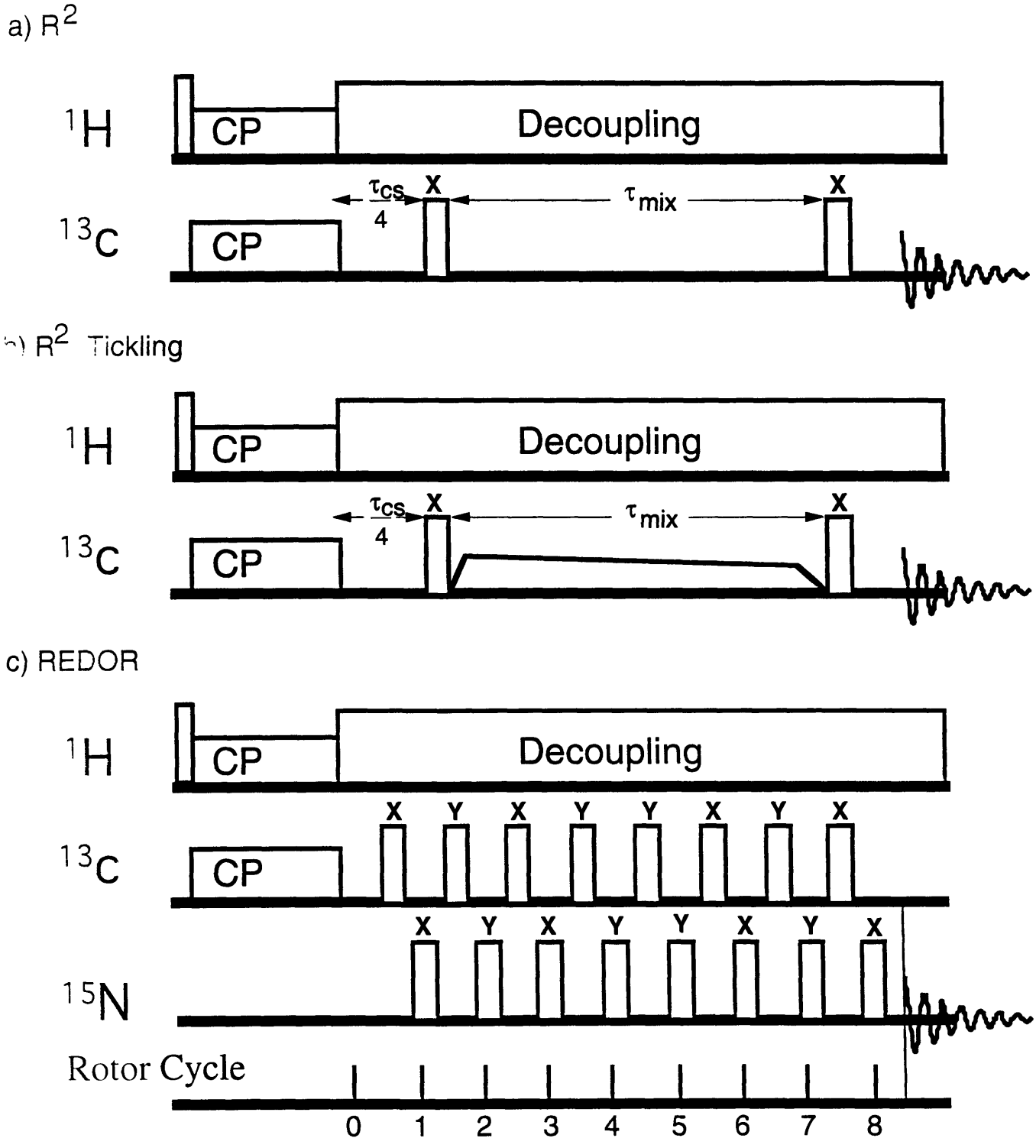

Figure 6-5 Dipolar recoupling pulse sequences.

speed above and below the resonance condition and monitoring the difference in R^2 exchange. R^2 tickling circumvents the need to accurately determine T_2^{ZQ} by using rf fields to ramp through the resonance condition. One spins at a frequency slightly higher than the chemical shift difference; a weak rf field is then applied to so that the combination of the chemical shift difference and the rf field match the spinning speed. The rate at which this combination proceeds through the resonance condition may be controlled by varying the ramp rate of the rf field. Measuring the degree of exchange as a function of the ramp rate yields the dipole coupling.

In the REDOR pulse sequence, rotor-synchronized pulses are applied to interrupt the spatial averaging of the dipolar coupling. Applying a π pulse changes the sign of the dipolar interaction; a minimum of 2 π pulses per rotor period leads to reintroduction of the heteronuclear dipolar coupling so that the magnetization is not completely refocused at the end of the rotor cycle. The rate at which the magnetization changes as a function of the number of rotor cycles the sequence is applied depends on the dipolar coupling. Analytic solutions for this dependence have been developed and have proved useful for large dipolar couplings (Mueller, 1995). In practice, one generally measures the time dependence of the magnetization both with and without pulses on the nonobserve channel to correct for loss of magnetization due to relaxation of the observed spin.

Figure 6-6 shows the REDOR exchange curve and simulated decay between the carbonyl carbon on the fourth amino acid and the nitrogen on the sixth amino acid. Also shown are experimental and simulated exchange curves for [1-^{13}C, ^{15}N]-glycine. In this model compound the coupling between the carbon and nitrogen is 200 Hz based on an x-ray crystal structure. The simulated curves for a REDOR experiment with infinitely large rf fields, a calculation with corrections for the finite pulsewidths used in the actual experiment, and the predicted dephasing including both relative decay of two spin coherences and correction for finite pulsewidths are indicated. From these simulations, it is apparent that failure to include finite pulsewidths in the calculation can lead to significant underestimation

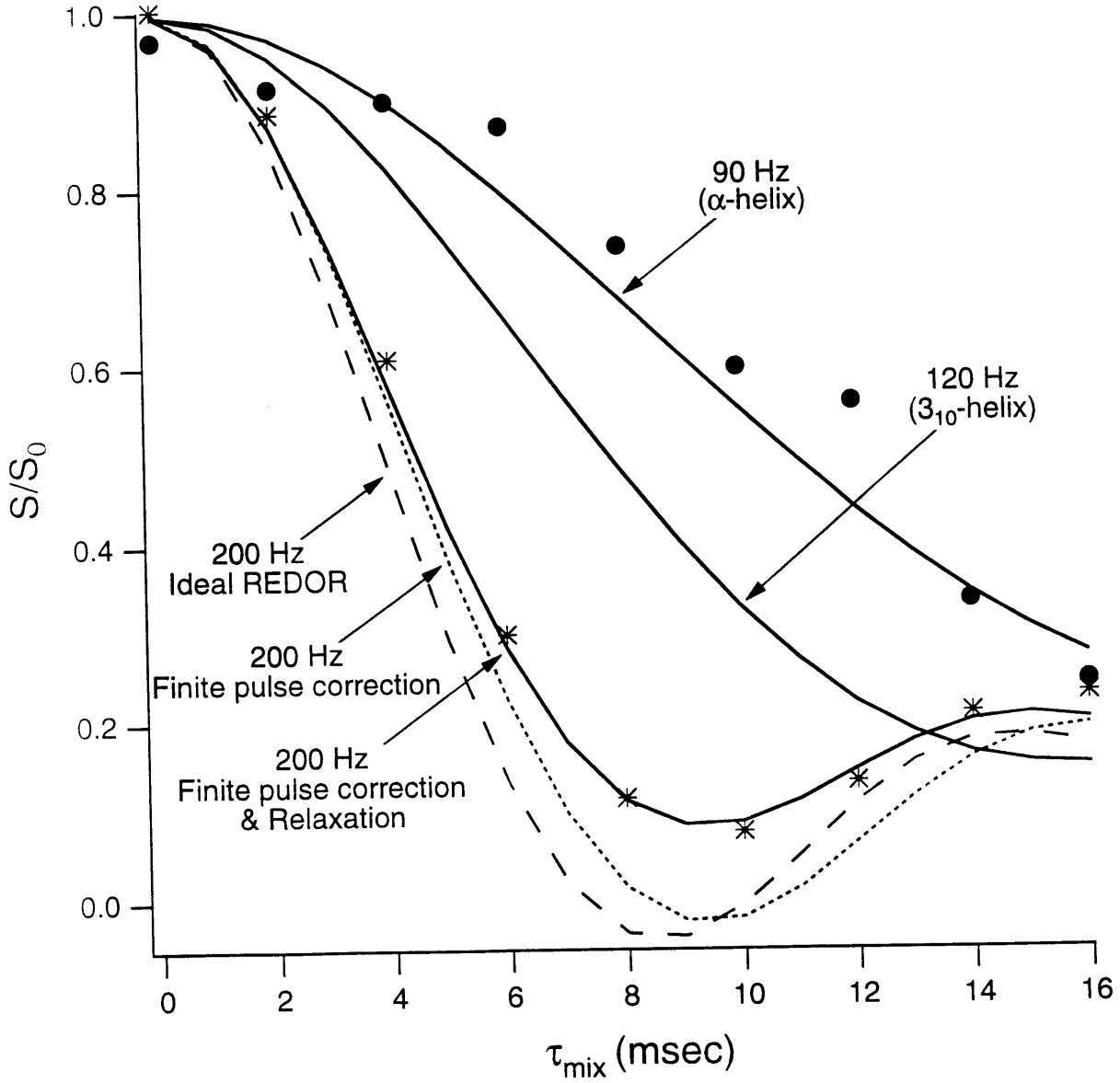

Figure 6-6 REDOR exchange curves for (●) 4-^{13}C=O, 6-^{15}N peptide and (*) [1-^{13}C,^{15}N] glycine with simulations as indicated.

of the dipole coupling and consequent overestimation of the internuclear distance. The effect of relaxation is to decrease the amount of dephasing observed, but the time course of the oscillation is unchanged (Bennett, 1995). However, for longer distances where collecting data at timepoints long enough to see oscillation is unfeasible, omission of either finite pulsewidth correction or relaxation leads to overestimation of the internuclear distance.

The exchange curve for the labelled peptide can be more consistently fit with a longer distance indicating the peptide is alpha-helical for this portion of the helix. However, the exact distance measured is somewhat questionable. Another possibility is that more than one folded structures exists and that the curve could arise from a combination of two or more dipole couplings. A less model-dependent approach to measuring the internuclear distance or distances would be to use stronger rf fields (50-75 kHz as opposed to 30 kHz) on the low frequency channels and to acquire data for a significantly longer mixing time (32 msec vs. 16 msec) so that oscillation of the decay may be observed. If these criteria were met, the decay curve could be transformed into the frequency domain and the dipole couplings and their distribution could be directly measured (Mueller et al., 1995). However, this would require extremely good signal to noise in addition to strong rf fields. To date, this technique has only been applied to couplings greater than 200 Hz (Jarvie et al., 1996).

An independent means of varying this distance would be to measure a second internuclear distance, preferably one that would be shorter in the alpha-helical conformation in comparison to the distance in the 3_{10}-helix. One possibility is the carbon-carbon distance between the carbonyl of the third amino acid and the beta carbon of the sixth amino acid. Figure 6-7 shows the R^2 exchange curves with and without inversion for this coupling at spinning speeds equal to half the chemical shift difference (n=2) along with polynomial fits. However, theoretical fitting of a dipolar coupling to this data is highly dependent on the choice of T_2^{ZQ} and one can match a smaller (larger) dipolar coupling by merely decreasing (increasing) T_2^{ZQ}. The linewidths of the resonances in these peptides are typically

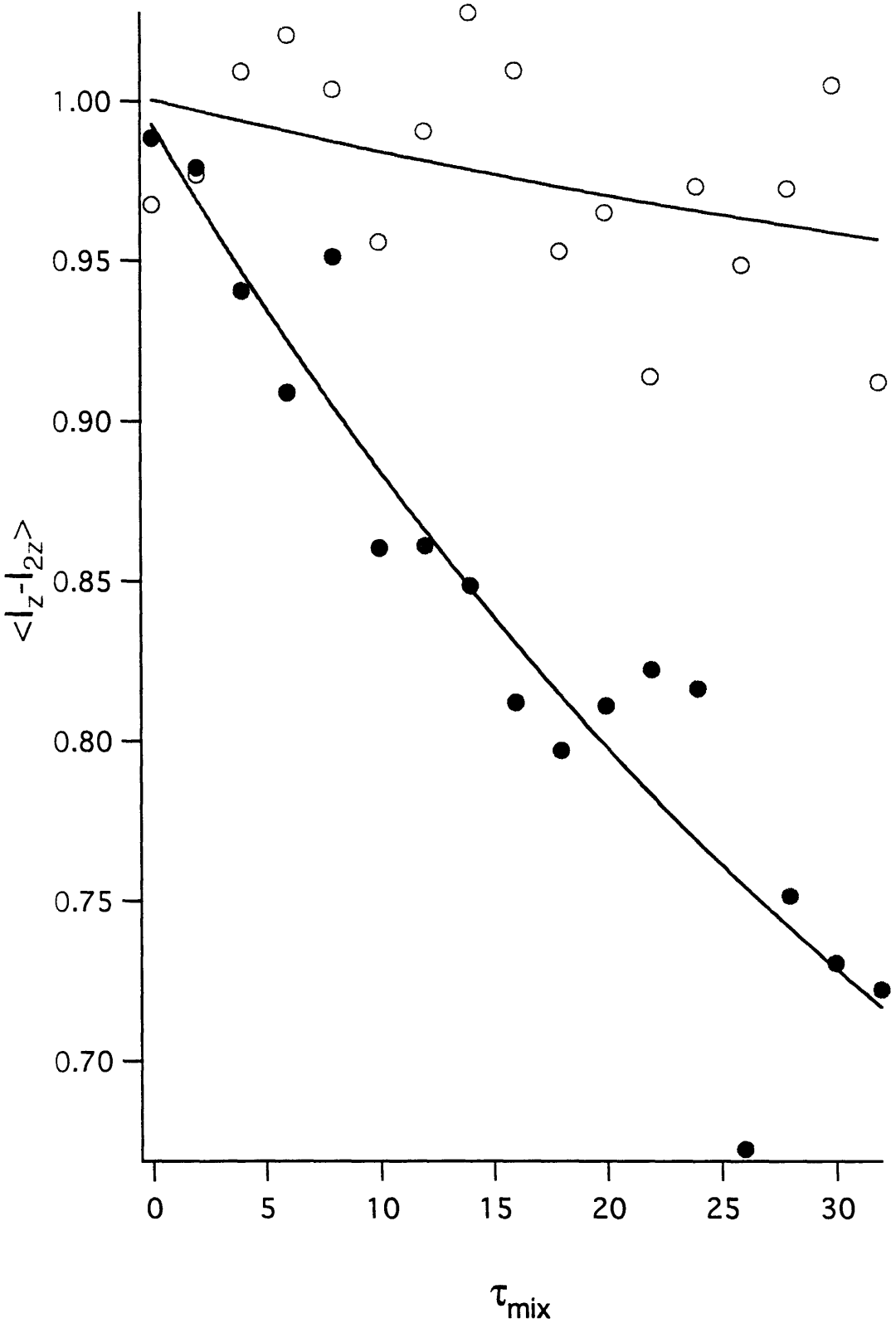

Figure 6-7 n=2 R^2 exchange curve for 3-^{13}C=O, 6-$^{13}C\beta$ peptide (●) with and (O) without inversion; solid lines are polynomial fits *not* theoretical simulations.

on the order of 200 Hz (see Figure 6-4) which can either be attributed to chemical shift dispersion or T_2. One can estimate their contributions by measuring T_2 directly via an echo experiment or by measuring the dependence of the exchange with respect to the spinning speed. However, even if T_2 is known, the problem of chemical shift dispersion still exists. Rotational resonance can only be achieved for all parts of the lines if the chemical shifts of the two carbons are correlated correctly; i.e. when the structure is slightly altered, do both the carbon resonances shift upfield or does the carbonyl shift downfield and the beta carbon shift move upfield? One way to circumvent this problem and to make the exchange rate less dependent on T_2^{ZQ} would be to use R^2 Tickling.

6.1.c Materials and Methods

Sample Preparation. Alanine specifically ^{13}C-labelled and ^{15}N-labelled was purchased from Cambridge Isotopes Laboratory and N-α-Fmoc protected. TLC showed the protected amino acids to be of high purity. Peptides were synthesized using standard solid phase Fmoc chemistry on MBHA resin (Novabiochem) with Kaiser tests after each coupling, repeated couplings if necessary, and acetic anhydride capping to terminate any residual deletion peptides, and a final capping with acetic anhydride at the amino terminus. Cleavage was accomplished with neat TFA after several washes with methylene chloride and N,N-dimethyl formamide. The peptide was subsequently washed repeatedly with ether. Analytical HPLC and MS indicated a high degree of purity so no further purification was done. The dried peptide was then dissolved in 5 mmol MOPS, pH 7.0 and allowed to equilibrate at 0° C. The chilled solution was sprayed into an isopentane bath at -130° C. After removing the isopentane under vacuum, the resulting snow was lyophilized overnight. The dry powder was then packed in a rotor and examined at room temperature. Chemical shift spectra indicate that the powder is stable over a typical spectrometer run (less than 7 days) but over the course of a few months at room temperature the amount of hydrogen bonding decreases, especially near the ends, indicating some fraying.

NMR experiments. The ^{13}C spectra were acquired at 100 MHz on a homebuilt spectrometer using a homebuilt transmission line probe equipped with a 4 mm Chemagnetics spinner assembly. The proton rf field (resonant frequency 397.8 MHz) was typically 100 kHz. For the REDOR experiment the ^{13}C π pulsewidth was 15.0 μsec , the ^{15}N π pulsewidth was 19.4 μsec, and the initial ^{1}H pulse was 2.5 μsec. XY-8 phase cycling was employed on both channels and data was taken every 16 rotor cycles at a spinning speed of 8 kHz. Typically 512 scans were acquired for each time point both with and without ^{15}N pulses using a recycle delay of 3 sec. In R^2 a delay between the cross polarization and the initial ^{13}C $\pi/2$ pulse was used to accomplish inversion. The ^{13}C $\pi/2$ pulsewidth was 7.5 μsec and the ^{1}H $\pi/2$ pulsewidth was 2.5 μsec. The mixing time was varied from 0 to 32 msec. Spectra were taken both with and without the delay for inversion at each timepoint with 512 scans per spectrum and a recycle delay of 3 sec.

Generation of decay curves. The decay for each resonance in both experiments was measured and corrected for natural abundance background. Additionally, the amount of disordered peptide was estimated by fitting the resonances with a linear combination of two gaussian lines using Sigmafit and subtracted from the decay since unfolded structures would generally have a coupling of less than 20 Hz. Examination of the final timepoints showed this assumption to be valid. Numerical simulations for the REDOR decay curves were done using a computer program developed by Andrew Bennett (Bennett, 1995) which simulates exchange between two spins subject to relaxation both during and between the rf pulses. For both the glycine and peptide curves generated in Figure 6, a relaxation parameter, Γ=60 Hz, was introduced. R^2 simulations were done using a program written by Malcolm Levitt, with improvements by Boqin Sun and Phil Costa.

6.2 Dynamics

Previous chapters have demonstrated the utility of deuterium NMR in examining various kinds of motion as well as the rates at which they occur. Peptide folding is another area in which this technique can provide insights. However, in order to gain useful information, it is necessary to make the peptide behave anisotropically; i.e. the peptide needs to be attached to a support to prevent rapid isotropic tumbling of the peptide. Once this is accomplished, more specific dynamics such as helix formation may be investigated. The simplest way to accomplish this is to leave the peptide attached to resin on which it is synthesized. The more widely-used resins are polystyrene based and thus hydrophobic (Stewart & Young, 1984), but in recent years considerable work has been done to develop resins which are more polar. There are now several commercially available resins which are based on the incorporation of polyamide, polyethylene glycol, or some other polar substance onto a more stable support such as polystyrene or Kieselguhr (Dryland & Sheppard, 1986; Small & Sherrington, 1989). In fact, immunization using peptides attached to resins has become a popular method for generating antibodies (Hanin & al., 1989).

The recent surge in popularity of generating peptide libraries using combinatorial chemistry has led to investigations of the peptides attached to the resins on which they are synthesized. NMR spectra obtained using magic angle spinning indicate that the dipole couplings are somewhat averaged by molecular motion making the attainment of high resolution spectra using standard liquid NMR pulse experiments possible. This motion led to concern about whether a peptide attached to a resin would still exhibit too much motion for useful information to be extracted from deuterium spectra. To investigate this possibility, peptides containing eight alanines deuterated at the methyl group were synthesized on two different resins with good water absorption characteristics. NovaSyn® KD resin is a copolymer of acrylsarcosine methyl ester, dimethylacrylamide and bis-acryloylethylenediamine within the pores of a Kieselguhr support. It is functionalized with ethylenediamine.

NovaSyn® TG resin consists of a low-cross linked polystyrene resin to which polyethylene glycol is attached and functionalized with an amino group.

6.2a ^{2}H NMR

The samples were hydrated using deuterium-depleted water and then examined with deuterium NMR at several temperatures. Figures 6-8 and 6-9 show the resulting spectra for the peptide attached to the TG and KD resins, respectively. What is striking about these spectra is the dissimilarity between the two resins. The spectra of the peptide on the TG resin exhibit lineshapes consistent with a system consisting of two phases for which exchange between the two phases is slower than the timescale of the experiment. This is reminiscent of the two phase spectra seen for NPGS and Cholesterol in Chapter 5. The peptide spectra are a combination of a powder lineshape produced by fast axial hopping of the methyl group and an isotropic peak resulting from large amplitude (or highly symmetric), fast motions. The splitting observed in the powder lineshape is that expected for a methyl group which is only undergoing fast axial rotation ($\Delta\nu_Q$=42 kHz); it is not averaged further by other motion. Thus the sample consists of two populations: one which is highly constricted in its motion and a second one with little constraints on its dynamics. The effect of changing the temperature is to change the relative populations of the two phases, but the overall characteristics of the lineshapes remain unchanged. It should be noted that almost all the spectra are taken below 0° C so a high amount of helix formation is expected although it may be somewhat altered due to attachment to the resin.

In contrast, the spectra taken of the peptide attached to KD resin exhibit a strong temperature dependence. The lineshape and intensity are both highly dependent on temperature and indicate that motion on the timescale of the quadrupole echo sequence is occurring. Also of note is that only at -11° C does the spectrum appear to be a combination of two lineshapes; at all other temperatures only one powder pattern is observed. (It is even possible that the spectrum at -11° C is only one powder pattern, similar to the pattern seen for three-site hops at intermediate rates.) This means that only one phase exists or that

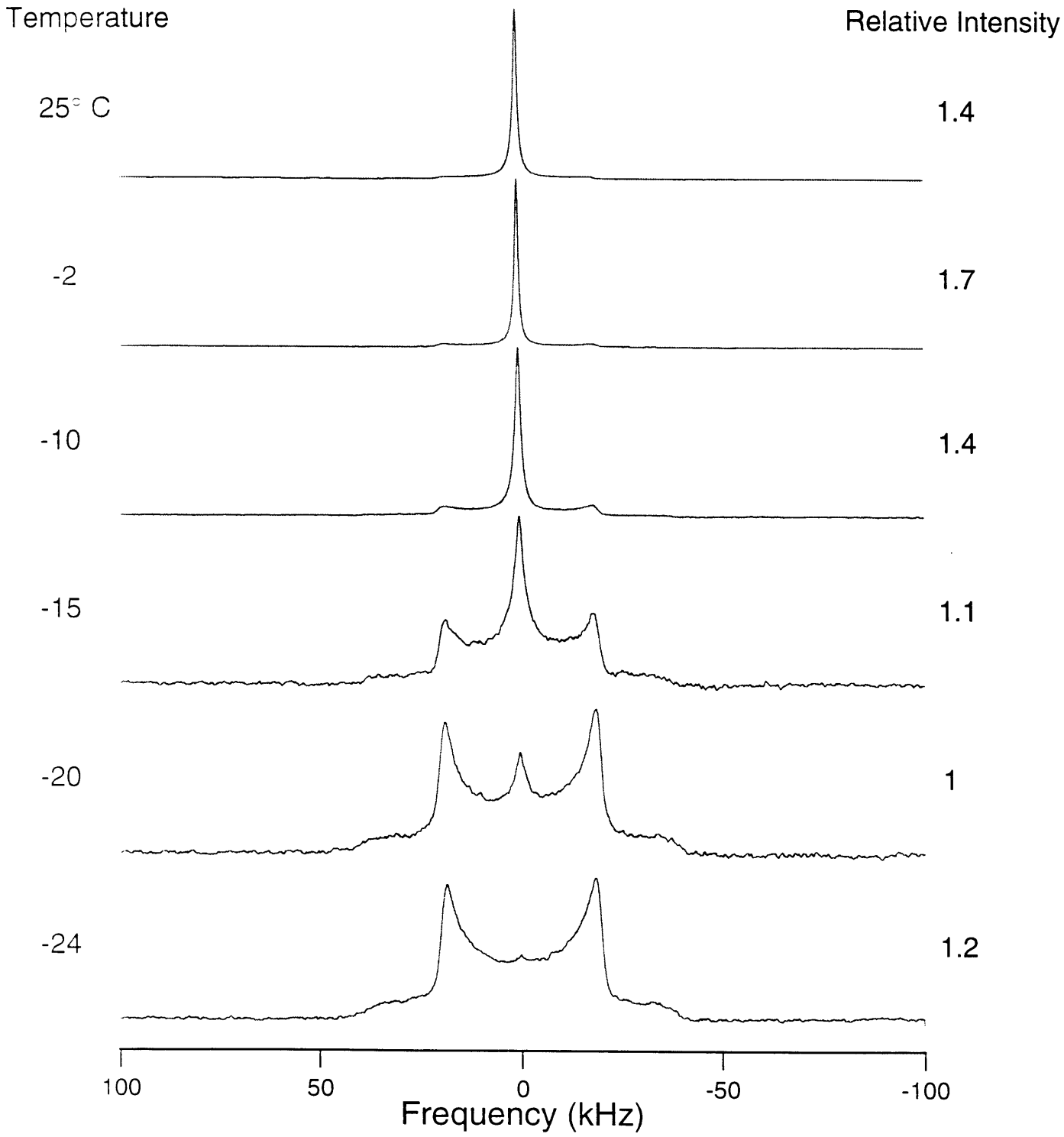

Figure 6-8 Deuterium spectra of 8-[Ala-CD_3] peptide attached to TG resin.

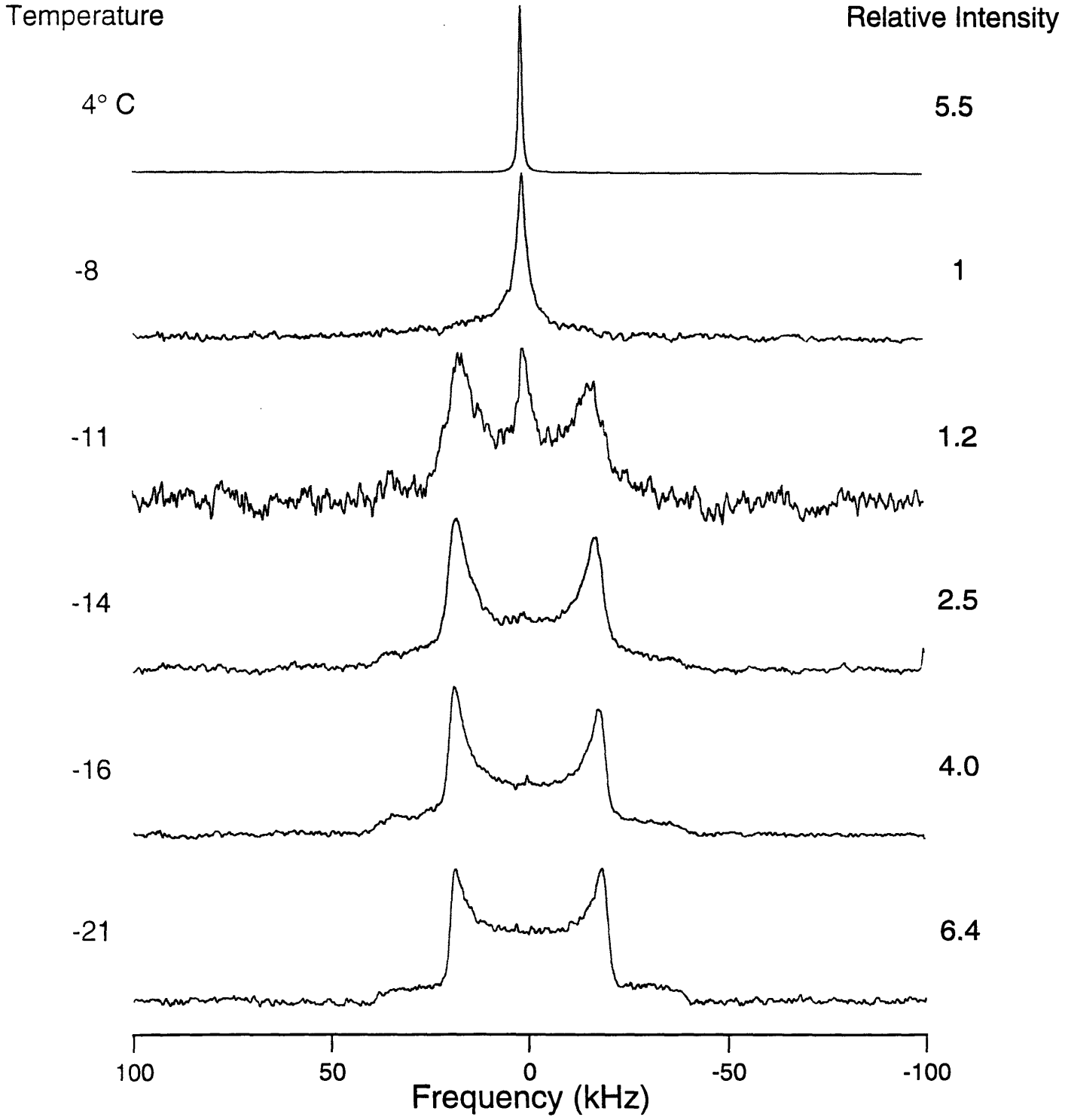

Figure 6-9 Deuterium spectra of 8-[Ala-CD_3] peptide attached to KD resin.

exchange between any phases is fast on the NMR timescale. Given the splittings observed, the existence of only one phase is more probable. The spectrum observed at -21° C is consistent with fast-limit methyl group three-site hopping being the only type of motion. As the temperature is increased, the intensity in the middle of the powder lineshape decreases; this is similar to what has been seen in DNA with the onset of restricted diffusion or wobble (Gary Drobny and Mary Hatcher, private communication). The intensity continues to drop until at between -11° C and -8° C the motion becomes isotropic. Even at -8° C the intensity is still somewhat diminished suggesting that even though there is significant motional averaging occurring, it is still on the timescale of the experiment.

A common feature of both systems is that all eight of the labelled alanines in the peptides give the same splittings; this is in contrast to what is seen in perdeuterated lipids. This suggests that motions occurring in these systems are highly cooperative. A high degree of cooperativity is predicted in Zimm-Bragg theory given the high barrier to the formation of the first helical conformation due to loss of entropy. Once helix formation is initiated, subsequent hydrogen bonding does not result in a large loss of entropy and is highly favored.

One explanation for the two phases seen in spectra of peptides on the TG resin is that the concentration of peptide is high enough that interpeptide hydrogen bonding may occur. A study of polyglycine attached to polystyrene suspended in DMF had similar deuterium spectra for peptides longer than six amino acids (Ludwick et al., 1986). ^{13}C spectra of this system exhibited losses of isotropic resonances for the polystyrene matrix concurrent with the conditions under which the deuterium spectra showed the appearance of static powder lineshapes suggesting that intermolecular interactions were leading to a loss of mobility. For these experiments, the concentration was 0.5 mequiv of peptide/g of polystyrene; for the peptide/TG resin system, the concentration is 0.3 mequiv peptide/g of resin. The polyethylene glycol in the resin provides a tether of length and mobility to fur-

ther make interpeptide hydrogen bonding possible. In effect, the local concentration of the peptide could be high enough to result in aggregation.

If interpeptide interactions are occurring in the peptide/TG resin system, this has significant ramifications for the development of rapid screening methods of small peptide libraries. This resin has been developed to respond well in aqueous media so that peptides may be left attached to it for antibody screening. For short peptides this is probably not a problem, but for peptides greater than 5 or 6 amino acids, the possibility of interpeptide interactions should be kept in mind when developing protocols for antibody screening. Decreasing the loading potential of the resin would eliminate this problem, but this leads to a greater need for materials, an important consideration when developing a 6mer library (with 20^6 possible combinations). To confirm that intermolecular interactions are occurring, ^{13}C and ^{1}H experiments should be conducted on the peptide/TG resin system.

6.2.b Materials and Methods

Sample preparation. The Kieselguhr based (KD) resin has a somewhat lower loading concentration--0.1 mequiv peptide/g of resin and a much shorter tether. These two characteristics may explain why the two peptide/resin systems yield such disparate deuterium spectra. It is clear from the deuterium spectra of the peptide on the KD resin that a motion on the order of 10^5-10^6/sec is occurring at -11° C. What this motion is is open to debate. It appears all eight of the labelled alanines are equally affected by the motion, suggesting a high degree of cooperatively. Two possibilities are equally plausible: the peptide is undergoing a phase transition and the exchange between the two phases is on the timescale of the pulse experiment or the peptide is exhibiting a type of motion which is intermediate in rate at this temperature. If it is a phase transition, intermolecular interactions may be implicated as was suggested for the peptide on the TG resin. However, aggregation seems unlikely in light of the spectrum at -14° C. This spectrum indicates some motion is already ongoing although no isotropic peak is evident. If a specific type of motion is governing the spectra at these temperatures, what the origin of the motion is open to debate.

One explanation is that the resin to which the peptide is attached is undergoing a concerted motion and the peptide indirectly displays the effects of this motion. The other possibility is that the peptide itself has a characteristic motion on the appropriate timescale at these temperatures. To investigate which of these phenomena is the cause, deuterium spectra of a single alanine attached to the resin should be taken.

Sample Preparation. Methyl-deuterated alanine was purchased from Cambridge Isotopes Laboratory and N-α-Fmoc protected. TLC showed the protected amino acids to be of high purity. Peptides were synthesized using standard solid phase Fmoc chemistry with Kaiser tests after each coupling, repeated couplings if necessary, and acetic anhydride capping to terminate any residual deletion peptides and a final acetic anhydride cap. The first amino acid of the peptide was directly attached to the resins without an acid labile linker. The Boc protecting groups on the lysines were removed using a 1:1 mixture of TFA:Dichloromethane. The peptide/resin system was then washed repeatedly with methylene chloride and methanol and dried overnight under high vacuum. The dried peptide/resin was then suspended in an excess of 5 mmol MOPS in deuterium-depleted water (CIL), pH 7.0 and sealed in glass.

NMR experiments. The ^{2}H spectra were acquired at 61 MHz on a homebuilt spectrometer using a homebuilt probe equipped with a 5 mm coil. Typically the ^{2}H pulse was 2.4 μsec, and an echo delay of 30 μsec was used in the quadrupole echo sequence. Phase cycling and quadrature detection were employed with a recycle delay of 1 sec. Typically 256- 2048 scans were acquired, depending on the intensity at a specific temperature.

References

Bennett, A.E. (1995) *Dipolar recoupling and decoupling in solid state nuclear magnetic resonance spectroscopy,* Massachusetts Institute of Technology,

Bennett, A.E., Griffin, R.G. & Vega, S. (1994) in *Solid-State NMR IV: Methods and Applications of Solid-State NMR* (Blumich, B., Ed.) 1-77, Springer-Verlag, Berlin.

Bierzynski, A., Kim, P.S. & Baldwin, R.L. (1982) *Proc. Nat. Acad. Sci. 79*, 2470-2474.

Brown, J.E. & Klee, W.A. (1971) *Biochemistry 10*, 470-476.

Dryland, A. & Sheppard. (1986) *J. Chem. Soc., Perkins Trans. 1986*, 125.

Griffiths, J.M. & Griffin, R.G. (1993) *Anal. Chim. Acta 283*, 1081-1101.

Hanin, V. et al. (1989) *Peptide Research 2*, 367.

Jarvie, T.P., Went, G.T. & Mueller, K.T. (1996) *J. Amer. Chem. Soc. 118*, 5330-5331.

Ludwick, A.G., Jelinski, L.W., Live, D., Kintanar, A. & Dumais, J.J. (1986) *J. Amer. Chem. Soc. 108*, 6493-6496.

Marqusee, S., Robbins, V. & Baldwin, R.L. (1989) *Proc. Nat. Acad. Sci. 86*, 5286-90.

Miick, S.M., Martinez, G.V., Fiori, W.R., Todd, A.P. & Millhauser, G.L. (1992) *Nature 359*, 653-655.

Mueller, K.T. (1995) *J. Mag. Res. A 113*, 81-93.

Mueller, K.T., Jarvie, T.P., Aurentz, D.J. & Roberts, B.W. (1995) *Chem. Phys. Lett. 242*, 535-542.

Saito, H., Tabeta, R., Ando, I., Ozaki, T. & Shoji, A. (1983) *Macromolecules 16*, 1050.

Shoemaker, K.R., Kim, P.S., Brems, D.N., Marqusee, S., York, E.J., Chaiken, I.M., Stewart, J.M. & Baldwin, R.L. (1985) *Proc. Nat. Acad. of Sci. 82*, 2349-2353.

Small, P.W. & Sherrington, D.C. (1989) *J. Chem. Soc., Chemical Comm. 1989*, 1589.

Stewart, J.M. & Young, J.D. (1984) *Solid Phase Peptide Synthesis*, Pierce Chemical Company, Illinois.

Voet, D. & Voet, J. (1990) *Biochemistry*, John Wiley & Sons, New York.

5778-11